PhD Thesis

Integrated Modelling of Hydrodynamic Processes, Faecal Indicator Organisms and Related Parameters with Improved Accuracy using Parallel (GPU) Computing

Author:

Brian Adjetey Boye

brian.boye@brinsy.com

www.brinsy.com

Supervisor:

Prof. Roger A. Falconer

Industrial Supervisor:

Dr. Kunle Akande

May 28, 2014

Dedicated to my parents, Mrs. Sarah Narkie Boye and Hon. Emmanuel Adjei Boye,

for supporting and believing in me throughout this PhD

Abstract

Environmental problems and issues are not limited by artificial boundaries created by man. Usually there are different teams or individuals working on the catchments, estuaries, rivers and coastal basins in different countries using different parameters and formulations for various processes. However, the system is a natural one and as such no boundaries exist. When a rain drop of water moves from a catchment to a stream, river or estuary and to the sea, it does not know at any stage whether it is in the catchment, river, estuary or sea.

In recent years there has been growing concern about the impact of diffuse source pollution on river, estuarine and coastal water quality and particularly with regard to non-compliance of bathing waters. Hydro-environmental impact assessment modelling studies are generally regarded as having several fundamental shortcomings in model simulations, which can lead to erroneous environmental impact assessment outcomes.

These shortcomings were addressed in this project and included:

1. Applying a Cloud to Coast (C2C) approach to modelling flow and solute transport processes in river, estuarine and coastal waters;

2. Improving the computational linking of catchment, river and estuarine-coastal models;

3. Improving the kinetic decay process representation in deterministic models, to include the impacts of salinity, solar irradiance, turbidity and temperature, and;

4. Using parallel (GPU based) computing to enhance the computational speed in executing bathing water quality models.

In this research study, the Ribble Estuary and Fylde Coast model was refined to more accurately predict bathing water quality and use parameters which give a

better representation of the existing physical and bio-chemical processes. A Cloud to Coast (C2C) approach to modelling was implemented by using common input parameters and formulations in both the 1-D and 2-D domains of the Ribble Estuary and Fylde Coast model. An empirical formulation linking the mortality (decay) rate of bacterial water quality indicators to environmental conditions such as solar irradiation, turbidity, temperature and salinity was added to the numerical code. The linked boundary between the 1-D and 2-D domains of the numerical model was improved by removing the large overlapped linked region.

An existing numerical code was rewritten to take advantage of the parallel computing capability of the Graphics Processing Unit (GPU). This was tested on the Ribble Estuary and the Thames Estuary model. Thames Estuary models of varying mesh density were prepared in this research study using lots of bathymetric data (over 80 million points) and tested on the GPU.

This research study improved the ability to predict bathing water quality accurately by introducing more realistic representation of environmental conditions and using parallel computing. This improved the ability to carry real time forecasting of bathing water quality and hence prevent failure to meet the requirements of the EU Bathing Water Directive.

Acknowledgements

There are many people to whom, I am most grateful for their help and contribution to this research work.

I would like to thank God for giving me the strength and motivation to start and complete this research work.

I would like to thank my parents, Mrs Sarah Boye and Mr Emmanuel Boye, for their invaluable support throughout my studies.

I would like to express my gratitude and appreciation to Professor Roger A. Falconer for his continued advice, support and encouragement throughout the period of this research project.

I also acknowledge the Natural Environmental Research Council (NERC) and CH2M Hill (Halcrow) who funded the Industrial Case Studentship under which this research work was carried out. I am also grateful to the Environment Agency for providing data for the Thames Estuary.

Members of the Cloud to Coast project on the Scientific Technical and Management Board, Carl Stapleton, David Kay, etc.

The help provided by those people who created and made available TEX, LATEX, Linux, gnuplot and other tools which made my research study easier is also greatly appreciated.

I would like to thank all of the Research Staff and members of the Hydro-environmental Research Centre for their kindness and continuous assistance during my PhD. And also, to all my friends for all their help and encouragement throughout my studies.

Contents

List of Figures

List of Tables

List of Symbols

α_i	coefficient of irradiation which is dependent on the type of bacteria (area per unit energy)
a	Tube radius
β_c	River channel shape parameter
B	River half width
c_p	heat capacity of water (energy per unit mass per unit temperature)
C_{sal}	Salinity in parts per thousand
ΔI_y	Moment of inertia about the y axis
δ_{ij}	The Kronecker delta
Δt	time step
Δx,Δy,Δz	grid size in x, y and z dimensions
D_l	Longitudinal dispersion coefficient
D_{xx}	dispersion-diffusion coefficient in xx direction
D_{xy}	dispersion-diffusion coefficient in xy direction
D_{yy}	dispersion-diffusion coefficient in yy direction
ε_{xx}	Normal strain in xx direction

ε_{yy}	Normal strain in yy direction
ε_{zz}	Normal strain in zz direction
E	Young's modulus (Force per unit area)
e	Volume of dilation
F_n	Froude number
F_p	Fraction of bacteria attached to sediment
γ_{xy}	Angular strain in xy direction
γ_{xz}	Angular strain in xz direction
γ_{yz}	Angular strain in yz direction
G	Shear modulus (Force per unit area)
g	Acceleration due to gravity
H	Depth of flow
I_0	Solar irradiation intensity at the surface of the water body (power per unit area)
$I_0(t)$	Solar irradiation intensity at the surface of the water body as a function of time (power per unit area)
k_e	light extinction coefficient
K	the overall heat exchange coefficient (power per unit area per unit temperature)
k_b'	total effective bacterial decay rate
k_0	zero order growth (+ve)/decay (-ve)
k_1	first order growth (+ve)/decay (-ve)

k_d	dark coliform decay rate coefficient at 20 °C
k_i	coliform decay rate due to depth averaged effect of solar radiation
k_l	Longitudinal dispersion constant
k_t	Turbulent dispersion constant
k_{sal}	bacterial decay rate due to salinity
μ	dynamic viscosity
ν	Poisson's ratio
ω_y	Angular acceleration
p	Hydrostatic pressure (Force per unit area)
P_r	generalized roughness parameter incorporating the influence of resistance and blockage effects
ppt	parts per thousand
Q	Discharge / flow
Q_{Li}	Lateral flow at node in one-dimensional model
R	Hydraulic radius
ρ	mass / unit volume or mass density of fluid
ρ_w	density of water
S_f	Slope of energy grade line or friction slope
σ_{xx}	Normal stress in xx direction (Force per unit area)
σ_{yy}	Normal stress in yy direction (Force per unit area)
σ_{zz}	Normal stress in zz direction (Force per unit area)

s	mass concentration of solute
S_n	River channel sinuosity
τ_{xy}	Shear stress in xy direction (Force per unit area)
τ_{xz}	Shear stress in xz direction (Force per unit area)
τ_{yz}	Shear stress in yz direction (Force per unit area)
θ_w	empirical coefficient for water temperature effects
θ_{sal}	coefficient for salinity effect
T_e	equilibrium temperature
T_{90}	Time for 90 % of bacteria to decay
T	Water temperature
t	time
u	velocity in x direction
U	Mean velocity
U^*	Shear velocity
U_w	Wind speed
v	velocity in y direction
v_s	Settling velocity of sediment
w	velocity in z direction
W	Flow width
X	Body force per unit mass in x direction
Y	Body force per unit mass in y direction

Z	Body force per unit mass in z direction
z_{SD}	Secchi-disk depth

Chapter 1

Introduction

1.1 Research Drivers

There is an ever increasing need to ensure clean and healthy bathing waters. Water is essential for human life, nature and the economy. All forms of life, including plants and animals, need water to survive. In humans, water is essential for a lot of bodily functions. These include temperature regulation, metabolism, flushing out toxins, delivering nutrients to cells, etc. Polluted water can therefore have a negative impact on our health. Apart from the need for drinking water to survive, the numerous other uses of water include: cooking, washing/cleaning, recreation, farming and the manufacture of goods etc. Water is also a major contributor to the advancement of civilisation. Most sectors of the economy therefore need water to be successful. This research project focuses on modelling and predicting the quality of water in recreational bathing waters. The quality of water in bathing waters is important because of the potential negative health and economic impacts that can occur if the water is polluted.

The principal sources of bathing water pollution are: diffuse sources, such as background losses (e.g. forests), losses from agriculture, losses from scattered dwellings and atmospheric deposition on water bodies (e.g. marine areas or lakes); and point sources such as discharges from urban waste water and industry. Polluted

water is spread from its source to the bathing sites via advection and diffusion processes, which can be enhanced by factors such as storm events, wind and the morphology of local water bodies.

The measurement of pollution levels is done by testing for the presence of Faecal Indicator Organisms (FIOs). These organisms are usually present in the faeces of humans and warm blooded animals. The coliform group of bacteria are easily detected by simple laboratory tests, but these bacteria are generally not present in unpolluted waters and the number of indicator bacteria tends to correlate with the extent of contamination (Thomann and Mueller, 1987).

Efforts of the European Union to ensure clean and healthy bathing waters commenced in the 1970s. The 2006 Bathing Water Directive has provisions for: the monitoring and classification of bathing water quality; the management of bathing water quality; and the provision of information to the public on bathing water quality (European Parliament, 2006). Bathing waters are monitored and in accordance with the criteria set out in the Directive, they are classified as 'poor', 'sufficient', 'good' or 'excellent'. Member States are required to ensure that by the end of the 2015 bathing season, all bathing waters will be at least classified as 'sufficient'. A bathing water may be temporarily classified as 'poor' and still remain in compliance with the Directive provided that adequate management measures, including a bathing prohibition or advice against bathing, are implemented. If a bathing water is classified as 'poor' for five consecutive years, a permanent bathing prohibition or permanent advice against bathing must be implemented. Putting up signage with advice against bathing can have severe social and economic impacts, especially for towns like Blackpool, which is a major seaside resort.

The occurrence of polluted water is undesirable because of the health, social and economic impacts. It is therefore important to have a tool which aids management of the bathing water quality, such as deterministic Computational Fluid Dynamic (CFD) models. These models help to assess the water quality in bathing coastal waters,

estuaries and associated rivers. The models take account of both the hydrodynamic and solute transport processes involved in spreading pollutants from their sources through the bathing waters. Typically, different organisations or companies model different parts of the water system using differing assumptions and mathematical formulations. As a result, independent calibration of the different models can lead to different values for the parameters used to represent the underlying physics. For a more holistic assessment, all water bodies or systems need to be integrated into one model, from the rainfall catchments to the coast. This research seeks to show the benefits of more holistic models and a better representation of the physical and bio-chemical processes.

As a result of the modelling of these systems, several infrastructure projects are typically implemented. These projects include new improved sewerage systems, management of agricultural run-off and public awareness campaigns. However, even though the water quality of bathing waters has improved significantly in the UK since the 1970s, there are still occasional failures in complying with the EU Directive. As a result of these occasional failures it is becoming more important that the models used in accessing bathing water quality are more sophisticated and more accurate. This research seeks to refine the kinematic decay process of Faecal Indicator Organisms (FIOs). The ability to predict the quality of site specific bathing waters in a short period of time, before the high pollutant levels actually occur, is now more important because this will mean that warning signs about 'poor' water quality can be on display for a minimum time. This research also seeks to improve the ability to run existing models much faster so that they can be used as bathing water quality forecasting tools.

In summary, the main research drivers are: to use better physical representation, more holistic models and refined kinetic decay processes to improve the accuracy of bathing water quality prediction; and to improve the runtimes of models so that they can be used for realtime forecasting.

1.2 Research Objectives

The main aim of this research is to improve the ability to predict bathing water quality accurately by introducing more realistic representation of environmental conditions and using parallel computing. This will also improve the ability to carry real time forecasting of bathing water quality and hence prevent failure to meet the requirements of the EU bathing water Directive.

This research, driven by the issues in Section 1.1 raises several challenges. Firstly, implementing a holistic approach by combining different models introduces boundary issues. What is the best way to ensure continuity over the boundary? What is the best location for the boundary? How is information transferred across the boundary? This research takes an existing model and improves on the boundary and process representations on a number of fronts.

Secondly, using model parameters which better represent real world physical conditions may not give a better correlation with measured results. However, it is expected that this will give a better understanding of the predominant factors affecting the results and thereby lead to better management of water quality.

Thirdly, refining the kinetic decay processes of faecal indicator organisms will mean introducing an increased number of model parameters, so that real world effects are better represented. An increased number of model parameters influencing results means that more calibration of the model is required together with a greater number of model runs.

Finally, reducing the run times of the models will require parallel computation. This may mean expensive computer hardware, hardware specific code, difficult to debug code and code optimisation.

In order to meet the above challenges, the scope of the main issues was defined. The main models combined in this project were a 1D model and a 2D model. The factors included in the kinetic decay process representation were limited to solar radiation, turbidity, salinity and temperature. Parallel computing was implemented

using Graphics Processing Units (GPU), manufactured by NVIDIA.

In summary, the main objectives of this research are:

- Applying a C2C (Cloud to Coast) approach to modelling flow and solute transport processes in river, estuarine and coastal waters. This will be done by applying the same values and formulations for decay rates, longitudinal dispersion constants and bed friction parameters in both the one-dimensional (1D) and two-dimensional (2D) domains of a dynamically linked model.;

- Improving the computational linking of catchment, river and estuarine coastal models. This will be done by reducing the length of overlap at the interface between the one-dimensional (1D) and two-dimensional (2D) domains of a dynamically linked model.;

- Improving the kinetic decay process representation in deterministic models, through including the impact of salinity, solar radiation, turbidity and water temperature. This will be done by introducing formulations to include the effects of salinity, solar irradiation, turbidity and temperature on the decay rate. This will also require the additional modelling of salinity and water temperature in the model.; and

- Using parallel (GPU based) computing to enhance the computational speed, thereby increasing the ability to run more model scenarios, improve calibration, run bigger models and carry out real time water quality forecasting. This will be done by rewriting existing fortran code in C/C^{++}to utilise the parallel computing capability of graphics cards manufactured by NVIDIA.

1.3 Background Information

1.3.1 Ribble Estuary

The Ribble is a partially mixed shallow macrotidal estuary located in the United Kingdom (UK) on the northwest coast of England (Figure 1.1). Until the late 1970s the main channel of the estuary, which is enclosed within a training wall, was regularly dredged to allow passage to the upper estuary for shipping (Lyons, 1997). The Ribble is a sizeable river with a catchment area of over 860 square miles. The estuary itself is among the largest in the UK at over 10 miles wide, and is an important protected site for overwintering sea birds.

Figure 1.1: Location of Ribble Estuary (Google Earth)

At the mouth of the estuary are two well known seaside resorts, namely Lytham St Annes and Southport, with both being designated EU (European Union) bathing waters. The coast (i.e. the Flyde Coast) near the mouth of the Estuary, includes one of the most famous beaches in England for tourism, namely Blackpool, with an

average of more than 17 million visitors per annum.

In order to enhance the bathing water quality along the Fylde Coast, a major civil engineering investment programme was undertaken to reduce the input of bacterial loads to the estuary. About £600 million was invested over the past 20 years in new works and treatment plants along the Flyde Coast and the Ribble Estuary. Although the reduction in input of bacterial loads has resulted in a marked decrease in the concentration of bacterial indicators in the coastal receiving waters, occasional elevated bacterial counts were still measured. As a result, the bathing waters still occasionally failed to comply with the EU mandatory water quality standards of the Bathing Framework Directive.

Currently, a vast £160 million project is being undertaken by United Utilities Plc which will enhance the sewer in Preston, in order to reduce pollution to the river Ribble (United Utilities, 2013). The project is expected to be completed by the end of March 2014. The project is split into two projects which are called Preston Tunnel and Preston 32.

This research seeks to improve existing hydro-environmental models by adopting an integrated (Cloud to Coast) approach, whilst refining the impact of temperature, salinity, solar radiation and turbidity on the decay of bacterial water quality indicators. The Ribble Estuary was chosen as the main case study for this research because of the location of the designated European Union (EU) bathing waters at Lytham St Annes and Southport. The site was also chosen because of the availability of measured data and information from a previous study by Kashefipour *et al.* (2002).

1.3.2 Thames Estuary

The Thames Estuary is located in London the capital city of the United Kingdom (Figure 1.2). It is the estuary where the River Thames meets the North Sea.

The Thames Estuary has a history of sewage sludge disposal, dating back to

about 1889 (Whitelaw and Andrews, 1988). It had a period of decline which climaxed in the 1950s when the river was completely devoid of oxygen and any fish put into the river would, in all probability, have choked to death. However, the water quality has continued to improve since that time. Projects such as the Lee Tunnel continue to help in improving the water quality of the Thames.

The Thames Estuary is particularly vulnerable to flooding. After the floods of 1928 the banks were raised and again in 1971 (Doxat, 1977). It has been recorded that fourteen people died during the floods of 1928 and 307 people died in the North Sea flood of 1953. The threat of flooding continues to increase slowly over time due to sea level rise and the sinking of the south east of England (post-glacial rebound). Mitigation against flooding has involved schemes to be progressed, such as the Thames Barrier.

The increasing need to predict flood levels means that longer model simulation runs are required for predicting floods of a long return period. Also, finer grid resolution meshes are required to predict flood levels to a greater level of accuracy. This research uses the Thames Estuary as a case study for assessing the benefits of the Graphics Processing Unit (GPU) as a platform for faster computations.

Figure 1.2: Location of the Thames Estuary in the UK (Google Earth)

1.4 Thesis Outline

This thesis has been organised into ten chapters and these chapters are outlined here as follows:

Chapter 1 : Introduction - Introducing the wider research drivers and more specific objectives for this PhD research. Background information about the two main case study sites is also given.

Chapter 2 : Literature Review - Review of the main literature applicable to this research study.

Chapter 3 : Derivation of the Governing Equations - Describes the theory behind the derivation of the general governing equations for fluid flow and solute transport.

Chapter 4 : Adaptation of the Governing Equations - Describes the theory behind the adaptation of the general governing equations for one-dimensional and two-dimensional flow by using time and spatial averaging.

Chapter 5 : Numerical Solution of Governing Equations - Describes how the adapted governing equations are discretised and solved numerically.

Chapter 6 : Development of Numerical Code - Describes the modifications and refinements to the numerical codes used in this research study.

Chapter 7 : Application to the Ribble Basin - Describes the application of the model to the Ribble Estuary. This includes an overview of previous work, revised analysis of the model, final model calibration and timing results of the GPU runs.

Chapter 8 : Application to the Thames Estuary - Describes the application of the model to the Thames Estuary. How the new model was set up, the hydrodynamic results and timing results of the GPU runs.

Chapter 9 : Conclusions - Outlines the final conclusions resulting from this research study.

Chapter 10 : Recommendations for Further Study - Outlines potential future research studies following on from this.

Chapter 2

Literature Review

2.1 Introduction

In this chapter the current state-of-the-art in the field of bathing water compliance and the relevant modelling of the governing hydrodynamic and water quality processes are reviewed. In Section 2.2, evidence of links between poor bathing water quality and health issues are presented based on the literature reviewed. In Section 2.3, the requirements of current European environmental legislation affecting bathing water quality is presented. Based on the literature, sources of bathing water contamination likely to cause failures in meeting European legislation requirements are reviewed in Section 2.4. In Section 2.5, the different types of bacteria used as indicators of water quality are reviewed. In Section 2.6, several aspects of the numerical modelling of bathing water quality are reviewed, including: the governing equations in Sub Section 2.6.1; the numerical schemes in Sub Section 2.6.2; dispersion in Sub Section 2.6.3; the coupling of models in Sub Section 2.6.4; and parallel computing in Sub Section 2.6.5. Finally in Section 2.7, the representation of the mortality of the bacterial indicators is reviewed.

2.2 Bathing Water Quality

Bathing water quality is an important public health issue, mainly due to faecal contamination (Mansilha *et al.*, 2009). In 2006 the European Commission (EC) adopted a new directive (European Parliament, 2006) with respect to recreational bathing waters that calls for stricter standards, replacing policies of the EC Bathing Water Directive that have existed since 1976.

There is considerable epidemiological evidence in the literature to suggest that contact with polluted recreational waters is a risk factor for gastrointestinal illness, including serious health problems, such as infection with Shigella sonneri, Escherichia coli O157, protozoan parasites and enteric viruses, mainly derived from human sewage or animal sources (Prüss, 1998; Pond, 2005; Nicholis, 2006). Epidemiological studies have used bathing trials to examine the relationship between microbiological indicators of water quality and diaries of symptoms kept by the participating volunteers (Kay *et al.*, 1994). In a study by Kueh *et al.* (1995), it was observed that gastrointestinal (GI) symptoms were directly related to the pollution level and bacterial content of beach water. Turbidity of beach water was also closely linked with GI and highly credible GI symptoms. The groups at highest risk of disease from contamination are children, who tend to play for longer periods of time in recreational waters and may swallow more water, either intentionally or accidentally, than adults, and tourists, who lack immunity against local endemic pathogens (World Health Organization, 2003). Schets *et al.* (2011) who collected exposure data for swimmers in fresh water, seawater and swimming pools, also found that children behaved differently: they swam more often, stayed in the water longer, submerged their heads more often and swallowed more water. In 1986, the United States Environmental Protection Agency (USEPA) recommended that E. coli and enterococci monitoring replace faecal coliform monitoring in ensuring State Water Quality Standards (US Environmental Protection Agency, 1986). The recommendation was based upon a study that demonstrated a statistically significant relationship between the rate

of swimming-related illnesses and the concentrations of E. coli and enterococci at freshwater beaches (Dufour, 1984; Edberg *et al.*, 1997). From the evidence presented in the literature, it can be concluded that there is a link between bathing water quality and health issues, mainly gastrointestinal illness with children at a high risk and particularly due to their vulnerability to infection.

2.3 The Bathing Water Directive (2006/7/EC)

In 1976, one of the first pieces of European environmental legislation came into existence. The European Union (EU) Bathing Water Directive (76/160/EEC) set out standards for designated bathing waters to be complied with by all member states.

A new Bathing Water Directive (2006/7/EC) was adopted on 15 February 2006 after a long debate, which required a final agreement between the European Council and Parliament (European Parliament, 2006). The main point of deliberation was the higher designations that bathing sites must attain to comply with the revised directive. The four classification designations specified in the Bathing Water Directive are: 'poor', 'sufficient', 'good' and 'excellent'. The bathing water quality thresholds for the later three designations according to Annex I of the European Union (EU) Bathing Water Directive (76/160/EEC) are shown in Table 2.1. The water quality

Table 2.1: Bathing water quality thresholds for coastal waters and transitional waters (European Parliament, 2006)

	Parameter	Excellent	Good	Sufficient
1	Intestinal enterococci (cfu/100 ml)	100 *	200 *	185 **
2	Escherichia coli (cfu/100 ml)	250 *	500 *	500 **

* Based upon a 95-percentile evaluation
** Based upon a 90-percentile evaluation

thresholds in Table 2.1 are lower for the 'Excellent' classification as compared to the 'Good' classification which means that the 'Excellent' classification is a more stringent requirement. The shown thresholds for the 'Good' classification are the same or

higher than that of the 'sufficient' classification. However, the 'Good' classification is still more stringent than the 'sufficient' classification. This is because a higher percentage (95 %) of the samples collected have to achieve the 'Good' classification as compared to 90 % for the 'Sufficient' classification.

According to Article 5 of the Bathing Water Directive (European Parliament, 2006), EU Member States are required to ensure that by the end of the 2015 bathing season, all bathing waters have achieved at least the 'sufficient' status. 36No (5.8 %) coastal bathing waters in the UK were found to be non-compliant or 'poor' for the 2012 bathing season according to European Environment Agency (2013). For example, in the Fylde Coast and Ribble Estuary considered in this research study, the water sampling point at St Annes (latitude/longitude: 53.75, -3.040; Ordnance Survey Easting/Northing: 331491, 428585) failed to meet the requirements of European Bathing Water Directive in 2010, 2011 and 2013. Achieving the more stringent 2015 standards will therefore be challenging. The Directive also allows bathing waters subject to short term pollution to be deemed as having met the requirements if adequate management measures are being taken, including surveillance, early warning systems and monitoring, with a view to preventing bathers' exposure, by means of a warning or, where necessary, a bathing prohibition. This means that predicting pollution events before they occur can help the UK meet the Directive's requirements. One of the aims of this research study is to improve the ability to run more accurate bathing water quality prediction simulations faster. Hence, the bathing water quality can be forecasted accurately and adequate management measures can be taken to ensure that the requirements of the bathing water Directive are still met.

2.4 Sources of Faecal Contamination

Faecal coliform sources include: agricultural and surface run-off, bank soils, sewage, wild and domestic animal faeces etc (Howell *et al.*, 1995; Geldreich, 1996; Alderisio

and DeLuca, 1999; Gerba, 2000; Ferguson *et al.*, 2003; Guber *et al.*, 2006; Wilkinson *et al.*, 2006; Garcia-Armisen and Servais, 2007; Kim *et al.*, 2007; Servais *et al.*, 2007; Cho *et al.*, 2010b). The main sources of faecal contamination in coastal waters can be divided into two broad categories (Thomann and Mueller, 1987), these are:

1. Point Sources
    (a) Combined sewer overflows (CSO) - Discharge of wastewater and stormwater
    (b) Industrial discharges
2. Diffuse Sources
    (a) Agricultural
    (b) Silviculture (Forests)
    (c) Atmospheric
    (d) Run-off from urban and suburban land through separate sewers
    (e) Groundwater

Gerba (2000) made an assessment to determine the potential shedding of bacterial organisms and viruses into drinking water supply reservoirs by body contact recreation. He confirmed that organisms of faecal origin are shed from the body during bathing. This is additional evidence confirming one of the sources of faecal coliforms for this study. Even though his study was related to drinking water supply reservoirs and not coastal waters. It is relevant because the coastal waters in this research study are used for recreation or bathing during the summer months.

Pathways by which pathogens reach susceptible water users include ingestion of contaminated water, body contact with polluted recreational waters and consumption of salad crops irrigated by polluted freshwaters (Geldreich, 1996). Another potential source of faecal contamination is the release of faecal coliform from stream-beds. Previous studies have demonstrated that bed sediments can contain one to three orders of magnitude more faecal coliform than the overlying water column (Goyal

et al., 1977; Doyle *et al.*, 1992; Buckley *et al.*, 1998; Crabill *et al.*, 1999; Smith *et al.*, 2008; Rehmann and Soupir, 2009; Cho *et al.*, 2010b; Pachepsky and Shelton, 2011). These sediments can be eroded into the water column, thereby causing an additional source of water contamination through the process of desorption, wherein the contamination is desorbed from being attached to the sediment particle to being in solution in the water column.

Coliform sources from sewage, polluted surface waters and storm-water run-off are intensified during periods of major floods (Geldreich, 1996). Studies of microbial concentrations (total coliforms, faecal coliforms and faecal streptococci) in streams showed concentrations to be elevated by an order of magnitude or more following a rainfall event (Wyer *et al.*, 1996). Crabill *et al.* (1999) carried out a study which showed that sediment agitation by recreational activity and storm surges associated with the summer storm season were responsible for the occasional adverse impact to water quality. Kay *et al.* (2005b) carried out a study on the Ribble catchment focusing on the relationships between land use and faecal indicator organism concentrations in surface waters and found that the faecal indicator organism concentration levels were significantly elevated at high flow, compared to base flow. High-flow geometric mean bacterial concentrations were between 4 and 63 times higher than base-flow values (mean: 15 X) and was found to be statistically significant based on Student's *t*-tests. Resuspension of sediments during or shortly after rainfall events can cause sharp increases in water-borne faecal indicator bacteria (Cho *et al.*, 2010b). High elevations in faecal indicator and pathogen concentrations following rainfall events have been reported in the literature (McDonald and Kay, 1981; Wyer *et al.*, 1994, 1996, 1998a,b; Crowther *et al.*, 2002, 2003; Ferguson *et al.*, 2003; Kay *et al.*, 2005c). These are attributable to a combination of increased surface runoff, the extension of the stream network and corresponding expansion of the contributing areas of the catchment, collectively producing enhanced connectivity to faecal indicator source areas, plus the entrainment of organisms from stream bed stores (Kay *et al.*, 2005b).

Historically, most effort in preventing aquatic pollution has generally been focused on controlling point-sources, such as effluent discharges (Yuan *et al.*, 2007). However, Wyer *et al.* (1997) carried out two case studies and concluded that non-outfall sources of faecal indicators can significantly affect the compliance of bathing waters, even after expensive engineering projects have been implemented. The importance of diffuse source pollution has therefore increased in recent years, as reported by Garcia-Armisen and Servais (2007), and Yuan *et al.* (2007).

From the literature reviewed, the main sources of faecal contamination that are likely to cause non-compliance of the bathing waters are from diffuse sources and sediment agitation during storm or high flow events, together with inputs from CSOs.

2.5 Indicators of Bathing Water Quality

The coliform group of bacteria are commonly used as indicators of water quality (Thomann and Mueller, 1987; Chapra, 2008). This is because coliform groups meet many of the criteria for a suitable indicator organism. They are easily detected by simple laboratory tests, not generally present in unpolluted waters, and the number of indicator bacteria tends to be correlated with the extent of contamination (Thomann and Mueller, 1987). Within the coliform group, there are three main groups used as indicators of communicable diseases. These are the total coliform (TC), the faecal coliform (FC) group and faecal streptococci (FS). The total coliform (TC) group are a large group of bacteria that have been isolated from both polluted and non-polluted soil samples as well as faeces of humans and other warm blooded animals. The faecal coliform (FC) bacteria group are indicative of organisms from the intestinal tract of humans and other animals. The faecal streptococci (FS) bacteria group are varieties of streptococci whose normal habitat is the intestines of humans and animals.

Except for certain strains of pathogenic *E. coli* (e.g. O157), coliform bacteria are

not a threat to human health (Hipsey *et al.*, 2008). However there is a correlation between the concentration of coliform bacteria and the presence of pathogens (such as *Salmonella*). This correlation has been studied by several investigators (Brezenski and Russomanno, 1969; Smith *et al.*, 1971; Geldreich, 1970, 1978; Townsend, 1992). The high abundance of coliform bacteria make them easy to detect and useful water quality indicators.

Most investigations that have focused on quantifying the kinetics of enteric organisms in surface and coastal waters under different environmental conditions have focused on coliforms and E. coli in particular (Hipsey *et al.*, 2008). Brookes *et al.* (2004) reviewed the use of surrogates to estimate pathogen risks and concluded that, while no single water quality indicator can reliably assess the bacterial, protozoan and viral contamination of aquatic environments in all circumstances, it is feasible that a suite of surrogates may be identified that will estimate levels of microbial contamination within defined circumstances.

This research study uses faecal coliform as the main indicator of water quality. From the literature reviewed faecal coliform are one of the major bacterial indicators used for bathing waters. It was also noted that the Bathing Water Directive specifies Escherichia coli (E. coli) and intestinal enterococci as the water quality indicators for monitoring bathing waters.

2.6 Numerical Modelling of Bathing Water Quality

2.6.1 Governing Equations

To predict the temporal and spatial variation of bathing water quality indicators, deterministic models have been used in this research study. Deterministic models are based on solving the mathematical equations which describe the underlying physics and biochemical processes that drive the changes in concentration of the bathing water quality indicators. Other types of models have been used to predict

water quality in the literature. These include physical models, simplified conceptual models, Genetic Algorithms (Kuo *et al.*, 2006), Artificial Neural Networks (Zhang and Stanley, 1997; Huang and Foo, 2002; Kuo *et al.*, 2006; Singh *et al.*, 2009; Maier *et al.*, 2010; Motamarri and Boccelli, 2012), Bayesian models (Schoen *et al.*, 2010) and Stochastic models. There are also hybrid models which combine both deterministic and non-deterministic models. For example, Lin *et al.* (2008) combines an artificial neural network model with a deterministic model. Deterministic models may also use empirical equations to estimate some parameters. The underlying physics and biochemical processes behind deterministic models can be divided into two categories, the hydrodynamics and the solute transport processes. Deterministic models have been used in this research study as opposed to other types of models such as Genetic Algorithms and Articial Neural Networks because deterministic models can easily be applied from one site or scenario to another with minimal new work. For example, an Articial Neural Network with new be retrained to be applied at a new site.

The hydrodynamic processes are based on the Navier-Stokes equations. These equations describe the motion of fluids (water in this case) in a continuum. They are named after Claude-Louis Navier (1822 paper) and George Gabriel Stokes (1845 paper) who derived the equations independently. The Navier-Stokes equations are derived by combining the general stress-strain equations for solids, based on Hookes' law (Timoshenko and Goodier, 1970), and the shear stress-strain relationship for fluids under laminar flow, based on Stokes' law (Douglas *et al.*, 2011). For this research study, the governing equations were adapted for one-dimensional and two-dimensional flow by making several simplifying assumptions. These assumptions are not expected to have an adverse effect on the calculation velocities and water elevations as the same equations have been applied in numerous other studies and shown to give satisfactory results.

The solute transport processes are based on the law of conservation of solute mass and estimation of the mortality rates of the bacterial indicators using empirical

formulae. These empirical formulae are based on experiments conducted in the laboratory. Limitations of the formulation of the solute transport processes include the fact that they do not take into account the potential growth/reproduction of bacteria and may not capture all the mechanisms for loss of bacteria.

The governing equations can only be solved analytically for very simple cases involving simple boundary conditions and geometry (Yuen, 2008). However, the use of computers to solve these equations numerically is generally adopted in industry and particularly where the geometry and bathymetry of the domain do not generally allow for an analytical solution (Falconer and Chen, 1991; Falconer and Lin, 1997; Kashefipour *et al.*, 2006; Gao *et al.*, 2011). For this research study, the bathymetry of the domain does not allow for an analytical solution to be used. Hence, numerical solutions were used as opposed to analytical solutions.

2.6.2 Numerical Schemes

Computational models for solving fluid dynamics problems can be categorized in several ways. These include: the method of solving the equations, the number of spatial dimensions (i.e. 1D, 2D or 3D), the method of discretization in time and space and the type of grid or mesh.

There are several methods for numerically solving the water elevations, velocity fields and the water quality characteristics of an estuary, river, reservoir etc. Some of the most popular methods are: the Method of Characteristics (Lai, 1977), the Finite Difference Method (FDM), the Finite Element Method (FEM), the Finite Volume Method (FVM) and the Smooth Particle Hydrodynamics method (SPH).

In the FEM (Zienkiewicz and Taylor, 1989), the FDM (Abbott and Basco, 1989) and the FVM (LeVeque, 2002), the spatial domain is discretised into meshes. A mesh is defined as any of the open spaces or interstices between the strands of a net that is formed by connecting nodes in a predefined manner (Liu, 2010). In the FDM, the meshes are often called grids; in the FVM, the meshes are called volumes

or cells; and in the FEM, the meshes are called elements. Mesh based methods are very mature and have dominated the field of Computational Fluid Dynamics (CFD) for many decades. This makes them robust and well-developed because they have been applied to very many applications in industry. Mesh based methods are good for: confined computational domains and computations where the boundaries are not moving. However, for cases where intricate mesh generation is required and highly non-linear deformations occur for the fluid body then meshless methods are ideal. Meshless methods have not been used in this research study, because the case studies do not involve moving boundaries and also using meshless methods will require additional computational time and programming effort.

The Finite Element Method (FEM) is a general discretization procedure of continuum problems posed by mathematically defined statements (Zienkiewicz and Taylor, 1989). This method involves dividing the continuum into a finite number of parts (elements), the behaviour of which is specified by a finite number of parameters, and the solution of the complete system is obtained as an assembly of its elements, following precisely the same rules as those applicable to standard discrete problems. This method provides flexibility to handle complex geometries and irregular boundaries. Due to the large matrix to be solved at every time step, it can be slower and less efficient in comparison with the FDM. Cunha and Rosman (2005) developed a model to solve the shallow water equations for natural water bodies using finite elements in the spatial discretization and finite differences in the time discretization. TELEMAC is a finite element software for solving the shallow water equations which has been applied extensively in industry by various researchers (Galland *et al.*, 1991; Jones and Davies, 2006; Briare *et al.*, 2007; Brown and Davies, 2009; Moulinec *et al.*, 2011; Villaret *et al.*, 2013).

The Finite Volume Method (FVM) has the flexibility of the FEM, but has efficiency levels similar to the FDM. For complex geometries it can provide more accurate solutions than the FDM (Levasseur *et al.*, 2007; Xia *et al.*, 2010b). It

has low precision and can be difficult to run in high order discretization. Available software implementing the FVM include the Finite Volume Coastal and Ocean Model (FVCOM). FVCOM has been applied to several coastal and estuarine basins (Shore, 2009; Wu and Tang, 2010; Bai *et al.*, 2013; Tang *et al.*, 2013).

The FDM is one of the principal means of translating flow equations for a continuum into differences based on a truncated form of Taylor's series (Abbott and Basco, 1989). Errors in the FDM mainly result from the truncation of Taylor's series (Chen, 1994; Armenio, 1997).

Richtmyer (1963) described several finite-difference approximations to the hyperbolic equations of fluid dynamics and their qualities assessed (e.g. accuracy and stability). The Lax-Wendroff scheme, for a system of conservation laws, is discussed for problems in one and in two space variables. Richtmyer (1963) also considered a non-viscous fluid as in this research study. However, the Lax-Wendroff scheme is explicit which means that it had more restrictive time step constraints as compared to the implicit scheme used in this research study. A much smaller time step will be required for the Lax-Wendroff scheme to satisfy the stability and accuracy requirements, hence computational time is much longer. The restrictive time step constraint was the von Neuman stability condition, given as:

$$\sqrt{U^2 + V^2}\frac{\Delta t}{\Delta x} < \frac{1}{\sqrt{2}} \tag{2.1}$$

where U, V are the depth averaged velocities in the x and y directions, Δt is the time step, Δx is the grid size which is the same in both directions.

Fennema and Chaudhry (1990) solved two typical hydraulic engineering problems, using the MacCormack and Gabutti explicit finite difference schemes, and compared the results for the different schemes. The first typical hydraulic engineering problem was a partial dam breach which was non-symmetrical to demonstrate analysis of a general case. The second problem was the passage of a flood wave through a channel

contraction. The main advantage of the MacCormack and Gabutti explicit finite difference scheme was the ability to capture shocks. The shocks refered to here are steep changes in water elevations and velocities (sharp discontinuities) which are characteristic of dam breach problems. In this research study, the ability to capture shocks was not necessary because the type of problem studied did not involve sharp discontinuities.

Casulli and Cattani (1994) presented and discussed the stability analysis, the accuracy and the efficiency of a semi-implicit finite difference scheme for the numerical solution of a three-dimensional shallow water model. The formulation of the numerical scheme adopted by Casulli and Cattani (1994), is very similar to that used in this research study, even though theirs was three-dimensional as compared to two-dimensional in this study. The same two-dimensional formulation was applied in layers to form the three-dimensional model with each layer equivalent to the model used in this study. Their model was applied to several sites including San Francisco Bay, California and the Lagoon of Venice, Italy. Their model was able to deal with repeated flooding and drying of the tidal marshes for the Lagoon of Venice. This showed that similar models to that used in this study have been found to be successful and give satisfactory results.

Lin and Falconer (1995) refined and extended a boundary-fitted finite difference numerical model, capable of predicting two-dimensional depth-integrated tidal flows, to include sediment transport processes. The numerical model used by Lin and Falconer (1995) was found to give good comparisons of the predicted velocities and water elevation for the coastal flows in the Humber Estuary in the U.K. which were predominantly horizontal flows.

Armenio (1997) proposed a modified semi-implicit marker and cell method (SIMAC), which solved the Navier–Stokes equations in primitive variables on a non-uniform staggered Cartesian grid by means of a finite difference scheme. The scheme accurately treats unsteady high-Reynolds free surface flow problems. The work by Armenio

(1997) was focused on problems in ship hydrodynamics which are characterised by unsteady flows in the presence of a free surface and which are affected by the water viscosity. Their numerical scheme involves tracking massless particles (markers), which is not really efficient for the problem being solved in this research study. It is more suitable for liquid sloshing problems in ship tanks.

Falconer and Lin (1997) developed and applied a refined three-dimensional layer integrated model to predict water elevations, layer averaged velocity components, distributions of conservative and non-conservative water-quality constituents and sediment transport fluxes in several estuarine and coastal waters, including the Humber Estuary in the United Kingdom (UK). The model involved using the finite difference technique to solve the equations of mass and primitive momentum conservation and the transport equations for a range of water quality indicators and sediment transport forms. The work by Falconer and Lin (1997) did not relate the decay of solutes with other factors such as salinity, temperature and solar irradiation. The model allowed the decay of the solutes to be specified directly whereas this research study links the decay rates of solutes (coliforms) dynamically with the effects of water temperature, salinity, turbidity and solar irradiation.

Falconer *et al.* (2005) applied finite difference methods in three studies, namely Cardiff Bay, the Ribble Estuary in the UK and the Lower Mekong River Basin in South-east Asia. The Ribble estuary model used in the study by Falconer *et al.* (2005) is based on the same bathymetric and measured water quality data used by Kashefipour (2002). It also confirmed that finite difference methods had been applied to the same Ribble Estuary and given satisfactory results.

Lin *et al.* (2008) combined a numerical model based on the finite difference method with Artificial Neural Networks (ANNs) to develop a more accurate and rapid tool for assessing the bathing water status for the Ribble Estuary and the Fylde Coast, UK. The study by Lin *et al.* (2008) confirmed the need for tool for the rapid assessment of water quality in the Ribble Estuary. However, the ANN required a

calibrated hydrodynamic and water quality model to be used to generate input data for the neural networks. This is a key disadvantage of ANNs in that its performance is based on input from deterministic models. If the deterministic models perform poorly, there is no reason to believe that the ANN will perform better.

In this research study, a two dimensional, depth integrated, hydrodynamic and solute transport, time variant, finite difference model, which has been developed for estuarine and coastal modelling, was used. This model is known as DIVAST (Depth Integrated Velocities And Solute Transport), which was initially developed by Falconer (1977) and has undergone continuous development within the Hydro-environmental Research Centre (HRC), at Cardiff University. DIVAST has been applied to several estuarine and coastal waters (Kashefipour *et al.*, 2002; Bockelmann *et al.*, 2004; Kashefipour *et al.*, 2006; Gao *et al.*, 2011; Yang *et al.*, 2010; Yang and bo Jiang, 2011; Ahmadian and Falconer, 2012; Ahmadian *et al.*, 2012). DIVAST has been benchmarked against other software in industry using test cases provided by the Environment Agency (EA). Other finite difference software available in industry include: MIKE21, ISIS-2D and EFDC, to mention but a few. MIKE21 is a two-dimensional finite difference modelling tool developed by the Danish Hydrologic Institute (DHI) and has been applied in several research studies (Chubarenko and Tchepikova, 2001; Babu *et al.*, 2006; Xu *et al.*, 2012). EFDC (Environmental Fluid Dynamics Code) is a finite difference, curvilinear grid model, which was developed by U.S. Environmental Protection Agency and has been applied to several coastal basins (Bai and Lung, 2005; Wu and Xu, 2011; Chan *et al.*, 2013; Zhou *et al.*, 2014).

For the one dimensional model in this research study, an integrated modelling system known as FASTER (Flow And Solute Transport in Estuaries and Rivers) was used. This model is capable of predicting water elevations, velocities, solute and sediment concentration distributions in well-mixed rivers or narrow estuaries. FASTER was developed in house at the Hydro-environmental Research Centre of Cardiff University by Kashefipour (2002) and validated by using several test cases. It

has been applied in several studies (Kashefipour, 2002; Kashefipour *et al.*, 2002; Yang *et al.*, 2002; Falconer *et al.*, 2005; Lin *et al.*, 2008; Ahmadian and Falconer, 2012; Ahmadian *et al.*, 2012). Yang *et al.* (2002) modified FASTER to include a graphical user interface based on an object-oriented methodology and applied the model to the Ribble Estuary. Other available one dimensional software tools used in industry include: MIKE11, ISIS and HEC-RAS. MIKE11 is a widely used one-dimensional flow routing modelling tool, developed by the Danish Hydrologic Institute (DHI), and has been used in several applications (Post *et al.*, 2003; Guoqing *et al.*, 2012). HEC-RAS, a one-dimensional (1D) computer code for open surface water calculations, was developed by the United States Army Corps of Engineers, and has been applied extensively in calculating the hydraulic characteristics of rivers (Pappenberger *et al.*, 2005; Carson, 2006; Rodriguez *et al.*, 2008; Drake *et al.*, 2010).

This literature review has shown the extent of previous application of similar models. It has also highlighted other numerical schemes that could have been used but were not suitable. It also helped to identify the most suitable models for this study as two well established and tested numerical schemes, namely, DIVAST and FASTER. The source code for both models are readily available, making it suitable for adaptation and refinement for this research study. Compared to other popular numerical schemes, it wasis expected that these models had the potential to give accurate results for the research case studies, especially because it has been applied to the Ribble Estuary in previous studies.

2.6.3 Dispersion

The processes of dispersion, dilution, and horizontal and vertical transport determines the distribution of pathogens in rivers, estuaries, and coastal waters. Settling of pathogen particles operates in conjunction with these hydrodynamic processes. Dispersion describes both the turbulent dispersion of particles (for example, in the surface mixed layer) and shear dispersion due to the presence of a horizontal or vertical

velocity gradient. Both processes are important in determining the distribution of particles, not only the changes in concentration of an initial distribution or cloud, but also the differential advection of particles within an initial cloud leading to some particles travelling significantly further than the centre of the initial cloud.

The longitudinal dispersion coefficient (D_l) is used to describe the change in the characteristics of a solute cloud along the axis of flow of the solute. The characteristics of the solute cloud change from a high concentration with very little change in concentration spatially along the axis of flow to a lower concentration with greater change in concentration spatially as the solute flows downstream along the same axis. The flow axis is the longitudinal direction for one-dimensional flows which were used for the first studies of longitudinal dispersion coefficient. So the longitudinal dispersion coefficient is important in estimating the changes in concentration of a solute as it flows downstream. In the following paragraphs, the development of formulae for estimating the longitudinal dispersion coefficient is reviewed in literature.

Early experiments by Taylor (1954) established an empirical formula (2.2) for the longitudinal dispersion coefficients for longitudinal mixing in a straight circular tube under turbulent flow. Taylor (1954) demonstrated theoretically the role of turbulent motion in producing a Fickian dispersion (Similar to Fick's first law of diffusion. See Section 3.7) of tracer about the centre of a cloud, which is advected along a channel at the same average velocity as the fluid, and presented a series of laboratory experiments to verify his theory, wherein it was shown that:

$$D_l = 10.1 a U^* \tag{2.2}$$

where D_l is the longitudinal dispersion coefficient, a is the tube radius, U^* is the shear velocity $= \sqrt{\frac{\tau_0}{\rho}}$, τ_0 is the bed/boundary shear stress and ρ is the density of the fluid. The shear velocity (U^*) is a way of writing the bed shear stress in units of

velocity and relates to the rate of shear at the boundary or bed. It can be written in other forms ($U^* = \sqrt{gRS_f} = \frac{U\sqrt{g}}{C}$, where g is the acceleration due to gravity, R is the hydraulic radius, S_f is the slope of the total energy line, U is the flow velocity and C is the Chezy coefficient) as later shown in Section 4.4.3 of this thesis.

Elder (1959) extended Taylor's method for flow in an open channel of infinite width. Elder (1959) published an analysis of the longitudinal dispersion coefficient, assuming a logarithmic vertical velocity distribution (A logarithmic vertical velocity distribution was first defined by Theodore von Karman in 1930) and that the mixing coefficients for momentum transfer and mass transfer in the vertical direction were the same, to give the equation:

$$D_l = 5.93HU^* \tag{2.3}$$

where H is the depth of flow and U^* is the shear velocity calculated using the depth averaged flow velocity. Elder's equation (2.3) has been widely used because it is simple to use and has a sound theoretical basis. However, it has been suggested that Elder's equation may not be sufficiently accurate to describe dispersion in natural streams (Fischer *et al.*, 1979). The accuracy problem arises in choosing an appropriate value of the longitudinal dispersion constant (5.93 in (2.3)) for natural channels. Both Elder (1959) and Taylor (1954) conclude that the longitudinal dispersion coefficient is proportional to the product of the flow depth (H) and the shear velocity (U^*). However, they propose differing dispersion constants $\left(\frac{D_l}{HU^*}\right)$.

Parker (1961) adapted Taylor's turbulent flow equation to an open channel by substituting the hydraulic radius for the half pipe radius to give:

$$D_l = 14.28R^{1.5}\sqrt{2gS_f} \tag{2.4}$$

where S_f is the slope of the energy grade line and R is the hydraulic radius. (2.4) is not fundamentally different from that proposed by Elder (1959) and Taylor (1954)

because the slope of the energy grade line (S_f) can be related to the bed friction and hence the bed shear velocity. So the longitudinal dispersion coefficient is still proportional to the product of the flow depth and the bed shear velocity (U^*).

Godfrey and Frederick (1970) analysed field data from five natural streams and one canal and observed that there was considerable discrepancy between the magnitudes of theoretical (Formula by Taylor (1954)) and measured values of the dispersion constant ($\frac{D_l}{HU^*}$) also known as the dimensionless dispersion coefficient .

Fischer (1967a,b) carried out several experiments and studies on the longitudinal dispersion, including studying the effects of bends on dispersion coefficients (Fischer, 1969). The observed longitudinal dispersion coefficient for the Missouri and Green-Duwamish rivers were found to be 1500 m^2/s and 8.4 m^2/s respectively. Fischer *et al.* (1979) concluded that the longitudinal dispersion coefficient could be obtained from:

$$D_l = \frac{0.011U^2W^2}{HU^*} \tag{2.5}$$

where W is the flow width, U is the mean velocity at each cross-section of the river and U^* is the shear velocity. Fischer's equation can be rewritten as:

$$D_l = 0.011\left(\frac{U}{U^*}\right)^2\left(\frac{W}{H}\right)^2 HU^* \tag{2.6}$$

Equations (2.5) and (2.6) still agree the equations proposed by Elder (1959) and Taylor (1954) in that the longitudinal dispersion coefficient is still proportional to the product of the flow depth and the shear velocity. However, this time the longitudinal dispersion constant ($\frac{D_l}{HU^*}$) is estimated with an expression. The longitudinal dispersion constant is assumed to be proportional to the width to depth ratio ($\frac{W}{H}$) and the velocity to shear velocity ratio ($\frac{U}{U^*}$). The work by Fischer (1967a,b) is one of the first attempts to explain the discrepancy between the theoretical and measured longitudinal dispersion constants ($\frac{D_l}{HU^*}$) using an expression. However Fischer (1967a,b) does not provide a theoretical basis for the proposed expression (2.6) but the some factors which can

affect the longitudinal dispersion coefficient are highlighted. These factors include the effects of bends in rivers and the river width to depth ratio. Knowing that these factors can affect the values of longitudinal dispersion coefficient is important for assessing the suitability of values of the dispersion coefficient for the riverine parts of this research study.

McQuivey and Keefer (1974) presented an equation based on combining linear one-dimensional flow and dispersion equations to give:

$$D_l = 0.058 \frac{Q}{S_f W} \tag{2.7}$$

for $F_n < 0.5$ where Q is the discharge at steady base flow, S_f the slope of the energy line, W is the flow width and F_n the Froude number. This equation disagrees with previous equations by Taylor (1954); Elder (1959); Parker (1961); Fischer (1967a,b); Godfrey and Frederick (1970) in two ways. Firstly, the slope of the energy grade line (S_f) which can be related to the shear velocity ($U^* = \sqrt{gRS_f}$) is inversely proportional to the longitudinal dispersion coefficient. Secondly, the flow width (W) is given as inversely proportional to the longitudinal dispersion coefficient. The formula proposed by McQuivey and Keefer (1974) therefore contradicts with most of the expressions for the longitudinal dispersion coefficient given in the literature.

Liu (1977) derived a dispersion coefficient equation using Fischer's equation taking into account the role of lateral velocity gradients in dispersion in natural streams. This work further confirmed the suitability of the formulae by Fischer (1967a,b).

Smith (1977) derived a formula for parabolic channels as:

$$D_l = 0.096 \frac{W^2 U}{H} = 0.096 \left(\frac{W}{H}\right)^2 UH \tag{2.8}$$

The work by Smith (1977) is based on the formulae by Fischer (1967a,b) and hence still agrees that the longitudinal dispersion coefficient is proportional to the width (W) to flow depth (H) ratio $\left(\frac{W}{H}\right)$. It can also be concluded that the

longitudinal dispersion coefficient is still proportional to the shear velocity (U^*) because the shear velocity ($U^* = \frac{U\sqrt{g}}{C}$) is a function of the mean velocity (U). However, bed friction characteristics ($\frac{\sqrt{g}}{C}$) have been captured in the constant of proportionality in Equation (2.8).

West and Mangat (1986) developed the following empirical formula for longitudinal dispersion for the one-dimensional case:

$$D_l = \frac{k_l B^2 U}{H} = 0.25 k_l \left(\frac{W}{H}\right)^2 UH \tag{2.9}$$

where k_1 is a dispersion constant, B is the river half width (0.5 W) and H is the maximum depth of cross-section. To a first approximation $k_l = 0.10$ for the ebb flow and k_l =0.025 for the flood tide. Equation (2.9) is of the same form as that proposed by Smith (1977), however with different constants of proportionality.

Magazine *et al.* (1988) experimentally studied the effect of large-scale bed and side roughness on dispersion. They derived an empirical equation for the estimation of a dimensionless dispersion coefficient ($\frac{D_l}{HU^*}$) using roughness parameters of the channel, details of boundary size and spacing of the roughness elements to account for blockage effects. They developed the following expression.

$$D_l = 75.86 P_r^{-1.632} HU* \tag{2.10}$$

where P_r is a generalized roughness parameter incorporating the influence of resistance and blockage effects, which are the results of the roughness elements. The formulation given by Magazine *et al.* (1988) highlights the effect of resistance and blockage effects on the longitudinal dispersion constant ($\frac{D_l}{HU^*}$), however the parameter (P_r) cannot easily be applied to new situations or natural streams. This is because the parameter (P_r) was derived for a flume in the laboratory with rectangular roughness elements introduced at the bottom.

Falconer and Hartnett (1993) used the following formula (2.11) for calculating

the dispersion-diffusion coefficients in a two-dimensional flow:

$$\begin{aligned} D_{xx} &= \frac{(k_l U^2 + k_t V^2)\, H f_d}{\sqrt{2(U^2+V^2)}} + D_w \\ D_{yy} &= \frac{(k_l V^2 + k_t U^2)\, H f_d}{\sqrt{2(U^2+V^2)}} + D_w \\ D_{xy} = D_{yx} &= \frac{(k_l - k_t)\, UV f_d}{\sqrt{2(U^2+V^2)}} \end{aligned} \tag{2.11}$$

where k_l is the longitudinal dispersion constant (typically 5.93 for a logarithmic velocity distribution), k_t is the turbulent diffusion constant (typically 0.15), D_w is the wind-induced dispersion and diffusion coefficient and f_d is the Darcy friction factor. Equation (2.11) can be written in one-dimensional form as $D_l = k_l H U^* + D_w$ by substituting $f_d = \frac{\sqrt{2g}}{C}$ and $V = 0$. Hence the equation used by (2.11) is only different from the equation proposed by Elder (1959) in terms of the number of dimensions (two-dimensional as opposed to one-dimensional).

Hansen (1996) uses MODQUAL, a deterministic, one-dimensional steady-state model with a longitudinal dispersion coefficient of 15 m^2/sec to study the Porsuk River in Turkey. This work gives a typical value of longitudinal dispersion coefficient adopted for a natural river, which can serve as a reference point for this research study.

Seo and Cheong (1998) concluded, for large rivers with channel widths larger than 200 m, Fischer's equation overestimates the dispersion coefficient significantly. Seo and Cheong (1998) developed an equation for predicting dispersion coefficients of the following form:

$$D_l = 5.915 \left(\frac{W}{H}\right)^{0.62} \left(\frac{U}{U^*}\right)^{1.428} H U^* \tag{2.12}$$

Equation (2.12) is very similar to that by Fischer (1967a,b) however it's not applicable to channels of any width. However, it confirms that the general form of Fischer's equation still applies.

Koussis and Rodriguez-Mirasol (1998) using the original theory and equation proposed by Fischer (1967a,b) derived an equation of the form:

$$D_l = k_l \frac{U^* W^2}{H} = k_l \left(\frac{W}{H}\right)^2 H U^* \tag{2.13}$$

They proposed a value of 0.6 for k_l and obtained this value by applying a regression analysis on 16 field data sets. Equation (2.13) further confirms that the longitudinal dispersion coefficient is proportional to the flow width to depth ratio, flow depth and shear velocity as proposed by Fischer (1967a,b). However the proportionality constant proposed by Koussis and Rodriguez-Mirasol (1998) is different to that by Fischer (1967a,b).

Atkinson and Davis (2000) carried out a tracer experiment to measure longitudinal dispersion in a 14 km reach of the River Severn in the United Kingdom. This is a further attempt to capture the complexity of the longitudinal dispersion process. The river's discharge was measured at six points and the depth, width and cross-sectional area were measured at 86 points along the test reach. The concentrations of the tracer were measured at stations between 210 m to 13775 m. Atkinson and Davis (2000) provided some the results of the data collected in their paper. However, no estimates of the longitudinal dispersion coefficient were given in their paper.

Deng *et al.* (2001, 2002) derived a formula (2.14) for the longitudinal dispersion coefficient and verified their equation using 70 sets of field data, collected from 30 streams in the United States ranging from straight man made canals to sinuous natural rivers. Their equation is of the form:

$$D_l = \frac{0.15}{8\varepsilon_{t0}} \left(\frac{W}{H}\right)^{\frac{5}{3}} \left(\frac{U}{U^*}\right)^2 H U^* \tag{2.14}$$

where

$$\varepsilon_{t0} = 0.145 + \left(\frac{1}{3520}\right)\left(\frac{U}{U^*}\right)\left(\frac{W}{H}\right)^{1.38} \tag{2.15}$$

Equation (2.14) further confirms the form of the equation proposed by Fischer (1967a,b), however with further refinements.

Kashefipour and Falconer (2002) developed an equation (2.16) for predicting the longitudinal dispersion coefficient in riverine flows, based on 81 sets of measured data, and obtained from 30 rivers in the USA. This empirical equation is given as:

$$D_{xx} = \left[7.428 + 1.775 \left(\frac{W}{H}\right)^{0.62} \left(\frac{U*}{U}\right)^{0.572}\right] H \times U \left(\frac{U}{U*}\right) \tag{2.16}$$

This equation was applied in the earlier studies of Kashefipour *et al.* (2002) to the Ribble river and estuary. This gives this research study a previous values of longitudinal dispersion coefficient which can be used as a reference point.

Toprak *et al.* (2004) developed a model for predicting longitudinal dispersion coefficients in natural streams using fuzzy-logic. Even though the fuzzy-logic model can estimate the longitudinal dispersion coefficients with better accuracy. It is dependent on measured data and is not easy to implement. It was therefore not considered for this research study.

In the study by Seo and Baek (2004), an equation for the longitudinal dispersion coefficient that is based on the beta probability density function for the transverse velocity profile was developed. The proposed equation is one of the most complex in the literature.

Tayfur and Singh (2005) developed an artificial neural network (ANN) model to predict the longitudinal dispersion coefficient in natural streams and rivers. The hydraulic variables (i.e. flow discharge Q, flow depth H, flow velocity U, shear velocity U^*, and relative shear velocity U/U^*) and geometric characteristics (i.e. channel width W, channel sinuosity S_n, and channel shape parameter β_c) constituted inputs to the ANN model, whereas the dispersion coefficient D_l was the target output. The ANN model was trained and tested using 71 data sets of hydraulic and geometric parameters and dispersion coefficients measured on 29 streams and rivers in the

United States and found to be superior to most empirical equations for predicting the longitudinal dispersion coefficient. Even though the ANN is superior to most of the empirical equations, it is not easy to implement for new sites and hence was not considered for this reseaarch study.

Azamathulla and Wu (2011) used the support vector machine (SVM) approach to predict the longitudinal dispersion coefficients in natural rivers. The support vector machine approach is a supervised learning approach which requires training data. It has similar problems as compared to ANN in terms model implementation at new sites.

Bashitialshaaer *et al.* (2011) considered the effects of river sinuosity on the longitudinal dispersion coefficient, developed a new equation and verified it using 43 sets of measured field data to give:

$$D_l = 20.95 \left(\frac{U}{U^*}\right)^{0.87} \left(\frac{W}{H}\right)^{0.5} (S_n)^{0.3} HU^* \tag{2.17}$$

where S_n is the sinuosity of the river. The river sinuosity is a measure of the degree of bendiness of the river. That is the ratio of the curvilinear length to the straight line length of the river. This further confirmed the effect of bends on the longitudinal dispersion coefficient which was previously investigated by Fischer (1967a,b) and was also considered in an ANN model by Tayfur and Singh (2005).

Guoqing *et al.* (2012) calibrated the longitudinal dispersion based on the agreement obtained between measured, observed and predicted values of salinity using the MIKE11 river model. Salinity is a non-conservative solute. That is, it does not decay (zero decay rate). A non-conservative tracer is usually used in experimental studies of the longitudinal dispersion coefficient as adopted by Atkinson and Davis (2000) in the study of the Severn Estuary in the U.K. Salinity is therefore suitable for calibrating the longitudinal dispersion coefficient. Realistic value ranges of salinity are easier to determine than with the coliform concentrations which depend on input

sources. Therefore salinity can be used in this research study to discard unrealistic values of the longitudinal dispersion coefficient.

More recently Zeng and Huai (2013) evaluated the accuracy of some of the commonly used equations using 116 sets of measured data for rivers in the U.S. and U.K. The evaluation showed that most of the equations underestimated the longitudinal dispersion when the surface water width (W) to water depth (H) ratio was between 20 and 100 ($20 < \frac{W}{H} < 100$). Zeng and Huai (2013) developed a new formula for estimating the longitudinal dispersion using regression analysis, which is of the form:

$$D_l = 5.4 \left(\frac{W}{H}\right)^{0.7} \left(\frac{U}{U^*}\right)^{0.13} HU \tag{2.18}$$

This further highlighted the effects of the flow width (W) to water depth (H) ratio on the longitudinal dispersion coefficient. However, the power of $\frac{W}{H}$ (0.7) in the new equation (2.18) is varies from that previously proposed by others researchers (Fischer, 1967a,b; Smith, 1977; Seo and Cheong, 1998; Koussis and Rodriguez-Mirasol, 1998; Deng *et al.*, 2001, 2002; Kashefipour and Falconer, 2002; Bashitialshaaer *et al.*, 2011) which vary from a value of 2 proposed by the initial researchers to about 0.5 to 0.7 by later researchers. However, the use of the width in the formulae is only applicable to one-dimensional models of rivers.

The longitudinal dispersion coefficient is affected by several factors including channel geometry and flow properties. Several formulae for estimating the longitudinal dispersion have been reviewed. Some are based on theory, whilst others are more empirical. However, the extent of the available literature shows the need to have simple formula that suits differing geometries and flow properties. Several methods have been used to derive the formula for estimating the dispersion coefficient. These include dimensional analysis, regression techniques, artificial neural networks (ANN), machine learning and fuzzy-logic. There has been a rise recently in the use of informatics tools (ANN, machine learning, etc) to predict the longitudinal dispersion coefficient. While these methods are useful (Rowinski *et al.*, 2005), they are reliant on

training data and the need for a simple theoretical formulae which are physically-based and suitable of all applications still persists.

The current research study seeks to show the benefits of adopting a holistic approach in the formulation adopted to estimate the longitudinal dispersion coefficient. The same formulation of the form (Equation (2.3)) proposed by Elder (1959) will be used in both the one-dimensional and two-dimensional domains of the numerical model, with particular application to the Ribble river and estuary.

2.6.4 Model Linking

It is often more computationally efficient to use different types of hydrodynamic models in different regions of a domain. It may not be feasible to use 2D and 3D models for a long narrow river reach during and for a long simulation period, because they require much more computational time than 1D models (Wu, 2008). It may also be desirable to build an integrated model by coupling catchment (or watershed), groundwater, hydrodynamic, and rainfall models, etc.

Liang *et al.* (2007) linked a 2D research code (DIVAST) with a commercial 1D program (ISIS-1D), achieving good mass conservation and commented on how better momentum transfer could be achieved. ISIS-1D is a widely accepted model in the water industry for predicting flows with one dominant direction such as river flows. For this research study, knowing that the momentum transfer across the link was one of the main problems with 1D to 2D linked interfaces helped focus the research work.

Rodriguez *et al.* (2008) used an iterative process to couple HEC-RAS, a one-dimensional river model, with MODFLOW, the U.S. Geological Survey's three-dimensional finite difference groundwater model. The linked interface achieved very good mass conservation, however, the author was unclear about momentum conservation over the interface.

Wu and Tang (2010) coupled a 3D CFD model with a Finite Volume Coastal Ocean Model (FVCOM). The solution domains of the CFD model and FVCOM overlap over a region (Figure 2.1). The two models exchanged solutions for the velocity distributions at grid interfaces between the two open boundaries. The author comments that in order to achieve accurate, and robust coupling between CFD model and FVCOM, further study on related issues such as conservation at interfaces between the models and a systematical numerical experiment on the coupling strategies and algorithms is necessary.

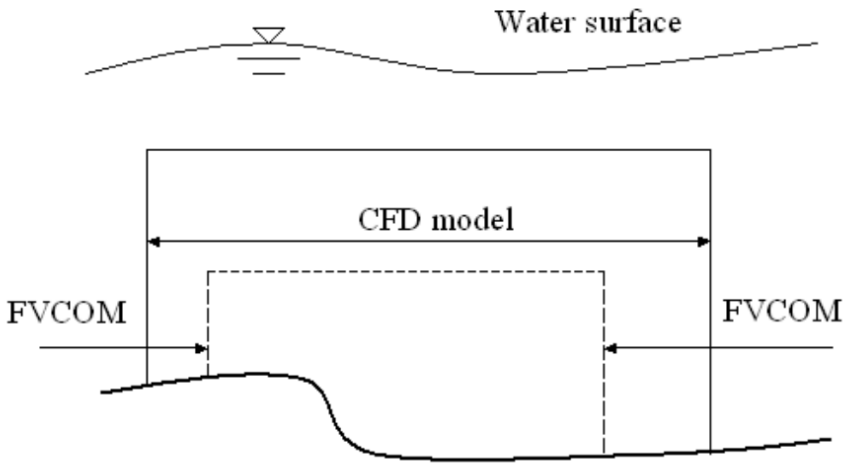

Figure 2.1: Schematic representation of CFD model and FVCOM coupling (Wu and Tang, 2010)

In a study by Tang *et al.* (2013), an unstructured mesh and a surface water model (SWM), they coupled this model to the unstructured grid Finite Volume Coastal Ocean Model (FVCOM). The coupling was two-way and included the use of the domain decomposition method, implemented with overlapping meshes (Figure 2.2), and the Schwarz alternative iteration. In using the domain decomposition method, the flow domain is divided into several sub-domains, and either SWM or FVCOM is assigned to each of them, depending on which solution method is deemed to be better for the flow phenomena within it.

Zhou *et al.* (2014) commented on the use of a linked 1D-2D model for the Severn estuary in the UK, with the linked model being allowed to overlap for a distance to

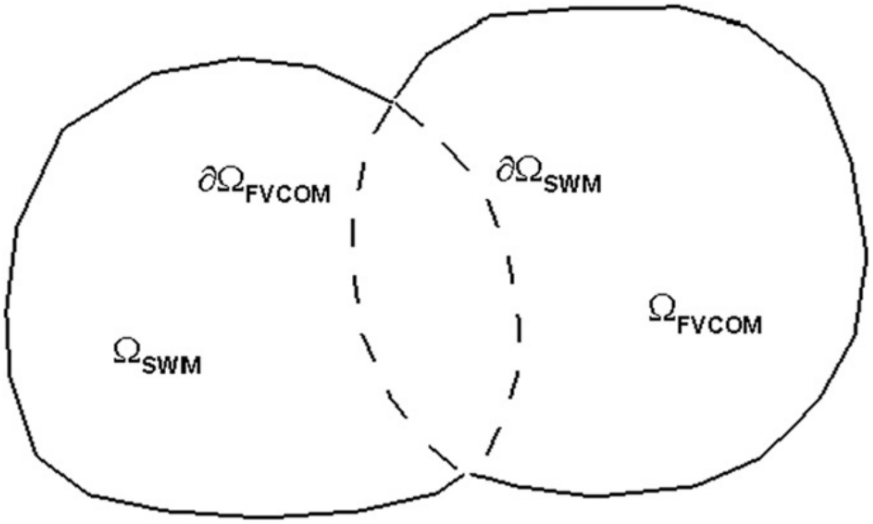

Figure 2.2: Schematic representation of domain decomposition. SWM and FVCOM are respectively assigned to subdomain Ω_{SWM} and Ω_{FVCOM} , which overlap with each other. $\partial\Omega_{\mathrm{SWM}}$ and $\partial\Omega_{\mathrm{FVCOM}}$ are model interfaces (Tang *et al.*, 2013)

ensure numerical stability between the two models. The linked 1D-2D model may yield an inconsistent problem of accuracy between the 1D and 2D models, which further affects the accuracy of an integrated model solution (Zhou *et al.*, 2014). This inconsistent problem arises because the values of velocities in the overlapped region can differ considerability between the two models. And the solute transport solver will be using two different velocities to calculate the transport of the same solute in the same area which is not consistent. The same solute cannot be travelling at two different velocities.

From a review of the recent literature, it is evident that there is a need to link different types of models, given the wide variety of applications in the literature. The method of overlapping one domain with another is often used. This can create an inconsistent problem of accuracy between the two domains if the overlap area is relatively large. Furthermore, whilst mass conservation can be accomplished, it is difficult to ensure momentum conservation across the overlapping domains. In this research study, a one-dimensional model (FASTER) is dynamically linked with a two-dimensional model (DIVAST) and the overlap area has been significantly

reduced from the original linked model, which has led to improvements in accuracy across the linked boundary. DIVAST and FASTER were previously linked with a large overlap in the study by Kashefipour (2002).

2.6.5 Parallel Computing

The implementation of the numerical schemes to solve Computational Fluid Dynamics (CFD) problems in realistic scenarios imposes huge demands on computing power. The performance of a numerical scheme in terms of speed relies on several aspects of the computer hardware. These include the clock frequency or speed, data transfer or bus speed, types of memory, memory access speeds, processor speed, etc.

It is noted that over the past 30 years, the performance of processors has increased whilst the speed of data transfer (memory bandwidths, hard disk read/write speeds, etc) has improved at a slower rate. Throughout the 80's and 90's, CPUs were able to run virtually any kind of software twice as fast every 18-20 months. The pace of change has been considerable. However, following the turn of the century, progress slowed down considerably for single-threaded software (which includes most software).

Perhaps the turning point came in May 2004, when Intel cancelled its latest single-core development effort to focus on multi-core designs. Later that year, Herb Sutter wrote his now famous article, The Free Lunch Is Over (Sutter, 2005): 'Not all software will run remarkably faster year-over-year any more', he warned us. Concurrent software would continue its meteoric rise, but single-threaded software was about to get left behind.

Clearly, multi-core computing has become mainstream. Everybody acknowledges that single-threaded CPU performance no longer increases as quickly as it did previously (Figure 2.3).

Driven by the insatiable market demand for realtime, high-definition 3D graphics, the programmable Graphic Processor Unit, or GPU, has evolved into a highly parallel,

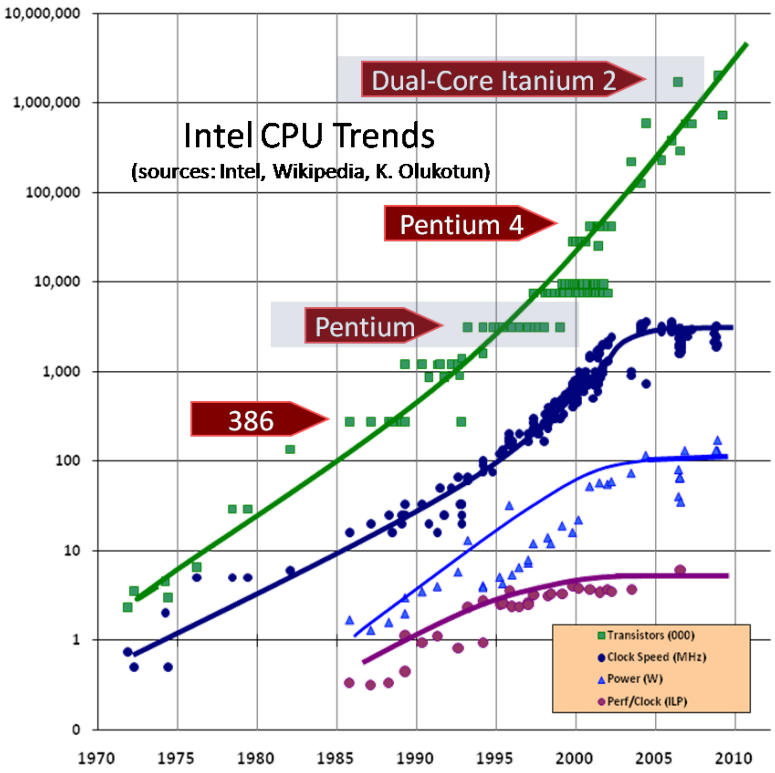

Figure 2.3: Intel CPU Introductions (graph updated August 2009; article text original from December 2004)

multithreaded, many core processors with tremendous computational power and very high memory bandwidths, as illustrated in Figures 2.4 and 2.5.

The reason behind the discrepancy in floating-point capability between the CPU and the GPU is that the GPU is specialized for compute-intensive, highly parallel computations – exactly what graphics rendering is about – and therefore designed such that more transistors are devoted to data processing, rather than data caching and flow control (NVIDIA, 2011b).

Paglieri *et al.* (1997) applied parallel computating to the shallow water equations using a finite volume numerical scheme. His work targeted distributed memory systems. This research study focuses on shared memory systems. These are more applicable to desktop computers.

Kalyanapu *et al.* (2011) presents a study of the computational enhancement that a Graphics Processing Unit (GPU) has made to a 2D flood model. A 2D dynamic flood model based on the shallow water equations was parallelized

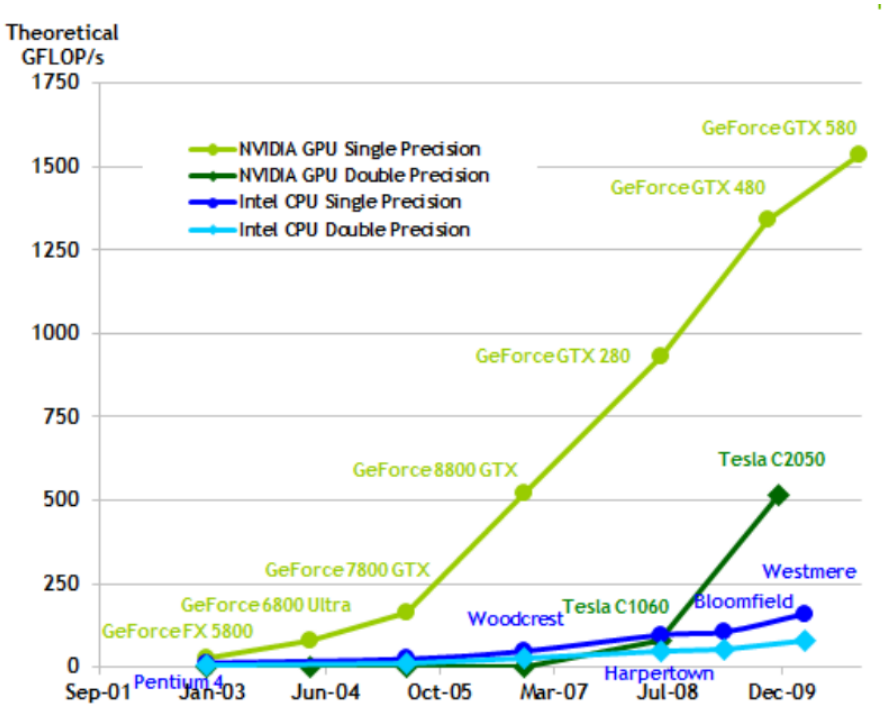

Figure 2.4: Floating-Point Operations per Second for the CPU and GPU (NVIDIA, 2011b)

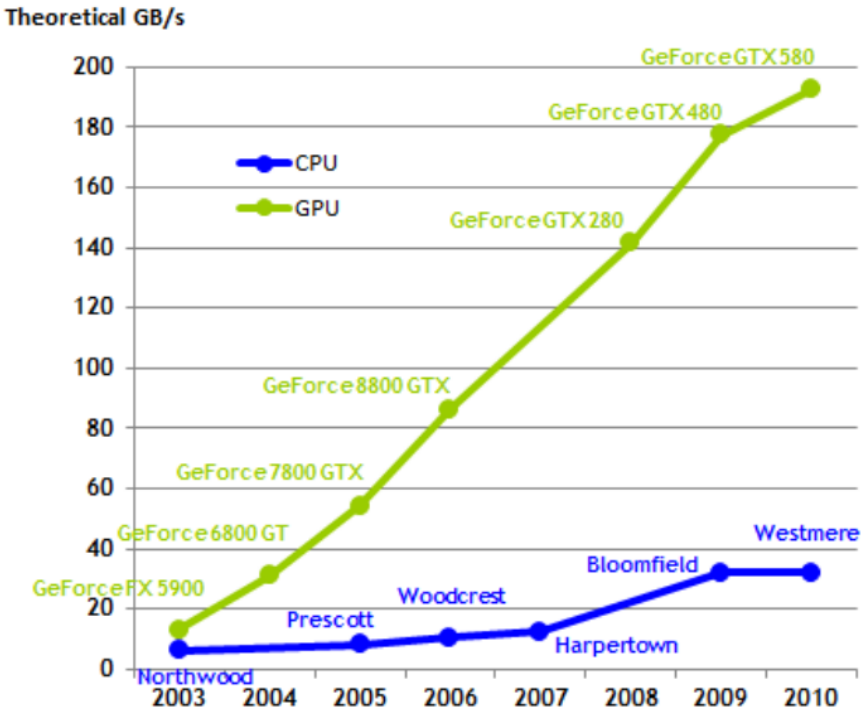

Figure 2.5: Memory Bandwidth for the CPU and GPU (NVIDIA, 2011b)

using the GPU approach, developed in NVIDIA's Compute Unified Development Architecture (CUDA). Computational domains ranging from 65.5 K to 1.05 M cells were tested. Thirty minutes of event time were simulated by the GPU model in 2 min, 15 times faster than real time.

Asuncion *et al.* (2012) present a paper on tackling the acceleration of CFD simulations in triangular meshes by exploiting the combined power of several CUDA-enabled GPUs in a GPU cluster. An improvement of a path conservative Roe-type finite volume scheme, which is ideally suited to GPU implementation, is presented. A distributed implementation of this scheme, which uses CUDA and MPI to exploit the potential of a GPU cluster, has also been developed and reported in their paper. Close to linear weak and strong scaling was observed for up to four GPUs on unstructured meshes with more than 10^6 cells.

Aackermann and Pedersen (2012) investigated the acceleration of DHIs commercial product MIKE 21 HD, by formulating a parallel solution scheme and implementing it to be executed on a CUDA-enabled GPU (massive parallel hardware). Two different parallel solution schemes were implemented. The first (S1) solved each tri-diagonal in parallel using a single CUDA thread for each system. This approach used the same solution algorithm as MIKE 21 HD, the Thomas algorithm. The other solution schemes (S2) added more parallelism into the system by using several threads to solve each system in parallel. In order to do this efficiently, several parallel solution algorithms were investigated. The focus was on the Parallel Cyclic Reduction (PCR) algorithm and a hybrid algorithm of Cyclic Reduction (CR) and PCR. Aackermann and Pedersen (2012) found that S2 was beneficial for small domains, while S1 yielded better results for larger systems. Speed ups of 42x and 80x were obtained in double-precision for S1 and S2 respectively, compared to a representative sequential C implementation of MIKE 21. Furthermore, the impact of switching to perform calculation in single-precision was investigated, which resulted in 145x and 203x speed up for S1 and S2, respectively. However, this had some precision lost when

using single-precision. All tests by Aackermann and Pedersen (2012) were performed on the graphics card NVIDIA GeForce GTX 590.

This research study, seeks to accelerate a finite difference CFD code namely DIVAST using the power of a CUDA-enabled GPU.

2.7 Bio-kinetic Representation

2.7.1 General

In this research study, the movement of bacterial indicators of water quality is modelled from point and diffuse sources to the coastal waters and the beaches. The bacterial indicators are mainly transported by the processes of advection, diffusion, dispersion, growth and mortality of the bacteria, etc.

According to McCambridge and McMeekin (1979); Thomann and Mueller (1987), the factors that influence the kinetic behaviour of bacterial indicators are: sunlight, temperature, salinity, predation, nutrient deficiencies, toxic substances, settling of the organism population after discharge, re-suspension of particulates with associated sorbed organisms and the growth of organisms in the water body.

McCambridge and McMeekin (1979) studied the effects of predation and found that the survival of E. coli was mainly dependent on the presence of protozoan predators and not on the presence of predacious bacteria.

Chigbu *et al.* (2005) studied the mortality rates of faecal coliform bacteria in the north-central Gulf of Mexico estuary. It was observed that faecal coliforms typically peaked within 48 h after a rain event, and then decreased rapidly, whereas for the Pearl River (a major inflow into the western Mississippi Sound) the stage often peaked within 96 h. Faecal coliform disappearance rates varied from 0.214 d^{-1} to 0.743 d^{-1} (mean = 0.428 d^{-1}). Loss rates were found to be higher in November and December (typically 0.64 d^{-1} $\pm$ 0.06 Standard Error (SE)) than in January (typically 0.45 d^{-1} $\pm$ 0.03 SE) or February and March (typically 0.35 d^{-1} $\pm$ 0.03 SE). This was

attributed to seasonal differences in water temperature and/or intensities of solar radiation.

According to Chapra (2008), the total decay rate for faecal indicator organisms is given by:

$$k_b' = (\underbrace{k_d}_{\text{Natural}} + \underbrace{0.02C_{sal}}_{\text{Salinity}}) \underbrace{\theta_w^{T-20}}_{\text{Temperature}} + \underbrace{\frac{\alpha_i I_0}{k_e H}\left(1 - e^{-k_e H}\right)}_{\text{Light}} + \underbrace{F_p \frac{v_s}{H}}_{\text{Settling}} \tag{2.19}$$

where k_d = 0.8 d^{-1} is the decay rate at 20 °C in the dark, C_{sal} is the salinity in parts per thousand (ppt), θ_w=1.07 is the empirical coefficient for water temperature effects, T is the water temperature, α_i is the coefficient of solar irradiation which is dependent on the type of bacteria, I_0 is the solar irradiation intensity at the surface of the water body, k_e is the light extinction coefficient, H is the flow depth, F_p is the fraction of bacteria attached to sediment and v_s is the settling velocity of the sediment.

Decay rates are typically measured in per time units. For example per day (d^{-1}). The decay rate can also be quoted in terms of the T_{90} value which is the time for 90 % to decay.

$$T_{90}\text{value} = \frac{ln\,(10)}{\text{Decay rate}} = \frac{2.302}{\text{Decay rate}} \tag{2.20}$$

For a decay rate of 0.8 d^{-1}, the equivalent T_{90} value is $\frac{2.302}{0.8d^{-1}} = \frac{2.302\times 24h}{0.8}$ which is 69 hr. Therefore this means, it takes 69 hr for 90 % of the bacteria to decay.

Chan *et al.* (2013) used a spatial-temporal dependent E. coli decay rate formulation specifically developed for sub-tropical Hong Kong waters. This is a new thing in the literature reviewed, as most of the research papers found did not use a decay rate formulation but had the decay rate as an input value that was calibrated to give the best prediction of coliform concentrations.

2.7.2 Natural Mortality

A freshwater decay rate of 0.8 d^{-1} (equiv. T_{90} = 69.1 hr) for total coliforms is assumed by Mancini (1978); Thomann and Mueller (1987). In research studies by Auer and Niehaus (1993), the dark death rate coefficient at 20°C (k_d = 0.73 d^{-1} or T_{90} = 75.7 hr) was established in laboratory experiments utilizing raw sewage diluted with filtered lake water. This provided typical values of dark decay rates for this research study.

2.7.3 Solar Radiation and Turbidity

Solar radiation is one of the most significant factors affecting the fate of faecal coliform (Cho *et al.*, 2012). In the water column, transmission of solar irradiation is influenced by turbidity produced by suspended material (Kay *et al.*, 2005a).

Gameson and Saxon (1967) conducted experiments which showed high mortality rates of coliform bacteria in seawater when exposed to daylight. The surface radiation required to produce 90 percent mortality was found to increase with increasing depth of immersion. According to Gameson and Gould (1975), the rate of die-off of coliforms in water is much greater in daylight than in darkness and the die-off of E. coli was slower than that of total coliforms. Gameson and Gould (1975) give a linear proportionality constant of unity between the decay and intensity of solar radiation. Bellair *et al.* (1977) carried out an experimental study of the diurnal variation in the rate of faecal coliform die-off in seawater. The results showed that T_{90} values varied from a maximum of 40 hours during the night to a minimum of 1.9 hours during the day. A relationship between the T_{90} value and hourly solar radiation was established. Mancini (1978) found a strong relationship between die-off rates and solar radiation from in-situ studies and developed a relationship that can be used to generate an estimate of coliform mortality rates in natural bodies of water. Mortality rate estimates included the individual effects of temperature, sea water, solar radiation, and the light extinction coefficient (i.e. related to turbidity).

Fujioka *et al.* (1981) found that the presence of sunlight was a major factor affecting the stability of natural populations of faecal coliforms and faecal streptococci in raw sewage diluted 1:1000 in seawater or phosphate-buffered water at 24±2°C. In the absence of sunlight, these bacteria survived for days, whereas in the presence of sunlight 90 % of the faecal coliforms and faecal streptococci were inactivated within 30 to 90 min and 60 to 180 min, respectively. The bactericidal effect of sunlight was shown to penetrate glass, translucent polyethylene, and at least 3.3 m of clear seawater, suggesting that the visible rather than the ultraviolet light spectrum of sunlight was primarily responsible for the observed bactericidal effect. McCambridge and McMeekin (1981) studied the effect of solar radiation and predacious microorganisms on the survival of bacteria of faecal and plant origin. The decline in the numbers of Escherichia coli (E. coli) cells in estuarine water samples was found to be significantly greater than in the presence of both naturally occurring microbial predators and solar radiation than when each of these factors was acting independently. The effect of solar radiation on microbial predators was negligible, whereas the susceptibility of bacteria to light-induced decay varied from one organism to another.

The decay rate was assumed to be linearly proportional to the intensity of solar irradiation by Thomann and Mueller (1987). Solic and Krstulovic (1992) observed an increase in die-off rate in response to high intensity of solar radiation in laboratory experiments. Auer and Niehaus (1993) conducted field and laboratory studies to develop and verify the kinetic expressions and attendant coefficients required to simulate the loss of faecal coliform bacteria in lakes due to death (as mediated by irradiance (light) and temperature) and sedimentation. The irradiance-mediated death rate (k_i) was shown to be proportional to irradiance (I_0) in water column incubations of raw sewage, using a dialysis tube technique, and giving an equation of the form: $k_i = \alpha_i I_0$; where $\alpha_i = 0.00824$ cm^2 cal^{-1} $= 0.0170$ m^2 W^{-1} d^{-1} . Sinton *et al.* (1999) compared sunlight inactivation rates of somatic coliphages, F-specific RNA bacteriophages (F-RNA phages), and faecal coliforms in seven summer and

three winter survival experiments.

Previous models have more often focused on the coliform parameters and assumed two static day-time and night-time T_{90} values to characterise the decay process (Kay *et al.*, 2005a). More recent models, such as that by Chan *et al.* (2013) seek to include the gradual variation of solar radiation during the day.

Kay *et al.* (2005a) carried out irradiated microcosm experiments using simulated sunlight to investigate the decay of intestinal enterococci in the highly turbid estuarine and coastal waters of the Severn Estuary and Bristol Channel, UK. Results of the experiments suggested that modelling turbidity and or suspended solids offers a potential means of predicting T_{90} values in 'real-time' for discrete cells of a hydrodynamic model.

Cho *et al.* (2010a) reported that in-stream levels of faecal coliform are sensitive to solar radiation and therefore the solar radiation intensity is one of the control factors to model faecal coliform in surface waters.

The depth averaged effect of solar radiation on decay rate (k_i) is given as (Thomann and Mueller, 1987):

$$k_i = \alpha_i I_0(t) \frac{1.0 - e^{-k_e H}}{k_e H} \tag{2.21}$$

where α_i is the coefficient of irradiation, which is dependent on the type of bacteria, $I_0(t)$ is the intensity of solar radiation, k_e is the extinction coefficient of light and H is the depth of water over which the average is taken.

The intensity solar radiation ($I_0(t)$) is known to vary during the day and according to Burgess (2009), this variation approximates to a sinusoidal function as shown in Figure 2.6.

It is noted that this variation may be affected by cloud cover. Actual measured values of solar radiation intensity ($I_0(t)$) which can be obtained from a weather station may be used if available.

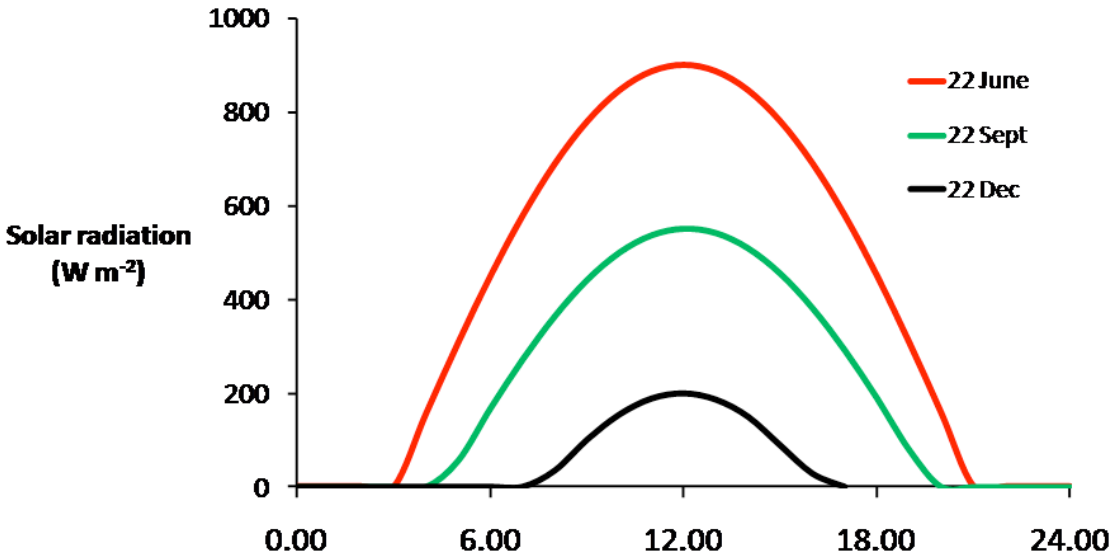

Figure 2.6: Schematic diagram showing the diurnal variation in the solar radiation receipt on three days with no cloud at a latitude of 52°N. This approximates to a sinusoidal function (Burgess, 2009).

The effects of solar radiation on decay rates are further influenced by the ability of light to travel through the water body. The presence of water itself attenuates or reduces the distance travelled by the incident solar radiation. In addition to this, the presence of any suspended particulate matter in the water column further reduces this distance. The effect of turbidity can be taken into account by introducing a light extinction coefficient, k_e in Equation (2.21). Possible values are 1.0 m^{-1} to 0.1 m^{-1} in clear water and greater than 20 m^{-1} for very turbid waters.

The specific depth used to determine the extinction coefficient is based on the Secchi-depth. The Secchi-depth is originally measured with a so called Secchi disc, which is about 25 cm in diameter, and the depth at which the disc cannot be recognized reflects the point where the photosynthetic active radiation is about 10 to 20 % of the radiation measured at the surface. Sverdrup *et al.* (1942) and Beeton (1958) and others have developed empirical relationships between the Secchi depth and the light extinction coefficient as given by:

$$k_e = \frac{\text{1.7-1.9}}{z_{\text{SD}}} \tag{2.22}$$

where z_{SD} is the Secchi-disk depth (m).

Toro (1978) has provided a theoretical and empirical basis for estimating the extinction coefficient as a function of non-volatile suspended solids (N), detritus (D), both in mg/l, and phytoplankton chlorophyll (P) in μg/l. For a vertical sun angle, his estimate of k_e is:

$$k_e = 0.052N + 0.174D + 0.031P \tag{2.23}$$

Turbidity is measured in nephelometric turbidity units (ntu) and a reading in excess of 5 ntu is noticeable to consumers (Ritter, 2010). It is also, one of the main key indicators of drinking water quality. Oliver *et al.* (1999) found that the turbidity (ntu) is related linearly to the vertical light extinction coefficient for the Darling River in Australia (Figure 2.7). The linear relationship from Figure 2.7 is:

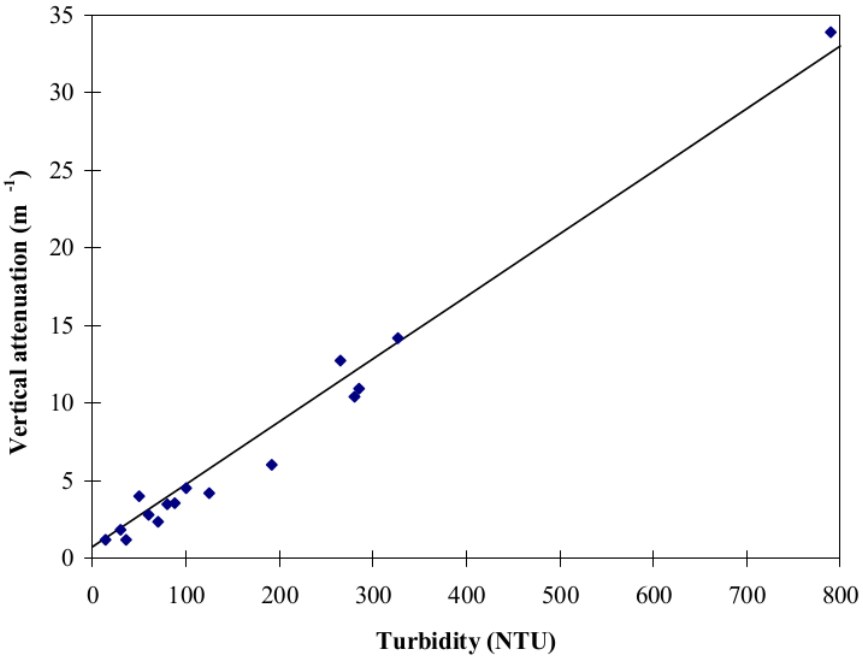

Figure 2.7: Linear regression between the vertical attenuation coefficient for downwelling irradiance and turbidity for sites on the Darling River

$$k_e = 0.04 \times \text{Turbidity (ntu)} + 0.73 \tag{2.24}$$

From the literature it can be concluded that solar radiation has a substantial influence on the survival of faecal coliform in natural waters (Bellair *et al.*, 1977;

Mancini, 1978; Fujioka *et al.*, 1981; McCambridge and McMeekin, 1981; Auer and Niehaus, 1993; Sinton *et al.*, 1999, 2007; Cho *et al.*, 2010a). Including the gradual variation of solar irradiation is important and aids the move towards 'real-time' predictions of water quality.

2.7.4 Salinity

Several authors have included the effects of salinity when estimating the mortality rates of bacterial indicators (World Health Organization, 2003; Chigbu *et al.*, 2005). According to Mancini (1978); Thomann and Mueller (1987); Chapra (2008), salinity is linearly proportional to the decay rate of total coliform, with a proportionality constant of 0.02 d^{-1} per ppt or g L^{-1}. Goyal *et al.* (1977) found an inverse relationship between the concentration of indicator organisms and the salinity of water, occurring at a 99.9% level of significance. The decay rate due to salinity(k_{sal}) is given as:

$$k_{sal} = \theta_{sal} C_{sal} \tag{2.25}$$

where θ_{sal} is the coefficient for salinity taken as 0.02 as recommended by Chapra (2008) and C_{sal} is the salinity in parts per thousand (ppt). The salinity of seawater is known to range from about 31 ppt to 38 ppt.

2.7.5 Temperature

The temperature of a body of water is significant in water quality modelling for three main reasons: (a) temperature can rise due to the discharge of excess heat from effluents, (b) temperature affects the decay rate of bacterial indicators, and (c) variations in temperature influence all biological and chemical reactions (Thomann and Mueller, 1987). In this research study, only temperature effects on the decay of bacterial fluxes were modelled.

Primary references addressing water temperature modelling, or concepts related

to water temperature modelling, include Edinger and Brady (1974), Fischer *et al.* (1979), Orlob *et al.* (1983), Thomann and Mueller (1987) and Chapra (2008). A standard reference for general energy budget concepts is provided by Oke (1987). Several computer model user manuals include heat budget formulations, forming a valuable reference for the modeller. There are countless journal articles, too numerous to mention, that reproduce heat budget formulations, discuss particular components of the heat budget, or present temperature model applications.

The empirical coefficient for water temperature effects, θ_w, is assumed to be 1.07 by Chapra (2008). Typical values range from 1.0 to about 1.1 (Figure 2.8). A

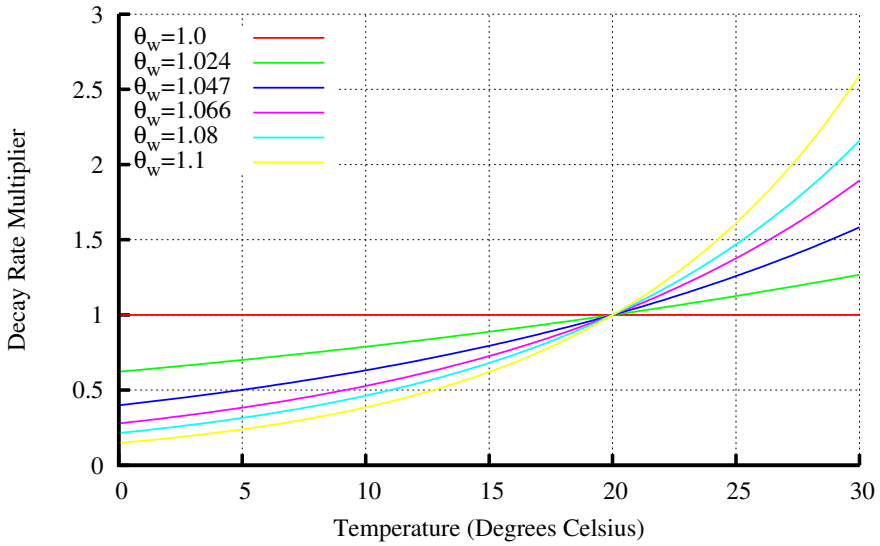

Figure 2.8: The effect of temperature on reaction rate for various values of θ_w (Chapra, 2008)

value of 1.0 for the empirical coefficient for water temperature effects, θ_w, means that the decay rate is not affected by temperature. Higher values lead to a greater decay rate multipliers for temperatures greater than 20 °C (See application of θ_w in Equation (2.19)).

The water temperature was modelled as a solute using a simplified heat balance equation with the source term being given by Edinger and Brady (1974):

$$\left(\frac{\mathrm{d}T}{\mathrm{d}t}\right)_{\text{source}} = \frac{K(T_e - T)}{\rho_w c_p H} \tag{2.26}$$

where ρ_w is the water density, c_p is the heat capacity of water (4186 J/kg/ °C), H is the depth over which the heat is vertically well mixed, K is the overall heat exchange coefficient ($W/m^2/$ °C) and T_e is the equilibrium temperature. This temperature T_e is the temperature that a body of water would reach if meteorological conditions were constant in time. It is as if all conditions were "frozen" at specific values and the water body is allowed to reach a steady temperature equal to T_e. The equilibrium temperature is therefore the temperature at which there is no net heat exchange across the water surface (Thomann and Mueller, 1987).

The overall heat exchange coefficient K is a complex function of the water temperature, wind speed, and other meteorological parameters, such as the saturated vapour pressure (Thomann and Mueller, 1987). An estimation of the overall heat exchange coefficient was made using a formula given by Edinger and Brady (1974):

$$K = 4.5 + 0.05T + \beta_k f(U_w) + 0.47 f(U_w) \tag{2.27}$$

The wind function $f(U_w)$ is given as:

$$f(U_w) = 9.2 + 0.46{U_w}^2 \tag{2.28}$$

The coefficient β_k is given as:

$$\beta_k = 0.35 + 0.015T_m + 0.0012{T_m}^2 \tag{2.29}$$

where

$$T_m = \frac{T + T_d}{2} \tag{2.30}$$

Falconer (1981) assumed a heat exchange co-efficient of 30 $W/m^2/$ °C for studying the background temperature rise in Poole Harbour and Holes Bay due to a power station.

Several authors have included the effects of water temperature when estimating the

mortality rates of bacterial indicators (Solic *et al.*, 1999; World Health Organization, 2003; Chigbu *et al.*, 2005). Sinton *et al.* (1999) conducted outdoor experiments and found that dark inactivation rates (k_d) were higher in summer (temperature range: 14 to 20 °C) than in winter (temperature range: 8 to 10 °C).

2.8 Summary

The purpose of this literature review to establish the theoretical framework behind this research study by reviewing research papers in each theoretical aspect of the research problem, find out what methodology was adopted in previous research and identify the gaps that this research intends to fill.

Poor bathing water quality is not desirable because of the potential health issues it can cause to bathers. One of the main reasons for striving to improve bathing water quality is to mitigate the health risks to bathers. Section 2.2 of the literature review looks at research papers which link poor bathing water quality to health issues. It was important to review this literature to check whether there is a real link to health issues and what these health problems are. If there is no link between poor bathing water quality and public health, then the research problem may need to be redefined. It important to check the links between this research project and the person at the end of the line who the problem affects. In this case, the person at the end of the line is the member of the public bathing in the coastal waters. The literature showed considerable evidence of the links between bathing water quality and health issues. The health problems identified in the literature were mainly gastrointestinal illness with children being at high risk. The main cause of gastrointestinal illness was from waters contaminated by bacteria and viruses derived from human sewage or animal sources. So the evidence of this link in the literature further verifies that the use of bacterial water quality indicators in this research study is directly linked to health issues in bathers. This also confirms why it is important for the

EU to monitor bathing water quality. Also, learnt from the literature that major international bodies such as the World Health Organisation (WHO) and the Unities States Environmental Protection Agency (USEPA) are trying to solve bathing water quality issues. Hence, this research is not only limited to U.K. application but it's very international.

One of the implications of poor bathing water quality is failure to meet the requirements of European legistislation for the U.K. Section 2.3 reviews the details of the European Bathing Water Directive and its current and future requirements. The literature showed that the EU Bathing Water Directive is going to become more stringent in the future. The literature review also showed that there is an opportunity to prevent the U.K. from failing to meet the Directive by identifying short term pollution events before they occur. The importance of real time forecasting in this research study is based on this opportunity to predict short term pollution events before they occur.

In order to predict the levels of bacterial water quality indicators, it is important to identity their sources. Section 2.4 reviews the potential sources of bacterial water quality indicators in the literature. The literature showed that historically most of the effort in controlling bathing water quality had been directed at point sources. However, more recent literatures have focused on diffuse sources. Storm water runoff during high flow events was one of the main times when bacterial contamination from diffuse sources was released according to most of the literature reviewed. Also, sediment agitation during these rainfall events could cause sharp increases in bacterial levels according to some of the literature. This research study focused on a high discharge event as this was one of the main times when potential failures of bathing water quality requirements can occur. However, the sediments were not modelled due to limited data availability. The modelling of the sediments and bacteria released from sediments is included in the recommendations for further study after this research.

What is the most appropriate bathing water quality indicator for this research? Section 2.5 reviews literature on the different types of bacteria that can be used as bathing water quality indicators. The literature shows that even though the coliform group of bacteria do not directly cause health problems, there a correlation between the concentration of the coliform group of bacteria and human health. This correlation has been studied for a long time by various researchers. It is therefore a well established correlation. Faecal coliforms have been used previously in the Ribble Estuary and other studies as the main bathing water quality indicator. More recently bathing water quality legislators like USEPA and the EU have moved from using Faecal Coliforms to E. coli. This research study uses faecal coliform as the bathing water quality indicator because it's a well established bathing water quality indicator and also allows comparison of results directly with a previous study.

In Section 2.6, several aspects of numerical modelling of bathing water quality were explored in the literature. In section 2.6.1, several methods of defining the governing relationships or equations, from probabilistic methods, numerical to analytical methods, are reviewed in the literature relating to the numerical modelling of water quality. It what concluded that for this research study, deterministic numerical models were the most suitable because of their suitability to situations where there was very little measured data and in forecasting scenarios.

Section 2.6.2 reviews several numerical schemes in the literature for modelling hydrodynamics and solute transport. There was a wide range of literature covering several techniques from mesh based to meshless techniques. From the wide range of literature available, it can be said that this subject area has lots of techniques each suited to differing industrial applications. Mesh based techniques were prefered in this research study mainly because of the additional time and programming effort required to implement meshless methods. Of the mesh based methods, the finite difference method was preferred because it had been tried and tested in other studies and found to be adequate for coastal applications. The finite difference method

is well suited to nearly horizontal shallow water tidal flows as is the case for the Ribble Estuary. This research study applies the DIVAST (2D) and FASTER (1D) models developed at Cardiff University (CU). These models have the same basis as various commercial programs such as ISIS which have been benchmarked by the Environmental Agency (EA).

One of the parameter that affect the spreading of solutes is the longitudinal dispersion coefficient. Section 2.6.3 reviews literature on formulae used to estimate the longitudinal dispersion coefficient from the early developments in 1954 to more recent methods. Early formulae were theoretical and were verified in the laboratory with experiments. These early formulae showed that the longitudinal dispersion coefficient was proportional to the product of the shear velocity and the depth of flow (HU^*). However, these formulae have not given comparable values to actual values of the longitudinal dispersion coefficient measured in natural rivers and coastal waters. Because the wide discrepancy in the values, several authors have attempted to come up with an adequate equation using several techniques from linear regression to more probabilistic methods. Several factors which affect the longitudinal dispersion coefficient have been identified by the authors. Some these factors include the flow depth, shear velocity, width to depth ratio, bed friction characteristics and river bends. The conclusion drawn from the literature is that the longitudinal dispersion process is very complex process in natural streams and identification of all the possible factors that can affect the value of the longitudinal dispersion coefficient is needed. Development of a single theoretical formula to cater for all the differing factors has been difficult in the literature because of the complexity of the processes involved. There is still a need to establish a single theoretical formula which can be applied in every situation and can be related to real features of the fluid flow. This research study, adopts a single formula based on the early theoretical assumptions in both the 1D and 2D domains of a linked model. Because of the large range of measured values in literature available for similar rivers, it is difficult to conclude

that one formula predicts better than the other. This research study will use values of longitudinal dispersion coefficient on the basis that they give good correlation with the measured data for the Ribble Estuary.

In Section 2.6.4 the methods of linking models is reviewed in the literature. There is a need to link models and most models links have an overlap area for numerical stability between the two domains. Achieving good momentum conservation is a problem when a large overlap area is used. Also, there is an inconsistent problem of accuracy between in two domains in the overlap area. This is especially a problem in solute transport modelling, as the solute particles are advected by differing velocities depending on whether they are in the 2D domain or 1D domain in the same overlap area. This research study seeks to eliminate these problems in the Ribble Estuary model by reducing the length of the overlap area whilst maintaining numerical stability. The knowledge gap identified in the literature is that there a not many studies devoted to improving how models are linked and this research study also seeks to contribute to this knowledge gap.

The use of the Graphics cards for parallel scientific computing is reviewed in the literature in Section 2.6.5. The literature review confirms that, the year on year increasing performance of single threaded software has drastically reduced in recent years. However, the concurrent / parallel capability of computer hardware is on the rise. One of the parallel computing technologies is the Graphics Processing Unit (GPU). There is very limited literature on the application of GPU computing to the shallow water equations. This is mainly because the technology is new. There was only one paper, in 2012, found that looked at the performance of the shallow water equations solved using a tri-diagonal algorithm on the GPU. This research study seeks to apply GPU technology to the shallow water equations. This is a new contribution to current knowledge in this area and is important as many companies seek to apply new GPU technology to their existing CFD codes.

In Section 2.7, the theoretical framework for representing the decay of bacterial

indicators is explored in the literature. It is noted that one of the main gaps in the literature is the use of the theoretical framework for representing bacterial decay in water quality models. Even though there is some theory in the literature for linking the decay rate with environmental factors, most water quality models calibrate the decay rate directly without linking it to any environmental factors. One of the new things in this research study, is the establishment of this link between the decay rate and environmental factors in the water quality model.

Section 2.7.1 explores the range of differing environmental factors that could affect the bacterial decay rate in the literature. Some of the environmental factors identified in the literature include: sunlight, temperature, salinity, predation, nutrient deficiencies, toxic substances, settling and re-suspension of organisms attached to sediment particles. A formula (2.19) based on experiments in the literature relating the some of these environmental factors to the decay rate is also presented. This formula was adapted for this research study.

Section 2.7.2 reviews typical values of the natural mortality rate, that is the decay rate (k_d) at 20 °C under dark conditions in freshwater. Values of 0.73 to 0.8 d^{-1} were found in the literature. These values were based on experiments conducted by the authors. These typical values provided a reference point for this research study.

Section 2.7.3 reviews the formulation for the effects of solar irradiation on decay rates in the literature. The literature indicated that the effects of solar irradiation was a major factor which affects decay rates and therefore its modelling is important in this research study. The typical variation of solar irradiation was reviewed in the literature. This gave a sinusoidal variation which was adopted for this research study. Incorporation of this sinusoidal variation is new and compared to previous models which adopted static values of solar irradiation for day-time and night-time. A typical value of the proportionality constant, α_i, was also obtained in the literature which was used to validate the value adopted for this research study. The formulation of the effects of solar radiation also involves the light extinction coefficient. The literature

was also reviewed for typical values of light extinction coefficient (k_e). Values of turbidity are also measured in nephelometric turbidity units (ntu), links between ntu and k_e was also investigated in the literature. This provided an empirical relationship which was used in this research study.

Section 2.7.4 reviews the relationship between salinity and effect of the decay rate of the bacterial indicator. This relationship was described as linear in the literature. The recommended proportionality constant of 0.02 d^{-1} per ppt or g L^{-1} in the literature was adopted for this research study.

The theoretical framework for incorporating the effects of water temperature is reviewed in the literature in Section 2.7.5. The effects of differing values of the empirical coefficient for water temperature effects, θ_w, is described based on information obtained from the literature review. A recommended value of θ_w is adopted for this research study based on the literature. The heat balance equation for modelling the temperature effects in this research study was obtained from the literature. Typical values of the heat exchange co-efficient, K, of 30 $W/m^2/°C$ was observed in the literature and served as a validation of the value adopted for this research study.

This literature review has established the theoretical framework for this research study, by reviewing current and past research papers on different aspects of the study. It has identified gaps in knowledge which this research study contributes to and compared the methodology adopted in this research study with current state-of-the-art in the field of bathing water compliance and the relevant modelling of the governing hydrodynamic and water quality processes.

Several parameters used in this research study were based on typical values obtained from the literature review. These parameters included the natural mortality rate (k_d) of faecal coliform, the light extinction coefficient (k_e), empirical coefficient for water temperature effect (θ_w), the heat exchange coefficient (K) and the proportionality constant for the effects of salinity (θ_{sal}) on faecal coliform.

The current state-of-the-art in the field of bathing water compliance and the relevant modelling of the governing hydrodynamic and water quality processes was reviewed in this chapter. The literature reviewed highlighted the evidence of links between poor bathing water quality and health issues. The requirements of current European environmental legislation affecting bathing water quality were presented. Based on the literature, sources of bathing water contamination likely to cause failures in meeting European legislation requirements were found to be from diffuse sources and sediment agitation during storm or high flow events, together with inputs from non-treated CSOs. The different types of bacteria used as indicators of water quality were reviewed. Several aspects of the numerical modelling of bathing water quality were also reviewed, including: the governing equations; the numerical schemes; dispersion; the coupling of models; and parallel computing. The representation of the mortality of the bacterial indicators was also reviewed.

Chapter 3

Derivation of the Governing Equations

3.1 Introduction

In this chapter, the general governing equations (including continuity and momentum) for fluid flow and solute transport are derived. Whilst the theory behind these derivations is not new, it has been included in this thesis to clarify the assumptions made during these derivations.

The fluid is assumed to be in a continuum. This means that quantities such as density, specific volume, pressure, velocity and acceleration are assumed to vary continuously throughout the fluid (Valliappan, 1981). The continuum assumption is valid in cases where there is enough fluid such that the probability of fluid molecules colliding with the flow boundaries is high. For most coastal, river and estuarine flows this assumption is valid. The derivation process involves considering an elemental control volume in a Cartesian co-ordinate system. The Eulerian description of the fluid flow field is used. This is a way of looking at fluid motion which focuses on specific locations in the space, through which the fluid flows as time passes (Lamb, 1932).

The general stress equations for a deformable body are derived in Section 3.2. It

is assumed that the angular accelerations about the control volume do not become infinitely large and that the density of a fluid particle does not change as it moves (i.e. the flow is incompressible). The equations for the rate of strain in a fluid are derived in Section 3.3. The general stress-strain relations for an isotropic solid material are derived in Section 3.4 and an analogy with fluids is made to give the constitutive equations. It is assumed that the flow is laminar and the fluid is Newtonian (i.e. constant laminar viscosity).

In Section 3.6, the constitutive equations are then substituted into the general stress equations for a deformable body to give the Navier-Stokes equations (Schlichting, 1979). The fluid is then assumed to be an ideal fluid, which means that the fluid is inviscid (zero viscosity). This gives the Euler equations (i.e. momentum equations) for the fluid flow. Mass conservation across the elemental control volume is considered in Section 3.5 assuming incompressible flow, to give the continuity equation. In Section 3.7, the conservation of the solute concentration across the elemental control volume is considered, assuming that any molecular diffusion is negligible.

3.2 Stress Equations for a Deformable Body

The normal and shear stresses on an elemental control volume in a continuum are considered in this section. Newton's second law is then used to relate the movement of the control volume with external (i.e. body) forces, normal and shear stresses acting on the faces of the control volume. The density of a fluid particle is then assumed to be constant (i.e. incompressible flow). In other words, the density does not change as the particle moves.

An elemental control volume $\Delta x \Delta y \Delta z$ is considered in a Cartesian system of co-ordinates with axes (x, y, z), velocity components (u, v, w) and body forces per unit mass (X, Y, Z) as shown in Figure 3.1.

In this control volume, there will be normal and shear stresses acting on the

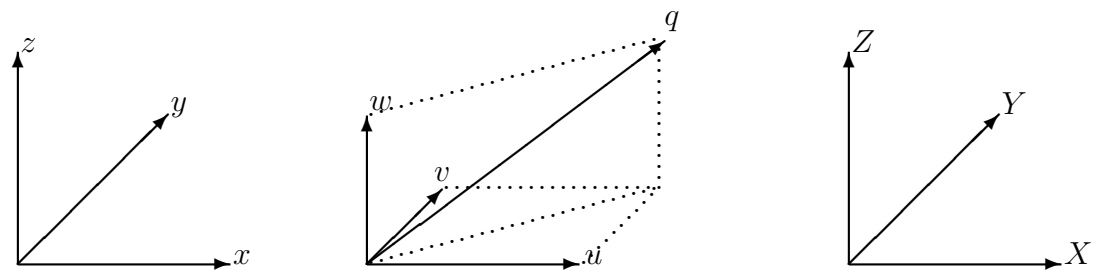

(a) Axes $\{x,\, y,\, z\}$ (b) Velocity components $\{u,\, v,\, w\}$ (c) Body forces per unit mass $\{\mathrm{X},\, \mathrm{Y},\, \mathrm{Z}\}$

Figure 3.1: Cartesian System for control volume

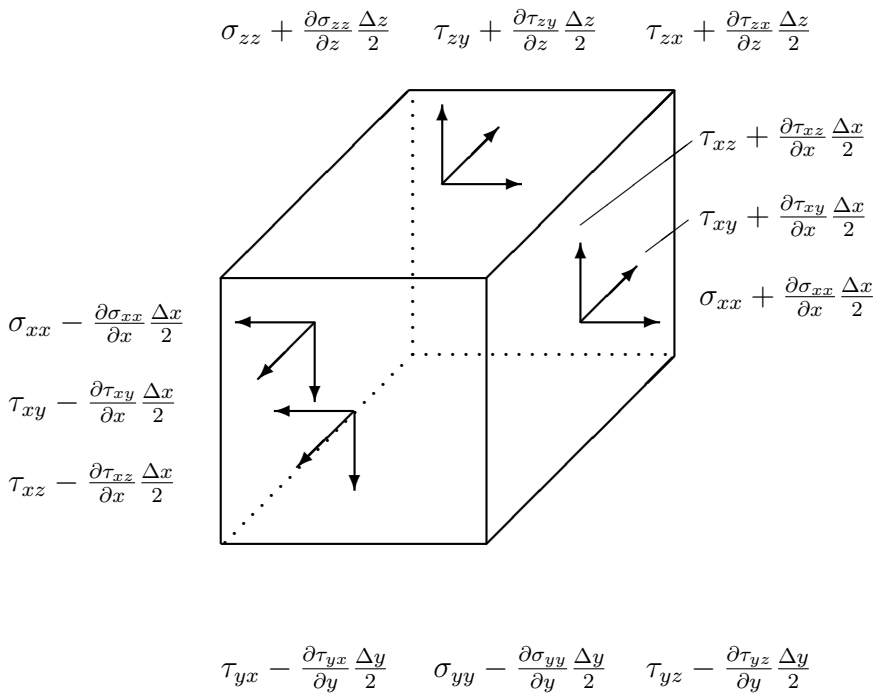

Figure 3.2: Stresses on elemental control volume

element faces, as shown in Figure 3.2, where τ_{xz} and τ_{xy} are the shear stresses and σ_{xx} is a normal stress.

Notation:

- 1st subscript defines the plane normal to subscript
- 2nd subscript defines the direction on the plane

The complete stress tensor is:

$$\sigma_{ij} = \begin{bmatrix} \sigma_{xx} & \tau_{xy} & \tau_{xz} \\ \tau_{yx} & \sigma_{yy} & \tau_{yz} \\ \tau_{zx} & \tau_{zy} & \sigma_{zz} \end{bmatrix} \tag{3.1}$$

where $i, j = 1, 2, 3 = x, y, z$.

From dynamic considerations (Timoshenko and Goodier, 1970) we get:

$$\omega_y \Delta I_y = (\tau_{xz} \Delta y \Delta z)\Delta x - (\tau_{zx} \Delta x \Delta y)\Delta z = (\tau_{xz} - \tau_{zx})\Delta V \tag{3.2}$$

where ΔI_y is the elementary moment of inertia about the y axis and ω_y is the corresponding angular acceleration. As $\Delta V \to 0$, in order that ω_y does not become infinitely large (i.e. $\Delta I \propto \Delta x^5, \Delta V \propto \Delta x^3$) .

$$\tau_{xz} - \tau_{zx} = 0 \tag{3.3}$$

The stress tensor is thus symmetrical about the diagonal, wherein:$\tau_{xy} = \tau_{yx}$, $\tau_{xz} = \tau_{zx}$ and $\tau_{yz} = \tau_{zy}$ giving the six different stress components (σ_{xx} σ_{yy} σ_{zz} τ_{xy} τ_{xz} τ_{yz}).

Newton's second law of motion states that the sum of the external forces acting on a unit mass must be equal to the rate of change of linear momentum :

$$\sum \vec{f} = \frac{\mathrm{d}m\vec{u}}{\mathrm{d}t} \tag{3.4}$$

Considering the forces on the control volume and applying Newton's second law gives:

$$\Delta x\Delta y\Delta z\frac{\mathrm{d}\rho u}{\mathrm{d}t} = \rho \mathrm{X}\Delta x\Delta y\Delta z + \frac{\partial \sigma_{xx}}{\partial x}\Delta x(\Delta y\Delta z) + \frac{\partial \tau_{yx}}{\partial y}\Delta y(\Delta x\Delta z) + \frac{\partial \tau_{zx}}{\partial z}\Delta z(\Delta x\Delta y) \tag{3.5}$$

Dividing by the volume of the element, $\Delta x\Delta y\Delta z$ gives:

$$\begin{aligned}
\frac{\mathrm{d}\rho u}{\mathrm{d}t} &= \rho \mathrm{X} + \frac{\partial \sigma_{xx}}{\partial x} + \frac{\partial \tau_{yx}}{\partial y} + \frac{\partial \tau_{zx}}{\partial z} \\
\frac{\mathrm{d}\rho v}{\mathrm{d}t} &= \rho \mathrm{Y} + \frac{\partial \tau_{xy}}{\partial x} + \frac{\partial \sigma_{yy}}{\partial y} + \frac{\partial \tau_{zy}}{\partial z} \\
\frac{\mathrm{d}\rho w}{\mathrm{d}t} &= \rho \mathrm{Z} + \frac{\partial \tau_{xz}}{\partial x} + \frac{\partial \tau_{yz}}{\partial y} + \frac{\partial \sigma_{zz}}{\partial z}
\end{aligned} \tag{3.6}$$

Assuming incompressible flow (i.e. that the density of a fluid particle does not change as it moves in the plane) then $\left(\frac{\mathrm{d}\rho}{\mathrm{d}t} = 0\right)$:

$$\begin{aligned}
\rho\frac{\mathrm{d}u}{\mathrm{d}t} &= \rho \mathrm{X} + \frac{\partial \sigma_{xx}}{\partial x} + \frac{\partial \tau_{yx}}{\partial y} + \frac{\partial \tau_{zx}}{\partial z} \\
\rho\frac{\mathrm{d}v}{\mathrm{d}t} &= \rho \mathrm{Y} + \frac{\partial \tau_{xy}}{\partial x} + \frac{\partial \sigma_{yy}}{\partial y} + \frac{\partial \tau_{zy}}{\partial z} \\
\rho\frac{\mathrm{d}w}{\mathrm{d}t} &= \rho \mathrm{Z} + \frac{\partial \tau_{xz}}{\partial x} + \frac{\partial \tau_{yz}}{\partial y} + \frac{\partial \sigma_{zz}}{\partial z}
\end{aligned} \tag{3.7}$$

3.3 Strain Relationships for a Fluid Element

The relationships between the strains on an elemental control volume and the velocity components are considered in this section.

Linear Strains

Linear strains are due to normal stresses caused by velocity gradients. In fluids, the rates of strain are considered giving (See Figure 3.3).

Defining:

$$\varepsilon_{xx} = \text{strain per unit time} = \frac{\text{elongation per unit time}}{\text{original length}} = \frac{\partial u}{\partial x}\Delta x\Delta t\frac{1}{\Delta t\Delta x} \tag{3.8}$$

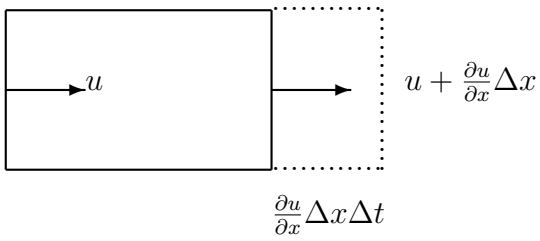

Figure 3.3: Extension in x-direction in time Δt

Then:

$$\varepsilon_{xx} = \frac{\partial u}{\partial x} \tag{3.9}$$

and

$$\varepsilon_{yy} = \frac{\partial v}{\partial y} \tag{3.10}$$

similarly

$$\varepsilon_{zz} = \frac{\partial w}{\partial z} \tag{3.11}$$

Note that $\varepsilon_{xx} + \varepsilon_{yy} + \varepsilon_{zz} = \frac{\partial u}{\partial x} + \frac{\partial v}{\partial y} + \frac{\partial w}{\partial z} = e =$ volume dilation. And $e = 0$ for incompressible flow

Angular Strains

The angular strains can be defined by considering the total angular deformations after a small change in time (Δt) as shown in Figure 3.4.

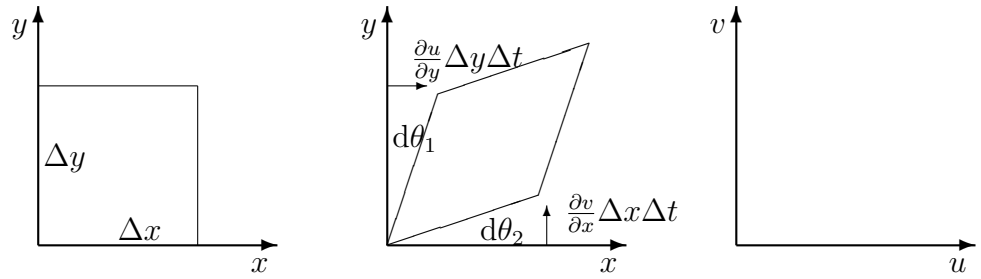

(a) $t = 0$ (b) $t = \Delta t$ (c) Velocity

Figure 3.4: Angular Strain in xy-plane at time Δt

Defining: $\gamma_{xy} = 2\varepsilon_{xy}$ = angular strain = total deformation of the right angle

$\gamma_{xy} = 2\varepsilon_{xy} = \mathrm{d}\theta_1 + \mathrm{d}\theta_2$

then:

$$\gamma_{xy} = 2\varepsilon_{xy} = \left(\frac{\partial u}{\partial y} + \frac{\partial v}{\partial x}\right)\Delta t \tag{3.12}$$

$$\gamma_{yz} = 2\varepsilon_{yz} = \left(\frac{\partial v}{\partial z} + \frac{\partial w}{\partial y}\right)\Delta t \tag{3.13}$$

$$\gamma_{xz} = 2\varepsilon_{xz} = \left(\frac{\partial w}{\partial x} + \frac{\partial u}{\partial z}\right)\Delta t \tag{3.14}$$

The complete strain tensor may then be written as:

$$\varepsilon_{ij} = \begin{bmatrix} \varepsilon_{xx} & \varepsilon_{xy} & \varepsilon_{xz} \\ \varepsilon_{yx} & \varepsilon_{yy} & \varepsilon_{yz} \\ \varepsilon_{zx} & \varepsilon_{zy} & \varepsilon_{zz} \end{bmatrix} = \begin{bmatrix} \varepsilon_{xx} & \frac{\gamma_{xy}}{2} & \frac{\gamma_{xz}}{2} \\ \frac{\gamma_{yx}}{2} & \varepsilon_{yy} & \frac{\gamma_{yz}}{2} \\ \frac{\gamma_{zx}}{2} & \frac{\gamma_{zy}}{2} & \varepsilon_{zz} \end{bmatrix} \tag{3.15}$$

which is again symmetric, $\varepsilon_{ij} = \varepsilon_{ji}$, giving six different strain components (ε_{xx},ε_{yy},ε_{zz}, ε_{xy}, ε_{xz}, ε_{yz}).

Equations (3.9), (3.10), (3.11), (3.12), (3.14) and (3.13) can be combined into a single equation in Cartesian-tensor notation to give:

$$\varepsilon_{ij} = \frac{1}{2}\left(u_{i,j} + u_{j,i}\right) \tag{3.16}$$

where $i, j = 1, 2, 3 = x, y, z$ and $u_{x,y} = \frac{\partial u_x}{\partial y}$.

Angular strain may take place with

Translation $u\Delta t$ in the x-direction, and $v\Delta t$ in the y-direction

Linear deformation $\frac{\partial u}{\partial x}\Delta x\Delta t$ in the x-direction, etc

Rotation $\Omega_z = \frac{\mathrm{d}\theta_2 - \mathrm{d}\theta_1}{\mathrm{d}t} = \frac{1}{2}\left(\frac{\partial v}{\partial x} - \frac{\partial u}{\partial y}\right) = \frac{1}{2}\omega_z$ (vorticity)

It is worth noting herein that the

(i) components of vorticity are $\omega_x = \frac{\partial w}{\partial y} - \frac{\partial v}{\partial z}$, $\omega_y = \frac{\partial u}{\partial z} - \frac{\partial w}{\partial x}$, $\omega_z = \frac{\partial v}{\partial x} - \frac{\partial u}{\partial y}$

(ii) angular strain components ε_{ij} give the distortion of the right angle in the plane normal to the k-axis. The distortion is volume preserving and affects only the shape of the element.

(iii) mathematicians like to use half the value of strain used by engineers. $\gamma_{xy} = 2\varepsilon_{xy}$, $\gamma_{xz} = 2\varepsilon_{xz}$ $\gamma_{yz} = 2\varepsilon_{yz}$ Engineers use the change in angle (angular strain) because it is easily measurable whereas mathematicians use the actual theoretical strain.

3.4 Stress-Strain Equations for Solids and Fluids

The stresses on the elemental control volume are related to the strains, which lead to the constitutive equations in this section using Stokes's law.

Pure Normal Stresses

Consider the analogy of an elastic solid subject only to normal stresses (Figure 3.5).

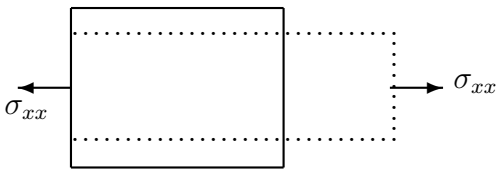

$\sigma_{xx} = E\varepsilon_{xx}$ (E = Young's modulus)

$\varepsilon_{yy} = -\nu\varepsilon_{xx}$ (ν = Poisson's ratio)

Figure 3.5: Deformation of elastic solid

Consider strains resulting from applying normal stresses in one direction only (See Table 3.1).

Hence applying the normal stresses, σ_{xx} σ_{yy} and σ_{zz} simultaneously by the principle of superposition, which is valid for small strains, gives the following strains:

$$\varepsilon_{xx} = \frac{1}{E}\left[\sigma_{xx} - \nu(\sigma_{yy} + \sigma_{zz})\right] \tag{3.17}$$

Table 3.1: Superposition of Normal Stresses

	x-direction (ε_{xx})	y-direction (ε_{yy})	z-direction (ε_{zz})
Apply σ_{xx} only	$\frac{1}{E}\sigma_{xx}$	$-\frac{1}{E}\nu\sigma_{xx}$	$-\frac{1}{E}\nu\sigma_{xx}$
Apply σ_{yy} only	$-\frac{1}{E}\nu\sigma_{yy}$	$\frac{1}{E}\sigma_{yy}$	$-\frac{1}{E}\nu\sigma_{yy}$
Apply σ_{zz} only	$-\frac{1}{E}\nu\sigma_{zz}$	$-\frac{1}{E}\nu\sigma_{zz}$	$\frac{1}{E}\sigma_{zz}$

$$\varepsilon_{yy} = \frac{1}{E}\left[\sigma_{yy} - \nu(\sigma_{xx} + \sigma_{zz})\right] \tag{3.18}$$

$$\varepsilon_{zz} = \frac{1}{E}\left[\sigma_{zz} - \nu(\sigma_{xx} + \sigma_{yy})\right] \tag{3.19}$$

Pure Shear Stresses

Consider the two dimensional analogy with an elastic solid subject to only shear stresses (τ_{xy}).

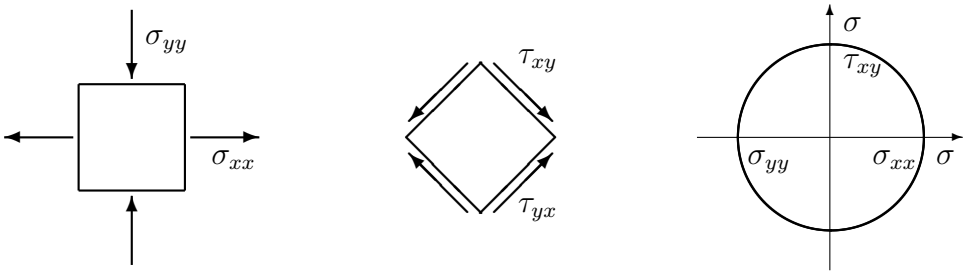

(a) Normal stresses (b) Pure shear (c) Mohr's circle

Figure 3.6: Pure shear strains

The stress states are shown in Figure 3.6. At the maximum shear stress on Mohr's circle, the mean stress ($\frac{1}{3}(\sigma_{xx} + \sigma_{yy})$) is zero. Hence $\sigma_{xx} = -\sigma_{yy}$ and $\tau_{xy} = \sigma_{xx}$. In considering Equations (3.17) and (3.18) without the component of stress in the z-axis direction gives:

$$\varepsilon_{xx} = \frac{1}{E}\left[\sigma_{xx} - \nu\sigma_{yy}\right] \tag{3.20}$$

$$\varepsilon_{yy} = \frac{1}{E}\left[\sigma_{yy} - \nu\sigma_{xx}\right] \tag{3.21}$$

Substituting $\sigma_{yy} = -\sigma_{xx}$ gives:

$$\varepsilon_{xx} = \frac{1}{E}\sigma_{xx}\,(1+\nu) \tag{3.22}$$

$$\varepsilon_{yy} = -\frac{1}{E}\sigma_{xx}\,(1+\nu) \tag{3.23}$$

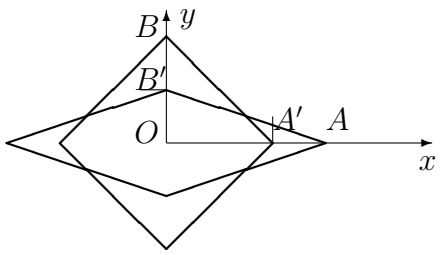

Figure 3.7: Geometrical consideration of shear strain

The change in the angle $OAB - OA'B'$ is equal to the engineering strain ε_{xy}. Therefore:

$$tan\left(\frac{\pi}{4} - \frac{\gamma_{xy}}{2}\right) = \frac{OB'}{OA'} = \frac{1+\varepsilon_{yy}}{1+\varepsilon_{xx}} \tag{3.24}$$

Expanding the tangent function and substituting Equations (3.22) and (3.23) gives:

$$\frac{1 - \tan\left(\frac{\gamma_{xy}}{2}\right)}{1 + \tan(\frac{\gamma_{xy}}{2})} = \frac{1 - \frac{1}{E}\sigma_{xx}(1+\nu)}{1 + \frac{1}{E}\sigma_{xx}(1+\nu)} \tag{3.25}$$

$$\tan\left(\frac{\gamma_{xy}}{2}\right) = \frac{1}{E}\sigma_{xx}(1+\nu) \tag{3.26}$$

When $\gamma_{xy} << 1$ then $\tan(\frac{\gamma_{xy}}{2}) \approx \frac{\gamma_{xy}}{2}$ Hence:

$$\gamma_{xy} = \frac{2}{E}\sigma_{xx}(1+\nu) \tag{3.27}$$

Substituting $\sigma_{xx} = \tau_{xy}$ gives:

$$\gamma_{xy} = 2\varepsilon_{xy} = \frac{2}{E}(1+\nu)\tau_{xy} \tag{3.28}$$

Similarly:

$$\gamma_{yz} = 2\varepsilon_{yz} = \frac{2}{E}(1+\nu)\tau_{yz} \tag{3.29}$$

$$\gamma_{xz} = 2\varepsilon_{xz} = \frac{2}{E}(1+\nu)\tau_{xz} \tag{3.30}$$

Constitutive Equations

The relationship between stress and deformation in a continuum is known as a constitutive equation (Rossmann and Dym, 2009). Equations (3.17), (3.18), (3.19), (3.28), (3.30) and (3.29) can be contracted to a single equation in Cartesian-tensor notation (Schlichting, 1979) giving:

$$\varepsilon_{ij} = \frac{1+\nu}{E}\sigma_{ij} - \frac{\nu}{E}\delta_{ij}\sigma_{kk} \tag{3.31}$$

where $i, j, k = 1, 2, 3 = x, y, z$, the Kronecker delta $\delta_{ij} = 0$ for $i \neq j$ and $\delta_{ij} = 1$ for $i = j$.

For the case where $i = j$ Equation (3.31) can be rewritten as:

$$\varepsilon_{ii} = \frac{1+\nu}{E}\sigma_{ii} - \frac{\nu}{E}\delta_{ii}\sigma_{kk} = \frac{1+\nu}{E}\sigma_{ii} - \frac{3\nu}{E}\sigma_{kk} \tag{3.32}$$

Therefore:

$$\varepsilon_{ii} = \frac{1-2\nu}{E}\sigma_{ii} \tag{3.33}$$

Making σ_{ij} the subject of Equation (3.31) leads to :

$$\sigma_{ij} = \frac{E}{1+\nu}\varepsilon_{ij} + \frac{\nu}{1+\nu}\delta_{ij}\sigma_{kk} \tag{3.34}$$

Substituting σ_{kk} using Equation (3.33) gives:

$$\sigma_{ij} = \frac{E}{1+\nu}\varepsilon_{ij} + \frac{\nu}{(1+\nu)}\frac{E}{(1-2\nu)}\delta_{ij}\varepsilon_{kk} \tag{3.35}$$

Introducing the mean normal stress from Equation (3.33) gives:

$$\sigma_{ij} = \frac{E}{1+\nu}\varepsilon_{ij} + \frac{\nu}{(1+\nu)}\frac{E}{(1-2\nu)}\delta_{ij}\varepsilon_{kk} + \underbrace{\frac{\delta_{ij}\sigma_{kk}}{3}}_{\text{Mean Normal Stress}} - \underbrace{\frac{E}{3(1-2\nu)}\delta_{ij}\varepsilon_{kk}}_{\text{Mean Normal Stress}} \tag{3.36}$$

Simplifying:

$$\sigma_{ij} = \underbrace{\frac{\delta_{ij}\sigma_{kk}}{3}}_{\text{Mean Normal Stress}} + \frac{E}{1+\nu}\varepsilon_{ij} - \frac{E}{3(1+\nu)}\delta_{ij}\varepsilon_{kk} \tag{3.37}$$

which can also be written as:

$$\sigma_{ij} = \underbrace{\frac{\delta_{ij}\sigma_{kk}}{3}}_{\text{Mean Normal Stress}} + \underbrace{2G\varepsilon_{ij} - \frac{2G}{3}\delta_{ij}\varepsilon_{kk}}_{\text{deviatoric stress}} \tag{3.38}$$

where the shear modulus, $G = \frac{E}{2(1+\nu)}$.

Substituting the strain rates from Equation (3.16) into the above gives:

$$\sigma_{ij} = \underbrace{\frac{\delta_{ij}\sigma_{kk}}{3}}_{\text{Mean Normal Stress}} + \underbrace{G\left(u_{i,j} + u_{j,i}\right) - \frac{2G}{3}\delta_{ij}u_{k,k}}_{\text{deviatoric stress}} \tag{3.39}$$

Equation (3.39) relates the stresses and strains without the elastic constants E and ν(although G still occurs). The last two terms on the right hand side of equation (3.39) are known as the deviatoric stress, σ'_{ij} , since $\sigma_{ij} = -\mathrm{p} + \sigma'_{ij}$. An analogy between fluids and solids is used as shown in Table 3.2.

Hence the 6 stresses are related to the 6 rates of strain by the constitutive

Table 3.2: Analogy between fluids and solids

SOLIDS	FLUIDS
Deformation proportional to strain (i.e. Hookes' law)	Deformation proportional to rate of strain (i.e. Stokes' law)
$\tau_{xy} = G\varepsilon_{xy}$	$\tau_{xy} = \mu\frac{\mathrm{d}\varepsilon_{xy}}{\mathrm{d}t}$
$\sigma_{xx} = E\varepsilon_{xx}$	$\mathrm{dp} = -K\frac{\mathrm{d}V}{v}$
where G = shear modulus E = Young's modulus	where μ = dynamic viscosity K = bulk modulus

equations for an isotropic Newtonian fluid

$$\sigma_{xx} = -\mathrm{p} + 2\mu\frac{\partial u}{\partial x} - \frac{2\mu}{3}\left(\frac{\partial u}{\partial x} + \frac{\partial v}{\partial y} + \frac{\partial w}{\partial z}\right) \tag{3.40}$$

$$\sigma_{yy} = -\mathrm{p} + 2\mu\frac{\partial v}{\partial y} - \frac{2\mu}{3}\left(\frac{\partial u}{\partial x} + \frac{\partial v}{\partial y} + \frac{\partial w}{\partial z}\right) \tag{3.41}$$

$$\sigma_{zz} = -\mathrm{p} + 2\mu\frac{\partial w}{\partial z} - \frac{2\mu}{3}\left(\frac{\partial u}{\partial x} + \frac{\partial v}{\partial y} + \frac{\partial w}{\partial z}\right) \tag{3.42}$$

$$\tau_{xy} = \mu\left(\frac{\partial u}{\partial y} + \frac{\partial v}{\partial x}\right) \tag{3.43}$$

$$\tau_{yz} = \mu\left(\frac{\partial v}{\partial z} + \frac{\partial w}{\partial y}\right) \tag{3.44}$$

$$\tau_{xz} = \mu\left(\frac{\partial w}{\partial x} + \frac{\partial u}{\partial z}\right) \tag{3.45}$$

3.5 Mass Conservation (Continuity)

The conservation of mass requires that the net fluid mass entering an elemental control volume in a time interval Δt equals the amount by which the mass of the element changes during the time intervalΔt.

Mass inflow across entrance face(1) in time Δt is:

$$I_1 = \underbrace{\left(\rho u - \frac{\partial \rho u}{\partial x}\frac{\Delta x}{2}\right)}_{\text{mass per unit area/ time}} \Delta t \underbrace{\Delta z \Delta y}_{\text{Area}} \tag{3.46}$$

where ρ = mass / unit volume or mass density of fluid

Mass inflow across opposite/end face(2) is:

$$I_2 = \underbrace{-\left(\rho u + \frac{\partial \rho u}{\partial x}\frac{\Delta x}{2}\right)}_{\text{mass per unit area/ time}} \Delta t \underbrace{\Delta z \Delta y}_{\text{Area}} \tag{3.47}$$

Hence, summing Equations (3.46) and (3.47) gives the x-direction net mass inflow in time Δt as:

$$I_{\text{net inflow x}} = -\frac{\partial \rho u}{\partial x} \underbrace{\Delta x \Delta y \Delta z}_{\text{Volume}} \Delta t \tag{3.48}$$

and similarly for the y and z directions, giving:

$$I_{\text{NET INFLOW}} = -\left(\frac{\partial \rho u}{\partial x} + \frac{\partial \rho v}{\partial y} + \frac{\partial \rho w}{\partial z}\right) \underbrace{\Delta x \Delta y \Delta z}_{\text{Volume}} \Delta t \tag{3.49}$$

Also, if mass at time t, $\mathrm{M}_t = \rho \Delta x \Delta y \Delta z$, then mass at times $t - \frac{\Delta t}{2}$ and $t + \frac{\Delta t}{2}$ are, respectively:

$$\mathrm{M}_{t-\frac{\Delta t}{2}} = \rho \Delta x \Delta y \Delta z - \frac{\partial}{\partial t}\left(\rho \Delta x \Delta y \Delta z\right)\frac{\Delta t}{2} \tag{3.50}$$

and

$$\mathrm{M}_{t+\frac{\Delta t}{2}} = \rho \Delta x \Delta y \Delta z + \frac{\partial}{\partial t}\left(\rho \Delta x \Delta y \Delta z\right)\frac{\Delta t}{2} \tag{3.51}$$

Therefore the net mass increase in time Δt is given as:

$$= \frac{\partial}{\partial t} (\rho \Delta x \Delta y \Delta z) \, \Delta t \tag{3.52}$$

$$= \frac{\partial \rho}{\partial t} \Delta x \Delta y \Delta z \Delta t \tag{3.53}$$

Since the net increase of mass in the control volume with time equals the net inflow into the control volume then:

$$\therefore \frac{\partial \rho}{\partial t} \Delta x \Delta y \Delta z \Delta t = - \left(\frac{\partial \rho u}{\partial x} + \frac{\partial \rho v}{\partial y} + \frac{\partial \rho w}{\partial z} \right) \Delta x \Delta y \Delta z \Delta t \tag{3.54}$$

Cancelling out common terms gives the continuity equation for compressible flow:

$$\frac{\partial \rho}{\partial t} + \frac{\partial \rho u}{\partial x} + \frac{\partial \rho v}{\partial y} + \frac{\partial \rho w}{\partial z} = 0 \tag{3.55}$$

Assuming incompressible flow (i.e. the density of a fluid particle does not change as it moves) $\left(\frac{\mathrm{d}\rho}{\mathrm{d}t} = 0 \right)$ gives :

$$\frac{\partial u}{\partial x} + \frac{\partial v}{\partial y} + \frac{\partial w}{\partial z} = 0 \tag{3.56}$$

3.6 Momentum Conservation

Navier-Stokes Equations

The Navier-Stokes equations describe the motion of fluids. They are named after Claude-Louis Navier, a French Engineer who mainly designed bridges (1822 paper) and George Gabriel Stokes, a Professor of Mathematics at Cambridge (1845 paper).

Inserting the constitutive equations, (3.40) to (3.45), into the general stress equations for a deformable body, Eq. (3.7), gives the equations of motion for viscous flow (also known as the Navier Stokes Equations).

Considering the x-direction gives:

$$\rho\frac{\mathrm{d}u}{\mathrm{d}t} = \rho\mathrm{X} + \frac{\partial}{\partial x}\left[-\mathrm{p} + 2\mu\frac{\partial u}{\partial x} - \frac{2\mu}{3}\left(\frac{\partial u}{\partial x} + \frac{\partial v}{\partial y} + \frac{\partial w}{\partial z}\right)\right] + \frac{\partial}{\partial y}\left[\mu\left(\frac{\partial u}{\partial y} + \frac{\partial v}{\partial x}\right)\right] + \frac{\partial}{\partial z}\left[\mu\left(\frac{\partial w}{\partial x} + \frac{\partial u}{\partial z}\right)\right] \quad (3.57)$$

$$\rho\frac{\mathrm{d}u}{\mathrm{d}t} = \rho\mathrm{X} + \frac{\partial}{\partial x}\left[-\mathrm{p} + \frac{\mu}{3}\frac{\partial u}{\partial x} - \frac{2\mu}{3}\frac{\partial v}{\partial y} - \frac{2\mu}{3}\frac{\partial w}{\partial z}\right] + \mu\frac{\partial}{\partial y}\left[\frac{\partial u}{\partial y} + \frac{\partial v}{\partial x}\right] + \mu\frac{\partial}{\partial z}\left[\frac{\partial w}{\partial x} + \frac{\partial u}{\partial z}\right] \quad (3.58)$$

$$\rho\frac{\mathrm{d}u}{\mathrm{d}t} = \rho\mathrm{X} - \frac{\partial \mathrm{p}}{\partial x} + \mu\left[\frac{\partial^2 u}{\partial x^2} + \frac{\partial^2 u}{\partial y^2} + \frac{\partial^2 u}{\partial z^2}\right] + \frac{\mu}{3}\frac{\partial}{\partial x}\left[\frac{\partial u}{\partial x} + \frac{\partial v}{\partial y} + \frac{\partial w}{\partial z}\right] \quad (3.59)$$

and similarly for the y and z directions.

Since $u = f(x, y, z, t)$then the acceleration term can be expanded to give:

$$\mathrm{d}u = \frac{\partial u}{\partial t}\Delta t + \frac{\partial u}{\partial x}\Delta x + \frac{\partial u}{\partial y}\Delta y + \frac{\partial u}{\partial z}\Delta z \quad (3.60)$$

$$\therefore \frac{\mathrm{d}u}{\mathrm{d}t} = \frac{\partial u}{\partial t} + u\frac{\partial u}{\partial x} + v\frac{\partial u}{\partial y} + w\frac{\partial u}{\partial z} \quad (3.61)$$

hence

$$\begin{aligned}
\rho\left(\frac{\partial u}{\partial t} + u\frac{\partial u}{\partial x} + v\frac{\partial u}{\partial y} + w\frac{\partial u}{\partial z}\right) &= \rho\mathrm{X} - \frac{\partial \mathrm{p}}{\partial x} + \mu\left[\frac{\partial^2 u}{\partial x^2} + \frac{\partial^2 u}{\partial y^2} + \frac{\partial^2 u}{\partial z^2}\right] \\
\rho\left(\frac{\partial u}{\partial t} + u\frac{\partial u}{\partial x} + v\frac{\partial u}{\partial y} + w\frac{\partial u}{\partial z}\right) &= \rho\mathrm{Y} - \frac{\partial \mathrm{p}}{\partial y} + \mu\left[\frac{\partial^2 v}{\partial x^2} + \frac{\partial^2 v}{\partial y^2} + \frac{\partial^2 v}{\partial z^2}\right] \\
\rho\left(\frac{\partial u}{\partial t} + u\frac{\partial u}{\partial x} + v\frac{\partial u}{\partial y} + w\frac{\partial u}{\partial z}\right) &= \rho\mathrm{Z} - \frac{\partial \mathrm{p}}{\partial z} + \mu\left[\frac{\partial^2 w}{\partial x^2} + \frac{\partial^2 w}{\partial y^2} + \frac{\partial^2 w}{\partial z^2}\right]
\end{aligned} \quad (3.62)$$

Equations (3.56) and (3.62) constitute 4 equations for 4 unknowns, { u v w, and p } in terms of { x y z, and t }. They represent the simplified form of the Navier-Stokes equations for incompressible flow.

Euler Equations

The Euler equations are an approximation of the Navier-Stokes equations, where the fluid is assumed to be inviscid. They are named after Leonhard Euler (1705-1783). in considering an inviscid fluid, that is, one whose viscosity is zero ($\mu = 0$), then the Navier-Stokes Equations (3.62) can be rewritten as:

$$\begin{aligned}
\rho\left(\frac{\partial u}{\partial t} + u\frac{\partial u}{\partial x} + v\frac{\partial u}{\partial y} + w\frac{\partial u}{\partial z}\right) &= \rho\mathrm{X} - \frac{\partial \mathrm{p}}{\partial x} \\
\rho\left(\frac{\partial u}{\partial t} + u\frac{\partial u}{\partial x} + v\frac{\partial u}{\partial y} + w\frac{\partial u}{\partial z}\right) &= \rho\mathrm{Y} - \frac{\partial \mathrm{p}}{\partial y} \\
\rho\left(\frac{\partial u}{\partial t} + u\frac{\partial u}{\partial x} + v\frac{\partial u}{\partial y} + w\frac{\partial u}{\partial z}\right) &= \rho\mathrm{Z} - \frac{\partial \mathrm{p}}{\partial z}
\end{aligned} \tag{3.63}$$

Upon substituting $\mu = 0$ into the constitutive model for a Newtonian fluid, Equations (3.40) to (3.45), the state of stress in an inviscid fluid is found to be :

$$\sigma_{xx} = \sigma_{yy} = \sigma_{zz} = -\mathrm{p} \tag{3.64}$$

$$\tau_{xy} = \tau_{xz} = \tau_{yz} = 0 \tag{3.65}$$

where p is the hydrostatic pressure. This shows that an inviscid fluid is incapable of exerting a shear stress (Shaughnessy *et al.*, 2005). The absence of a shear stress indicates that an inviscid fluid does not obey the no-slip condition and therefore must slip along a solid surface.

3.7 Solute Conservation (Advective-Diffusion)

The continuity and momentum equations for incompressible flow can be solved using numerical methods to predict velocity fields and water elevations in complex basins such as rivers, lakes, estuaries, coastal embayments, ports, etc. However, in most engineering problems knowledge of the velocity field and water elevations is of limited

value for water engineers and scientists and, in addition, the advective-diffusion equation is solved to give concentration distributions of constituents (or solutes) in a fluid, such as heat (or temperature), dye, pollution, salinity, Dissolved Oxygen (DO), Biochemical Oxygen Demand (BOD), nutrients, etc.

Two transport mechanisms exist:

Advection is the process by which a fluid and any of its constituents moves bodily from one point to another in a flow field

Diffusion is the movement of mass, heat, momentum or other constituents relative to time-averaged motion of the fluid

Fick's law of molecular diffusion states that the magnitude of the solute flux is proportional to the gradient of the solute concentration giving:

$$\frac{\partial s}{\partial t} = D\frac{\partial^2 s}{\partial x^2} \tag{3.66}$$

where s = mass concentration of solute and D = constant of proportionality or coefficient of molecular diffusion (units of m^2/s)

The conservation of mass (or matter) equation for a solute introduced into a fluid media can be expressed as:

$$\text{Net mass of solute entering control volume in time } \Delta t = \text{Net change of mass of solute within control volume in time } \Delta t \tag{3.67}$$

Molecular diffusion (e.g. typically $10^{-9} m^2/s$) is small in comparison with macroscopic turbulent mixing and can be neglected.

The mass of the substance entering an element in the x-direction in a time interval Δt is:

$$M_{\text{in}} = \left(su - \frac{\partial su}{\partial x}\frac{\Delta x}{2} \right) \Delta y \Delta z \Delta t \tag{3.68}$$

where u is the instantaneous fluid velocity component in the x-direction and s is the instantaneous solute concentration of a diffusing substance (mass of solute / volume

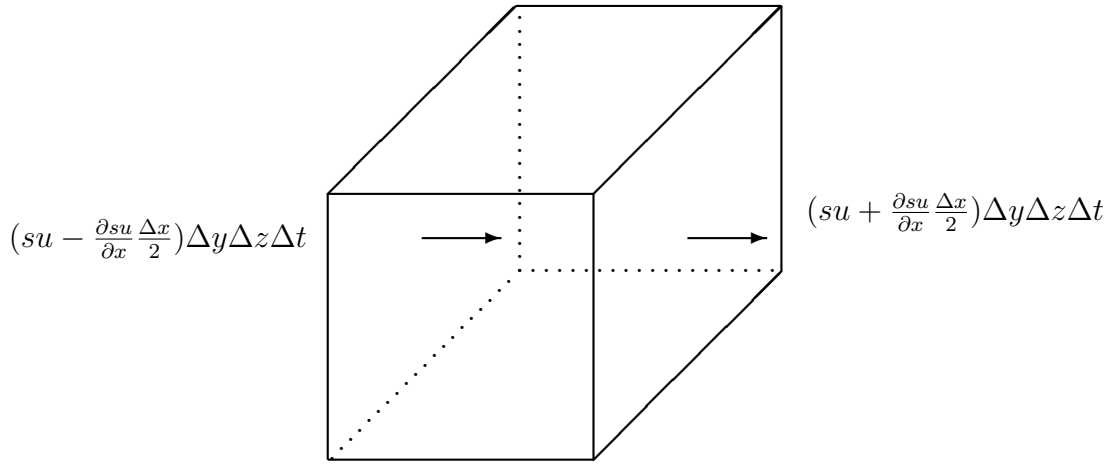

Figure 3.8: Solute entering and leaving an elemental control volume

of diffusion).

Likewise, the mass of the substance leaving an element in the x-direction in a time interval Δt is given as:

$$M_{\text{out}} = \left(su + \frac{\partial su}{\partial x}\frac{\Delta x}{2} \right) \Delta y \Delta z \Delta t \tag{3.69}$$

Hence, the net mass entering an elemental control volume in the x-direction in a time interval Δt is given as:

$$M_{\text{net x}} = M_{\text{in}} - M_{\text{out}} = -\frac{\partial su}{\partial x}\Delta x \Delta y \Delta z \Delta t \tag{3.70}$$

and therefore the net mass entering the control volume in all 3 directions in a time interval Δt can be written as:

$$M_{\text{net}} = -\left(\frac{\partial su}{\partial x} + \frac{\partial sv}{\partial y} + \frac{\partial sw}{\partial z} \right) \Delta x \Delta y \Delta z \Delta t \tag{3.71}$$

If the mass of solute in the elemental control volume at time t is: $M_t = s\Delta x \Delta y \Delta z$, then the mass at time $t + \frac{\Delta t}{2}$ and $t - \frac{\Delta t}{2}$ is respectively:

$$M_{t+\frac{\Delta t}{2}} = s\Delta x \Delta y \Delta z + \frac{\partial s}{\partial t}\Delta x \Delta y \Delta z \frac{\Delta t}{2} \tag{3.72}$$

$$M_{t-\frac{\Delta t}{2}} = s\Delta x\Delta y\Delta z - \frac{\partial s}{\partial t}\Delta x\Delta y\Delta z\frac{\Delta t}{2} \tag{3.73}$$

Hence, the net mass change in the elemental control volume in time t is:

$$M_{t+\frac{\Delta t}{2}} - M_{t-\frac{\Delta t}{2}} = \frac{\partial s}{\partial t}\Delta x\Delta y\Delta z\Delta t \tag{3.74}$$

Equating the net mass inflow of solute with the net mass change of solute in the control volume gives:

$$-\left(\frac{\partial su}{\partial x} + \frac{\partial sv}{\partial y} + \frac{\partial sw}{\partial z}\right)\Delta x\Delta y\Delta z\Delta t = \frac{\partial s}{\partial t}\Delta x\Delta y\Delta z\Delta t \tag{3.75}$$

$$\frac{\partial s}{\partial t} + \frac{\partial su}{\partial x} + \frac{\partial sv}{\partial y} + \frac{\partial sw}{\partial z} = 0 \tag{3.76}$$

3.8 Summary

The general governing equations (including continuity and momentum) for the fluid flow and solute transport in a continuum have been derived in this chapter. The Eulerian description of fluid flow has been used. The assumptions made in deriving the governing equations for mass conservation (Eq. (3.56)) and momentum (Eq. (3.63)) for a continuum include incompressible and inviscid (zero laminar viscosity) flow. In deriving the equations for solute transport (Eq. (3.76), it was assumed that molecular diffusion is negligible. Whilst the theory behind these derivations is not new, it has been included in this thesis to clarify the assumptions made during these derivations. In the next chapter, the general governing equations will be adapted for one dimensional (1D) and two dimensional (2D) flows in rivers and estuaries.

Chapter 4

Adaptation of the Governing Equations

4.1 Introduction

In this chapter the governing hydrodynamic and solute transport equations are adapted for one dimensional (1D) and two dimensional (2D) flow problems. In Section 4.2, the instantaneous velocities, pressure and solute concentrations are separated into mean and fluctuating components, which are then substituted into the Navier-Stokes equations to give the Reynold's Averaged Navier-Stokes (RANS) equations (Figure 4.1). The turbulence model used for this research study is described in Section 4.3. The formulation for flow resistance and bed friction is then described in Section 4.4. Section 4.5 gives the formulation for the Coriolis forces. The Reynold's Averaged Navier-Stokes (RANS) Equations are integrated over the cross-section area and depth of flow for 1D and 2D problems respectively in Sections 4.6 and 4.7 (Figure 4.1). Finally, the source terms are described in Section 4.8.

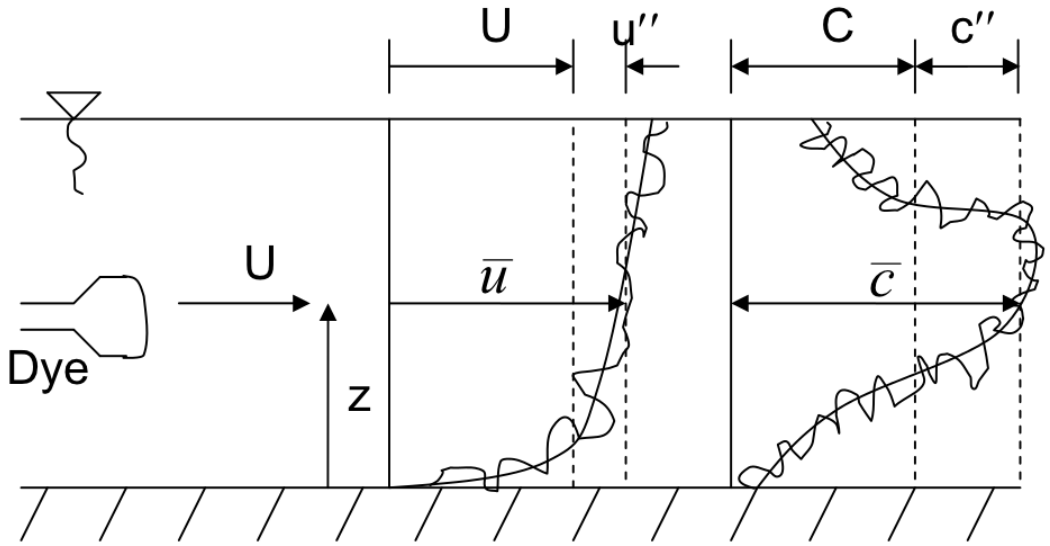

Figure 4.1: Time and Spatial Averages of velocity and concentration

4.2 Reynolds Averaged Navier-Stokes Equations

4.2.1 Introduction

The three components of velocity, u, v, w, pressure, p and solute concentration, s are decomposed according to the Reynolds conceptualization into mean and fluctuating components: $u = \overline{u} + u'$, $v = \overline{v} + v'$, $w = \overline{w} + w'$, $\mathrm{p} = \overline{\mathrm{p}} + \mathrm{p}'$, $s = \overline{s} + s'$ where u, v, w, p, s are the instantaneous velocity components, pressure and solute concentration, $\overline{u}, \overline{v}, \overline{w}, \overline{\mathrm{p}}, \overline{s}$ are the time averaged components and $u', v', w', \mathrm{p}', s'$ are the fluctuating components.

The following approximations are introduced in the Navier-Stokes equations:

The Boussinesq approximation: the density variation in a water body is much smaller than the density itself; therefore, constant density can be used in the equation of motion, except in the term for the buoyancy force.

The hydrostatic approximation: the vertical velocity component is assumed to be very small. Therefore, the vertical component of acceleration is much smaller than the gravitational acceleration.

In this section, the expressions above for instantaneous velocities, pressure and

solute concentration are substituted into the Navier-Stokes, continuity and solute transport equations. Time averages of the equations are then taken to obtain the corresponding Reynolds Averaged Navier-Stokes equations.

4.2.2 Reynolds Stresses

In 1886 Osborne Reynolds showed that expressions for the momentum interchange across two adjacent fluid layers consist of a time-average value plus a fluctuating component (Massey and Ward-Smith, 2006).

Consider a plane normal to the x-axis of area ΔA as shown in Figure 4.2.

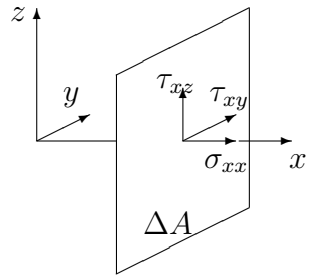

Figure 4.2: Momemtum flux across a plane

In a time interval Δt, the mass flow through ΔA is $\rho u \Delta A \Delta t$. Therefore, the momemtum flux $= \rho u^2 \Delta A \Delta t$ and momemtum flux per unit time is $\rho u^2 \Delta A$. Averaging over a period of time, the three momentum fluxes are:

$$\begin{aligned} \overline{\Delta M_x} &= \Delta A \rho \overline{uu} \\ \overline{\Delta M_y} &= \Delta A \rho \overline{uv} \\ \overline{\Delta M_z} &= \Delta A \rho \overline{uw} \end{aligned} \tag{4.1}$$

Since $uu = (\overline{u} + u')(\overline{u} + u') = \overline{uu} + 2\overline{u}u + u'u'$ and $\overline{u'} = 0$, it follows that

$$\begin{aligned} \overline{\Delta M_x} &= \Delta A \rho (\overline{\overline{uu}} + \overline{u'u'}) \\ \overline{\Delta M_y} &= \Delta A \rho (\overline{\overline{uv}} + \overline{u'v'}) \\ \overline{\Delta M_z} &= \Delta A \rho (\overline{\overline{uw}} + \overline{u'w'}) \end{aligned} \tag{4.2}$$

However, the rate of change of momentum ($\overline{\Delta M_x}$) is equivalent to a force. Therefore dividing by ΔA gives the stress on the area. Hence the stress on the fluid is:

$$\begin{aligned} \sigma_{xx} &= -\rho(\overline{\overline{u}\overline{u}} + \overline{u'u'}) \\ \tau_{xy} &= -\rho(\overline{\overline{u}\overline{v}} + \overline{u'v'}) \\ \tau_{xz} &= -\rho(\overline{\overline{u}\overline{w}} + \overline{u'w'}) \end{aligned} \tag{4.3}$$

These show that the fluctuations on the mean motion give rise to three additional stresses:

$$\begin{aligned} \sigma'_{xx} &= -\rho\overline{u'u'} \\ \tau'_{xy} &= -\rho\overline{u'v'} \\ \tau'_{xz} &= -\rho\overline{u'w'} \end{aligned} \tag{4.4}$$

which are the Reynolds stresses. The instantaneous fluctuations u' and v' are thus correlated at a point to give an instantaneous value of shear stress. When averaged over a period of time, such values give rise to the mean shear stress τ'_{xy}.

4.2.3 Momentum and Continuity

The equation (3.56) for incompressible flow is first multiplied by u and then added to the general momentum equation (3.62) for the x-direction to give:

$$\rho\left(\frac{\partial u}{\partial t} + \frac{\partial uu}{\partial x} + \frac{\partial uv}{\partial y} + \frac{\partial uw}{\partial z}\right) = \rho\mathrm{X} - \frac{\partial \mathrm{p}}{\partial x} + \mu\left[\frac{\partial^2 u}{\partial x^2} + \frac{\partial^2 u}{\partial y^2} + \frac{\partial^2 u}{\partial z^2}\right] \tag{4.5}$$

Turbulence implies that fluctuations are imposed on the flow (Figure 4.3).

$$\overline{u} = \frac{1}{\Delta t}\int_t^{t+\Delta t} u\,\mathrm{d}t$$

u' is the fluctuating velocity component where $\overline{u'} = 0$

i.e.

$$\frac{1}{\Delta t}\int_t^{t+\Delta t} u'\,\mathrm{d}t = 0$$

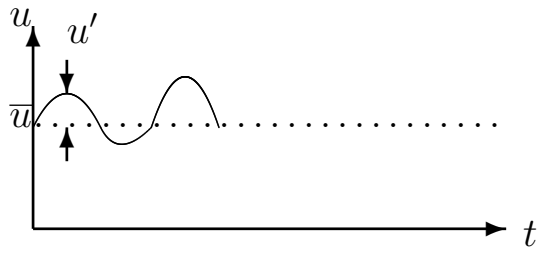

Figure 4.3: Mean and fluctuating components of velocity, u

Substituting for the time average and fluctuating components in Equation (4.5) gives:

$$\rho\left(\frac{\partial(\overline{u}+u')}{\partial t}+\frac{\partial(\overline{u}+u')^2}{\partial x}+\frac{\partial(\overline{u}+u')(\overline{v}+v')}{\partial y}+\frac{\partial(\overline{u}+u')(\overline{w}+w')}{\partial z}\right)$$
$$=(\rho+\rho')\left(\bar{\mathrm{X}}+\mathrm{X}'\right)-\frac{\partial(\overline{\mathrm{p}}+p')}{\partial x}+\mu\left[\frac{\partial^2(\overline{u}+u')}{\partial x^2}+\frac{\partial^2(\overline{u}+u')}{\partial y^2}+\frac{\partial^2(\overline{u}+u')}{\partial z^2}\right] \quad (4.6)$$

Expanding and time averaging the whole equation gives:

$$\rho\left(\frac{\partial\overline{(\overline{u}+u')}}{\partial t}+\frac{\partial\overline{(\overline{u}^2+2\overline{u}u'+u'^2)}}{\partial x}+\frac{\partial\overline{(\overline{uv}+u'\overline{v}+\overline{u}v'+u'v')}}{\partial y}+\frac{\partial\overline{(\overline{uw}+u'\overline{w}+\overline{u}w'+u'w')}}{\partial z}\right)$$
$$=\overline{\rho\left(\bar{\mathrm{X}}+\mathrm{X}'\right)}-\frac{\partial\overline{(\overline{\mathrm{p}}+p')}}{\partial x}+\mu\left[\frac{\partial^2\overline{(\overline{u}+u')}}{\partial x^2}+\frac{\partial^2\overline{(\overline{u}+u')}}{\partial y^2}+\frac{\partial^2\overline{(\overline{u}+u')}}{\partial z^2}\right] \quad (4.7)$$

Now:

$$\overline{\overline{u}+u'}=\frac{1}{\Delta t}\int_t^{t+\Delta t}\overline{u}+u'\,\mathrm{d}t$$

But $\overline{u}=$ constant i.e. $\neq f(t)$

$$\frac{1}{\Delta t}\int_t^{t+\Delta t}u'\,\mathrm{d}t=0$$

$$\therefore\ \overline{\overline{u}+u'}=\overline{u} \quad (4.8)$$

and similarly for the other terms of this form.

Likewise:

$$\overline{(\overline{u}^2 + 2\overline{u}u' + u'^2)} = \frac{1}{\Delta t}\int_t^{t+\Delta t} (\overline{u}^2 + 2\overline{u}u' + u'^2)\,\mathrm{d}t$$

but $\overline{u}^2 =$ constant and:

$$\frac{1}{\Delta t}\int_t^{t+\Delta t} 2\overline{u}u'\,\mathrm{d}t = \frac{2\overline{u}}{\Delta t}\int_t^{t+\Delta t} u'\,\mathrm{d}t = 0 \tag{4.9}$$

and similarly for the other terms of this form.

Substituting Equations (4.8) and (4.9) in (4.7) gives:

$$\rho\left(\frac{\partial\overline{u}}{\partial t} + \frac{\partial(\overline{\overline{u}^2 + u'^2})}{\partial x} + \frac{\partial(\overline{\overline{u}\overline{v} + u'v'})}{\partial y} + \frac{\partial(\overline{\overline{u}\overline{w} + u'w'})}{\partial z}\right) = \rho\bar{\mathrm{X}} + \rho'\mathrm{X}' - \frac{\partial\overline{\mathrm{p}}}{\partial x} + \mu\left[\frac{\partial^2\overline{u}}{\partial x^2} + \frac{\partial^2\overline{u}}{\partial y^2} + \frac{\partial^2\overline{u}}{\partial z^2}\right] \tag{4.10}$$

$$\rho\left(\frac{\partial\overline{u}}{\partial t} + \frac{\partial\overline{u}\overline{u}}{\partial x} + \frac{\partial\overline{u}\overline{v}}{\partial y} + \frac{\partial\overline{u}\overline{w}}{\partial z}\right) = \rho\bar{\mathrm{X}} - \frac{\partial\overline{\mathrm{p}}}{\partial x} + \mu\left[\frac{\partial^2\overline{u}}{\partial x^2} + \frac{\partial^2\overline{u}}{\partial y^2} + \frac{\partial^2\overline{u}}{\partial z^2}\right] - \rho\left[\frac{\partial\overline{u'u'}}{\partial x} + \frac{\partial\overline{u'v'}}{\partial y} + \frac{\partial\overline{u'w'}}{\partial z}\right] \tag{4.11}$$

Applying the same procedure to the continuity equation (3.56) for incompressible flow gives:

$$\frac{\partial\overline{u}}{\partial x} + \frac{\partial\overline{v}}{\partial y} + \frac{\partial\overline{w}}{\partial z} = 0 \tag{4.12}$$

Multiplying Equation (4.12) by $\overline{u}$ and subtracting from Equation (4.11) gives the

Navier-Stokes equation for incompressible turbulent flow in the x-direction:

$$\rho\left(\frac{\partial\overline{u}}{\partial t}+\overline{u}\frac{\partial\overline{u}}{\partial x}+\overline{v}\frac{\partial\overline{u}}{\partial y}+\overline{w}\frac{\partial\overline{u}}{\partial z}\right)=\rho\bar{\mathrm{X}}-\frac{\partial\overline{\mathrm{p}}}{\partial x}+\mu\left[\frac{\partial^2\overline{u}}{\partial x^2}+\frac{\partial^2\overline{u}}{\partial y^2}+\frac{\partial^2\overline{u}}{\partial z^2}\right]-\rho\left[\frac{\partial\overline{u'u'}}{\partial x}+\frac{\partial\overline{u'v'}}{\partial y}+\frac{\partial\overline{u'w'}}{\partial z}\right] \quad (4.13)$$

$$\rho\left(\frac{\partial\overline{u}}{\partial t}+\overline{u}\frac{\partial\overline{u}}{\partial x}+\overline{v}\frac{\partial\overline{u}}{\partial y}+\overline{w}\frac{\partial\overline{u}}{\partial z}\right)=\rho\bar{\mathrm{X}}-\frac{\partial\overline{\mathrm{p}}}{\partial x}+\frac{\partial}{\partial x}\left(\mu\frac{\partial\overline{u}}{\partial x}-\rho\overline{u'u'}\right)+\frac{\partial}{\partial y}\left(\mu\frac{\partial\overline{u}}{\partial y}-\rho\overline{u'v'}\right)+\frac{\partial}{\partial z}\left(\mu\frac{\partial\overline{u}}{\partial z}-\rho\overline{u'w'}\right) \quad (4.14)$$

Similarly for the y-direction:

$$\rho\left(\frac{\partial\overline{v}}{\partial t}+\overline{u}\frac{\partial\overline{v}}{\partial x}+\overline{v}\frac{\partial\overline{v}}{\partial y}+\overline{w}\frac{\partial\overline{v}}{\partial z}\right)=\rho\bar{\mathrm{Y}}-\frac{\partial\overline{\mathrm{p}}}{\partial y}+\frac{\partial}{\partial x}\left(\mu\frac{\partial\overline{v}}{\partial x}-\rho\overline{v'u'}\right)+\frac{\partial}{\partial y}\left(\mu\frac{\partial\overline{v}}{\partial y}-\rho\overline{v'v'}\right)+\frac{\partial}{\partial z}\left(\mu\frac{\partial\overline{v}}{\partial z}-\rho\overline{v'w'}\right) \quad (4.15)$$

Similarly for the z-direction:

$$\rho\left(\frac{\partial\overline{w}}{\partial t}+\overline{u}\frac{\partial\overline{w}}{\partial x}+\overline{v}\frac{\partial\overline{w}}{\partial y}+\overline{w}\frac{\partial\overline{w}}{\partial z}\right)=\rho\bar{\mathrm{Z}}-\frac{\partial\overline{\mathrm{p}}}{\partial z}+\frac{\partial}{\partial x}\left(\mu\frac{\partial\overline{w}}{\partial x}-\rho\overline{w'u'}\right)+\frac{\partial}{\partial y}\left(\mu\frac{\partial\overline{w}}{\partial y}-\rho\overline{w'v'}\right)+\frac{\partial}{\partial z}\left(\mu\frac{\partial\overline{w}}{\partial z}-\rho\overline{w'w'}\right) \quad (4.16)$$

Rewriting Equations (4.14) to (4.16) in the form of the general stress equation for a deformable body gives:

$$\begin{aligned}\rho\left(\frac{\partial\overline{u}}{\partial t}+\overline{u}\frac{\partial\overline{u}}{\partial x}+\overline{v}\frac{\partial\overline{u}}{\partial y}+\overline{w}\frac{\partial\overline{u}}{\partial z}\right)&=\rho\bar{\mathrm{X}}+\frac{\partial\sigma_{xx}}{\partial x}+\frac{\partial\tau_{yx}}{\partial y}+\frac{\partial\tau_{zx}}{\partial z}\\ \rho\left(\frac{\partial\overline{v}}{\partial t}+\overline{u}\frac{\partial\overline{v}}{\partial x}+\overline{v}\frac{\partial\overline{v}}{\partial y}+\overline{w}\frac{\partial\overline{v}}{\partial z}\right)&=\rho\bar{\mathrm{Y}}+\frac{\partial\tau_{xy}}{\partial x}+\frac{\partial\sigma_{yy}}{\partial y}+\frac{\partial\tau_{zy}}{\partial z}\\ \rho\left(\frac{\partial\overline{w}}{\partial t}+\overline{u}\frac{\partial\overline{w}}{\partial x}+\overline{v}\frac{\partial\overline{w}}{\partial y}+\overline{w}\frac{\partial\overline{w}}{\partial z}\right)&=\rho\bar{\mathrm{Z}}+\frac{\partial\tau_{xz}}{\partial x}+\frac{\partial\tau_{yz}}{\partial y}+\frac{\partial\sigma_{zz}}{\partial z}\end{aligned} \quad (4.17)$$

where:

$$\begin{aligned}
\sigma_{xx} &= -\overline{\mathrm{p}} + \mu\frac{\partial\overline{u}}{\partial x} - \rho\overline{u'u'} \\
\sigma_{yy} &= -\overline{\mathrm{p}} + \mu\frac{\partial\overline{v}}{\partial y} - \rho\overline{v'v'} \\
\sigma_{zz} &= -\overline{\mathrm{p}} + \mu\frac{\partial\overline{w}}{\partial z} - \rho\overline{w'w'} \\
\tau_{xy} &= \mu\frac{\partial\overline{u}}{\partial y} - \rho\overline{u'v'} \\
\tau_{yx} &= \mu\frac{\partial\overline{v}}{\partial x} - \rho\overline{u'v'} \\
\tau_{xz} &= \mu\frac{\partial\overline{u}}{\partial z} - \rho\overline{u'w'} \\
\tau_{zx} &= \mu\frac{\partial\overline{w}}{\partial x} - \rho\overline{u'w'} \\
\tau_{yz} &= \mu\frac{\partial\overline{v}}{\partial z} - \rho\overline{v'w'} \\
\tau_{zy} &= \mu\frac{\partial\overline{w}}{\partial y} - \rho\overline{v'w'}
\end{aligned} \tag{4.18}$$

Comparing Equation (4.14) with the corresponding Navier-Stokes equations (3.62) shows that the instantaneous values of velocity and pressure have been replaced by mean velocity and that three additional terms appear on the right hand side of the equation, including: $\frac{\partial\rho\overline{u'u'}}{\partial x}$, $\frac{\partial\rho\overline{u'v'}}{\partial y}$ and $\frac{\partial\rho\overline{u'w'}}{\partial z}$

The expressions $\rho\overline{u'u'}$, $\rho\overline{u'v'}$ and $\rho\overline{u'w'}$ are known as the Reynolds (or apparent) stresses with their form being similar to the viscous shear stresses. They arise solely from the presence of turbulence and for laminar flow are zero.

The complete turbulent stress tensor is: $\begin{bmatrix} \sigma'_{xx} & \tau'_{xy} & \tau'_{xz} \\ \tau'_{yx} & \sigma'_{yy} & \tau'_{yz} \\ \tau'_{zx} & \tau'_{zy} & \sigma'_{zz} \end{bmatrix} = -\begin{bmatrix} \rho\overline{u'u'} & \rho\overline{u'v'} & \rho\overline{u'w'} \\ \rho\overline{u'v'} & \rho\overline{v'v'} & \rho\overline{v'w'} \\ \rho\overline{u'w'} & \rho\overline{v'w'} & \rho\overline{w'w'} \end{bmatrix}$

For practical applications, water generally has a high Reynolds Number and the laminar viscosity term is generally negligible. For these cases, the inertia forces are large compared to the viscous forces. According to Schlichting (1979), the influence of viscosity is concentrated in a thin boundary layer near the bed.

The Navier-Stokes Equations for incompressible flow can therefore be written

without the viscous terms as:

$$\begin{aligned}
\rho\left(\frac{\partial\overline{u}}{\partial t}+\overline{u}\frac{\partial\overline{u}}{\partial x}+\overline{v}\frac{\partial\overline{u}}{\partial y}+\overline{w}\frac{\partial\overline{u}}{\partial z}\right) &= \rho\bar{\mathrm{X}}-\frac{\partial\overline{\mathrm{p}}}{\partial x}+\frac{\partial\sigma'_{xx}}{\partial x}+\frac{\partial\tau'_{yx}}{\partial y}+\frac{\partial\tau'_{zx}}{\partial z}\\
\rho\left(\frac{\partial\overline{v}}{\partial t}+\overline{u}\frac{\partial\overline{v}}{\partial x}+\overline{v}\frac{\partial\overline{v}}{\partial y}+\overline{w}\frac{\partial\overline{v}}{\partial z}\right) &= \rho\bar{\mathrm{Y}}-\frac{\partial\overline{\mathrm{p}}}{\partial y}+\frac{\partial\tau'_{xy}}{\partial x}+\frac{\partial\sigma'_{yy}}{\partial y}+\frac{\partial\tau'_{zy}}{\partial z}\\
\rho\left(\frac{\partial\overline{w}}{\partial t}+\overline{u}\frac{\partial\overline{w}}{\partial x}+\overline{v}\frac{\partial\overline{w}}{\partial y}+\overline{w}\frac{\partial\overline{w}}{\partial z}\right) &= \rho\bar{\mathrm{Z}}-\frac{\partial\overline{\mathrm{p}}}{\partial z}+\frac{\partial\tau'_{xz}}{\partial x}+\frac{\partial\tau'_{yz}}{\partial y}+\frac{\partial\sigma'_{zz}}{\partial z}
\end{aligned} \tag{4.19}$$

4.2.4 Solute Conservation (Advective-Diffusion)

For turbulent flow, instantaneous velocities and concentrations are replaced with the time average and fluctuating components, i.e.: $u=\overline{u}+u'$ and $s=\overline{s}+s'$. Substituting the instantaneous velocities and concentrations in Equation (3.76) and averaging each term with respect to time gives:

$$\frac{\partial\overline{(\overline{s}+s')}}{\partial t}+\frac{\partial\overline{(\overline{s}+s')(\overline{u}+u')}}{\partial x}+\frac{\partial\overline{(\overline{s}+s')(\overline{v}+v')}}{\partial y}+\frac{\partial\overline{(\overline{s}+s')(\overline{w}+w')}}{\partial z}=0 \tag{4.20}$$

Substituting Equation (4.8) and (4.9) and similarly for other terms of this form to give:

$$\frac{\partial\overline{s}}{\partial t}+\frac{\partial\overline{s}\overline{u}}{\partial x}+\frac{\partial\overline{s}\overline{v}}{\partial y}+\frac{\partial\overline{s}\overline{w}}{\partial z}+\frac{\partial\overline{s'u'}}{\partial x}+\frac{\partial\overline{s'v'}}{\partial y}+\frac{\partial\overline{s'w'}}{\partial z}=0 \tag{4.21}$$

Multiplying the continuity equation (4.12) for turbulent flow by $\overline{s}$ and subtracting from the left hand side of the equation gives:

$$\frac{\partial\overline{s}}{\partial t}+\overline{u}\frac{\partial\overline{s}}{\partial x}+\overline{v}\frac{\partial\overline{s}}{\partial y}+\overline{w}\frac{\partial\overline{s}}{\partial z}+\frac{\partial\overline{c'u'}}{\partial x}+\frac{\partial\overline{c'v'}}{\partial y}+\frac{\partial\overline{c'w'}}{\partial z}=0 \tag{4.22}$$

Terms such as $\overline{s'u'}$ represent the mass flux of concentrate in the x-direction due to turbulent fluctuations. By analogy with Fick's law of diffusion it is assumed that the mass flux is proportional to the mean concentration gradient and that the flux is

in direction of decreasing gradient. i.e.:

$$\begin{aligned} \overline{c'u'} &= -D_{tx}\frac{\partial \overline{s}}{\partial x} \\ \overline{c'v'} &= -D_{ty}\frac{\partial \overline{s}}{\partial y} \\ \overline{c'w'} &= -D_{tz}\frac{\partial \overline{s}}{\partial z} \end{aligned} \tag{4.23}$$

Substitution of Equation (4.23) in Equation (4.22) gives:

$$\frac{\partial \overline{s}}{\partial t} + \overline{u}\frac{\partial \overline{s}}{\partial x} + \overline{v}\frac{\partial \overline{s}}{\partial y} + \overline{w}\frac{\partial \overline{s}}{\partial z} = D_{tx}\frac{\partial^2 \overline{s}}{\partial x^2} + D_{ty}\frac{\partial^2 \overline{s}}{\partial y^2} + D_{tz}\frac{\partial^2 \overline{s}}{\partial z^2} \tag{4.24}$$

Adding back into the continuity equation multiplied by $\overline{s}$ to the left hand side gives:

$$\frac{\partial \overline{s}}{\partial t} + \frac{\partial \overline{us}}{\partial x} + \frac{\partial \overline{vs}}{\partial y} + \frac{\partial \overline{ws}}{\partial z} = D_{tx}\frac{\partial^2 \overline{s}}{\partial x^2} + D_{ty}\frac{\partial^2 \overline{s}}{\partial y^2} + D_{tz}\frac{\partial^2 \overline{s}}{\partial z^2} \tag{4.25}$$

D_{tx}, D_{ty} and D_{tz} are termed turbulent diffusion coefficients and are not necessarily the same in the three co-ordinate directions.

4.3 Turbulence Model

4.3.1 Overview

The presence of turbulence means that fluctuating components of velocity and concentration exist. Turbulent mixing motion is responsible not only for an exchange of momentum but it also enhances the transfer of heat and mass in fields of flow associated with non-uniform distributions of temperature or concentration (Schlichting, 1979). The methods for the calculation of turbulent flow, temperature and concentration fields are based on empirical hypotheses which endeavour to establish a relationship between the Reynolds stresses produced by the mixing motion and the mean values of the velocity components.

Boussinesq (1877) worked on establishing a relationship between the Reynolds stresses and the mean velocity components. By analogy with the coefficient of viscosity in Stokes's law for laminar flow, Boussinesq (1877) proposed an eddy viscosity (mixing) coefficient in the form:

$$\tau_{zx} = -\rho\overline{u'v'} = \rho\epsilon_t \frac{\partial \overline{u}}{\partial z} \tag{4.26}$$

where ϵ_t = eddy viscosity. The eddy viscosity is not a fluid property but a flow property depending on the local structure of the turbulence or the mean velocity. It is typically several orders of magnitude larger than the molecular viscosity. There are several ways of determining the eddy viscosity. These include the depth-averaged parabolic model, modified mixing length model and the depth-averaged linear $k - \varepsilon$ turbulence models (Wu, 2008). For this research, the parabolic eddy viscosity model was used.

4.3.2 Parabolic Eddy Viscosity Model

Prandtl (1926) proposed a distribution law for the eddy viscosity based on a mixing length hypothesis (4.27). He assumed that in shear layers the fluid was continuously being exchanged by virtue of the fluctuations of velocity normal to the mean direction of flow. The distance over which these exchanges took place is called the mixing length (ℓ_m). Therefore:

$$\tau_{zx} = -\rho\overline{u'v'} = \rho\ell_m^2 \frac{\partial u}{\partial z}\left|\frac{\partial u}{\partial z}\right| \tag{4.27}$$

Prandtl (1926) proposed that the shear stress in the fluid is constant and the mixing length varies linearly with distance from the boundary. For many realistic flows, this is modified by assuming that:

i) the shear stress in the fluid varies linearly with depth

$$\tau = \tau_o\left(1 - \frac{z}{H}\right) \tag{4.28}$$

ii) the size of the turbulent eddy varies parabolically with the distance from the boundary,

$$\ell_m = \kappa z \left(1 - \frac{z}{H}\right)^{\frac{1}{2}} \tag{4.29}$$

where κ is Von Karman's constant and H is the depth of flow

Substituting (4.28) and (4.29) into (4.27) gives:

$$\tau_{zx} = \rho \ell_m^2 \left(\frac{\partial u}{\partial z}\right)^2 \tag{4.30}$$

$$\tau_o \left(1 - \frac{z}{H}\right) = \rho \kappa^2 z^2 \left(1 - \frac{z}{H}\right) \left(\frac{\partial u}{\partial z}\right)^2 \tag{4.31}$$

$$\therefore \frac{\mathrm{d}u}{\mathrm{d}z} = \frac{1}{\kappa z}\sqrt{\frac{\tau_o}{\rho}} = \frac{U^*}{\kappa z} \tag{4.32}$$

Integrating Eq. (4.32), gives a logarithmic velocity distribution of form.

$$\frac{u}{U^*} = \frac{1}{\kappa} \ln\left(\frac{z}{z_o}\right) \tag{4.33}$$

when $z = z_o$ then $vx = 0$.

Combining Boussinesq's eddy viscosity (4.26) with Prandtl's mixing length equation (4.27) gives:

$$\epsilon_t = \ell_m^2 \frac{\partial u}{\partial z} \tag{4.34}$$

Substituting Eqs. (4.29) and (4.32) into Eq. (4.34) gives the parabolic eddy viscosity model:

$$\epsilon_t = \kappa z U^* \left(1 - \frac{z}{H}\right) \tag{4.35}$$

Integrating the parabolic eddy viscosity model (4.35) over the flow depth gives:

$$\bar{\epsilon_t} = \frac{1}{H}\int_0^H U^* \kappa z \left(1 - \frac{z}{H}\right) \mathrm{d}z = \frac{U^* \kappa}{H}\left[\frac{z^2}{2} - \frac{z^3}{3H}\right]_0^H = \frac{1}{6}\kappa U^* H \tag{4.36}$$

$$\bar{\epsilon_t} = \alpha_1 U^* H \tag{4.37}$$

Theoretically $\alpha_1 = \frac{\kappa}{6}$, however, based on field data for real rivers and estuaries it has been shown that a range of values are applicable for this coefficient, due to the anisotropic structure of the turbulence in the horizontal and vertical directions and the effects of dispersion (Wu, 2008). According to experiments by Elder 1959, α_1 is typically 0.23 for the longitudinal turbulent diffusion in laboratory channels. For transverse turbulent diffusion, Fischer *et al.* (1979) proposed that α_1 is about 0.15 in laboratory channels and 0.6 (0.3-1.0) in irregular waterways with weak meanders. For actual tidal flows in estuaries and coastal areas, the value of α_1 is frequently much larger than that determined in the laboratory. A value of $\alpha_1 \approx 1.0$ is used in this research study. This value had been used in similar estuaries by Falconer (1993); Kashefipour (2002) and shown to give satisfactory flow predictions.

The turbulence model used in this work gives an indication of the impact of the bed generated turbulent momentum exchange on the overall time-averaged flow profile. This approach assumes that the turbulent shear stress is dominated by turbulence near the bottom. It does not describe the turbulent fluctuation of the velocity or specific coherent structures, such as turbulent wakes behind objects. The turbulence smooths the velocity gradients and aids the stability of the numerical solution while contributing to the generation of vorticity. Other available turbulence models include the $k - \varepsilon$ turbulence model and the Reynolds stress model. Each turbulence model has its limitations and may be more suited to certain types of flows than others.

4.4 Bed Friction

4.4.1 Flow Resistance

At the boundary of a natural channel with the bed there is a shear stress (τ_0) which resists the flow. This shear stress can be related to the total energy line ("energy

slope" or "friction slope") by the equilibrium equation (Henderson, 1966):

$$\rho g A \Delta x S_f = \tau_0 P \Delta x \tag{4.38}$$

solving for the bed shear stress τ_0 gives:

$$\tau_0 = \rho g R S_f \tag{4.39}$$

4.4.2 The Chezy Equation

The bed shear stress can be related to the square of the mean velocity (Henderson, 1966) with the equation:

$$\tau_0 = a \rho U^2 \tag{4.40}$$

Combining equations (4.40) and (4.39) gives:

$$U = \sqrt{\frac{g}{a} R S_f} \tag{4.41}$$

writing $\sqrt{\frac{g}{a}}$ as one constant C gives the Chezy equation:

$$U = C \sqrt{R S_f} \tag{4.42}$$

The Chezy equation was introduced by a French engineer in 1768. This equation (4.42) describes the mean flow velocity of steady, turbulent open channel flow.

4.4.3 Colebrook-White Equations

The value of the Chezy coefficient, as used in this research study, may be obtained from the well-known Moody diagram which is based on the work of Nikuradse, Colebrook and White (Henderson, 1966). There are three possible types of turbulent flow: smooth, transition and fully rough turbulent flow. These types of flow are

distinguished from each other by the size of the dimensionless number $\rho k_s U^*/\mu$, which is recognizable as a form of Reynolds number.

According to Henderson (1966), the quantity U^*, known as the shear velocity is defined as:

$$U^* = \sqrt{\frac{\tau_0}{\rho}} = \sqrt{gRS_f} \tag{4.43}$$

Equation (4.43) can be related to the mean flow by combining with equation (4.42) to give:

$$U^* = \frac{U\sqrt{g}}{C} \tag{4.44}$$

The transition region of the flow is defined approximately by the limits:

$$4 < \frac{\rho k_s U^*}{\mu} < 100 \tag{4.45}$$

the lower limit defining the end of the smooth region and the upper limit the beginning of the fully rough region.

For smooth turbulent flow, where Re $< 10^5$ the chezy coefficient is given as:

$$C = 28.6\mathrm{Re}^{\frac{1}{8}} \tag{4.46}$$

and when Re $>= 10^5$

$$C = 4\sqrt{2g}\log_{10}\left(\frac{\mathrm{Re}\sqrt{8g}}{2.51C}\right) \tag{4.47}$$

The flow conditions may be hydraulically smooth, even when the surface is rough, provided that the roughness projections are small enough to be buried within the laminar sublayer.

For fully rough flow, the Chezy coefficient is given as:

$$C = -2\sqrt{8g}\log_{10}\left(\frac{k_s}{12R}\right) \tag{4.48}$$

For transistion flow, the Chezy coefficient is given as:

$$C = -2\sqrt{8g}\log_{10}\left(\frac{k_s}{12R} + \frac{2.5C}{\mathrm{Re}\sqrt{8g}}\right) \tag{4.49}$$

4.4.4 The Manning Equation

In 1869 Ganguillet and Kutter published a complex formula for C, however Gauckler in 1868 and Hagen in 1881 arrived independently at the conclusion that the data used by Ganguillet and Kutter were fitted just as well by a simpler formulas stating that C varies as the sixth root of R. In 1891 the Frechman Flamant wrongly attributed this conclusion to the Irishman R. Manning and expressed it in the form:

$$C = \frac{R^{\frac{1}{6}}}{n} \tag{4.50}$$

or

$$U = \frac{1}{n}R^{\frac{2}{3}}S_f^{\frac{1}{2}} \tag{4.51}$$

where n is characteristic of the surface roughness alone. The Manning equation is only applicable for fully rough turbulent flow. However it is popular amongst end-users in industry and government agencies etc.

4.5 Body Forces: Coriolis Forces

The Coriolis effect is the deflection of the flow when viewed in a rotating reference frame, such as the earth. The Coriolis force is named after a French mathematician Gaspard Gustave de Coriolis (1792-1843), who published a mathematical expression for the Coriolis force in 1835. If only gravitational forces act on the body of fluid then the body forces are given as, X = 0, Y = 0, Z = $-g$. The Coriolis effect is caused by the rotation of the Earth and the inertia of the mass experiencing the effect. The Coriolis force is proportional to the rotation rate of the earth. For gravitational and

Coriolis forces, the body forces are given as $\mathrm{X} = 2\omega v \sin\phi$, $\mathrm{Y} = -2\omega u \sin\phi$, $\mathrm{Z} = -g$, where

$$\begin{aligned} \omega &= \text{angular frequency of the earth} = \text{one revolution per day} \\ &= \frac{2\pi}{24 \times 60 \times 60s} = 7.272 \times 10^{-5}\text{rad/s} \end{aligned} \tag{4.52}$$

and ϕ = latitude. The earth completes only one rotation per day, therefore the Coriolis force is quite small. Its effects generally become noticeable only for motions occurring over large distances and long periods of time, such as large-scale movement of water in the ocean.

4.6 Area Averaged Equations (1-D)

4.6.1 Description

For many hydraulic problems, the vertical and lateral velocity components, v and w are small in comparison with the stream wise velocity component, u, e.g. river flows, and the Navier-Stokes equations can be integrated to give the 1-D or Area averaged Saint-Venant equations.

4.6.2 Continuity Equation

The Area integration of the time averaged continuity equation (4.12) over the cross-sectional area, A gives:

$$\int_0^A \left(\frac{\partial \overline{u}}{\partial x} + \frac{\partial \overline{v}}{\partial y} + \frac{\partial \overline{w}}{\partial z} \right) \mathrm{d}A = 0 \tag{4.53}$$

$\Delta A = \Delta y \Delta z$ therefore:

$$\int_0^A \frac{\partial \overline{u}}{\partial x}\,\mathrm{d}A + \int_{-h}^{\eta}\int_0^B \frac{\partial \overline{v}}{\partial y}\,\mathrm{d}y\mathrm{d}z + \int_0^B\int_{-h}^{\eta} \frac{\partial \overline{w}}{\partial z}\,\mathrm{d}z\mathrm{d}y = 0 \tag{4.54}$$

where B is the width of the channel.

$$\int_0^A \frac{\partial \overline{u}}{\partial x}\,\mathrm{d}A + \int_{-h}^{\eta} \overline{v}|_0^B \mathrm{d}z + \int_0^B \overline{w}|_{-h}^{\eta} \mathrm{d}y = 0 \tag{4.55}$$

Using Leibnitz Rule gives:

$$\frac{\partial}{\partial x}\int_0^A \overline{u}\mathrm{d}A - \overline{u}_A \frac{\partial A}{\partial x}\bigg|_A + (\overline{v}_B - \overline{v}_0)(\eta + h) + B(\overline{w}_\eta - \overline{w}_{-h}) = 0 \tag{4.56}$$

The net horizontal velocity at the boundary is assumed to be zero (with boundaries not moving horizontally relative to each other) $(\overline{v}_B - \overline{v}_0) = 0$, therefore:

$$\frac{\partial}{\partial x}\int_0^A \overline{u}\mathrm{d}A - \overline{u}_A \frac{\partial A}{\partial x}\bigg|_A + B(\overline{w}_\eta - \overline{w}_{-h}) = 0 \tag{4.57}$$

At the surface, the kinematic free surface condition gives:

$$\overline{w}_\eta = \frac{\mathrm{d}\eta}{\mathrm{d}t} = \left[\frac{\partial \eta}{\partial t} + \frac{\partial \eta}{\partial x}\frac{\partial x}{\partial t}\right]_\eta \tag{4.58}$$

$$\overline{w}_\eta = \left[\frac{\partial \eta}{\partial t} + \overline{u}\frac{\partial \eta}{\partial x}\right]_\eta \tag{4.59}$$

Similarly, at the bed:

$$\overline{w}_{-h} = \left[\frac{\partial(-h)}{\partial t} + \overline{u}\frac{\partial(-h)}{\partial x}\right]_{-h} \tag{4.60}$$

Therefore:

$$\overline{w}_\eta - \overline{w}_{-h} = \frac{\partial \eta}{\partial t} - \frac{\partial(-h)}{\partial t} + \overline{u}\left(\frac{\partial \eta}{\partial x} - \frac{\partial(-h)}{\partial x}\right) \tag{4.61}$$

$$B(\overline{w}_\eta - \overline{w}_{-h}) = \frac{\partial A}{\partial t} + \overline{u}\frac{\partial A}{\partial x} \tag{4.62}$$

Substituting Eq. (4.62) into Eq. (4.57) gives:

$$\begin{aligned} \frac{\partial}{\partial x}\int_0^A \overline{u}\mathrm{d}A - \overline{u}_A\frac{\partial A}{\partial x}\bigg|_A + \left[\frac{\partial A}{\partial t} + \overline{u}\frac{\partial A}{\partial x}\right]_A = 0 \\ \frac{\partial}{\partial x}\int_0^A \overline{u}\mathrm{d}A + \frac{\partial A}{\partial t} = 0 \end{aligned} \tag{4.63}$$

The continuity equation for 1D flow therefore becomes:

$$\frac{\partial A}{\partial t} + \frac{\partial Q}{\partial x} = 0 \tag{4.64}$$

where:

$$Q = \int_0^A \overline{u}\mathrm{d}A \tag{4.65}$$

4.6.3 Momentum Equation

The velocity components, v and w, are usually small in comparison with the horizontal components u. The vertical accelerations are also generally assumed to be negligible. Thus for $v = 0$, $w = 0$, $\tau_{xy} = 0$, $\tau_{zy} = 0$, $\tau_{xz} = 0$ and $\tau_{yz} = 0$. Eq. (4.19) becomes:

$$\begin{aligned} \rho\left(\frac{\partial \overline{u}}{\partial t} + \overline{u}\frac{\partial \overline{u}}{\partial x}\right) &= -\frac{\partial \overline{\mathrm{p}}}{\partial x} + \frac{\partial \sigma'_{xx}}{\partial x} + \frac{\partial \tau'_{yx}}{\partial y} + \frac{\partial \tau'_{zx}}{\partial z} \\ 0 &= -\rho f\overline{u} - \frac{\partial \overline{\mathrm{p}}}{\partial y} + \frac{\partial \sigma'_{yy}}{\partial y} \\ 0 &= \rho g + \frac{\partial \overline{\mathrm{p}}}{\partial z} \end{aligned} \tag{4.66}$$

Substituting for the pressure terms gives:

$$\begin{aligned} \rho\left(\frac{\partial \overline{u}}{\partial t} + \overline{u}\frac{\partial \overline{u}}{\partial x}\right) &= -\rho g\frac{\partial \eta}{\partial x} + \frac{\partial \sigma'_{xx}}{\partial x} + \frac{\partial \tau'_{yx}}{\partial y} + \frac{\partial \tau'_{zx}}{\partial z} \\ 0 &= -\rho f\overline{u} - \rho g\frac{\partial \eta}{\partial y} + \frac{\partial \sigma'_{yy}}{\partial y} \end{aligned} \tag{4.67}$$

Adding the one-dimensional time averaged continuity equation, multiplied by

u (in the x-direction) to the left hand side of Eq. (4.67) gives:

$$\rho\left(\frac{\partial\overline{u}}{\partial t}+\frac{\partial\overline{u}^2}{\partial x}+\overline{u}\frac{\partial\overline{v}}{\partial y}+\overline{u}\frac{\partial\overline{w}}{\partial z}\right)=-\rho g\frac{\partial\eta}{\partial x}+\frac{\partial\sigma'_{xx}}{\partial x}+\frac{\partial\tau'_{yx}}{\partial y}+\frac{\partial\tau'_{zx}}{\partial z} \tag{4.68}$$

Integrating over the cross-sectional area, using Leibnitz' rule, and applying the kinematic free surface condition gives:

$$\begin{aligned}\rho\left(\frac{\partial}{\partial t}\int_0^A\overline{u}\mathrm{d}A+\frac{\partial}{\partial x}\int_0^A\overline{u}^2\mathrm{d}A\right)=&-\rho gA\frac{\partial\eta}{\partial x}+\frac{\partial}{\partial x}\int_0^A\sigma'_{xx}\,\mathrm{d}A+\frac{\partial}{\partial y}\int_0^A\tau'_{yx}\,\mathrm{d}A\\&+\frac{\partial}{\partial z}\int_0^A\tau'_{zx}\,\mathrm{d}A-\left[\sigma'_{xx}\frac{\partial A}{\partial x}+\tau'_{yx}\frac{\partial A}{\partial y}+\tau'_{zx}\frac{\partial A}{\partial z}\right]_A\end{aligned} \tag{4.69}$$

which can be written as:

$$\begin{aligned}\rho\left(\frac{\partial}{\partial t}\int_0^A\overline{u}\mathrm{d}A+\frac{\partial}{\partial x}\int_0^A\overline{u}^2\mathrm{d}A\right)=&-\rho gA\frac{\partial\eta}{\partial x}+\frac{\partial}{\partial x}\int_0^A\sigma'_{xx}\,\mathrm{d}A+\frac{\partial}{\partial y}\int_0^A\tau'_{yx}\,\mathrm{d}A\\&+\frac{\partial}{\partial z}\int_0^A\tau'_{zx}\,\mathrm{d}A-\tau_bP\end{aligned} \tag{4.70}$$

where:

$$\tau_bP=\left[\sigma'_{xx}\frac{\partial A}{\partial x}+\tau'_{yx}\frac{\partial A}{\partial y}+\tau'_{zx}\frac{\partial A}{\partial z}\right]_A \tag{4.71}$$

and P is the wetted perimeter.

In most cases τ_{wind} is assumed to be zero and the turbulent Reynolds stresses are also assumed to be zero therefore:

$$\rho\left(\frac{\partial AU}{\partial t}+\underbrace{\beta_1\frac{\partial U^2A}{\partial x}}_{\text{advection}}\right)=-\underbrace{\rho gA\frac{\partial\eta}{\partial x}}_{\text{pressure}}-\underbrace{\tau_bP}_{\text{friction}} \tag{4.72}$$

where

$$U=\frac{1}{A}\int_0^A\overline{u}\mathrm{d}A \tag{4.73}$$

and

$$\beta_1 = \frac{1}{U^2 A} \int_0^A \overline{u}^2 \mathrm{d}A \tag{4.74}$$

The bed shear stress is given as:

$$\tau_b = \rho g R S_f \tag{4.75}$$

where :

$$S_f = \frac{Q|Q|}{C^2 A^2 R} \tag{4.76}$$

The momentum equation (4.72) can be written in terms of the flow Q, by substituting $U = \frac{Q}{A}$ and applying the quotient rule, giving:

$$\frac{\partial Q}{\partial t} + \underbrace{\beta_1 \frac{\partial \frac{Q^2}{A}}{\partial x}}_{\text{advection}} = \underbrace{-gA\frac{\partial \eta}{\partial x}}_{\text{pressure}} \underbrace{- g\frac{Q|Q|}{C^2 A R}}_{\text{friction}} \tag{4.77}$$

$$\underbrace{\frac{\partial Q}{\partial t} + \beta_1 \frac{2Q}{A}\frac{\partial Q}{\partial x} - \beta_1 \frac{Q^2}{A^2}\frac{\partial A}{\partial x}}_{\text{advection}} = \underbrace{-gA\frac{\partial \eta}{\partial x}}_{\text{pressure}} \underbrace{- g\frac{Q|Q|}{C^2 A R}}_{\text{friction}} \tag{4.78}$$

4.6.4 Solute Transport Equation

Equation (4.25) does not take into account the effects of longitudinal dispersion. This is the result of longitudinal spreading of pollutants due to mixing of adjacent layers moving with different velocities, i.e. due to fluid shear.

To account for the mixing of the time averaged velocity and concentration components, these terms can be further split into the area averaged velocity (u) or concentration (s) and the deviation of the velocity (u'') or concentration (s'') from the area averaged values.

Therefore, substituting $\overline{u} = (U + u'')$ and $\overline{s} = (S + s'')$ into Equation (4.25), where u and S are the area averaged velocity and concentration components respectively gives:

$$\frac{\partial(S+s'')}{\partial t}+\frac{\partial(U+u'')(S+s'')}{\partial x}+\frac{\partial(V+v'')(S+s'')}{\partial y}+\frac{\partial(W+w'')(S+s'')}{\partial z}= D_{tx}\frac{\partial^2(S+s'')}{\partial x^2}+D_{ty}\frac{\partial^2(S+s'')}{\partial y^2}+D_{tz}\frac{\partial^2(S+s'')}{\partial z^2} \quad (4.79)$$

$$\begin{aligned}\overline{\overline{s''u''}} &= -D_{Lx}\frac{\partial\overline{s}}{\partial x}\\ \overline{\overline{s''v''}} &= -D_{Ly}\frac{\partial\overline{s}}{\partial y}\\ \overline{\overline{s''w''}} &= -D_{Lz}\frac{\partial\overline{s}}{\partial z}\end{aligned} \quad (4.80)$$

Hence, after integrating over the cross-section area, for uni-directional flow the advective-diffusion equation becomes:

$$\frac{\partial AS}{\partial t}+\frac{\partial AUS}{\partial x}=\frac{\partial}{\partial x}\left[A(D_{tx}+D_{Lx})\frac{\partial S}{\partial x}\right] \quad (4.81)$$

4.7 Depth Averaged Equations (2-D)

4.7.1 Description

For many hydraulics flow problems the vertical velocity component, w is small in comparison to the horizontal velocity components u and v. The continuity equation and Navier-Stokes equations can be integrated over the depth and solved numerically to give the depth averaged velocity (or flow) field. Such flow fields occur in wide estuaries, harbours, bays, etc. The following notation will be used in this research study:

where SWL = Still Water Level, h = depth of bed below the SWL and η is the level of the water surface above (positive) the SWL.

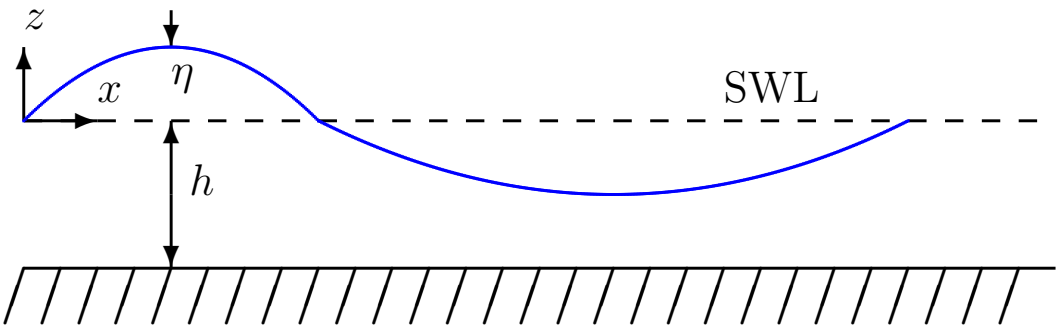

Figure 4.4: Notation describing water surface

4.7.2 Depth Averaged Continuity Equation

The depth integration of the time averaged continuity equation (4.12) gives:

$$\int_{-h}^{\eta} \left(\frac{\partial \overline{u}}{\partial x} + \frac{\partial \overline{v}}{\partial y} + \frac{\partial \overline{w}}{\partial z} \right) \mathrm{d}z = 0 \tag{4.82}$$

$$\int_{-h}^{\eta} \left(\frac{\partial \overline{u}}{\partial x} + \frac{\partial \overline{v}}{\partial y} \right) \mathrm{d}z + \overline{w}_{\eta} - \overline{w}_{-h} = 0 \tag{4.83}$$

Using Leibnitz Rule:

$$\int_{a}^{b} \frac{\partial f(x,y)\mathrm{d}x}{\partial y} = \frac{\partial}{\partial y} \int_{a}^{b} f(x,y)\mathrm{d}x - f(b,y)\frac{\partial b}{\partial y} + f(a,y)\frac{\partial A}{\partial y}$$

gives:

$$\frac{\partial}{\partial x} \int_{-h}^{\eta} \overline{u}\mathrm{d}z - \overline{u}_{\eta}\frac{\partial \eta}{\partial x}\bigg|_{\eta} + \overline{u}_{-h}\frac{\partial(-h)}{\partial x}\bigg|_{-h} + \frac{\partial}{\partial x} \int_{-h}^{\eta} \overline{v}\mathrm{d}z - \overline{v}_{\eta}\frac{\partial \eta}{\partial y}\bigg|_{\eta} + \overline{v}_{-h}\frac{\partial(-h)}{\partial y}\bigg|_{-h} + \overline{w}_{\eta} - \overline{w}_{-h} = 0 \tag{4.84}$$

At the surface, the kinematic free surface condition (namely a particle on the surface will remain on the surface) gives:

$$\overline{w}_{\eta} = \frac{\mathrm{d}\eta}{\mathrm{d}t} = \left[\frac{\partial \eta}{\partial t} + \frac{\partial \eta}{\partial x}\frac{\partial x}{\partial t} + \frac{\partial \eta}{\partial y}\frac{\partial y}{\partial t} \right]_{\eta} \tag{4.85}$$

$$\overline{w}_{\eta} = \left[\frac{\partial \eta}{\partial t} + \overline{u}\frac{\partial \eta}{\partial x} + \overline{v}\frac{\partial \eta}{\partial y}\right]_{\eta} \tag{4.86}$$

Similarly, at the bed, a particle on the bed will also remain there giving:

$$\overline{w}_{-h} = \frac{\mathrm{d}(-h)}{\mathrm{d}t} = \left[\frac{\partial(-h)}{\partial t} + \overline{u}\frac{\partial(-h)}{\partial x} + \overline{v}\frac{\partial(-h)}{\partial y}\right]_{-h} \tag{4.87}$$

Substituting Eqs. (4.86) and (4.87) in Eq. (4.84) gives:

$$\frac{\partial \eta}{\partial t} - \frac{\partial(-h)}{\partial t} + \frac{\partial}{\partial x}\int_{-h}^{\eta} \overline{u}\mathrm{d}z + \frac{\partial}{\partial x}\int_{-h}^{\eta} \overline{v}\mathrm{d}z = 0 \tag{4.88}$$

If it is assumed that the bed is stationary then $\left(\frac{\partial(-h)}{\partial t} = 0\right)$. Therefore the depth integrated form of the continuity equation can be written as:

$$\frac{\partial \eta}{\partial t} + \frac{\partial UH}{\partial x} + \frac{\partial VH}{\partial y} = 0 \tag{4.89}$$

where:

$$U = \frac{1}{H}\int_{-h}^{\eta} \overline{u}\,\mathrm{d}z \tag{4.90}$$

and

$$V = \frac{1}{H}\int_{-h}^{\eta} \overline{v}\,\mathrm{d}z \tag{4.91}$$

i.e. U, V = the depth averaged velocities in the x and y directions respectively, and H is the total depth = $h + \eta$

The depth averaged continuity equation (4.92) can also be written in terms of the depth integrated flows ($q_x = UH, q_y = VH$) to give:

$$\frac{\partial \eta}{\partial t} + \frac{\partial q_x}{\partial x} + \frac{\partial q_y}{\partial y} = 0 \tag{4.92}$$

4.7.3 Depth Averaged Momentum Equations

The vertical component of velocity, w, is usually small in comparison with the two horizontal components u and v. The vertical accelerations will also be assumed to be zero. Thus $w = 0$, $\tau'_{xz} = 0$, $\tau'_{yz} = 0$ and $\sigma'_{zz} = 0$ and equation (4.19) therefore becomes:

$$\begin{aligned}
\rho\left(\frac{\partial \overline{u}}{\partial t} + \overline{u}\frac{\partial \overline{u}}{\partial x} + \overline{v}\frac{\partial \overline{u}}{\partial y}\right) &= \rho 2\omega \sin\phi \overline{v} - \frac{\partial \overline{\mathrm{p}}}{\partial x} + \frac{\partial \sigma'_{xx}}{\partial x} + \frac{\partial \tau'_{yx}}{\partial y} + \frac{\partial \tau'_{zx}}{\partial z} \\
\rho\left(\frac{\partial \overline{v}}{\partial t} + \overline{u}\frac{\partial \overline{v}}{\partial x} + \overline{v}\frac{\partial \overline{v}}{\partial y}\right) &= -\rho 2\omega \sin\phi \overline{u} - \frac{\partial \overline{\mathrm{p}}}{\partial y} + \frac{\partial \tau'_{xy}}{\partial x} + \frac{\partial \sigma'_{yy}}{\partial y} + \frac{\partial \tau'_{zy}}{\partial z} \\
0 &= \rho g + \frac{\partial \overline{\mathrm{p}}}{\partial z}
\end{aligned} \tag{4.93}$$

where: $f = 2\omega \sin\phi$.

Equation 4.93 can be simplified for the z-direction and integrated to give the distribution of pressure with depth according to:

$$\begin{aligned}
\overline{\mathrm{p}}\,(z) &= -\int \rho g \,\mathrm{d}z \\
\overline{\mathrm{p}}\,(z) &= -\rho g z + \mathrm{C}
\end{aligned} \tag{4.94}$$

Using the boundary condition that the pressure at the free surface, $z = \eta$, is equal to atmospheric pressure p_0, then Eq. (4.94) becomes:

$$\overline{\mathrm{p}}\,(z) = \rho g\,(\eta - z) + \mathrm{p}_0 \tag{4.95}$$

The derivatives of the pressure in any horizontal direction can now be expressed in terms of the water elevations to give:

$$\begin{aligned}
\frac{\partial \overline{\mathrm{p}}}{\partial x} &= \rho g \frac{\partial \eta}{\partial x} + \frac{\partial \mathrm{p}_0}{\partial x} \\
\frac{\partial \overline{\mathrm{p}}}{\partial y} &= \rho g \frac{\partial \eta}{\partial y} + \frac{\partial \mathrm{p}_0}{\partial y}
\end{aligned} \tag{4.96}$$

In the scale of the motion being considered, the atmospheric pressure gradient is not a significant part of the hydrodynamic pressure gradient and can be neglected

therefore:

$$\begin{aligned}\frac{\partial \overline{\mathrm{p}}}{\partial x} &= \rho g \frac{\partial \eta}{\partial x} \\ \frac{\partial \overline{\mathrm{p}}}{\partial y} &= \rho g \frac{\partial \eta}{\partial y}\end{aligned} \tag{4.97}$$

Taking Eq. (4.93), and adding the time averaged continuity equation (4.12) multiplied by u (in the x-direction) or v (in the y-direction) to the right hand side of the equation giving:

$$\begin{aligned}\rho\left(\frac{\partial \overline{u}}{\partial t} + \frac{\partial \overline{u}^2}{\partial x} + \frac{\partial \overline{uv}}{\partial y} + \overline{u}\frac{\partial \overline{w}}{\partial z}\right) &= \rho 2\omega \sin\phi \overline{v} - \frac{\partial \overline{\mathrm{p}}}{\partial x} + \frac{\partial \sigma'_{xx}}{\partial x} + \frac{\partial \tau'_{yx}}{\partial y} + \frac{\partial \tau'_{zx}}{\partial z} \\ \rho\left(\frac{\partial \overline{v}}{\partial t} + \frac{\partial \overline{vu}}{\partial x} + \frac{\partial \overline{v}^2}{\partial y} + \overline{v}\frac{\partial \overline{w}}{\partial z}\right) &= -\rho 2\omega \sin\phi \overline{u} - \frac{\partial \overline{\mathrm{p}}}{\partial y} + \frac{\partial \tau'_{xy}}{\partial x} + \frac{\partial \sigma'_{yy}}{\partial y} + \frac{\partial \tau'_{zy}}{\partial z}\end{aligned} \tag{4.98}$$

Substituting the derivatives of the pressure in the horizontal direction, as given by Eqs. (4.97) into Eq. (4.98) gives:

$$\begin{aligned}\rho\left(\frac{\partial \overline{u}}{\partial t} + \frac{\partial \overline{u}^2}{\partial x} + \frac{\partial \overline{uv}}{\partial y} + \overline{u}\frac{\partial \overline{w}}{\partial z}\right) &= \rho 2\omega \sin\phi \overline{v} - \rho g \frac{\partial \eta}{\partial x} + \frac{\partial \sigma'_{xx}}{\partial x} + \frac{\partial \tau'_{yx}}{\partial y} + \frac{\partial \tau'_{zx}}{\partial z} \\ \rho\left(\frac{\partial \overline{v}}{\partial t} + \frac{\partial \overline{vu}}{\partial x} + \frac{\partial \overline{v}^2}{\partial y} + \overline{v}\frac{\partial \overline{w}}{\partial z}\right) &= -\rho 2\omega \sin\phi \overline{u} - \rho g \frac{\partial \eta}{\partial y} + \frac{\partial \tau'_{xy}}{\partial x} + \frac{\partial \sigma'_{yy}}{\partial y} + \frac{\partial \tau'_{zy}}{\partial z}\end{aligned} \tag{4.99}$$

Using Leibnitz' rule and integrating over the depth between $-h$ and η (bed and surface) gives for the x-direction:

$$\begin{aligned}&\rho\frac{\partial}{\partial t}\int_{-h}^{\eta} \overline{u}\,\mathrm{d}z + \rho\frac{\partial}{\partial x}\int_{-h}^{\eta} \overline{u}^2\,\mathrm{d}z + \rho\frac{\partial}{\partial y}\int_{-h}^{\eta} \overline{uv}\,\mathrm{d}z - \rho\left[\overline{u}\frac{\partial \eta}{\partial t} + \overline{u}^2\frac{\partial \eta}{\partial x} + \overline{uv}\frac{\partial \eta}{\partial y}\right]_{\eta} \\ &\qquad + \rho\left[\overline{u}\frac{\partial(-h)}{\partial t} + \overline{u}^2\frac{\partial(-h)}{\partial x} + \overline{uv}\frac{\partial(-h)}{\partial y}\right]_{-h} + \rho\left[\overline{uw}\right]_{-h}^{\eta} \\ &= \rho 2\omega \sin\phi \int_{-h}^{\eta} \overline{v}\,\mathrm{d}z - \rho g\left(\eta + h\right)\frac{\partial \eta}{\partial x} + \frac{\partial}{\partial x}\int_{-h}^{\eta} \sigma'_{xx}\,\mathrm{d}z + \frac{\partial}{\partial y}\int_{-h}^{\eta} \tau'_{yx}\,\mathrm{d}z + \int_{-h}^{\eta} \frac{\partial \tau'_{zx}}{\partial z}\mathrm{d}z \\ &\qquad - \left[\sigma'_{xx}\frac{\partial \eta}{\partial x} + \tau'_{yx}\frac{\partial \eta}{\partial y}\right]_{\eta} + \left[\sigma'_{xx}\frac{\partial(-h)}{\partial x} + \tau'_{yx}\frac{\partial(-h)}{\partial y}\right]_{-h}\end{aligned} \tag{4.100}$$

and for the y-direction:

$$\begin{aligned}
&\rho\frac{\partial}{\partial t}\int_{-h}^{\eta}\overline{v}\,\mathrm{d}z+\rho\frac{\partial}{\partial x}\int_{-h}^{\eta}\overline{uv}\,\mathrm{d}z+\rho\frac{\partial}{\partial y}\int_{-h}^{\eta}\overline{v}^2\,\mathrm{d}z-\rho\left[\overline{v}\frac{\partial\eta}{\partial t}+\overline{uv}\frac{\partial\eta}{\partial x}+\overline{v}^2\frac{\partial\eta}{\partial y}\right]_{\eta}\\
&\qquad+\rho\left[\overline{v}\frac{\partial(-h)}{\partial t}+\overline{uv}\frac{\partial(-h)}{\partial x}+\overline{v}^2\frac{\partial(-h)}{\partial y}\right]_{-h}+\rho\left[\overline{vw}\right]_{-h}^{\eta}\\
&=-\rho 2\omega\sin\phi\int_{-h}^{\eta}\overline{u}\,\mathrm{d}z-\rho g\left(\eta+h\right)\frac{\partial\eta}{\partial y}+\frac{\partial}{\partial x}\int_{-h}^{\eta}\tau'_{xy}+\frac{\partial}{\partial y}\int_{-h}^{\eta}\sigma'_{yy}\,\mathrm{d}z+\int_{-h}^{\eta}\frac{\partial\tau'_{zy}}{\partial z}\mathrm{d}z\\
&\qquad-\left[\tau'_{xy}\frac{\partial\eta}{\partial x}+\sigma'_{yy}\frac{\partial\eta}{\partial y}\right]_{\eta}+\left[\tau'_{xy}\frac{\partial(-h)}{\partial x}+\sigma'_{yy}\frac{\partial(-h)}{\partial y}\right]_{-h}
\end{aligned}\tag{4.101}$$

Substituting the kinematic free surface condition (Eq. (4.86)) and the fixed bed condition (Eq. (4.87)) gives for the x-direction

$$\begin{aligned}
&\rho\frac{\partial}{\partial t}\int_{-h}^{\eta}\overline{u}\,\mathrm{d}z+\rho\frac{\partial}{\partial x}\int_{-h}^{\eta}\overline{u}^2\,\mathrm{d}z+\rho\frac{\partial}{\partial y}\int_{-h}^{\eta}\overline{uv}\,\mathrm{d}z\\
&=\rho 2\omega\sin\phi\int_{-h}^{\eta}\overline{v}\,\mathrm{d}z-\rho g\left(\eta+h\right)\frac{\partial\eta}{\partial x}+\frac{\partial}{\partial x}\int_{-h}^{\eta}\sigma'_{xx}\,\mathrm{d}z+\frac{\partial}{\partial y}\int_{-h}^{\eta}\tau'_{yx}\,\mathrm{d}z+\underbrace{\tau_{xw}}_{\text{wind stress}}-\underbrace{\tau_{xb}}_{\text{bed stress}}
\end{aligned}\tag{4.102}$$

and for the y-direction:

$$\begin{aligned}
&\rho\frac{\partial}{\partial t}\int_{-h}^{\eta}\overline{v}\,\mathrm{d}z+\rho\frac{\partial}{\partial x}\int_{-h}^{\eta}\overline{uv}\,\mathrm{d}z+\rho\frac{\partial}{\partial y}\int_{-h}^{\eta}\overline{v}^2\,\mathrm{d}z\\
&=-\rho 2\omega\sin\phi\int_{-h}^{\eta}\overline{u}\,\mathrm{d}z-\rho g\left(\eta+h\right)\frac{\partial\eta}{\partial y}+\frac{\partial}{\partial x}\int_{-h}^{\eta}\tau'_{xy}+\frac{\partial}{\partial y}\int_{-h}^{\eta}\sigma'_{yy}\,\mathrm{d}z+\underbrace{\tau_{yw}}_{\text{wind stress}}-\underbrace{\tau_{yb}}_{\text{bed stress}}
\end{aligned}\tag{4.103}$$

where the bed and wind stresses are respectively:

$$\begin{aligned}
\tau_{xb}&=\left[-\sigma'_{xx}\frac{\partial(-h)}{\partial x}-\tau'_{yx}\frac{\partial(-h)}{\partial y}+\tau'_{zx}\right]_{-h}\\
\tau_{yb}&=\left[-\tau'_{xy}\frac{\partial(-h)}{\partial x}-\sigma'_{yy}\frac{\partial(-h)}{\partial y}+\tau'_{zy}\right]_{-h}
\end{aligned}\tag{4.104}$$

$$\begin{aligned}\tau_{xw} &= \left[-\sigma'_{xx}\frac{\partial\eta}{\partial x} - \tau'_{yx}\frac{\partial\eta}{\partial y} + \tau'_{zx}\right]_\eta \\ \tau_{yw} &= \left[-\tau'_{xy}\frac{\partial\eta}{\partial x} - \sigma'_{yy}\frac{\partial\eta}{\partial y} + \tau'_{zy}\right]_\eta\end{aligned} \tag{4.105}$$

Substituting $\overline{u} = U + (\overline{u} - U)$ and $\overline{v} = V + (\overline{v} - V)$ gives for the x-direction

$$\begin{aligned}&\frac{\partial UH}{\partial t} + \beta_2\frac{\partial U^2H}{\partial x} + \beta_2\frac{\partial UVH}{\partial y} = 2\omega\sin\phi VH - gH\frac{\partial\eta}{\partial x} \\ &+\frac{1}{\rho}\left[\frac{\partial}{\partial x}\int_{-h}^{\eta}\left(\sigma'_{xx} - \rho(\overline{u}-U)^2\right)\mathrm{d}z + \frac{\partial}{\partial y}\int_{-h}^{\eta}\left(\tau'_{yx} - \rho(\overline{u}-U)(\overline{v}-V)\right)\mathrm{d}z + \underbrace{\tau_{xw}}_{\text{wind stress}} - \underbrace{\tau_{xb}}_{\text{bed stress}}\right]\end{aligned} \tag{4.106}$$

and for the y-direction:

$$\begin{aligned}&\frac{\partial VH}{\partial t} + \beta_2\frac{\partial UVH}{\partial x} + \beta_2\frac{\partial V^2H}{\partial y} = -2\omega\sin\phi UH - gH\frac{\partial\eta}{\partial y} \\ &+\frac{1}{\rho}\left[\frac{\partial}{\partial x}\int_{-h}^{\eta}\left(\tau'_{xy} - \rho(\overline{u}-U)(\overline{v}-V)\right) + \frac{\partial}{\partial y}\int_{-h}^{\eta}\left(\sigma'_{yy} - \rho(\overline{v}-V)^2\right)\mathrm{d}z + \underbrace{\tau_{yw}}_{\text{wind stress}} - \underbrace{\tau_{yb}}_{\text{bed stress}}\right]\end{aligned} \tag{4.107}$$

where $H = \eta + h$, $U = \frac{1}{H}\int_{-h}^{\eta}\overline{u}\,\mathrm{d}z$ and

$$\beta_2 = \frac{1}{U^2H}\int_{-h}^{\eta}\overline{u}^2\,\mathrm{d}z = \frac{1}{UVH}\int_{-h}^{\eta}\overline{uv}\,\mathrm{d}z = \frac{1}{V^2H}\int_{-h}^{\eta}\overline{v}^2\,\mathrm{d}z \tag{4.108}$$

The integration over depth of the terms $(\overline{u}-U)^2$, $(\overline{u}-U)(\overline{v}-V)$ and $(\overline{v}-V)^2$ will be small and can be neglected. Therefore giving:

$$\begin{aligned}&\frac{\partial UH}{\partial t} + \beta_2\frac{\partial U^2H}{\partial x} + \beta_2\frac{\partial UVH}{\partial y} = 2\omega\sin\phi VH - gH\frac{\partial\eta}{\partial x} \\ &\qquad + \frac{1}{\rho}\left[\frac{\partial}{\partial x}\int_{-h}^{\eta}\sigma'_{xx}\,\mathrm{d}z + \frac{\partial}{\partial y}\int_{-h}^{\eta}\tau'_{yx}\,\mathrm{d}z + \underbrace{\tau_{xw}}_{\text{wind stress}} - \underbrace{\tau_{xb}}_{\text{bed stress}}\right]\end{aligned} \tag{4.109}$$

$$\frac{\partial VH}{\partial t} + \beta_2 \frac{\partial UVH}{\partial x} + \beta_2 \frac{\partial V^2 H}{\partial y} = -2\omega \sin\phi UH - gH\frac{\partial \eta}{\partial y} + \frac{1}{\rho}\left[\frac{\partial}{\partial x}\int_{-h}^{\eta} \tau'_{xy} + \frac{\partial}{\partial y}\int_{-h}^{\eta} \sigma'_{yy}\,\mathrm{d}z + \underbrace{\tau_{yw}}_{\text{wind stress}} - \underbrace{\tau_{yb}}_{\text{bed stress}}\right] \quad (4.110)$$

The effects of wind action can be represented as (Kinsman, 2002):

$$\begin{aligned} \tau_{xw} &= \rho_a C_w W_x \sqrt{W_x^2 + W_y^2} \\ \tau_{yw} &= \rho_a C_w W_y \sqrt{W_x^2 + W_y^2} \end{aligned} \quad (4.111)$$

where ρ_a is the density of air, W_x, W_y are components of wind velocity and C_w is a resistance coefficient which, on the basis of sea slope observations, Neumann suggested $C_w = 9$ x 10^{-3} $W^{-0.5}$ where W is in metres per second.

The Eq. (4.39) for bed shear stress was combined with the de Chezy Formula (4.42) and expressed in the form of a quadratic friction law for two-dimensional flow as:

$$\begin{aligned} \tau_{xb} &= \frac{\rho g U \sqrt{U^2 + V^2}}{C^2} \\ \tau_{yb} &= \frac{\rho g V \sqrt{U^2 + V^2}}{C^2} \end{aligned} \quad (4.112)$$

where U, V = depth averaged fluid velocity in the x and y directions and C = de Chezy roughness coefficient with the Chezy roughness coefficient.

From equation (4.18), the deviatoric normal and shear stresses for two-dimensional flow are given as:

$$\begin{aligned} \sigma'_{xx} &= \mu\frac{\partial \overline{u}}{\partial x} - \rho\overline{u'u'} \\ \sigma'_{yy} &= \mu\frac{\partial \overline{v}}{\partial y} - \rho\overline{v'v'} \\ \tau'_{xy} &= \mu\frac{\partial \overline{u}}{\partial y} - \rho\overline{u'v'} \\ \tau'_{yx} &= \mu\frac{\partial \overline{v}}{\partial x} - \rho\overline{u'v'} \end{aligned} \quad (4.113)$$

Boussinesq (1877) proposed for the Reynolds shear stresses:

$$\begin{aligned} -\overline{u'u'} &= \varepsilon_t \left(\frac{\partial \overline{u}}{\partial x} + \frac{\partial \overline{u}}{\partial x} \right) \\ -\overline{u'v'} &= \varepsilon_t \left(\frac{\partial \overline{u}}{\partial x} + \frac{\partial \overline{v}}{\partial y} \right) \\ -\overline{v'v'} &= \varepsilon_t \left(\frac{\partial \overline{v}}{\partial y} + \frac{\partial \overline{v}}{\partial y} \right) \end{aligned} \tag{4.114}$$

Substituting the Reynolds shear stresses (4.114) into the the deviatoric normal and shear stresses for two-dimensional flow (4.113) gives:

$$\begin{aligned} \sigma'_{xx} &= \mu \frac{\partial \overline{u}}{\partial x} + \rho\varepsilon \left(\frac{\partial \overline{u}}{\partial x} + \frac{\partial \overline{u}}{\partial x} \right) \\ \sigma'_{yy} &= \mu \frac{\partial \overline{v}}{\partial y} + \rho\varepsilon \left(\frac{\partial \overline{v}}{\partial y} + \frac{\partial \overline{v}}{\partial y} \right) \\ \tau'_{xy} &= \mu \frac{\partial \overline{u}}{\partial y} + \rho\varepsilon \left(\frac{\partial \overline{u}}{\partial x} + \frac{\partial \overline{v}}{\partial y} \right) \\ \tau'_{yx} &= \mu \frac{\partial \overline{v}}{\partial x} + \rho\varepsilon \left(\frac{\partial \overline{u}}{\partial x} + \frac{\partial \overline{v}}{\partial y} \right) \end{aligned} \tag{4.115}$$

For turbulent flows, $\rho\varepsilon >> \mu$.

Substituting the bottom friction (4.112), wind stress (4.111) and turbulent stress (4.115) terms into Eqs. (4.109) and (4.110) gives:

$$\begin{aligned} &\frac{\partial UH}{\partial t} + \beta_2 \frac{\partial U^2 H}{\partial x} + \beta_2 \frac{\partial UVH}{\partial y} = \underbrace{2\omega \sin\phi VH}_{\text{coriolis}} - gH\frac{\partial \eta}{\partial x} \\ &+ \underbrace{2\frac{\partial}{\partial x}\left[\varepsilon H \frac{\partial \overline{u}}{\partial x}\right] + \frac{\partial}{\partial y}\left[\varepsilon H \left(\frac{\partial \overline{u}}{\partial y} + \frac{\partial \overline{v}}{\partial x} \right)\right]}_{\text{turbulent/eddy stress}} + \underbrace{\frac{\rho_a}{\rho} C_w W_x \sqrt{W_x^2 + W_y^2}}_{\text{wind stress}} - \underbrace{\frac{gU\sqrt{U^2+V^2}}{C^2}}_{\text{bed stress}} \end{aligned} \tag{4.116}$$

$$\frac{\partial VH}{\partial t} + \beta_2 \frac{\partial UVH}{\partial x} + \beta_2 \frac{\partial V^2 H}{\partial y} = \underbrace{-2\omega \sin\phi UH}_{\text{coriolis}} - gH\frac{\partial \eta}{\partial y}$$
$$+ \underbrace{2\frac{\partial}{\partial x}\left[\varepsilon H \frac{\partial \overline{v}}{\partial x}\right] + \frac{\partial}{\partial y}\left[\varepsilon H\left(\frac{\partial \overline{v}}{\partial y} + \frac{\partial \overline{u}}{\partial x}\right)\right]}_{\text{turbulent/eddy stress}} + \underbrace{\frac{\rho_a}{\rho} C_w W_y \sqrt{W_x^2 + W_y^2}}_{\text{wind stress}} - \underbrace{\frac{gV\sqrt{U^2+V^2}}{C^2}}_{\text{bed stress}} \tag{4.117}$$

The depth averaged momentum equations (4.116) and (4.117) can also be written in terms of the depth integrated velocities ($q_x = UH, q_y = VH$) by substitution and using the quotient rule to give:

$$\frac{\partial q_x}{\partial t} + \beta_2\left(\frac{2q_x}{H}\frac{\partial q_x}{\partial x} - \frac{{q_x}^2}{H^2}\frac{\partial H}{\partial x}\right) + \beta_2\left(\frac{q_x}{H}\frac{\partial q_y}{\partial y} + \frac{q_y}{H}\frac{\partial q_x}{\partial y} - \frac{q_x q_y}{H^2}\frac{\partial H}{\partial y}\right) = \underbrace{2\omega \sin\phi q_y}_{\text{coriolis}} - gH\frac{\partial \eta}{\partial x}$$
$$+ \underbrace{2\frac{\partial}{\partial x}\left[\varepsilon H \frac{\partial \overline{u}}{\partial x}\right] + \frac{\partial}{\partial y}\left[\varepsilon H\left(\frac{\partial \overline{u}}{\partial y} + \frac{\partial \overline{v}}{\partial x}\right)\right]}_{\text{turbulent/eddy stress}} + \underbrace{\frac{\rho_a}{\rho} C_w W_x \sqrt{W_x^2 + W_y^2}}_{\text{wind stress}} - \underbrace{\frac{g q_x \sqrt{{q_x}^2 + {q_y}^2}}{H^2 C^2}}_{\text{bed stress}} \tag{4.118}$$

$$\frac{\partial q_y}{\partial t} + \beta_2\left(\frac{q_x}{H}\frac{\partial q_y}{\partial x} + \frac{q_y}{H}\frac{\partial q_x}{\partial x} - \frac{q_x q_y}{H^2}\frac{\partial H}{\partial x}\right) + \beta_2\left(\frac{2q_y}{H}\frac{\partial q_y}{\partial y} - \frac{{q_y}^2}{H^2}\frac{\partial H}{\partial y}\right) = \underbrace{-2\omega \sin\phi q_x}_{\text{coriolis}} - gH\frac{\partial \eta}{\partial y}$$
$$+ \underbrace{2\frac{\partial}{\partial x}\left[\varepsilon H \frac{\partial \overline{v}}{\partial x}\right] + \frac{\partial}{\partial y}\left[\varepsilon H\left(\frac{\partial \overline{v}}{\partial y} + \frac{\partial \overline{u}}{\partial x}\right)\right]}_{\text{turbulent/eddy stress}} + \underbrace{\frac{\rho_a}{\rho} C_w W_y \sqrt{W_x^2 + W_y^2}}_{\text{wind stress}} - \underbrace{\frac{g q_y \sqrt{{q_x}^2 + {q_y}^2}}{H^2 C^2}}_{\text{bed stress}} \tag{4.119}$$

4.7.4 Depth Averaged Solute Transport Equations

Equation (4.25) does not take into account the effects of longitudinal dispersion. This is the result of longitudinal spreading of pollutants due to mixing of adjacent layers moving with different velocities, i.e. due to fluid shear.

The time averaged velocity and concentration components can be further split

into depth averaged velocity or concentration and the deviation of the velocity or concentration from the depth averaged values. In addition, it is assumed that the vertical velocity component (w), is negligible compared to the horizontal velocity components (u and v) for two-dimensional flow.

Therefore substituting $\overline{u} = U + u''$, $\overline{v} = V + v''$ and $\overline{s} = S + s''$ into Eq. (4.25), where U and S are the depth averaged velocity and concentration respectively, and integrating over the depth of flow (H) gives:

$$\begin{aligned} \overline{\overline{s''u''}} &= -D_{Lx}\frac{\partial \overline{s}}{\partial x} \\ \overline{\overline{s''v''}} &= -D_{Ly}\frac{\partial \overline{s}}{\partial y} \\ \overline{\overline{s''w''}} &= -D_{Lz}\frac{\partial \overline{s}}{\partial z} \end{aligned} \tag{4.120}$$

Hence, for two-dimensional flow the advective-diffusion equation becomes:

$$\frac{\partial HS}{\partial t} + \frac{\partial HUS}{\partial x} + \frac{\partial HVS}{\partial y} = \frac{\partial}{\partial x}\left[H(D_{tx} + D_{Lx})\frac{\partial S}{\partial x}\right] + \frac{\partial}{\partial y}\left[H(D_{ty} + D_{Ly})\frac{\partial S}{\partial y}\right] \tag{4.121}$$

4.8 Source Terms

Where there is an outfall into a River or Estuary, source terms need to be added to the governing equations to model this effect.

The source term for the continuity equation can be written as:

$$\frac{\rho_s A_s u_s}{\rho \Delta x \Delta y \Delta z} \tag{4.122}$$

which, for 1-D flow, can be written as:

$$\frac{\rho_s Q_s}{\rho \Delta x A_{\text{flow}}} \tag{4.123}$$

The source term for the solute transport equation can be written as:

$$\frac{Q_o S_o}{A_o} - kHS_o \tag{4.124}$$

4.9 Summary

The general governing equations have been adapted for one dimensional (1D) and two dimensional (2D) flows in rivers and estuaries in this chapter. The adaption of the general governing equations involved separating the instantaneous velocities, pressure and solute concentrations into mean and fluctuating components, to give the Reynold's Averaged Navier-Stokes (RANS) equations. The RANS equations were then integrated over the cross-sectional area of flow to give equations for continuity (Eq. (4.64)), momentum (Eq. (4.72)) and solute transport (Eq. (4.81)) suitable for one-dimensional (1D) problems. Similarly, the RANS equations were then integrated over the depth of flow to give equations for continuity (Eq. (4.92)), momentum (Eqs. (4.116) and (4.117)) and solute transport (Eq. (4.121)) suitable for two-dimensional (2D) problems. In the next chapter, details will be given of how the adapted equations are solved numerically and how parallel computing is utilised in speeding up the computations.

Chapter 5

Numerical Solution of Governing Equations

5.1 Introduction

This Chapter provides details of the techniques used to solve the adapted governing equations from Chapter 4 for this research study. Details of the numerical schemes used to solve the adapted governing hydrodynamic and solute transport equations, for the two-dimensional (2D) model is given in Section 5.2 and that for the one-dimensional (1D) model is given in Section 5.3. In Section 5.4 details of the numerical schemes are discussed.

Numerical methods are techniques by which mathematical problems are formulated so that they can be solved by a series of arithmetic operations. Numerical methods involve large numbers of tedious arithmetic calculations. Computers provide a platform for solving, otherwise tedious, arithmetic calculations in a relatively short time.

Analytical solutions are exact methods for finding the answer to a problem. These solutions are useful in providing an insight into the behaviour of some systems. However, analytical solutions can only be provided for a limited class of problems. Most analytical solutions are linear models with simple geometry and

low dimensionality. These solutions are of limited practical value because most real problems are non-linear and involve complex shapes and processes. As the complexity increases, it becomes more suitable to use a numerical method.

The numerical method adopted for this research study is the same as that used in DIVAST, a two-dimensional numerical analysis code originally developed by Falconer (1986), and FASTER, a one-dimensional numerical analysis code developed in-house at Cardiff University. The numerical schemes are presented in this Chapter as part of the verification and validation process carried out in this research study.

5.2 Two-dimensional (2D) numerical model

5.2.1 Hydrodynamics - Alternating Direction Implicit (ADI) Scheme

For the two-dimensional model, the adapted governing equations for the hydrodynamics, as given in Chapter 4, include the continuity (4.92) and momentum equations [Eqs. (4.116) and (4.117)]. These equations are solved using the finite difference method (FDM). A regular rectangular grid has been adopted for the computational mesh. There are different ways of expressing any given partial differential equation using the finite difference method. These include numerical schemes which progressively solve forward, backward or central differences in space; time-marching explicit solutions, where the unknown value can be calculated directly from known values without solving a matrix; and implicit solutions, where the unknown value is represented in terms of other neighbouring unknowns.

Here, an Alternating Direct Implicit (ADI) method has been adopted for solving the hydrodynamic equations. Adopting the finite difference method (FDM) and a space staggered grid (Figure 5.1), for the first time step $\left(n \rightarrow n + \frac{1}{2}\right)$, the continuity

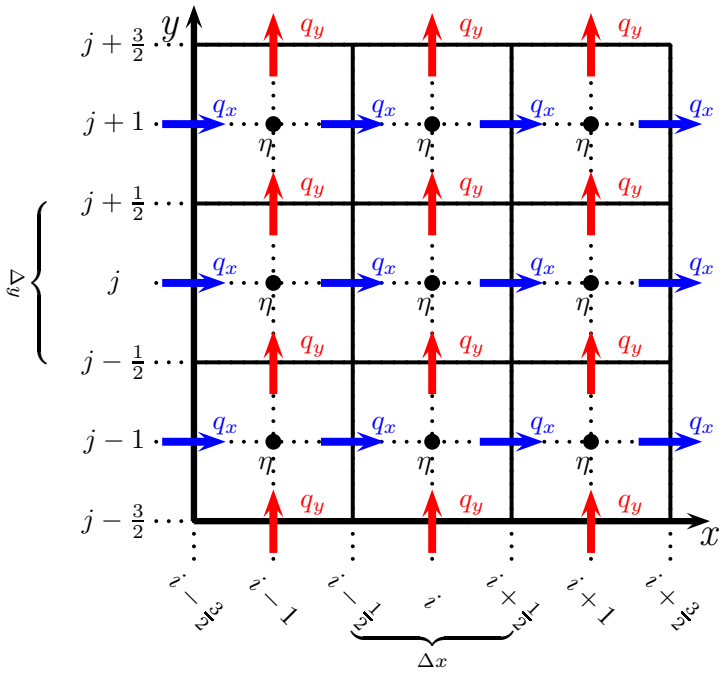

Figure 5.1: Staggered grid for space discretization using the finite difference method (FDM)

equation (4.92) can be written as:

$$\frac{\eta_{i,j}^{n+\frac{1}{2}} - \eta_{i,j}^{n}}{0.5\Delta t} + \frac{q_{x_{i+\frac{1}{2},j}}^{n+\frac{1}{2}} - q_{x_{i-\frac{1}{2},j}}^{n+\frac{1}{2}}}{\Delta x} + \frac{q_{y_{i,j+\frac{1}{2}}}^{n} - q_{y_{i,j-\frac{1}{2}}}^{n}}{\Delta y} = 0 \tag{5.1}$$

where $q_x = UH$, $q_y = VH$, and i, j = grid point location in the x and y directions respectively. The superscripts n and $n+\frac{1}{2}$ represent variables evaluated at time $t = n\Delta t$ and $t = (n+\frac{1}{2})\Delta t$ time levels respectively. Δt represents the time step for computation and n is the time step number.

Similarly, the x-direction momentum equation (4.116) can be discretised for the

first half time step $\left(n \to n+\frac{1}{2}\right)$ as:

$$\frac{q_{x_{i+\frac{1}{2},j}}^{n+\frac{1}{2}} - q_{x_{i+\frac{1}{2},j}}^{n-\frac{1}{2}}}{\Delta t} + \underbrace{\beta\frac{\left(\hat{U}\hat{q}_x\right)_{i+\frac{3}{2},j}^{n} - \left(\hat{U}\hat{q}_x\right)_{i-\frac{1}{2},j}^{n}}{2\Delta x} + \beta\frac{\left(\overline{V}\overrightarrow{\hat{q}_x}\right)_{i+\frac{3}{2},j+\frac{1}{2}}^{n} - \left(\overline{V}\overrightarrow{\hat{q}_x}\right)_{i+\frac{3}{2},j-\frac{1}{2}}^{n}}{\Delta y}}_{\text{advection}} =$$

$$\underbrace{2\omega\sin\phi \quad q_{y_{i+\frac{1}{2},j}}^{n}}_{\text{coriolis}} + \underbrace{\frac{\rho_a}{\rho}C_w W_x\sqrt{W_x^2+W_y^2}}_{\text{wind stress}} - \underbrace{\frac{g\left(q_{x_{i+\frac{1}{2},j}}^{n+\frac{1}{2}} + q_{x_{i+\frac{1}{2},j}}^{n-\frac{1}{2}}\right)\sqrt{\left(\hat{q}x_{i+\frac{1}{2},j}^{\,n}\right)^2 + \left(q_{y_{i+\frac{1}{2},j}}^{n}\right)^2}}{2\left(H_{i+\frac{1}{2},j}^{n}C_{i+\frac{1}{2},j}^{n}\right)^2}}_{\text{bed stress}}$$

$$\underbrace{-gH_{i+\frac{1}{2},j}^{n}\left[\frac{\frac{1}{2}\left(\eta_{i+1,j}^{n+\frac{1}{2}} + \eta_{i+1,j}^{n-\frac{1}{2}}\right) - \frac{1}{2}\left(\eta_{i,j}^{n+\frac{1}{2}} + \eta_{i,j}^{n-\frac{1}{2}}\right)}{\Delta x}\right]}_{\text{pressure}} + \underbrace{2\varepsilon H_{i+\frac{1}{2},j}^{n}\frac{\hat{U}_{i+\frac{3}{2},j}^{n} - 2\hat{U}_{i+\frac{1}{2},j}^{n} + \hat{U}_{i-\frac{1}{2},j}^{n}}{\Delta x^2}}_{\text{turbulent/eddy stress}}$$

$$+\underbrace{\varepsilon H_{i+\frac{1}{2},j}^{n}\frac{\hat{U}_{i+\frac{1}{2},j+1}^{n} - 2\hat{U}_{i+\frac{1}{2},j}^{n} + \hat{U}_{i+\frac{1}{2},j-1}^{n}}{\Delta y^2}}_{\text{turbulent/eddy stress}} + \underbrace{\varepsilon H_{i+\frac{1}{2},j}^{n}\frac{V_{i,j-\frac{1}{2}}^{n} - V_{i,j+\frac{1}{2}}^{n} + V_{i+1,j-\frac{1}{2}}^{n} + V_{i+1,j+\frac{1}{2}}^{n}}{\Delta x\Delta y}}_{\text{turbulent/eddy stress}} \tag{5.2}$$

where $\hat{U}$ denotes a value corrected by iteration, by setting:

$$\hat{U}^n = \begin{cases} U^{n-\frac{1}{2}} & \text{for the first iteration,} \\ \frac{1}{2}\left(U^{n-\frac{1}{2}} + U^{n+\frac{1}{2}}\right) & \text{for the second and remaining iterations,} \end{cases} \tag{5.3}$$

$\overline{V}$ denotes a value obtained by averaging the corresponding values at the surrounding grid points:

$$\overline{V}_{i+\frac{1}{2},j+\frac{1}{2}}^{n} = \frac{1}{2}\left(V_{i,j+\frac{1}{2}}^{n} + V_{i+1,j+\frac{1}{2}}^{n}\right) \tag{5.4}$$

and $\overrightarrow{q_x}$ denotes a value obtained from the upwind algorithm where

$$\overrightarrow{q_x}_{i+\frac{1}{2},j}^{n} = \begin{cases} q_{x_{i+\frac{1}{2},j-1}}^{n} & if \quad V_{i+\frac{1}{2},j}^{n} > 0, \\ q_{x_{i+\frac{1}{2},j+1}}^{n} & if \quad V_{i+\frac{1}{2},j}^{n} < 0 \end{cases} \tag{5.5}$$

Note: $\varepsilon H\frac{\partial^2 V}{\partial x\partial y}$ term is ignored in the current code.

The most efficient way to suppress spurious oscillations at the leading and trailing edges of a sharp wave-front is to adopt a so-called upwind differencing scheme. In such a scheme, the spatial differences are skewed in the 'upwind' direction; i.e., in

the direction from which the advecting flow emanates.

For the second half time step $\left(n+\frac{1}{2} \rightarrow n+1\right)$, the continuity equation and the y-direction momentum equation (4.117) can be discretised similarity (See Appendix F for details).

The use of a staggered grid in two space dimensions enables the continuity and momentum equations to be combined by coupling q_x,q_y and η solutions at adjacent grid points. A Taylor series expansion about the cell centre indicates that Eq. (5.1) has a truncation of $O(\Delta x^2, \Delta y^2)$. The use of a staggered grid prevents the occurrence of oscillatory solutions, particularly for η, that can occur if centred differences are used to discretise all derivatives on a non-staggered grid system (Fletcher, 1991). The oscillatory solution is a manifestation of two separate pressure solutions associated with alternate grid points, which the use of centred differences on a non-staggered grid permits. The water surface elevations are located at the cell centres and depth integrated velocities are located at the side centres (Figure 5.1). The source code for computer programs based on staggered grids can be harder to read because it is desirable to associate a cluster of dependent variables with corresponding storage locations. Thus arrays storing q_x, q_y and η might associate storage location (i, j) with $q_{x\,i+\frac{1}{2},j}$, $q_{y\,i,j+\frac{1}{2}}$ and $\eta_{i,j}$.

The system of equations to be solved in the first and second half time steps can be described as a tri-diagonal system of equations and can therefore be solved efficiently using the Thomas algorithm (named after Llewellyn Thomas).

For example, for a domain with a velocity/flow at the lower boundary, the continuity and momentum equations can be alternated to form a tri-diagonal system

of equations for the first half time step x-direction sweep, giving:

$$\begin{bmatrix} b_i & c_i & & & & 0 \\ a_{i+\frac{1}{2}} & b_{i+\frac{1}{2}} & c_{i+\frac{1}{2}} & & & \\ & a_{i+1} & b_{i+1} & c_{i+1} & & \\ & & a_{i+\frac{3}{2}} & b_{i+\frac{3}{2}} & \ddots & \\ & & & \ddots & \ddots & c_{\text{imax}-\frac{1}{2}} \\ 0 & & & & a_{\text{imax}} & b_{\text{imax}} \end{bmatrix} \begin{bmatrix} \eta_{i,j}^{n+\frac{1}{2}} \\ q_{x_{i+\frac{1}{2},j}}^{n+\frac{1}{2}} \\ \eta_{i+1,j}^{n+\frac{1}{2}} \\ q_{x_{i+\frac{3}{2},j}}^{n+\frac{1}{2}} \\ : \\ \eta_{\text{imax}} \end{bmatrix} = \begin{bmatrix} d_i - a_i q_{x_{i-\frac{1}{2},j}}^{n+\frac{1}{2}} \\ d_{i+\frac{1}{2}} \\ d_{i+1} \\ d_{i+\frac{3}{2}} \\ : \\ d_{\text{imax}} - c_{\text{imax}} q_{x_{\text{imax}+\frac{1}{2},j}}^{n+\frac{1}{2}} \end{bmatrix} \tag{5.6}$$

where the continuity equation recursion coefficients are:

$$\begin{aligned} a_i &= -\frac{\Delta t}{2\Delta x} \\ b_i &= 1.0 \\ c_i &= \frac{\Delta t}{2\Delta x} \\ d_i &= \eta_{i,j}^n - \frac{\Delta t}{2\Delta y}\left(q_{y_{i,j+\frac{1}{2}}}^n - q_{y_{i,j-\frac{1}{2}}}^n\right) \end{aligned} \tag{5.7}$$

and with the momentum equation recursion coefficients being:

$$\begin{aligned} a_{i+\frac{1}{2}} =& -\frac{\Delta t}{2\Delta x} g H_{i+\frac{1}{2},j}^n \\ b_{i+\frac{1}{2}} =& 1.0 \\ c_{i+\frac{1}{2}} =& \frac{\Delta t}{2\Delta x} g H_{i+\frac{1}{2},j}^n \\ d_{i+\frac{1}{2}} =& q_{x_{i+\frac{1}{2},j}}^{n-\frac{1}{2}} + \Delta t \times \text{coriolis} - \Delta t \times \text{advection} + \Delta t \times \text{turbulent stresses} \\ & + \Delta t \times \text{wind stress} - \Delta t \times \text{bed stress} - \Delta t \times g H_{i+\frac{1}{2},j}^n \frac{\left(\eta_{i+1,j}^{n-\frac{1}{2}} - \eta_{i,j}^{n-\frac{1}{2}}\right)}{2\Delta x} \end{aligned} \tag{5.8}$$

The tri-diagonal forms of the continuity and momentum equations for second

half time step can similarly be combined to form a tri-diagonal system of equation for the y-direction (See Appendix F for details).

The first sweep is done in the first half time step, with the x-direction matrix system of equations (5.6) being solved. The second sweep is done in the second half time step and the y-direction matrix system of equations (F.3) is solved. This means that the solution of a full two-dimensional matrix is not required, and one-dimension is solved implicitly in each half time step. The finite difference scheme adopted is fully centred in both time and space over the whole time step, giving second order accuracy.

The non-linear terms in the momentum equations can give rise to instabilities even though an implicit scheme has been used (Weare, 1976). This instability effect may be overcome by time centering the finite difference terms using three time levels (Falconer, 1977). The approach used in DIVAST for the non-linear advective acceleration and eddy viscosity terms involves time centred iteration (Roache, 1972), except for the cross product advective acceleration terms which are represented using a first order upwind method, thereby including sufficient artificial diffusion to eliminate grid scale oscillations in regions of high velocity gradients.

The numerical scheme for the hydrodynamics is basically second order accurate, both in time and space, with no stability constraints due to the time centred implicit character of the ADI technique. However, it has been recognised that the time step needs to be restricted so that a reasonable computational accuracy can be achieved (Chen, 1992). A maximum Courant number (C_f) has been suggested (Stelling *et al.*, 1986) as given by:

$$C_f = 2\Delta t \sqrt{gH\left(\frac{1}{\Delta x^2} + \frac{1}{\Delta y^2}\right)} \leq 4\sqrt{2} \tag{5.9}$$

with average depth conditions being used in their examples.

5.2.2 Solute Transport - Explicit Scheme

The two-dimensional solute transport equation (4.121) can be discretised using finite difference representations over a full time step ($n \rightarrow n+1$), giving:

$$\begin{aligned}
&\frac{S_{i,j}^{n+1} - S_{i,j}^{n}}{\Delta t} + \underbrace{\frac{\frac{1}{2}\left(U_{i+\frac{1}{2},j}^{n} + U_{i-\frac{1}{2},j}^{n}\right)\left(\nabla_{i+\frac{1}{2},j}^{n} - \nabla_{i-\frac{1}{2},j}^{n}\right)}{\Delta x}}_{\text{advection x-direction}} \\
&+ \underbrace{\frac{\frac{1}{2}\left(V_{i,j+\frac{1}{2}}^{n} + V_{i,j-\frac{1}{2}}^{n}\right)\left(\nabla_{i,j+\frac{1}{2}}^{n} - \nabla_{i,j-\frac{1}{2}}^{n}\right)}{\Delta y}}_{\text{advection y-direction}} = \\
&+ \underbrace{\frac{Dxx_{i+\frac{1}{2},j}^{n}\left(S_{i+1,j}^{n} + S_{i,j}^{n}\right) - \left(Dxx_{i-\frac{1}{2},j}^{n}\left(S_{i-1,j}^{n} + S_{i,j}^{n}\right)\right.}{2\Delta x^2}}_{\text{dispersion-diffusion}} \\
&+ \underbrace{\frac{Dyy_{i,j+\frac{1}{2}}^{n}\left(S_{i,j+1}^{n} + S_{i,j}^{n}\right) - Dyy_{i,j-\frac{1}{2}}^{n}\left(S_{i,j-1}^{n} + S_{i,j}^{n}\right)}{2\Delta y^2}}_{\text{dispersion-diffusion}} \\
&+ \underbrace{k_{0_{i,j}}^{n}}_{\text{zero order growth (+ve)/decay (-ve)}} + \underbrace{k_{1_{i,j}}^{n} S_{i,j}^{n}}_{\text{1st order growth (+ve)/decay (-ve)}} \\
&+ \underbrace{\frac{Q_{si,j}^{n} S_{si,j}^{n}}{\Delta x \Delta y H_{i,j}^{n}}}_{\text{input source}}
\end{aligned} \tag{5.10}$$

where $\nabla_{i+\frac{1}{2},j}^{n}$, $\nabla_{i-\frac{1}{2},j}^{n}$, $\nabla_{i,j+\frac{1}{2}}^{n}$ and $\nabla_{i,j-\frac{1}{2}}^{n}$ are the solute concentration face values obtained using the Universal Limiter for Transport Interpolation Modelling of the Advective Transport Equation (ULTIMATE) and the Quadratic Upstream Interpolation for Convective Kinematics with Estimated Streaming Terms (QUICKEST) scheme (Leonard, 1979, 1988, 1991). The ULTIMATE QUICKEST scheme was found by Wu and Falconer (2000) to show no oscillations and predict discontinuities with a very high resolution and better in comparison with other schemes, such as: the first-order upwind, second-order upwind, Lax-Wendrof, MacCormark, and QUICKEST schemes.

Solution of the finite difference equation (5.10) is explicit over each time step, however, the ULTIMATE QUICKEST scheme is third order accurate.

5.2.3 Numerical Treatment of Flooding and Drying

In regions of flood plains, a considerable area of the domain can dry out and flood again. For tidal basins, this generally happens repeatedly. The numerical model must be able to deal with moving boundaries of the wetted area. Numerical modelling of such moving boundaries can present serious problems as a result of the discretised representation of this hydrodynamic process, which generally varies in a smooth manner. The presence of steep bed slopes and/or sharp changes along the horizontal model boundary often results in challenging difficulties for numerical models, as an inaccurate treatment of wetting and/or drying fronts may lead to significant prediction errors (Xia *et al.*, 2010a). A common problem in numerically representing the flooding and drying processes is the fluctuation of the computed water elevations.

The flooding and drying routine adopted is that developed by Falconer and Chen (1991) and used in DIVAST which is based upon extensive numerical tests in idealised channels and natural estuaries (See Appendix F for details).

5.2.4 Initial and boundary conditions

At the start of the simulation period, the initial velocities are set to zero across the domain, the solute concentrations are set to a constant value if the solute distribution is uniform initially, and the water elevations are set to the high water level. If the simulation is split into separate runs, then in following runs during the simulation period, the velocities, elevations and solute concentrations are set to the conditions at the end of a previous run, so that equilibrium is rapidly approached.

At the edges of the computational domain boundary conditions of water elevations or flows are required for the hydrodynamics and solute concentrations for the solute transport processes. There are two main types of boundary conditions, namely closed and open boundaries. The main factors to consider due to the staggered nature of the grid are that the velocity components in the x and y directions are not specified at the same locations and boundary values just outside the grid may need to be

defined.

A closed boundary can be regarded as a 'wall' boundary so that no flow or solute fluxes are permitted to cross the closed boundary. This type of boundary occurs along coastlines or adjacent to structures. Values outside the modelling domain are obtained by assuming a 'no slip' condition (or zero flow velocity at the wall) parallel to the boundary and zero flow perpendicular to the boundary, which are described for the case of a wall at $i + \frac{1}{2}$ in Figure 5.2 using Equations (5.11) and (5.12).

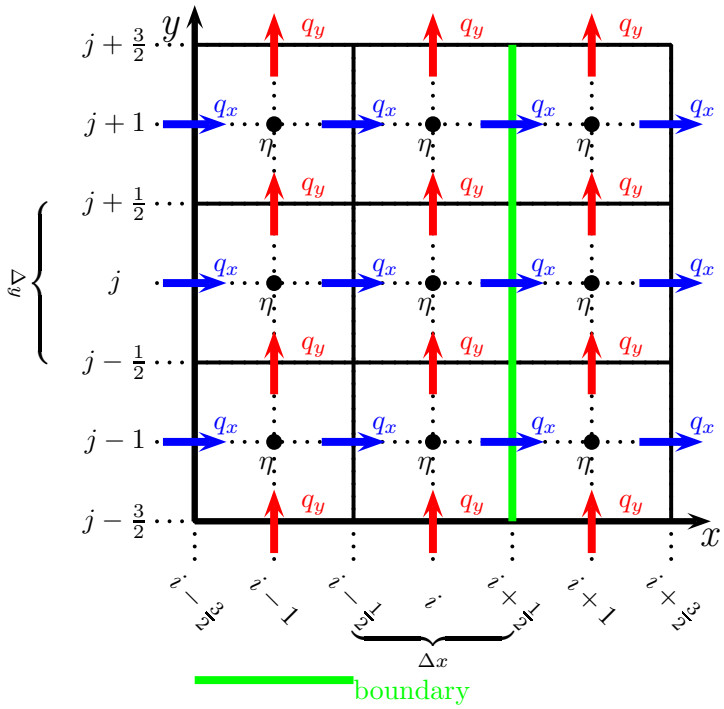

Figure 5.2: Example boundary at $i + \frac{1}{2}$

$$q_{x_{i+\frac{1}{2},j}} = 0 \quad (j = 1, 2, 3, ...) \tag{5.11}$$

$$q_{y_{i,j+\frac{1}{2}}} = -q_{y_{i+1,j+\frac{1}{2}}} \quad (j = 1, 2, 3, ...) \tag{5.12}$$

Hence all velocities parallel to the wall are set to zero, whereas the velocities outside that boundary are assigned the same value as the corresponding velocity inside the domain, but obtain a negative sign (5.12). This is done to satisfy the condition of zero flow across the boundary.

The closed boundary condition for the solute is:

$$\left.\frac{\partial S}{\partial x}\right|_{\text{wall}} = 0$$
$$\left.\frac{\partial^2 S}{\partial x^2}\right|_{\text{wall}} = 0 \tag{5.13}$$

meaning that the concentration does not change parallel to the closed boundary and that there is no solute flux across the solid boundary.

Unlike the closed boundary, the flow and solute fluxes are allowed to cross an open boundary. Appropriate hydrodynamic and solute conditions need to be specified, such as measured water surface elevations, velocities and solute values. A free slip boundary condition is used by assuming zero gradient of a variable perpendicular to the open boundary. If the boundary shown in Figure 5.2 is a flow boundary then the velocities at the boundary can be obtained for the hydrodynamics:

$$U_{i+\frac{1}{2},j} = \underbrace{U_{i+\frac{1}{2},j}}_{\text{known value}} \quad (j = 1, 2, 3, ...) \tag{5.14}$$

$$V_{i+1,j+\frac{1}{2}} = V_{i,j+\frac{1}{2}} \quad (j = 1, 2, 3, ...) \tag{5.15}$$

meaning that the U velocity at the flow boundary is set to the known boundary values and the corresponding V velocity outside the domain is set equal to the boundary values inside the domain.

If the open boundary condition at the location in Figure 5.2 is of the water elevation type, then the following condition can be obtained for the hydrodynamics:

$$\eta_{i+1,j} = \underbrace{\eta_{i+1,j}}_{\text{known value}} \quad (j = 1, 2, 3, ...) \tag{5.16}$$

The solute values at the open boundary are prescribed similarly, only when flows at the open boundary are entering the domain. However, if flows are leaving the

domain, the solute values outside the boundary are not needed.

5.3 One-dimensional (1D) numerical model

5.3.1 Hydrodynamics - Implicit Scheme

The numerical model adopted for the hydrodynamics is the same as that used in FASTER, a one-dimensional numerical analysis tool developed within the Hydro-environmental Research Centre, at Cardiff University. Details of the numerical scheme are provided herein for clarity. The model is based on an implicit finite difference scheme, which again uses the Thomas algorithm to solve the tri-diagonal system of equations. The one-dimensional continuity (4.64) and momentum equations (4.72) are solved numerically using the Crank-Nicholson central difference scheme, with a staggered grid and varying grid size. Due the staggered nature of the grid, the water surface elevations (η) are centred at the nodes (i) and the velocities are located halfway between the nodes (i.e. at $i+\frac{1}{2}$ or $i-\frac{1}{2}$).

The finite difference form of the continuity equation (4.64) can be written in the following form, using the Crank-Nicholson implicit method:

$$\frac{W_i^n\left(\eta_i^{n+1}-\eta_i^n\right)}{\Delta t}+\frac{\theta\left(Q_{i+\frac{1}{2}}^{n+1}-Q_{i-\frac{1}{2}}^{n+1}\right)+(1-\theta)\left(Q_{i+\frac{1}{2}}^{n}-Q_{i-\frac{1}{2}}^{n}\right)}{X_{i+\frac{1}{2}}-X_{i-\frac{1}{2}}}=\frac{Q_{Li}^n}{X_{i+\frac{1}{2}}-X_{i-\frac{1}{2}}} \tag{5.17}$$

where $0 \leq \theta \leq 1$ is a weighting coefficient to split the spatial derivatives between the upper $(n+1)$ and lower (n) time levels and Q_{Li}^{n+1} is lateral input flow at a particular node.

The finite difference form of the momentum equation (4.78), after substituting the continuity equation $\left(\frac{\partial Q}{\partial x}=-\frac{\partial A}{\partial t}+\frac{\partial Q_{Li}}{\partial x}\right)$, can be written in the following form

using the Crank-Nicholson implicit method.

$$\frac{Q_{i+\frac{1}{2}}^{n+1}-Q_{i+\frac{1}{2}}^{n}}{\Delta t}-\beta_1 2\frac{Q_{i+\frac{1}{2}}^{n}}{A_{i+\frac{1}{2}}^{n}}\frac{W_{i+\frac{1}{2}}^{n}\frac{1}{2}\left(\eta_{i+1}^{n+1}+\eta_{i}^{n+1}-\eta_{i+1}^{n}-\eta_{i}^{n}\right)}{\Delta t}$$
$$\underbrace{+\beta_1\frac{2\left[\theta Q_{i+\frac{1}{2}}^{n+1}+(1-\theta)Q_{i+\frac{1}{2}}^{n}\right]}{A_{i+\frac{1}{2}}^{n}}\quad\frac{Q_{Li+\frac{1}{2}}^{n+1}}{X_{i+1}-X_i}-\beta_1\frac{Q_{i+\frac{1}{2}}^{n+1}Q_{i+\frac{1}{2}}^{n}}{\left(A_{i+\frac{1}{2}}^{n}\right)^2}\quad\frac{A_{i+1}^{n}-A_{i}^{n}}{X_{i+1}-X_i}}_{\text{advection}}=$$
$$\underbrace{-gA_{i+\frac{1}{2}}^{n}\frac{\theta\left(\eta_{i+1}^{n+1}-\eta_{i}^{n+1}\right)+(1-\theta)\left(\eta_{i+1}^{n}-\eta_{i}^{n}\right)}{X_{i+1}-X_i}}_{\text{pressure}}-\underbrace{g\frac{Q_{i+\frac{1}{2}}^{n+1}\left|Q_{i+\frac{1}{2}}^{n}\right|}{\left(C_{i+\frac{1}{2}}^{n}\right)^2A_{i+\frac{1}{2}}^{n}R_{i+\frac{1}{2}}^{n}}}_{\text{friction}}\tag{5.18}$$

where $A_{i+\frac{1}{2}}=0.5(A_i+A_{i+1})$ with similar equations for $W_{i+\frac{1}{2}}$, $C_{i+\frac{1}{2}}$ and $R_{i+\frac{1}{2}}$.

The continuity (5.17) and momentum equation (5.18) for each time step can be combined by alternating the equations into one tri-diagonal system of equations, giving:

$$\begin{bmatrix} b_i & c_i & & & & 0\\ a_{i+\frac{1}{2}} & b_{i+\frac{1}{2}} & c_{i+\frac{1}{2}} & & & \\ & a_{i+1} & b_{i+1} & c_{i+1} & & \\ & & a_{i+\frac{3}{2}} & b_{i+\frac{3}{2}} & \ddots & \\ & & & \ddots & \ddots & c_{\text{imax}-\frac{1}{2}}\\ 0 & & & & a_{\text{imax}} & b_{\text{imax}} \end{bmatrix}\begin{bmatrix} \eta_i^{n+1}\\ Q_{i+\frac{1}{2}}^{n+1}\\ \eta_{i+1}^{n+1}\\ Q_{i+\frac{3}{2}}^{n+1}\\ :\\ \eta_{\text{imax}} \end{bmatrix}=\begin{bmatrix} d_i+\theta Q_{i-\frac{1}{2}}^{n+1}\\ d_{i+\frac{1}{2}}\\ d_{i+1}\\ d_{i+\frac{3}{2}}\\ :\\ d_{\text{imax}}-c_{\text{imax}}Q_{\text{imax}+\frac{1}{2}}^{n+1} \end{bmatrix}\tag{5.19}$$

where the recursion coefficients for the continuity equation are:

$$
\begin{aligned}
a_i =& -\theta \\
b_i =& \frac{W_i^n}{\Delta t}\left(X_{i+\frac{1}{2}} - X_{i-\frac{1}{2}}\right) \\
c_i =& \theta \\
d_i =& Q_{Li}^n + \frac{W_i^n \eta_i^n}{\Delta t}\left(X_{i+\frac{1}{2}} - X_{i-\frac{1}{2}}\right) - (1-\theta)\left(Q_{i+\frac{1}{2}}^n - Q_{i-\frac{1}{2}}^n\right)
\end{aligned}
\tag{5.20}
$$

and for the momentum equation can be written as:

$$
\begin{aligned}
a_{i+\frac{1}{2}} =& -\beta_1 \frac{W_{i+\frac{1}{2}}^n Q_{i+\frac{1}{2}}^n}{A_{i+\frac{1}{2}}^n \Delta t} - \frac{g A_{i+\frac{1}{2}}^n \theta}{X_{i+1} - X_i} \\
b_{i+\frac{1}{2}} =& \frac{1}{\Delta t} + \beta_1 \frac{2\theta Q_{Li+\frac{1}{2}}^{n+1}}{A_{i+\frac{1}{2}}^n \left(X_{i+1} - X_i\right)} - \beta_1 \frac{Q_{i+\frac{1}{2}}^n \left(A_{i+1}^n - A_i^n\right)}{\left(A_{i+\frac{1}{2}}^n\right)^2 \left(X_{i+1} - X_i\right)} + g \frac{\left|Q_{i+\frac{1}{2}}^n\right|}{\left(C_{i+\frac{1}{2}}^n\right)^2 A_{i+\frac{1}{2}}^n R_{i+\frac{1}{2}}^n} \\
c_{i+\frac{1}{2}} =& -\beta_1 \frac{W_{i+\frac{1}{2}}^n Q_{i+\frac{1}{2}}^n}{\Delta t A_{i+\frac{1}{2}}^n} + \frac{g A_{i+\frac{1}{2}}^n \theta}{X_{i+1} - X_i} \\
d_{i+\frac{1}{2}} =& \frac{Q_{i+\frac{1}{2}}^n}{\Delta t} - \beta_1 \frac{W_{i+\frac{1}{2}}^n Q_{i+\frac{1}{2}}^n \left(\eta_{i+1}^n + \eta_i^n\right)}{A_{i+\frac{1}{2}}^n \Delta t} - \beta_1 \frac{2(1-\theta) Q_{i+\frac{1}{2}}^n Q_{Li+\frac{1}{2}}^{n+1}}{A_{i+\frac{1}{2}}^n \left(X_{i+1} - X_i\right)} - \frac{g A_{i+\frac{1}{2}}^n (1-\theta)\left(\eta_{i+1}^n - \eta_i^n\right)}{X_{i+1} - X_i}
\end{aligned}
\tag{5.21}
$$

The implicit solution of the governing continuity and momentum equations is second order accurate in space and time. It is unconditionally stable and is numerically accurate when the Courant number ($C_f = \frac{\Delta t}{\Delta x}\sqrt{\frac{gA}{W}}$) is less than typically five.

For the Crank-Nicholson scheme, if $\theta = 1$ then the numerical solution is fully implicit and the solution is always stable. Likewise when $\theta = 0$ the numerical scheme is fully explicit. Also when $\theta \geq 0.5$, the scheme is unconditionally stable. In this research study, a value of $\theta = 0.5$ was used for the hydrodynamic simulations.

5.3.2 Solute Transport - Implicit Scheme

The numerical model adopted for the solute transport is the same as that used in the solute transport part of FASTER. In addition refinements to the representation of the bacterial decay processes were made in this research study. Details of the numerical scheme are provided here for clarity. As before, an implicit finite difference scheme is used, which includes a Thomas algorithm to solve the tri-diagonal system of equations. The one-dimensional solute transport equation (4.81) can be written using a central finite difference scheme as:

$$\begin{aligned}
&\frac{(AS)_i^{n+1} - (AS)_i^n}{\Delta t} + \frac{2}{X_{i+1} - X_{i-1}} \left\{ \theta \left[\frac{1}{2} \left(S_{i+1} + S_i \right)^{n+1} Q_{i+\frac{1}{2}}^{n+1} - \frac{1}{2} \left(S_i + S_{i-1} \right)^{n+1} Q_{i-\frac{1}{2}}^{n+1} \right] \right. \\
&\qquad \left. + (1-\theta) \left[\nabla_{i+\frac{1}{2}}^n Q_{i+\frac{1}{2}}^n - \nabla_{i-\frac{1}{2}}^n Q_{i-\frac{1}{2}}^n \right] \right\} = \\
&\qquad \frac{2}{X_{i+1} - X_{i-1}} \left\{ \theta \left[(AD_l)_{i+\frac{1}{2}}^{n+1} \left(\frac{S_{i+1}^{n+1} - S_i^{n+1}}{X_{i+1} - X_i} \right) - (AD_l)_{i-\frac{1}{2}}^{n+1} \left(\frac{S_i^{n+1} - S_{i-1}^{n+1}}{X_i - X_{i-1}} \right) \right] \right. \\
&\qquad \left. + (1-\theta) \left[(AD_l)_{i+\frac{1}{2}}^{n} \left(\frac{S_{i+1}^{n} - S_i^{n}}{X_{i+1} - X_i} \right) - (AD_l)_{i-\frac{1}{2}}^{n} \left(\frac{S_i^{n} - S_{i-1}^{n}}{X_i - X_{i-1}} \right) \right] \right\} \\
&\qquad + \underbrace{\frac{2 Q_{Li}^{n+1} S_{Li}^{n+1}}{X_{i+1} - X_{i-1}}}_{\text{source}} + \underbrace{A_i^{n+1} {k_0}_i^{n+1}}_{\text{zero order growth/decay}} + \underbrace{A_i^{n+1} {k_1}_i^{n+1} S_i^{n+1}}_{\text{1st order growth/decay}} \qquad (5.22)
\end{aligned}$$

where the growth/decay $({k_0}_i^{n+1}, {k_1}_i^{n+1})$ terms have the same definitions as per the two-dimensional model and $\nabla_{i+\frac{1}{2}}^n, \nabla_{i-\frac{1}{2}}^n$ are the cell face values calculated using the ULTIMATE QUICKEST scheme. In this research study, a value of $\theta = 0.5$ was again used for the weighting factor in the solute transport equation.

The solute transport equation (5.22) can be written in the tri-diagonal form (5.23)

and solved using the Thomas algorithm as follows:

$$\begin{bmatrix} b_i & c_i & & & 0 \\ a_{i+1} & b_{i+1} & c_{i+1} & & \\ & a_{i+2} & b_{i+2} & \ddots & \\ & & \ddots & \ddots & c_{\text{imax}-1} \\ 0 & & & a_{\text{imax}} & b_{\text{imax}} \end{bmatrix} \begin{bmatrix} S_i^{n+1} \\ S_{i+1}^{n+1} \\ S_{i+2}^{n+1} \\ : \\ S_{\text{imax}}^{n+1} \end{bmatrix} = \begin{bmatrix} d_i + a_i S_{i-1}^{n+1} \\ d_{i+1} \\ d_{i+2} \\ : \\ d_{\text{imax}} - c_{\text{imax}} S_{\text{imax}+1}^{n+1} \end{bmatrix} \tag{5.23}$$

where the recursion coefficients in the tri-diagonal matrix are:

$$a_i = -\frac{\theta Q_{i-\frac{1}{2}}^{n+1}}{X_{i+1} - X_{i-1}} - \frac{2\theta \left(AD_l\right)_{i-\frac{1}{2}}^{n+1}}{\left(X_{i+1} - X_{i-1}\right)\left(X_i - X_{i-1}\right)}$$

$$b_i = \frac{A_i^{n+1}}{\Delta t} + \frac{\theta\left(Q_{i+\frac{1}{2}}^{n+1} - Q_{i-\frac{1}{2}}^{n+1}\right)}{X_{i+1} - X_{i-1}} + \frac{2\theta}{X_{i+1} + X_{i-1}}\left(\frac{\left(AD_l\right)_{i+\frac{1}{2}}^{n+1}}{X_{i+1} - X_i} + \frac{\left(AD_l\right)_{i-\frac{1}{2}}^{n+1}}{X_i - X_{i-1}}\right) - A_i^{n+1} {k_1}_i^{n+1}$$

$$c_i = \frac{\theta Q_{i+\frac{1}{2}}^{n+1}}{X_{i+1} - X_{i-1}} - \frac{2\theta}{X_{i+1} - X_{i-1}}\left(\frac{\left(AD_l\right)_{i+\frac{1}{2}}^{n+1}}{X_{i+1} - X_i} + \frac{\left(AD_l\right)_{i-\frac{1}{2}}^{n+1}}{X_i - X_{i-1}}\right)$$

$$\begin{aligned} d_i = & \frac{\left(AS\right)_i^n}{\Delta t} - \frac{2\left(1-\theta\right)\left(\nabla_{i+\frac{1}{2}}^n Q_{i+\frac{1}{2}}^n - \nabla_{i-\frac{1}{2}}^n Q_{i-\frac{1}{2}}^n\right)}{X_{i+1} - X_{i-1}} \\ & + \frac{2\left(1-\theta\right)}{X_{i+1} - X_{i-1}}\left[\frac{\left(AD_l\right)_{i+\frac{1}{2}}^n\left(S_{i+1}^n - S_i^n\right)}{X_{i+1} - X_i} - \frac{\left(AD_l\right)_{i-\frac{1}{2}}^n\left(S_i^n - S_{i-1}^n\right)}{X_i - X_{i-1}}\right] \\ & + \underbrace{\frac{2Q_{Li}^{n+1} S_{Li}^{n+1}}{X_{i+1} - X_{i-1}}}_{\text{source}} + \underbrace{A_i^{n+1} {k_0}_i^{n+1}}_{\text{zero order growth/decay}} \end{aligned} \tag{5.24}$$

5.3.3 Initial and boundary conditions

At the start of the simulation, the discharges are set to zero across the domain of each reach and the water surface elevations are equated to the high water level or the maximum bed elevation plus 10 cm. The open boundary condition is either a measured discharge or water surface elevation. For a closed boundary, the discharge

at the boundary can be set to zero.

Where there is a network of reaches, internal boundaries or junctions exist between the reaches. For mass conservation, it can be assumed that the sum of flows entering the junction is zero ($Q_1 + Q_2 + Q_3 = 0$). To ensure water level compatibility, it is assumed that $\eta_1 = \eta_2 = \eta_3 = \eta_{\text{junction}}$. Before the water surface elevations (η) and velocities (U) can be undertaken for each separate reach at a new time step, the flow conditions for all the junctions must first be determined. The overall flow conditions in the channel network with several junctions are the determining factor in specifying the water elevations at the junctions for the new time step. Therefore, for the solution of the tri-diagonal matrix the boundaries must be specified together with the general flow conditions in the channel network, to determine the water elevation values at the internal boundaries. This means that the whole channel network must be solved simultaneously. One of the most convenient algorithms for solving this problem is the influence line technique, described by Dailey and Harleman (1972), and which is adopted for the one-dimensional numerical code FASTER.

5.4 Discussion

Different methods for solving the adapted governing equations were reviewed in the literature as presented in Section 2.6.1 and Section 2.6.2. Numerical methods were chosen as opposed to analytical methods due to the ability of numerical methods to solve problems of irregular geometry as is the case in this research study.

Of the numerical methods, several techniques were reviewed in Section 2.6.2. Of the methods reviewed, the Finite Difference Method (FDM) was found to be one of the most tried and tested methods in industry for estuarine and coastal flows. One of the reasons for using the DIVAST and FASTER models in this research study is that they are both based on the FDM which has been shown in the literature to give good results for swallow water flows.

The discretised equations in the FDM have properties which affect the ability to obtain an acceptable approximation to the governing differential equations. These properties are known as consistency, stability and convergence. Consistency means that the discretised equations should tend to the governing differential equations to which they are related when Δt and Δx tend to zero. The stability of a numerical scheme is its ability to prevent errors from growing indefinitely (divergence), that is, to be amplified without bound, as the solver proceeds from one time step to another. Convergence means that the numerical solution tends to the exact solution at a fixed point or time as Δt and Δx tend to zero. For this research study, an implicit scheme was adopted for the hydrodynamics in the DIVAST and FASTER numerical codes. In an implicit scheme finding unknown values necessitates the solution of simultaneous equations whilst in an explicit scheme unknown values are found by expressing them directly in terms of known values. In terms of stability, explicit schemes require a very small time step to be stable. However, an implicit scheme does not converge to or diverge from the correct solution, it is unconditionally stable. It calculates the unknown values accurately by solving simultaneous equations. Therefore in this research study there was no constraint on the time step in achieving stability for the hydrodynamics solver. However a ratio of Δt to Δx^2 was specified in the literature for maintaining the level of accuracy. The hydrodynamics schemes were both second order accurate in time and space. For the DIVAST code, Equation 5.9 needed to be satisfied to maintain the level of accuracy. The time step (Δt) for the Ribble Estuary was 9 sec with a grid size of 66.67 m for the two-dimensional domain of the model. The maximum depth of the estuary was 20 m. Therefore the value of $2\Delta t\sqrt{gH\left(\frac{1}{\Delta x^2}+\frac{1}{\Delta y^2}\right)} = 2\times 9\text{sec}\sqrt{9.81ms^{-1}\times 20m\left(\frac{2}{66.67m\times 66.67m}\right)} = 3.78\sqrt{2}$ which is less than the specified limit of $4\sqrt{2}$. For the one-dimensional domain, the Courant Number $C_f = \frac{\Delta t}{\Delta x}\sqrt{gH}$ was kept less than five to maintain the required second order level of accuracy. The minimum value of Δx was 10 m in the one-dimensional domain and the mean hydraulic depth was about 2.5 m, giving a Courant Number of 4.4

which is less than five.

Several benchmarking studies have been funded by the Environment Agency (EA) and published by Hunter *et al.* (2008); Neelz and Pender (2009, 2010). These studies confirm the accuracy of the DIVAST code by comparing it with other numerical codes.

Even though the DIVAST code allowed the transport of bacterial indicators to be modelled by specifying values of decay rates. The value of the decay rates was an input parameter and was not explicitly connected to the variation of environmental factors such as salinity and solar irradiation. The effects of water temperature was modelled as a constant spatially and therefore did not account for changes in water temperature between the upstream end of the river and the beaches further downstream.

In this Chapter details of several techniques used in the numerical computation have been described. These included: details of the numerical schemes used to solve the adapted governing hydrodynamic and solute transport equations, for both the one and two-dimensional models.

Chapter 6

Development of Numerical Code

6.1 Introduction

This Chapter provides details of the modifications and refinements to the DIVAST and FASTER numerical codes used in this research study. Details of the refinements to the bio-kinematic decay process are provided in Section 6.2. In Section 6.3 details of the method adopted in dynamically linking the one-dimensional domain with the two-dimensional domain are also given. In Section 6.4, details are provided as to how the existing DIVAST code was rewritten to take advantage of parallel computing and details of the method of model calibration are given in Section 6.5. Finally, the main implications of the new modifications and refinements are discussed in Section 6.6.

6.2 Refinement of bio-kinematic representation

For modelling bacterial decay, the zero order decay term (k_0) in the finite difference Equation (5.10) was set to zero and the 1st order decay term (k_1) was defined as:

$$k_{1_{i,j}}^{n} = -\left(\underbrace{k_b}_{\text{dark decay}} + \underbrace{\beta_{\text{ext}_{i,j}}^{n} \alpha_{\text{solar}} I_0}_{\text{solar irradiation}} + \underbrace{C_{\text{sal}} S_{\text{sal}_{i,j}}^{n}}_{\text{salinity}} \right) \underbrace{\theta_{\text{wat}}^{T_{i,j}^{n}-20}}_{\text{temperature}} \tag{6.1}$$

where ${\beta_{\text{ext}}}_{i,j}^{n} = \frac{1.0-e^{-k_e H_{i,j}^n}}{k_e H_{i,j}^n}$, k_b was the dark decay rate at 20°C, C_{sal} was the salinity coefficient, ${S_{\text{sal}}}_{i,j}^{n}$ is the salinity which varies with time and position in the model, α_{solar} is the solar irradiation coefficient, I_0 is the intensity of solar radiation, k_e is the light extinction coefficient, θ_{wat} is the water temperature coefficient and $T_{i,j}^n$ is the water temperature which varies with time and position in the numerical model.

For modelling salinity, the zero order decay term (k_0) and the 1st order decay term (k_1) in Equation (5.10) were both set to zero.

For modelling water temperature, the zero order decay term (k_0) in the finite difference Equation (5.10) was defined as:

$$ {k_0}_{i,j}^{n} = \frac{KT_{\text{e}}}{\rho c_p H_{i,j}^n} \tag{6.2} $$

where T_e is the equilibrium temperature , c_p is the heat capacity of water (4186 J/kg/°C) and K is the overall heat exchange coefficient (W/m^2/°C). The 1st order decay term (k_1) was defined as:

$$ {k_1}_{i,j}^{n} = -\frac{K}{\rho c_p H_{i,j}^n} \tag{6.3} $$

6.3 Computational Linking of the Models

In this research study the 1-D FASTER model is dynamically linked to the 2-D DIVAST model. Flow and solute concentration inputs (e.g. sewers, storm outfalls, etc.) are applied to the linked model as boundary conditions to account for the effects of other models (e.g. sewer networks, rainfall, etc.).

There are several ways of linking or coupling such models. One approach is to use a simpler (1-D) model over the entire solution domain and the more complex (2-D) model in confined sub-domains (Wu, 2008). For this case the simpler model provides boundary conditions for the more complex model, but they are not fully coupled. This approach is called hybrid modelling. Another approach is to fully couple the models

by simultaneously solving all component models. Overlapping and non-overlapping interfaces can be used to couple the models (Wu, 2008). The disadvantage of overlapping interfaces is that a region with two sets of differing formulations and results (i.e. velocities and water elevations) is created. The difference between the velocities in this region can introduce uncertainty into the overall model. This research seeks to remove the overlapping interface between the models and improve the accuracy of the information transferred over the interface.

In this research study, at the interface between the 1-D and 2-D models, velocities, water elevations and solute concentrations are all exchanged after each time-step (Figure 6.1). There are other types of models in industry which solve interface conditions differently. For example, TUFLOW uses an iterative mass balance equation solver which adds 5% to 10% to simulation time.

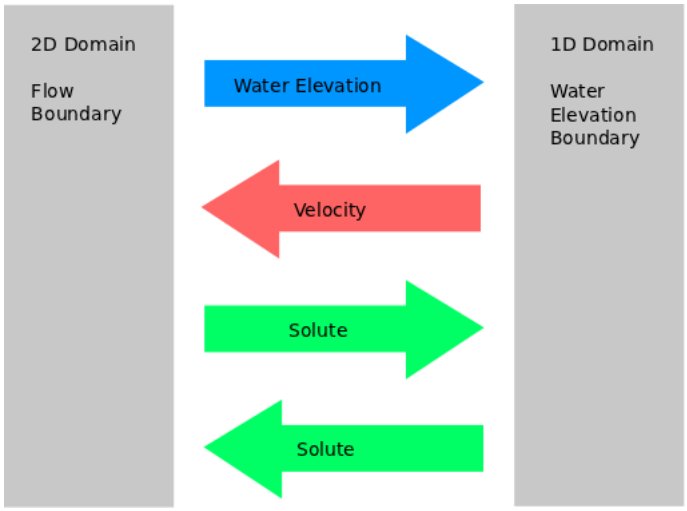

Figure 6.1: Exchange of data across 1D-2D link

The linking of 2-D models, such as DIVAST, with 1-D models has been previously done by other researchers. However, while good mass conservation has been achieved, momentum conservation is often a problem. For example, Liang *et al.* (2007) linked DIVAST with a commercial 1-D program (ISIS-1D), achieving good mass conservation. However, they commented on how better momentum transfer needed to be achieved.

In previously linked models, such as the Ribble, an overlap region existed between the 1D and 2D domains. This overlap region can be very large as compared to

the grid size of the 2D domain. The overlap is usually present to ensure numerical stability between the two domains, however, this can lead to an inconsistent problem of accuracy between the two domains (Zhou *et al.*, 2014). Figure 6.2 shows the typical configuration of the overlap region between the two domains. This research

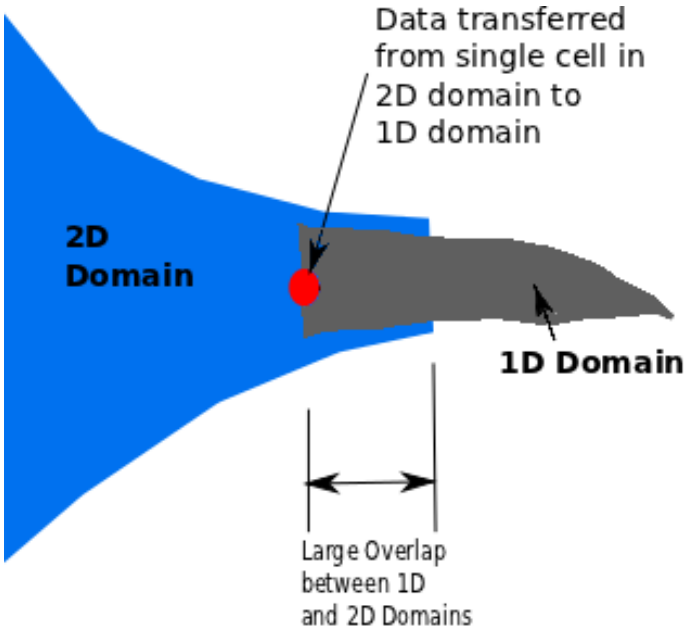

Figure 6.2: Old 2D-1D link

study proposes to remove the large overlap between the domains, whilst maintaining numerical stability between the two domains. To achieve this, the linked data (i.e. water surface elevations and solute concentrations) is transferred, not from just a single cell in the 2D domain, but from a row of cells at the linked boundary and averaged to obtain an optimum value before transferring the data into the 1D domain (Figure 6.3). This ensures better compatibility of the water surface elevations at the linked boundary and smooths out the solution at the boundary.

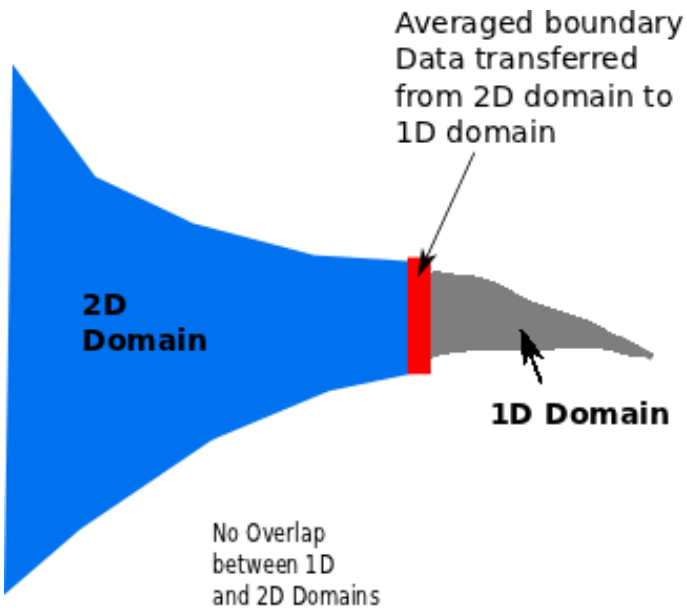

Figure 6.3: New 2D-1D link

6.4 Parallel Computing

6.4.1 Introduction

In parallel computing several tasks to be performed by the software are distributed, or shared, by several processing units so that the tasks can be performed at the same time and therefore reducing the overall runtime of the software application, as compared to a serial application. These processing units can be the Central Processing Unit (CPU) of a personal computer, a supercomputer or cores in a Graphics Processing Unit (GPU). There are several platforms for implementing parallelisation on various systems (Table 6.1), with these including open Multi-Processing (OpenMP), Compute Unified Device Architecture (CUDA) and Message Passing Interface (MPI) processes. The performance of a software application in terms of speed relies on several aspects of the hardware. These include the clock frequency or speed, data transfer or bus speed, types of memory, memory access speed, processor speed, etc. Driven by the insatiable market demand for real-time, high-definition 3D graphics, the programmable Graphic Processor Unit, or GPU, has evolved into a highly parallel, multi-threaded, many core processor, with considerable

Table 6.1: Different platforms for implementing parallelism

Hardware	Memory Architecture	Programming model
Multi-core CPU	Shared memory	OpenMP (Open Multi-Processing)
Single GPU	Shared memory	NVIDIA CUDA (Compute Unified Device Architecture)
Single GPU/CPU	Shared memory	OpenCL (Open Computing Language)
CPU Cluster	Distributed memory	MPI (Message Passing Interface)
GPU Cluster	Distributed memory	MPI + CUDA/OpenCL

computational power and very high memory bandwidths.

Most current computational fluid dynamics codes need to adopt a parallel computing approach, as single core computational performance approaches have stopped improving significantly year on year. This research study seeks to accelerate a finite difference CFD code, namely DIVAST, using the power of a CUDA-enabled GPU.

6.4.2 GPU Background

Current manufacturers of GPUs include Intel, NVIDIA and ATI. NVIDIA pioneered the use of GPUs for scientific computing. GPU development by NVIDIA started around the turn of the century, with the first programmable GPUs becoming available in 2006. A timeline of GPU development by NVIDIA is shown in Table 6.2.

This research study uses a Fermi Architecture GPU, with the CUDA 5.5 version of the programming model. The main advantage of the GPU over the CPU is that it has thousands of cores (Figure 6.4), as compared to the CPU and is specifically designed for parallel computation.

However, the GPU is not designed for handling a complex logic or branching, as shown in Table 6.3. This means that a program that performs well on a single processor may not necessarily perform better on a GPU. Also, the source code for any program seeking to take advantage of parallel computing has to be designed with the GPU architecture in mind.

Table 6.2: Timeline of Nvidia GPU development

Time	Development
1999	NVIDIA Invents GPU and rolls out first release
2003	A team of researchers led by Ian Buck unveiled Brook, the first widely adopted programming model to extend C with data-parallel constructs. Using concepts such as streams, kernels and reduction operators, the Brook compiler and runtime system exposed the GPU as a general-purpose processor in a high-level language
2006 Nov	G80 Architecture GPU released (first programmable in C)
2007 Jun	CUDA 1.0 released
2008 Jun	GT200 Architecture GPU released
2008 Aug	CUDA 2.0 released
2009 Sep	Fermi Architecture GPU released (About 8X faster than GT200 Architecture)
2010 Mar	CUDA 3.0 released
2011 Apr	CUDA 4.0 released
2012 Mar	Kepler Architecture GPU released (Expected to be 3X faster than Fermi)
2012 Oct	CUDA 5.0 released
2014*	Expected release of Maxwell Architecture GPU (Expected to be a combined CPU and GPU)
2016*	Expected release of Volta Architecture GPU

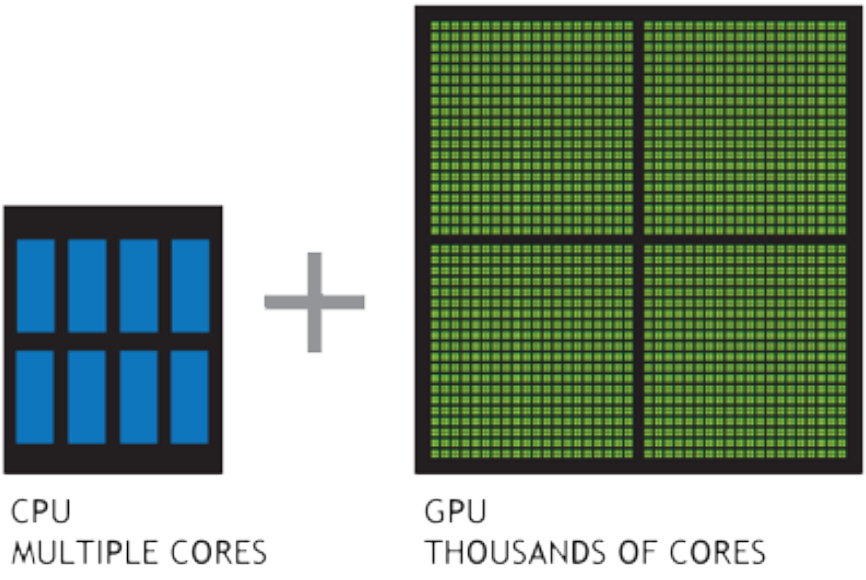

Figure 6.4: Number of Cores (NVIDIA, 2011b)

Table 6.3: Comparison CPU with GPU Architecture

	CPU	GPU
Computation Type	Serial computation with complex logic or branching	Concurrent computation without branching
Memory Access	Contiguous memory access	Scattered memory access
Memory Transfers	CPU to RAM or Hard Disk	Additional memory transfers between CPU and GPU required
Number of Cores	2-8	16-1536

6.4.3 Hardware

Using a GPU for scientific calculations involves heterogeneous computing. That is, both the CPU and GPU are used together. The CPU device is referred to as the host and the GPU as the device. The program is started on the CPU and the data are then transferred to the GPU device to be computed. The specification of the GPU device used in this research study is given in Table 6.4. After computation on the GPU, the results are returned back to the CPU and then written to the hard disk if required. This means that the speed of transfer of memory from the CPU to the GPU device is a factor that can affect performance. Therefore, minimising the number of data transfers during computation can improve performance. Table 6.5 highlights the memory bandwidths of the Quadro 4000 GPU used in this study. The Quadro 4000 graphics card cost about £600 in 2010. With about 256 cores

Table 6.4: Graphics Card Specification

	Quadro 4000
Driver Version	4.0
Compute Capability	2.0
Total Global Memory	2047MB
Constant memory	66kB
Shared memory per block	16kB
Registers per block	32kB
Number of Cores	256
(Multiprocessors X Cores/MP)	(8x64)
Threads per block	1024
Concurrent Kernel execution	Yes

in the GPU, it has a very low cost per processing unit, compared to CPU clusters

with the same number of processing units. The GPU has different types of memory, each of a different size and access level. The global memory is the largest, with 2 Gigabytes (GB) of memory for the Quadro 4000. With 2 GB of global memory, the DIVAST program is expected to solve a maximum domain size of about 4 million cells. However, the global memory has the slowest access level for the GPU device. Registers and shared memory have faster access levels, but are much smaller in size. Constant memory is designed for read only variables and is suitable for variables that do not change during every time step. However, the available constant memory on the GPU is limited.

Table 6.5: Memory Bandwidth for Quadro 4000 GPU

Type of Memory		Bandwidth (GB/sec)
Paged Memory	Host to Device	4.8
	Device to Host	4.6
	Device to Device	48.4
Pinned Memory	Host to Device	6.3
	Device to Host	6.2
	Device to Device	48.4

Two different desktop computers were used in this study (Table 6.6). Both computers had Intel® processors with four (4 No) cores, a Random Access Memory (RAM) capacity of 3.8 GigaBytes (GB) and a linux based Operating System (OS). Both computers had similar processors, but computer B had a faster memory access speed which could help it execute programs faster where lots of data access were involved.

A kernel can be defined as a function that runs on the device or GPU and a thread is the smallest sequence of programmed instructions that can be managed independently. Several threads can run concurrently in a kernel. The CUDA architecture is built around a scalable array of multi-threaded Streaming Multiprocessors (SMs). A multiprocessor is designed to execute hundreds of threads concurrently. To manage such a large amount of threads, the multiprocessor employs a unique architecture called SIMT (Single-Instruction, Multiple-Thread). The

Table 6.6: Computer system specifications

	Computer A	Computer B
Operating System (OS)	Ubuntu 12.04 (Linux)	Ubuntu 12.04 (Linux)
OS type	32-bit	32-bit
RAM Capacity	3.8GB	3.8GB
Cache Size	6MB	6MB
Memory Speed	800MHz	1333MHz
Processor Type	Intel®Core™2 Quad Q9550	Intel®Core™i5-2500
Processor Speed	2.83 GHz	3.30 GHz
No. of Cores	4	4

instructions are pipelined to leverage instruction-level parallelism within a single thread, as well as thread-level parallelisation being extensive, with simultaneous hardware multi-threading. Unlike CPU cores, they are issued in order, however, there is no branch prediction and no speculative execution with these multi-processors (NVIDIA, 2011b).

6.4.4 Software

6.4.4.1 Review of Old CPU Code

The original code for DIVAST was written using the Fortran 77 programming language. It consisted of three main files: the global common block defining data arrays and constants (DIVAST.CMN); the source code of the model (DIVAST.FOR) and the data input file defining the model domain and bed topography. It was written to optimise computational time on a single PC and uses very little memory. For example, the Poole model used a minimum of 64 MB memory (Falconer and Lin, 2001). The source code file was about 9000 lines long.

Common blocks used in the old DIVAST code are a Fortran specific mechanism for indirectly passing variables to procedures. The common block mechanism is a refinement of the global variables used in other programming languages, as it allows control of which procedures have access to a common block and which will not (by including or not the common statement in these procedures). Using common blocks

can shorten argument and declaration lists, but the indirect links created between different parts of the program are confusing and hard to trace, and can be a source of bugs, with some causing serious problems.

The old DIVAST code used statically declared arrays. That is, the maximum array lengths were hard coded constants in the source code. To allow efficient use of memory, programming language features, such as dynamic memory, are necessary. For larger model domains, this becomes more important.

To take full advantage of parallel computing, and to improve the ability to extend and manage the source code, it was necessary for the Fortran code to be rewritten in a later version of the Fortran language, such as Fortran 90, which has programming language features, such as: dynamic memory, derived types, etc.

To access the performance of the application, the runtime of different sections of the application code were measured. These main sections of code for the hydrodynamics are shown in Table 6.7 and for the solute transport in Table 6.8.

Table 6.7: Main sections of hydrodynamic code

No.	Section Name	Description of functions
1	HYDTIM	Total time for hydrodynamic calculations
2	HYDPRPS	Calculation of Chezy coefficients and eddy viscosity
3	HYDBND	Set of boundary and outfall velocities and/or water elevations
4	HYDMODX	Solve for flows and water elevations in x direction
5	HYDMODY	Solve for flows and water elevations in y direction
6	FLDRY	check for flooding and drying of cells
7	RESETH	reset flows and elevations for next half time step

To enable parallelism of the code, it was necessary to identify the main area of the code where most of the computational time was spent. Also, it was necessary to divide up the problem into different sections that could be solved by using different threads or processing units. For the hydrodynamics, the main area of code identified for parallelisation was HYDMODX and HYDMODY, where the tri-diagonal algorithm

Table 6.8: Main sections of solute transport code

No.	Section Name	Description of functions
1	SOLTIM	Total time for solute computations
2	SOLBND	Set boundary and outfall concentrations
3	DISPERSION	calculate dispersion coefficients
4	FACEVALS	Solve for cell face values of concentrations
5	CONCVALS	Solve for cell concentrations
6	SOLRESET	reset concentrations for next time step
7	SOLMISC	other miscellaneous solute calculations

was solved on each sweep of the ADI scheme. For the solute transport module, the main areas for parallelisation were FACEVALS and CONCVALS, where the face values were calculated using the ULTIMATE QUICKEST scheme, followed by the calculation of the cell concentrations.

The contiguous nature of computer memory means that two-dimensional arrays are stored as a continuous list of elements, even though each element is accessed using two indexes (typically refered to as i and j). The alternating direction nature of the hydrodynamic code meant that it was faster to iterate over the array in one direction, as compared to the other. Where the domain size was small (e.g., the Ribble model with 280,000 cells using 50 MB running on a computer with 6 MB cache), most of the array fitted into the CPU memory cache and therefore minimised the effect of the array traversal order. For very large domains, the array traversal effects was significantly amplified. Hence, the performance on a single CPU degraded rapidly with increasing domain size. One way of dealing with the array traversal order problem for a serial code was to transpose arrays so that the calculations were performed by iterating in the most efficient direction. Arrays whose values were constant over the simulation period could be transposed once, before starting the analysis. However, some arrays needed to be transposed every time step because the values held in the arrays changed for each time step. This meant that there was a time penalty for transposing the arrays.

The DIVAST code involved lots of branching in the computation due to checking

for wet or dry cells and executing other algorithms. Lots of branching can reduce the amount of speed up that parallelisation could achieve on the GPU.

6.4.4.2 Development of GPU Code

In this research study, the CPU DIVAST code was updated for the Fortran 2003 programming language. The update involved introducing dynamic data allocation and object oriented programming language features (i.e derived types). The existing code was reorganised for easier management. This included breaking big subroutines down into several smaller functions, splitting up the source file into several files, using comma separated value (csv) file format for data input and using derived types to group variables.

Applications written in C and C^{++}could use the C runtime for CUDA directly. Applications written in other languages could access the runtime via native method bindings. For this research study, the C/C^{++}language was used to access CUDA directly.

The main challenges dealt with, whilst developing the GPU version of the code included: the need to work with linear memory and calculate indexes for multi-dimensional arrays; reducing the amount of branching in the code; reducing the number of memory transfers between the device and host; debugging parallel code; and fully optimising the code.

A mixed language programming model was adopted. This involved combining Fortran and C/C^{++}code together. This allowed the transferring of code from the Fortran language to C/C^{++}in stages, testing for accuracy and errors at each stage, until all the code was in C/C^{++}. Also, in the C/C^{++}version, the functions were tested against the Fortran versions to ensure that the same results were achieved from both versions.

Since the CUDA programming model only works with linear memory, the C/C^{++}version of the code had to be designed for linear memory. This meant

that array indexes had to be calculated for multidimensional arrays. Debugging the application when it was running in parallel could be difficult. Therefore, a full C/C^{++}CPU version of the code was developed. This allowed most of the functions and subroutines to be debugged and tested in serial mode, instead of in parallel mode. The tested functions and subroutines were then reused in the GPU version of the code. The GPU version of the code was then tested with very minimal debugging.

To improve the runtime performance, the GPU version of the code was designed to minimise data transfers between the device and the host. This meant running all the computations in parallel on the GPU, even if the amount of parallelisation exposed was minimal. Constants, such as $\Delta x, \Delta t$, which did not change at every time step were stored in constant memory at the start of the simulation. The only data transfers permitted during the simulation were when the results needed to be written to file. The writing of data to file took place on the CPU whilst the calculations were done on the GPU. To further improve performance, OpenMP was used to run the two processes concurrently, performing tasks on the host (CPU) while the device (GPU) was busy performing calculations.

Full optimisation of the code for the GPU was not achieved because of time constraints. CUDA features such as shared memory were found not to improve performance of the GPU for the DIVAST code.

In summary, a new version of the DIVAST code has been developed which can be run in two modes, CPU mode or GPU mode. This version is organised into several files and consists of about 20,000 lines of C/C^{++}code. The GPU mode was developed using the CUDA C application programming interface (API) and can only run on GPUs developed by NVIDIA. Revised input data file formats, based on csv, are used in the new version of DIVAST. With the parallel capability of the GPUs, CFD models can be run much faster. This new version is later applied to the Ribble and Thames estuaries in this research study.

6.5 Calibration

Calibration refers to making adjustments to the input data, or parameters, so as to get the best agreement between the predicted and the measured values. Adjustments to the input data or parameters are usually made within a range of feasible values. In this research study, calibration was done in terms of different sets of input data, including the Manning's number for calibrating the hydrodynamics, the dispersion coefficient, water temperature, salinity and solar and light extinction coefficients for the solute transport simulations. Where there is some uncertainty in the initial input values, calibration can help improve the accuracy of the predicted results. For example, if it estimated that the actual salinity at the seaward boundary is between 35 ppt and 38 ppt, it is desirable to test the model with values of salinity within the range (35 ppt to 38 ppt) so as to get an idea of the model sensitivity to this parameter and potentially acquire more accurate results.

The basic approach in calibration is usually the same: an objective, or a merit function, is designed to measure the agreement between the measured data and a numerical model outcome for a particular choice of the coefficient set. In this research study, for the hydrodynamics, the objective function [given in Eq. (6.4)] was based on the sum of the mean absolute error (MAE) of the water surface elevations, and the squared velocities:

$$f_{\text{err}} = \frac{1}{n}\sum_{i=1}^{n}|\eta_{i,\text{pred}} - \eta_{i,\text{mea}}| + \frac{1}{2gn}\sum_{i=1}^{n}\left|U^2_{i,\text{pred}} - U^2_{i,\text{mea}}\right| \tag{6.4}$$

where the subscript "pred" refers to the predicted value and "mea" refers to the measured value. For the solute transport simulations, the objective function (6.5) was based on the MAE of the log transformed solute concentrations, giving:

$$f_{\text{err}} = \frac{1}{n}\sum_{i=1}^{n}\left|\log_{10} S_{i,\text{pred}} - \log_{10} S_{i,\text{mea}}\right| \tag{6.5}$$

The calibration was done by selecting different values of input data, or parameters, within a given feasible range and minimising the objective function. For some types of calibration, the search space for selecting different values could be large, leading to very long run times. Hence, in industry there are different methods for selecting the differing values. These include genetic algorithms, Bayesian models, simulated annealing, etc. Ostfeld and Salomons (2005) presented a calibration model for CE-QUAL-W2 using a genetic algorithm. However, even though search methods like genetic algorithms can obtain a good solution, they may not be tested for every value in the search space. In this research study, for simplicity, the search space was reduced by testing for a predefined number of values within the feasible range, typically about 5 to 10 values.

6.6 Discussion

The revised numerical code used in this study, allows the modelling of bathing water quality to a higher accuracy by introducing several new capabilities previously not present in the original code. First all, simulations can be run very much faster on the GPU, enabling more solutes to be simulated. Secondly, the decay rate is now a dynamic value which changes in space and time. The decay rate now includes the effects of water temperature, salinity, solar irradiation and turbidity. These effects also vary in space and time due to the simulation of temperature and salinity as solutes in the model. This will enable studies to be carried out now which were not feasible before. It will also contribute to development of water quality models in commercial codes. As currently, most commercial codes do not have this kind of water quality representation.

The reduced overlap at the linked interface prevents the inconsistent problem of having differing velocities in the same region of the model. Therefore the transport of bacterial indicators does not have solutes travelling at different velocities in the overlapped region of the domain. This is expected to improve the accuracy of velocity predictions.

Development of the GPU version of the code was not an easy task. It required lots of time and effort. The main development effort took about 6 months. This is mainly because its new technology. It is envisaged that in future the development of GPU code will be much more straightforward as the framework for writing and debugging the GPU code is improved. However, the knowledge gained in this research study, as to the performance of differing algorithms on the GPU can help in decision making of which numerical algorithms will benefit from GPU acceleration. It can also help in developing new algorithms for parallel computing. Most algorithms in industry have been developed to be optimal for serial computing and may not necessarily be optimal for parallel computing. It is envisaged that most future numerical codes will be parallel and therefore understanding the requirements of parallel computing is

important in the development of future algorithms.

The method calibration adopted in this study, allows the benefits of the faster code to be harnessed to automatically runs differing variations of an input parameter to determine the best fit value. The objective function used combines errors in water elevations and velocities in terms of the total energy. Therefore, velocity errors at high velocity are more significant than velocity errors at low velocities or near zero values. This is due to the squared velocity term in the energy equation adopted. In terms of the concentration of bacteria, the errors are based on the logarithm of the concentration errors. Hence, reduce the likelihood that the error at a single point will dominate the overall average error.

In this Chapter details of the modifications and refinements to the DIVAST AND FASTER numerical codes have been described. These included: details of the refinements to the bio-kinematic representation; details of the method adopted in dynamically linking the one and two-dimensional domain; details of how the existing DIVAST code was rewritten to take advantage of parallel computing and details of the method of model calibration.

Chapter 7

Application to the Ribble Basin

7.1 Introduction

In this chapter, new improvements in the kinematic representation of bacteria decay, model domain linking and the integrated approach to modelling developed in this research are applied to the Ribble Basin. Also, the impacts of parallelising the numerical code are presented for the Ribble Basin. In Section 7.2 a review of a previous study of the Ribble Basin is presented. A revised analysis using an integrated Cloud to Coast (C2C) approach and a refined kinematic representation of bacteria is presented in Section 7.3. In Section 7.4, the results of calibration of the Ribble Basin model are presented. The speed up of the numerical code due to GPU parallel computing is presented in Section 7.5.

7.2 Review of Previous Study

7.2.1 General

The Ribble Estuary stretches along the coast between the resorts of Southport and Lytham St Annes. Upstream of the estuary are three rivers: the River Darwen, the River Douglas and the River Ribble (Figure 7.1). The source of the Ribble is located in North Yorkshire at Ribblehead, where there is a confluence of two streams,

namely Cam Beck and Gayle Beck. The area has four main centres of population, namely: Blackpool and Lytham St Annes to the north of the estuary, Southport to the south of the estuary, and the town of Preston, which is inland and straddles the river Ribble at the tidal limit (Figure 7.1). The Ribble catchment has been chosen as

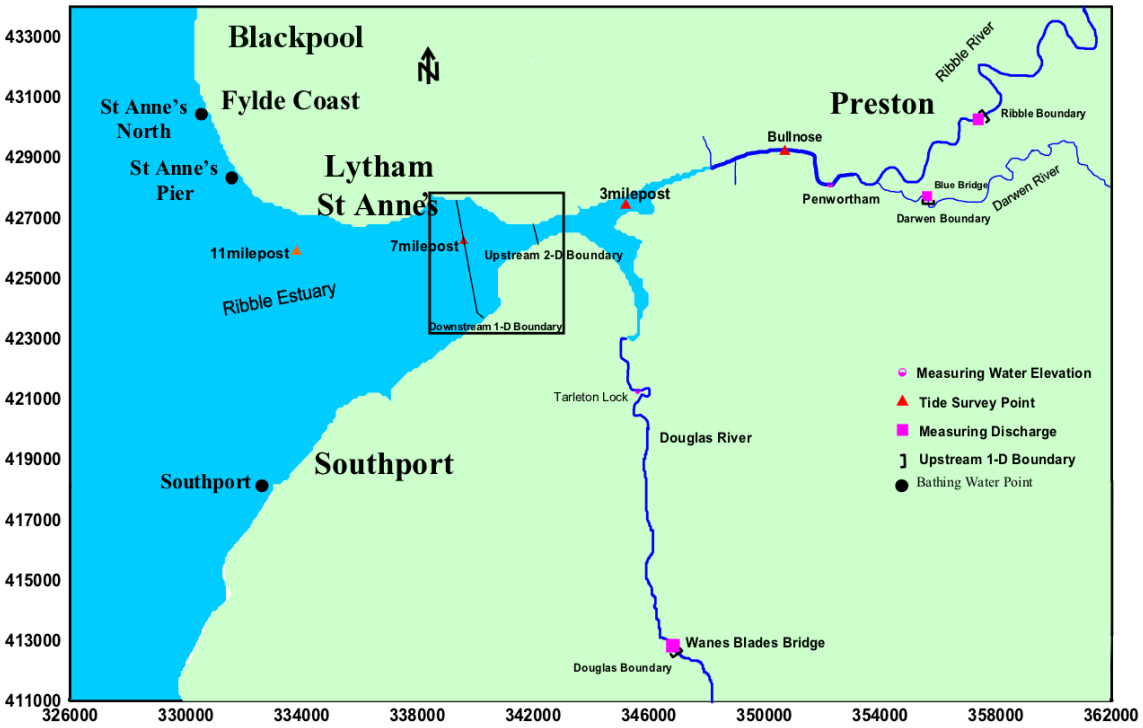

Figure 7.1: The Ribble Estuary and its tributaries

the most appropriate case study area for this investigation for the following reasons: it is the single UK research catchment for studies linked to the Water Framework Directive (WFD) implementation; it has a unique and rich resource of historical data defining past microbial source apportionment and effluent microbial quality produced by the sewerage infrastructure; considerable GIS data resources are available for the basin; and the Hydro-environmental Research Centre (HRC) at Cardiff University has hydrodynamic modelling experience within the Ribble Estuary waters and in the near-shore coastal zone around the key Fylde Coast bathing water compliance points. The tidal limit of the Ribble is 11 miles inland (above Preston). The River Ribble is home to a variety of protected species, including the Eurasian otter, Atlantic salmon and white-clawed crayfish. The mouth of the Ribble Estuary is 10 miles (16 km) wide. An average of 340,000 water birds over-winter on the Ribble Estuary, making

it the most important wetland site in Britain. The Ribble Estuary is the 7th largest estuary in the UK.

Kashefipour *et al.* (2002) carried out a comprehensive modelling study aimed at quantifying the impact of various bacterial inputs into the Ribble Estuary and surrounding coastal waters on the bathing water quality. The model used in this previous study was reviewed in this research study.

The model domain included the coastal area and the entire estuary up to the tidal limits of its tributaries (i.e. the Darwen, Douglas and Ribble). Faecal coliforms were used as the main water quality indicator organisms. The numerical model was based on dynamically linking DIVAST, for two-dimensional flow, and FASTER for one-dimensional flows. The previous model by Kashefipour *et al.* (2002) was calibrated using water level and velocity measurements from six surveys, including: a dry weather event on 3rd December 1998; a wet weather event on 10th December 1998; a wet weather event from 11th to 12th May 1999; a dry weather event from 19th to 20th May 1999; a wet weather event from 2th to 3rd June 1999; and a dry weather event from 9th to 10th June 1999. The wet weather events consist of storm events modelled using a high discharge at the upstream boundaries, whilst the dry weather events are modelled using a typical low discharge on a normal day. In reviewing the previous model in this research study, only the wet weather event from 2nd to 3rd June 1999 was used.

The previous model by Kashefipour *et al.* (2002) was reviewed in terms of an integrated systems approach in this research study. An integrated systems approach is not new; many research teams and companies have been modelling systems from the Cloud to the Coast (C2C) for many years, but in many of these instances there have been different teams or individuals working on modelling and monitoring the catchment, river, estuary and coastal basin (Falconer *et al.*, 2011; Boye *et al.*, 2013). All too often these teams have used different parameters and formulations for various processes within each sub-set of the system as a whole. When models are linked from

catchments to rivers, and particularly rivers to estuaries and coastal basins, artificial boundaries are created in a natural system where, in general, no such boundary exists in nature. When a raindrop falls from the cloud to the catchment and moves from the stream to the river, estuary and coast / sea, it does not know at any stage whether it is in the river or the estuary etc.

7.2.2 Input Data

The one-dimensional (1-D) part of the dynamic linked model was made up of five reaches, with two junctions (Figure 7.2), with a total reach length of about 40.7 km and extending up to the tidal limits. Over the whole 1D model, there were a total of

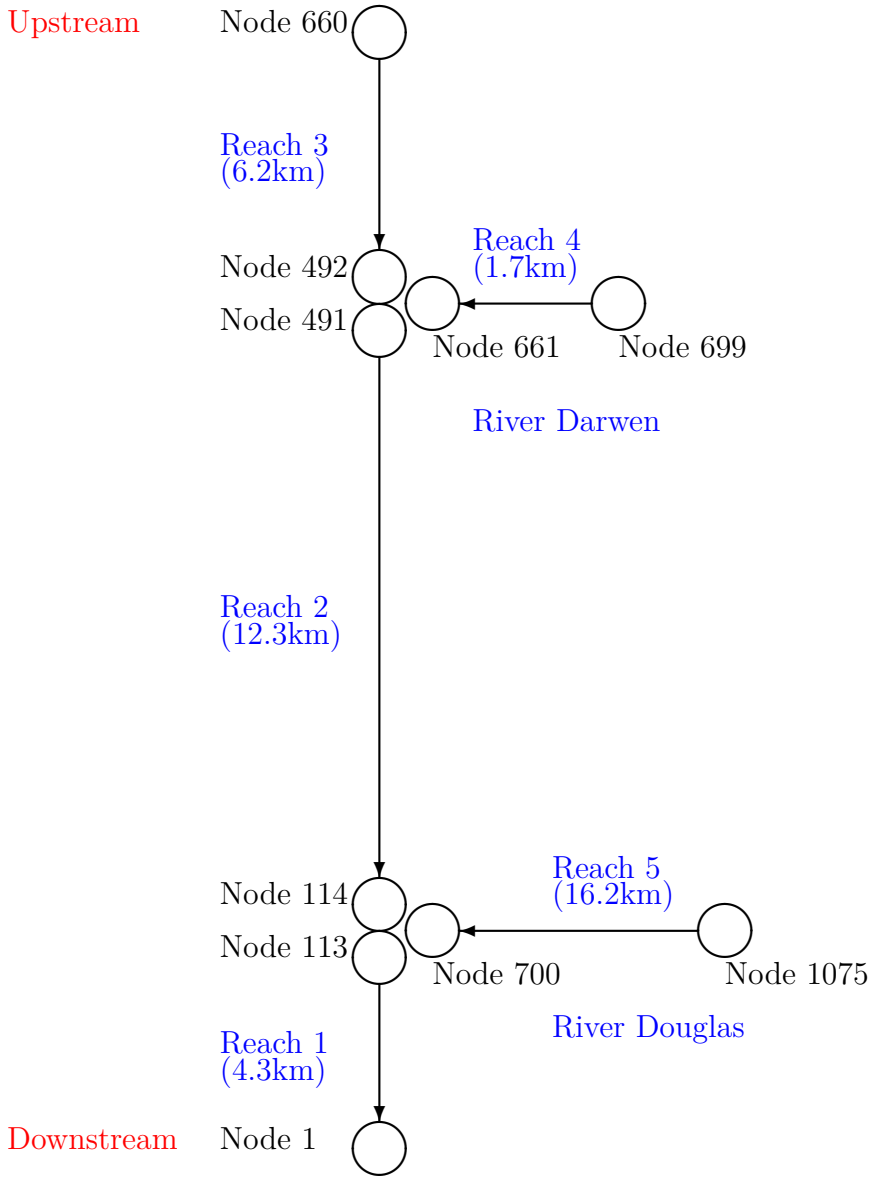

Figure 7.2: Schematic of the 1D Ribble model

1075 cross-sections with the distance between two consecutive cross-sections ranging from 10 m to 50 m. 153 of these cross-sections were provided by the Environment Agency (EA) and for a higher resolution 922 more cross-sections were created by Kashefipour (2002) using linear interpolation between the cross-sections provided by the Environment Agency (EA). The flow at the upstream boundaries were based on the data obtained for the 3rd June 1999 survey (Figure 7.3), which was a wet (Storm) event. Discharges from the Douglas and Darwen tributaries were considerably less than those of the river Ribble upstream, as shown in Figure 7.3. Discharges from 24 input sources, which included: Waste Water Treatment Works (WwTW), Combined Sewer Overflows (CSO), small rivers and storm overflows, were added to the 1D model as lateral flows. For more detailed information about the location, magnitude and variation of the discharges from these input sources, see Appendix A.2.3. The bed friction was based on the Manning's number ranging from 0.02 to 0.028.

The two-dimensional (2D) part of the dynamic linked model was represented using a mesh of 618 x 454 uniform grid squares, each with a length of 66.67 m, and giving a model size of 30 km x 41 km. A total of 5 No existing input sources were included in the 2D model, with most being intermittent and in the form of CSOs. The water surface elevations at the downstream boundary were the same as those used by Kashefipour (2002) which were based on data from the Proudman Oceanographic Laboratory (POL). The velocities in the x-direction for the northern and southern boundaries were set to zero to close all of the boundary condition requirements.

A time step of 9.0 seconds was used in both the one and two dimensional domains, with the model being run for a simulation time of 50 hr.

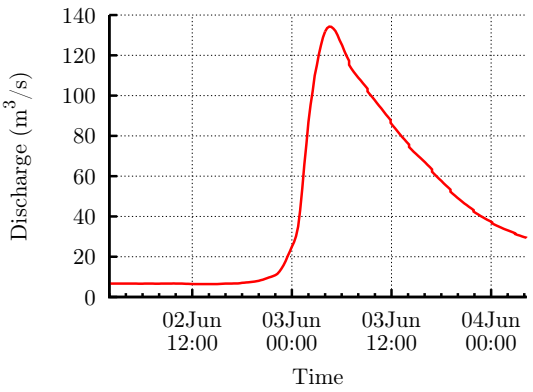

(a) River Ribble

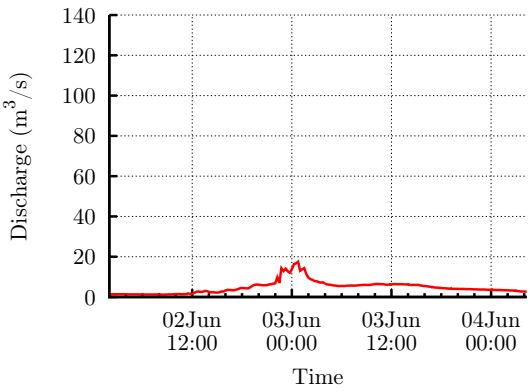

(b) River Darwen

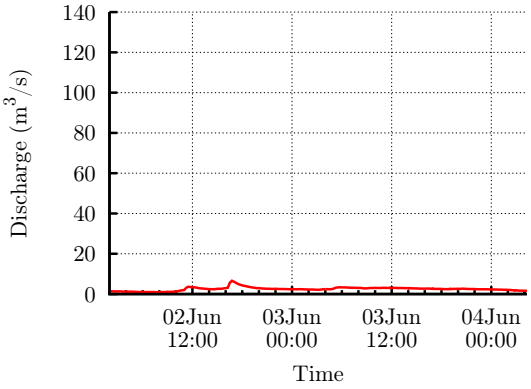

(c) River Douglas

Figure 7.3: Flow at Upstream Boundaries

7.2.3 Hydrodynamic Results of Previous Study by Kashefipour

The dynamic linked model was set up with similar conditions as that used by Kashefipour (2002). The Manning's numbers used were also similar to those for the previous study by Kashefipour (2002). The purpose of setting up this model was to establish a model similar to that used by Kashefipour (2002) for comparative studies. This was to ensure that when comparing hydrodynamic results in this research study to that of the old study (Kashefipour, 2002), any differences in results are only due to changes in parameters deliberately introduced in this study. The model was run again and a comparison of the hydrodynamic results was made with the old results (Figures 7.4 to 7.6). The results showed good agreement with the previous study for most of the survey points. At Milepost 7 (Figure 7.4), the difference between the velocities from the results of the simulations by Kashefipour

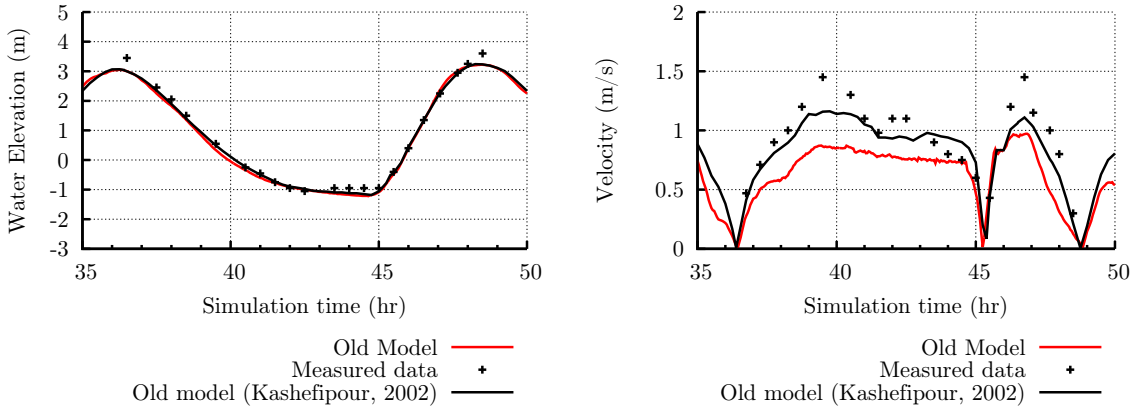

(a) Surface water elevations (b) Velocity magnitudes

Figure 7.4: Comparison of hydrodynamics at Milepost 7

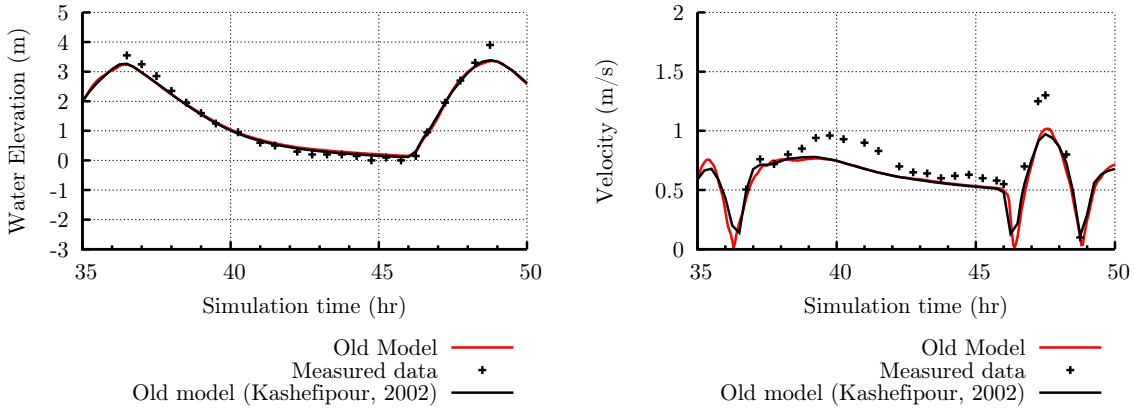

(a) Surface water elevations (b) Velocity magnitudes

Figure 7.5: Comparison of hydrodynamics at Milepost 3 (Node 160 of 1-D model)

(2002) and the similar model in this research study was the greatest. This can be attributed to several factors. First of all, running exactly the same code on two different computers can yield slightly varying results due to differences in machine architecture which can affect precision. This is often too small to be significant. Secondly, different compilers can also yield varying results especially as the old code was compiled with Fortran 77 and the revised code in this research study in being compiled with the NVIDIA compiler. This is again often a difference too small to be significant. Thirdly, the input data used by Kashefipour (2002) may be slightly different to that used in this study. It is difficult to be certain that all the input data is exactly the same as that used the previous study. This is more likely.

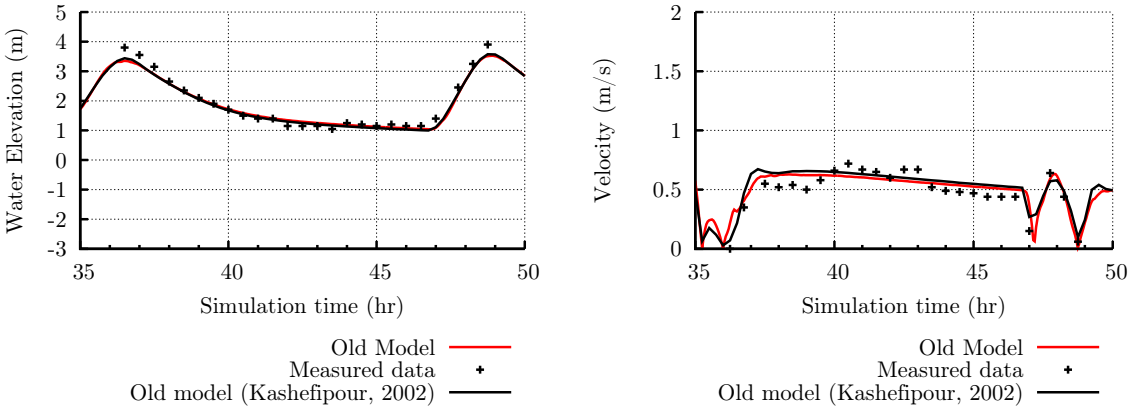

(a) Surface water elevations (b) Velocity magnitudes

Figure 7.6: Comparison of hydrodynamics at Bullnose (Node 325 of 1-D model)

The presence of some differences in the hydrodynamic results confirms the importance of creating a similar model to that of Kashefipour (2002), so that any comparison with the similar model will yield only differences due to changes of parameters introduced in this research study.

7.2.4 Solute Transport (Faecal Coliforms) results of previous study by Kashefipour

The dynamic linked model was set up with similar input and boundary faecal coliform concentrations as used by Kashefipour (2002) for the survey of 3rd June 1999. The purpose of this was part of establishing a model similar to that used by Kashefipour (2002) for comparative studies. This will ensure that when comparing faecal coliform results in this research study to that of the old study (Kashefipour, 2002), any differences in results are only due to changes in parameters deliberately introduced in this study. The predicted and measured faecal coliform concentrations were compared in Figure 7.7. The coliform concentrations are measured in the number of colony forming units (cfu) per 100 ml. It was observed that there was good agreement with the previous results by Kashefipour (2002) for most of the survey points (Figure 7.7b and Figure 7.7c). At Milepost 7 (Figure 7.7a), the difference in the faecal coliform concentration was the greatest with the similar model set up in this study closer to

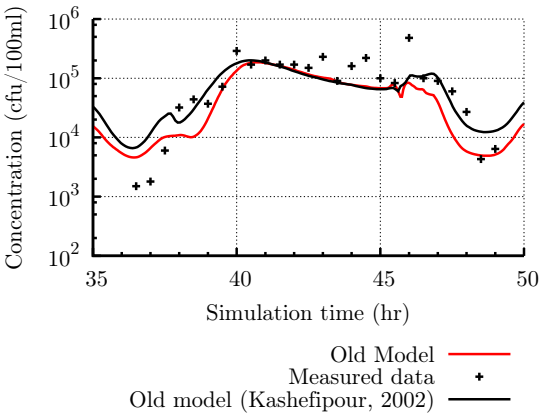

(a) Milepost 7

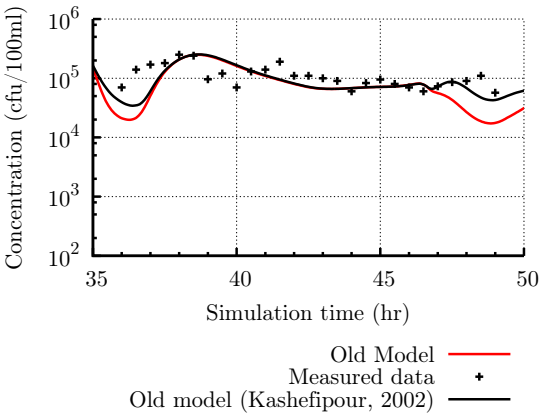

(b) Milepost 3

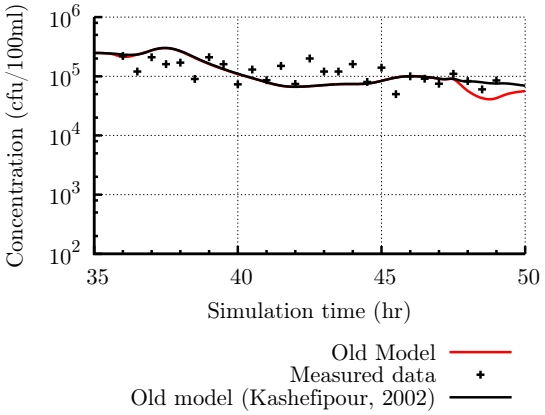

(c) Bullnose

Figure 7.7: Comparison of faecal coliform concentrations

the measured values at low concentrations.

The presence of some differences in the solute predictions further confirms the importance of creating a similar model to that of Kashefipour (2002), so that any comparison with the similar model will yield only differences due to changes of parameters introduced in this research study.

7.2.5 Overview of Previous Study by Kashefipour

The original study by Kashefipour (2002) was reviewed in the context of a Cloud to Coast (C2C) solutions approach. A number of anomalies were found with the original study and some key lessons were learnt for the future, particularly in the context of the principle that the raindrop, possibly with attached pollution (either in solution or in particulate form), does not know whether it is in a catchment, stream,

river, estuary or coastal basin. Taking account of these anomalies, the following observations were made with regard to the original studies:

(i) Different values and formulations were used for the roughness coefficient in the two-dimensional (Nikuradse equivalent sand grain roughness, k_s=20 mm [equiv. Manning's number approximately=0.208]) and one-dimensional (Manning's number n=0.021 to 0.028) domains of the linked model, when there was no physical reason for this change.

(ii) Different values of the decay rate were used in the 1-D and 2-D domains of the linked model (Table 7.1), with the decay rate being higher in the 2-D domain of the linked model in comparison with the 1-D domain. Again there was no physical justification for this change. The length of daytime was assumed to be 12 hr from sunset to sunrise.

(iii) Different values and formulations of the dispersion coefficient were used in the 1-D and 2-D domains of the linked model (Figure 7.8). An empirical formulation for rivers was used in the 1-D domain (Kashefipour and Falconer, 2002), whilst in the 2-D domain a formulation similar to that adopted by Falconer and Hartnett (1993) was used.

(iv) The same water temperature of 14°C was used in both the 1-D and 2-D domains of the linked model.

(v) The effects of salinity on the decay rate were not explicitly defined.

(vi) The effects of solar irradiation were considered in a step change manner from night to day in the decay rate.

(vii) There was a large overlap area, linking the 1-D and 2-D domains of the linked model.

In adopting a C2C solutions approach to the Ribble Estuary, the integrated Catchment to Coast model was re-run using the same formulations for the momentum

Table 7.1: Faecal Coliform Decay Rates for Old Model

		1-D domain		2-D domain	
		$k_b + k_i$	(k'_b)	$k_b + k_i$	(k'_b)
Day	decay rate (/day)	0.85	(0.645)	1.0	(0.759)
	T_{90} value (hrs)	65.0	(85.7)	55.3	(72.8)
Night	decay rate (/day)	0.5	(0.379)	0.68	(0.516)
	T_{90} value (hrs)	110.5	(145.8)	81.3	(107.1)

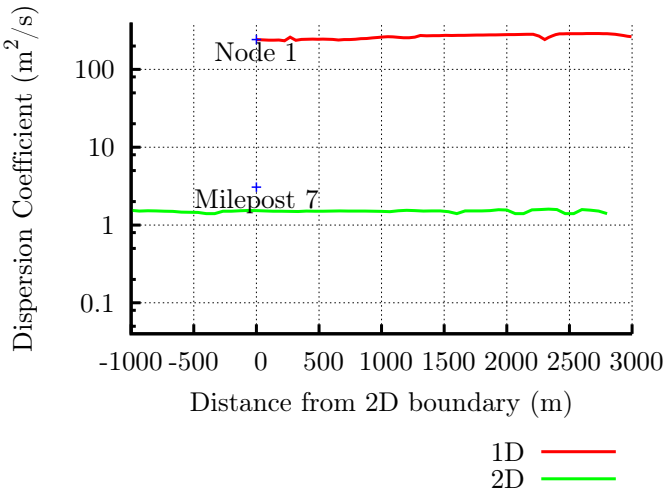

Figure 7.8: Dispersion Coefficients at 30 hr

correction coefficient, eddy diffusivity, Manning roughness coefficient, dispersion coefficients and the kinetic decay rates for bacteria along the whole river and coastal basin, with the various parameters only being changed where there were sound technical reasons for doing so. This differed from the previous study where the value of the parameter was very much based on whether the 'water package' was in the 1-D, 2-D or 3-D model domains.

7.3 Revised Analysis

7.3.1 General

In Section 7.3.2 to Section 7.3.10, differing parameters are introduced into the numerical model developed for this research study in Chapter 6, starting with input parameters similar to that by Kashefipour (2002) set up in Section 7.2.3 and Section 7.2.4. Finally, the effects of all the input parameters are considered

simultaneously in Section 7.3.11. A summary of these input parameters is given in Table 7.2.

Table 7.2: Summary of parameters used in revised analysis

	Old Model	Common Decay Rates (Section 7.3.2)	Common Dispersion (Section 7.3.4)	Improved Link (Section 7.3.5)	Common Friction (Section 7.3.6)	Water Temperature (Section 7.3.9)	Salinity (Section 7.3.10)	Solar Irradiation (Section 7.3.7)	Turbidity (Section 7.3.8)	Combined Effects (Section 7.3.11)
Night value k_b = 0.553/day (T_{90}=100 hr), Maximum Day value $k_b + k_i$ = 2.763/day (T_{90}=20 hr)		•	•	•	•	•	•	•	•	•
Use of the same dispersion formulation in both domains with k_l=90			•	•	•	•	•	•	•	•
Removal of linked boundary overlap				•	•	•	•	•	•	•
Use of Manning's N in both domains and gradual linear variation over linked boundary					•	•	•	•	•	•
18 °C at upstream boundary of 1-D domain, 14 °C at downstream boundary of 2-D domain and water temperature coefficient θ_w=1.047						•				•
0.5 ppt at upstream boundary of 1-D domain, 35 ppt at downstream boundary of 2-D domain and salinity coefficient θ_s=0.02 day^{-1} ppt^{-1}							•			•
Sinusoidal variation of irradiation with maximum of 900 W m^{-2}, day length = 12 hours and irradiation coefficient α= 2.456 day^{-1} m^2 kW^{-1}								•		•
Turbidity in the form of light extinction coefficient K_e=2.37 m^{-1}									•	•

7.3.2 Common Decay Rates

In the revised model, the T_{90} value was first set to 20 hr for daytime and 100 hr for night-time in both the 1-D and 2-D model domains (Table 7.3). The equivalent daytime rate (2.76 per day) was therefore higher than the values in the previous 'old' model by Kashefipour (2002). The equivalent night-time decay rate (0.55 per day) is lower than that in the 2-D domain of the old model.

According to Thomann and Mueller (1987), the overall decay rate for Faecal Coliform is about 37-110/day and for E. Coli about 0.08-2.0/day. The base mortality rate (k_b) in freshwater at 20°C is assumed to be 0.8/day by Chapra (2008).

A comparison of the resulting faecal coliform predictions is shown in Figure 7.9, both for the old and revised models. The results of this comparison showed that

Table 7.3: Revised Faecal Coliform Decay Rates

		$k_b + k_i$	(k'_b)
Day	decay rate (/day)	2.763	(2.097)
	T_{90} value (hrs)	20.0	(26.3)
Night	decay rate (/day)	0.553	(0.420)
	T_{90} value (hrs)	100.0	(131.6)

whilst the old model, which was calibrated for the best results in each reach, gave good agreement with the peak faecal coliform levels, the more holistic systems based approach for the C2C solutions predicted slightly lower concentration levels.

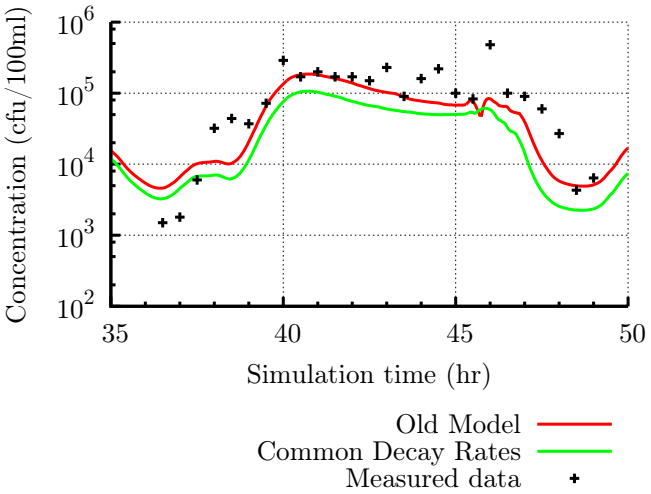

Figure 7.9: Faecal coliform levels at Milepost 7 due to common decay rates

7.3.3 Sensitivity to Decay Rates

The decay rates were also varied to establish the effect on varying decay rates on the model (Table 7.4). This was done to establish the sensitivity of the model to varying decay rates and confirm that the numerical model was behaving as expected. The results (Figure 7.10) showed that halving the decay rates increased the predicted coliform levels slightly, whilst doubling the decay rates significantly lowered the predicted concentration levels. The difference in concentration levels between the model with half the decay rates and that with twice the decay rates was larger at Milepost 11 (Figure 7.10a) than at Milepost 7 (Figure 7.10b). This further reduces

Table 7.4: Variation of Decay Rates in new models

Faecal Coliform Decay Rates	Decay rates		
	$k_b' \times \frac{1}{2}$	$k_b' \times 1$	$k_b' \times 2$
Day time Decay Rate (per day)	5.53	2.76	1.38
Equivalent Day time T_{90} value	10.0	20.0	40.0
Night time Decay Rate (per day)	1.11	0.55	0.28
Equivalent Night time T_{90} value	50.0	100.0	200.0

at Milepost 3 (Figure 7.10c) and at Bullnose (Figure 7.10d). Milepost 11 is the located furtherest downstream with the other survey points (Milepost 7, Milepost 3, Bullnose) at locations further upstream consecutively. Therefore the difference in concentration levels increases from upstream to downstream, from Bullnose through to Milepost 11. The peak concentration levels ($\approx 10^5$ cfu/100 ml) at half the common decay rate were similar over the four survey points. However, with twice the common decay rate the peak concentration levels decreased from the upstream survey points to the downstream points. Therefore, the effect of the decay rate on the model was performing as expected from theory (Equation (6.1)), with the peak concentrations being reduced further downstream. At higher decay rates less coliform was transported downstream (due to mortality of coliform) and therefore leading to the lower concentration levels in the coastal zone. The effect of varying the decay rates was higher downstream as shown in Figure 7.10. The greater the distance from the source, the higher the sensitivity of the concentration levels to the decay rate. This confirmed that an accurate estimation of the decay rate was very important for predicting the bathing water quality downstream especially at high decay rates. The results also showed that at very low decay rates, the predicted coliform concentrations were less sensitive to changes in the decay rate. Therefore, it is expected that other factors such as dispersion and advection of the coliforms will have more significant effects on concentration levels at lower decay rates, such as during night-time.

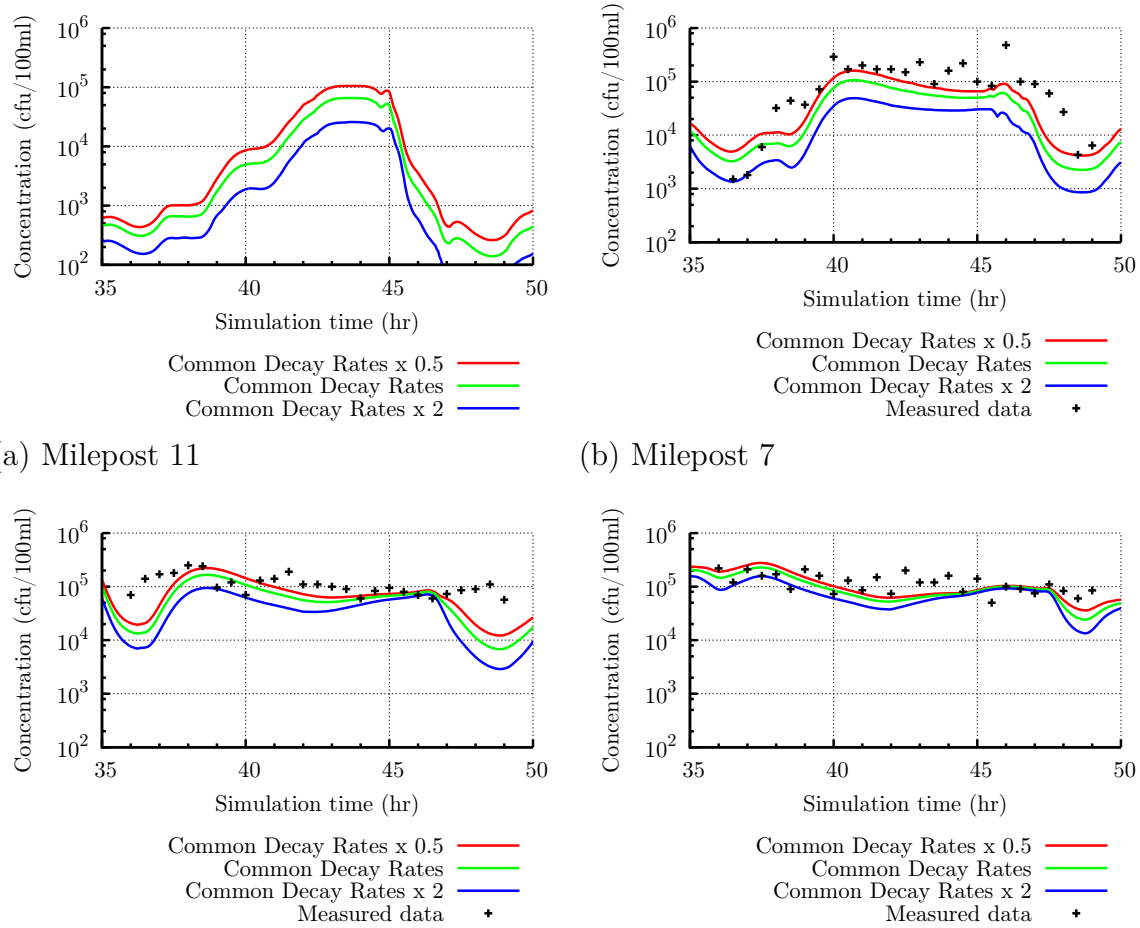

(a) Milepost 11

(b) Milepost 7

(c) Milepost 3

(d) Bullnose

Figure 7.10: Effect of varying decay rates

7.3.4 Common Longitudinal Dispersion

In the old model, there was great variation in the dispersion coefficient from the 2-D to the 1-D model. The dispersion coefficient was estimated using a different formula in the 1-D domain as compared to the 2-D domain of the model. The dispersion coefficients in the 1-D domain of the model were calculated using an empirical formula (2.16). The dispersion coefficients in the 2-D domain of the model were calculated using a formula (2.11) also adopted by Falconer and Hartnett (1993). Measured values of the dispersion constants, k_l and k_t, ranged from 8.6 to 7500 and 0.42 to 1.61 respectively, according to Fischer *et al.* (1979). In the absence of field data, Falconer *et al.* (2001) have suggested values of 13.0 and 1.2 to be used for k_l and k_t respectively. Both formulae showed that the dispersion coefficient is proportional

to the shear velocity and the depth of water as discussed in Section 2.6.3.

$$D_{xx} \propto U_* \times H \tag{7.1}$$

In the revised model, the same formula (2.11) was used to estimate the dispersion coefficients in both the 1-D and the 2-D domains of the model. This significantly reduced the magnitude difference in dispersion coefficients over the linked boundary (Figure 7.11).

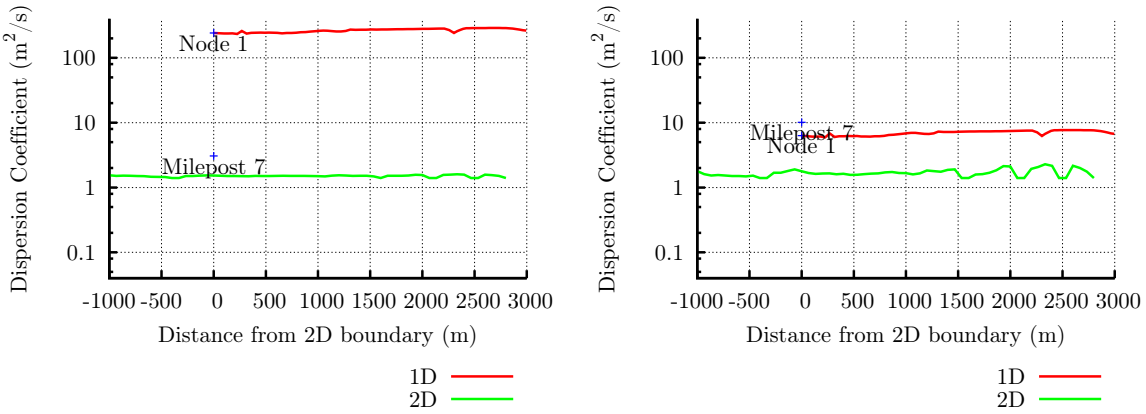

(a) old model (b) new model

Figure 7.11: Comparison of dispersion coefficients at 30 hr

The value of the longitudinal dispersion constant, k_l (identified as the variable 'GAMMA' in the source code), was set at 90 in both domains of the model. This ensured that the dispersion coefficients were higher in the 1-D domain of the model whilst maintaining lower dispersion coefficients in the 2-D domain and removing the large change in dispersion coefficients at the linked boundary. The value of the longitudinal dispersion constant, $k_l = 90$, was higher than typical values (13.0) for coastal domains and lower than typical values (8.6-7500) for rivers. However, the value of 90 is used in this research study because it allows a common value to be used in both domains whilst giving satisfactory coliform predictions. Better prediction of the lower coliform levels was achieved due to the introduction of a common longitudinal dispersion constant and dispersion formulae in both domains

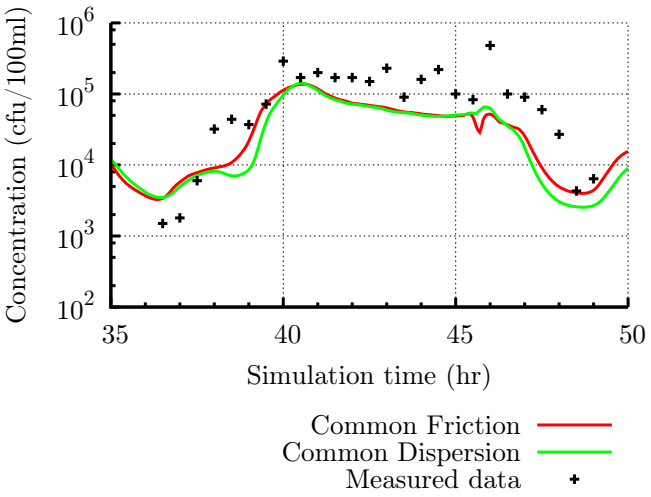

Figure 7.12: Faecal coliform levels due to common dispersion coefficients

of the model (Figure 7.12).

7.3.5 Linked Boundary Refinement

In the old model developed by Kashefipour (2002), the length of the link overlap between the 1-D and 2-D models was about 2.8 km (Figure 7.13). This overlap

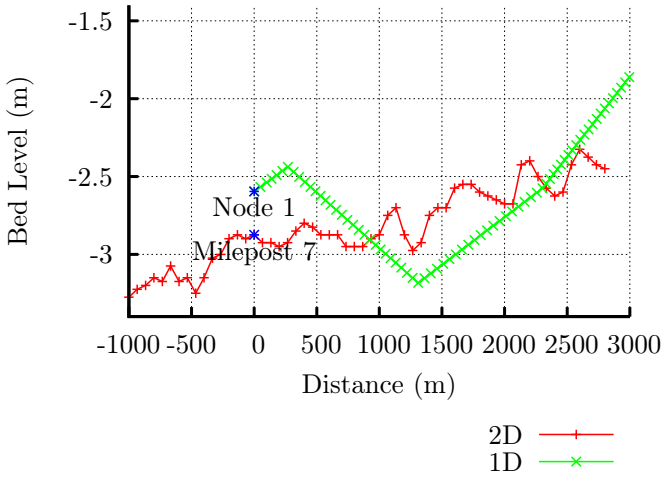

Figure 7.13: Longitudinal section through the link overlap area

length was relatively large compared to the grid size (66.67 m x 66.67 m) in the 2-D model and the distance between cross-sections (10 m to 50 m) in the 1-D model. The bathymetry varied significantly between the 1-D and 2-D domains in the overlap region (Figure 7.13. It was inferred that this difference was contributing to a poor conservation of mass and momentum over the linked overlap. Also, the agreement between cross-sections from the 1-D and 2-D models in the overlap area varied significantly (Figure 7.14). The linear nature of the variation of the minimum bed

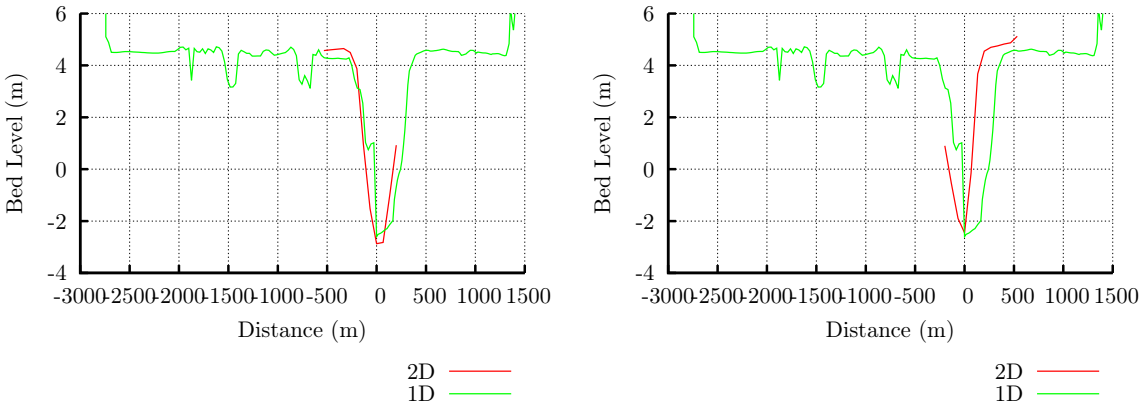

(a) 2-D end of link (b) 1-D end of link

Figure 7.14: Cross-sections at ends of the linked area

elevation with distance for the 1-D domain of the model, shown in Figure 7.14, showed that the cross-sections must have been generated using linear interpolation. This is confirmed in the thesis by Kashefipour (2002).

To improve the accuracy of continuity and momentum conservation over the linked boundary, the area of overlap therefore had to be reduced. The comparison of mass and momentum over the linked boundary for the old model are shown in Figure 7.15. In this section, the linked boundary is analysed and the effect of reducing

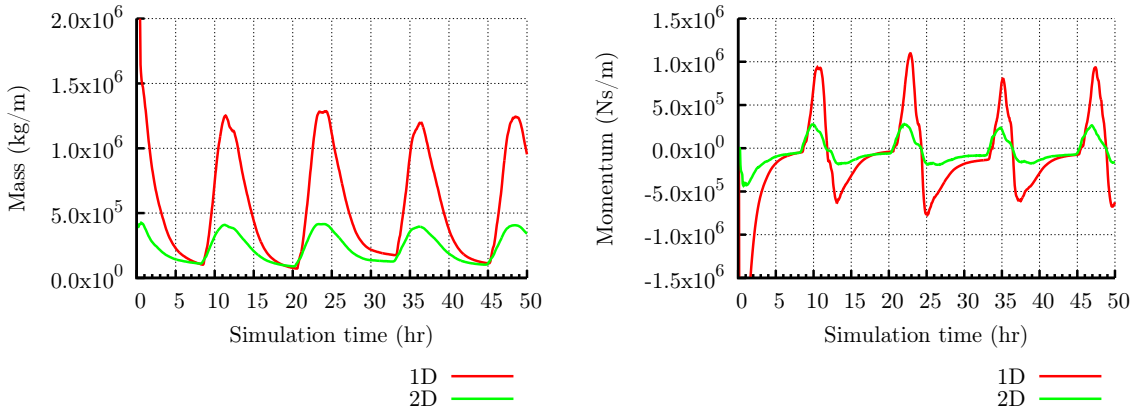

(a) Mass (b) Momentum

Figure 7.15: Comparison of conservation laws over the linked boundary

the overlap area is studied. The distance from Node 1 to Node 51 of the 1-D model was 2303 m, whilst the distance from j-index 412 to j-index 454 (2-D boundary) was 2.8 km. The implementation of the dynamic linked boundary involved transferring bed elevations (η), velocities (U) and solute concentrations (C) between the 1-D model nodes and a column of cells (i=309-320) in the 2-D model for every time step of the simulation. It was noted that the width of the 1-D model was wider than the size of a single cell in the 2-D model. The old model was revised so that the length of the linked boundary overlap was only a single cell (66.67 m) long. This was done by removing nodes 1-55 of the 1-D model, using j columns 453-454 of the 2-D model, modifying the data transfer by averaging to take into account any variation over the linked column of cells (See Table 7.5) and modifying the bed levels of the first cross-section in the 1-D domain to be the same as that of the 2-D model (Figure 7.17).

Table 7.5: Comparison of the dynamic coupling of boundary conditions

Old model			Revised model		
j column	Data exchange	Node	j column	Data exchange	Node
453	$U_i^{2D} \Longleftarrow \frac{Q^{1D}}{A^{1D}}$	51	453	$U_i^{2D} \Longleftarrow \frac{Q^{1D}}{A^{1D}}$	56
412	$\eta_i^{2D} \Longrightarrow \eta^{1D}$	1	453	$\frac{\sum^n \eta_i^{2D}}{n} \Longrightarrow \eta^{1D}$	56
412	$C_i^{2D} \Longrightarrow C^{1D}$	1	453	$\frac{\sum C_i^{2D} H_i^{2D}}{\sum H_i^{2D}} \Longrightarrow C^{1D}$	56
454	$C_i^{2D} \Longleftarrow C^{1D}$	51	454	$C_i^{2D} \Longleftarrow C^{1D}$	56

The revised geometry at the linked boundary is shown in Figures 7.16 and 7.17.

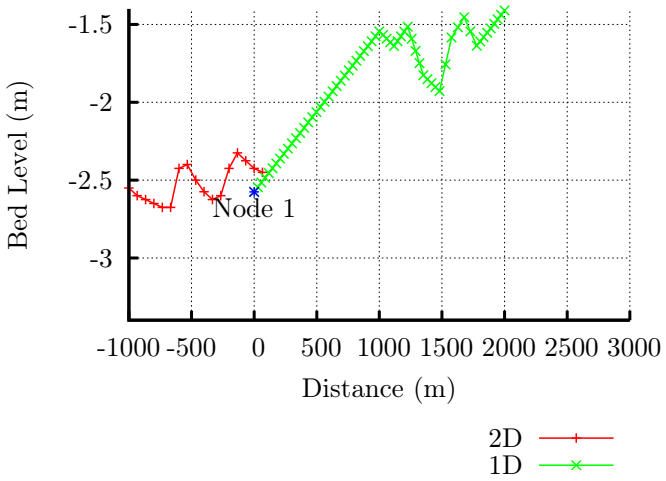

Figure 7.16: Longitudinal section through link overlap area of revised model

As a result of the changes to the linked boundary configuration, the conservation of mass was significantly improved (Figure 7.18), with only slight improvements to the momentum conservation.

The resulting effects on the surface water elevations and velocities are shown in Figures 7.19. Compared to the model without modifications at the linked boundary there were no significant changes. However, the improved boundary is expected to enhance the overall integrated model behaviour under varying conditions.

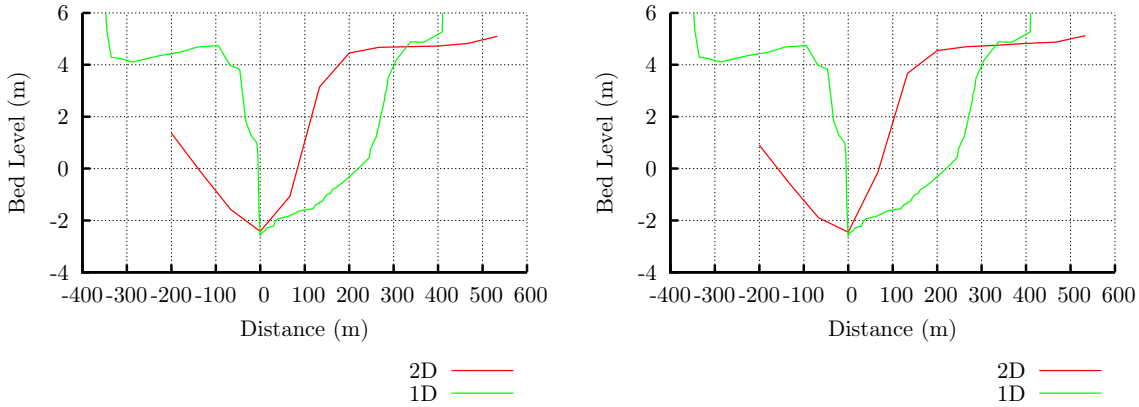

(a) 2-D end of link (b) 1-D end of link

Figure 7.17: Cross-sections at ends of the linked area of the revised model

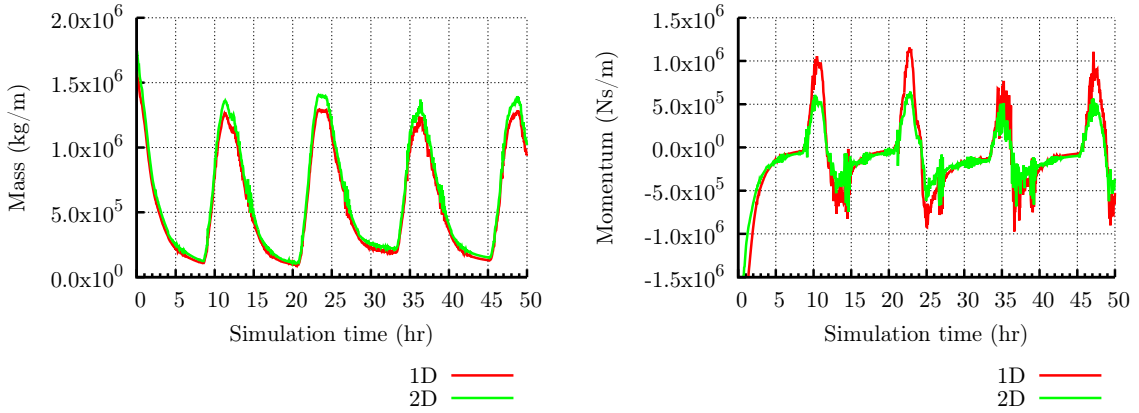

(a) Mass (b) Momentum

Figure 7.18: Comparison of conservation laws over the linked boundary

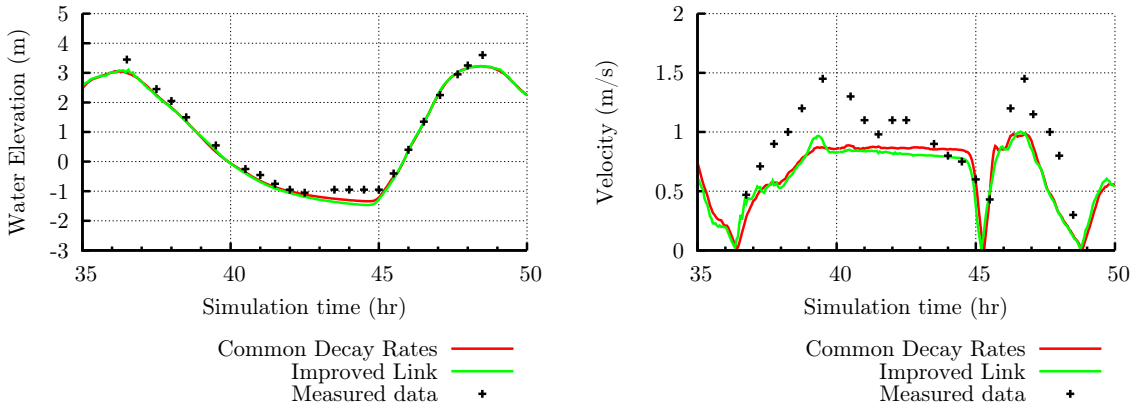

(a) Surface water elevations (b) Velocities

Figure 7.19: Water elevations and velocities at Milepost 7 due to improved linked boundary

7.3.6 Common Bed Friction

Different values and formulations of the roughness coefficient were used in the 1-D (Manning's number, $n = 0.021$ to 0.028) and 2-D (Nikuradse equivalent sand grain roughness, $k_s = 20$ mm) parts of the dynamic linked model. In the refined new model, the value of Manning's n was varied linearly over the first reach so that the bed friction varied gradually over the linked boundary. In addition, the Manning's number formulation was used to calculate the bed friction in both the 1D and 2D domains of the model.

The resulting water elevations, current speeds and faecal coliform levels were not significantly different (Figure 7.20), but were important in ensuring that any predictions are consistent with more realistic physical parameters over the linked boundary.

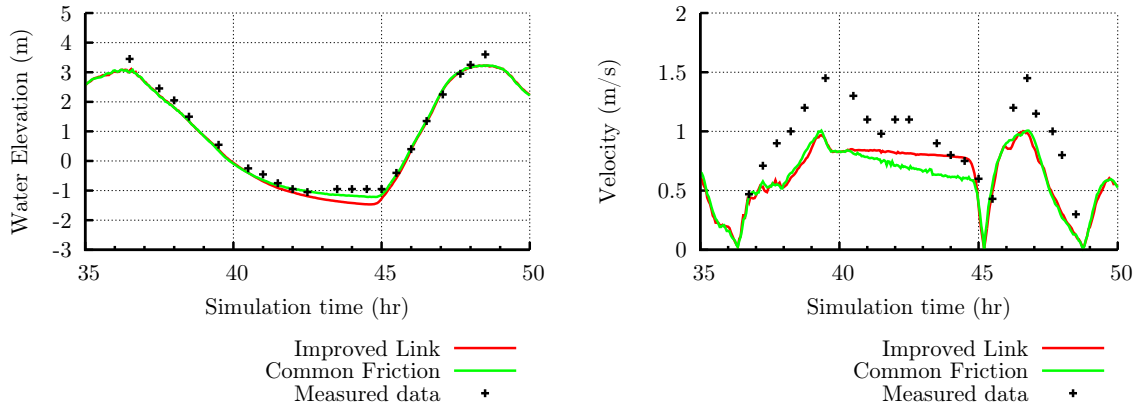

(a) Water Elevations (b) Velocities

Figure 7.20: Comparison of water elevations and velocities at Milepost 7 for the revised model

7.3.7 Solar Radiation Effects

In the old linked model, the length of daytime from sunrise to sunset was set at 12 hr and the full daylight decay rate was applied immediately at sunrise and stayed constant until sunset, when the value instantly reverted to the night-time decay rate. However, the change from total darkness to full daylight does not happen instantly

and therefore the variation in light intensity on the coliform concentration in the model needed to be refined to improve the kinematic representation of bacterial decay. Both the duration and intensity of sunshine or solar radiation varies during the day and during the year. The variation of solar radiation at a latitude of 52 °N is shown by Burgess (2009) to approximate to a sinusoidal function.

Typical values of solar radiation intensity (I_o) obtained from Clitheroe Weather Station during July 2012 had peak values of about 916 W/m^2. These data were obtained as part of the Natural Environmental Research Council (NERC) sponsored Cloud to Coast (C2C) project. This peak value is similar to that which can be inferred from Figure 2.6 by Burgess (2009) for the month of June.

A revised model was set up with a sinusoidal function representing how the light intensity varies during the day. The effects of solar radiation were modelled using the expression ($k_i = \alpha I_o$) given by Thomann and Mueller (1987) without considering the effect of turbidity (light extinction over the depth of water). The resulting variation in the effective decay rates are shown in Figure 7.21. The results in Figure 7.22 show

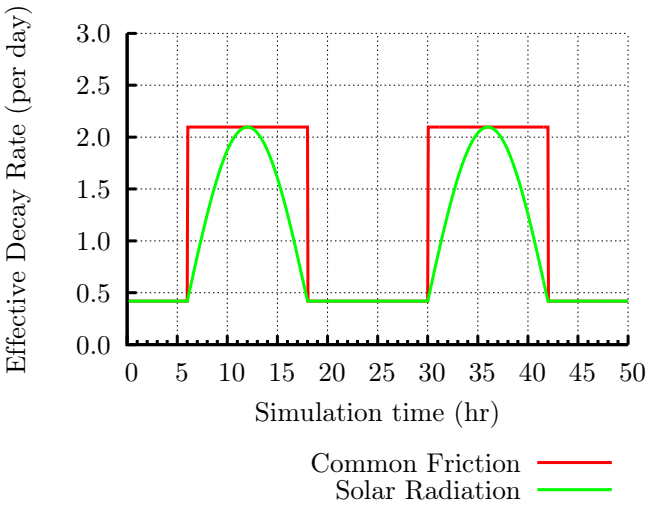

Figure 7.21: Effective decay rates (k_b') at Milepost 7

that the effects of a sinusoidal variation of day light intensity lead to a slightly higher peak concentration. It was also noted that even though the effects were small, this effect contributes to more accurate coliform concentration predictions. The scenario being modelled was a wet event in June of 1999. The length of the day (from sunrise

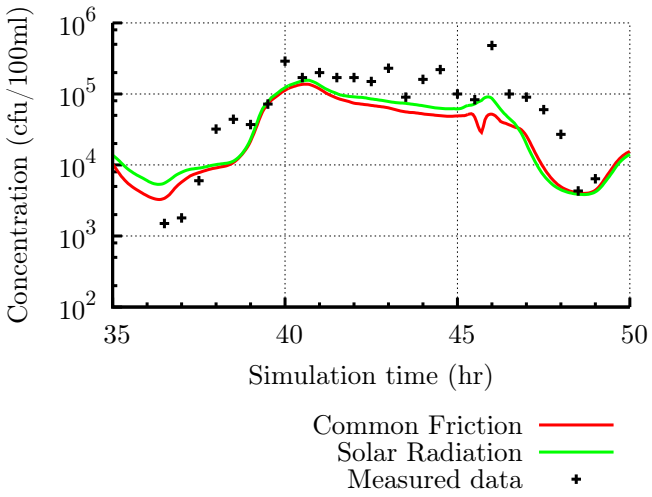

Figure 7.22: Faecal coliform levels at Milepost 7 due to solar irradiation

to sunset) in the United Kingdom (UK) is about 16 hr for the month of June. In spring and autumn, the length of the day is about 12 hr. Whilst in the winter, this reduces to about 8 hr.

7.3.8 Turbidity Effects

According to Burton *et al.* (1995), observations of the Ribble revealed the existence of a turbidity maximum between the head of the estuary at Penwortham and the Ribble/Douglas confluence. Burton (1994) observed substantial storage of intertidal mud during neap tidal periods within the upper estuary. In a recent survey of the Ribble Estuary, an average turbidity of 40.97 ntu was observed with a peak value of 958 ntu. The empirical formula (Equation (2.24)) by Oliver *et al.* (1999) was applied to give an estimated average light extinction coefficient of 2.37 m^{-1}. The effects of turbidity were assessed in this research study by introducing a light extinction coefficient (k_e) of 2.37 m^{-1} in the model. This was done without inclusion of the sinusoidal variation of solar radiation so that the effects of turbidity could be assessed in isolation. The effective decay rates due to the applied light extinction coefficient are shown in Figure 7.23. The same light extinction coefficient was applied at all locations in the model. With the availability of more data, the light extinction coefficient could be varied with location in future models. The variation of the

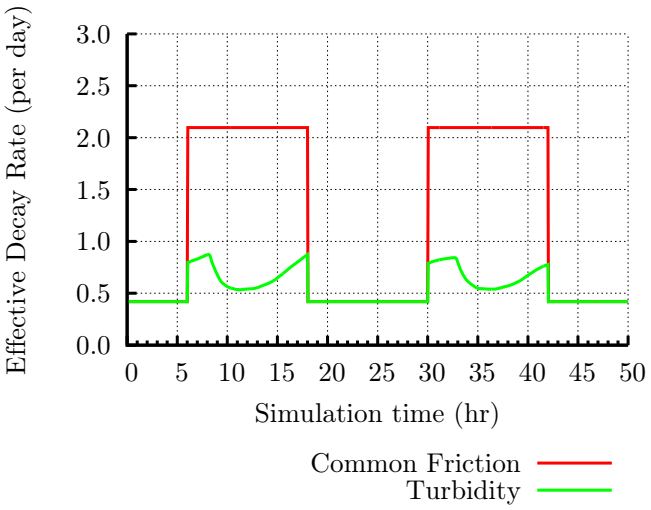

Figure 7.23: Effective Decay Rates (k_b') due to turbidity at Milepost 7

coliform concentrations due to turbidity are shown in Figure 7.24.

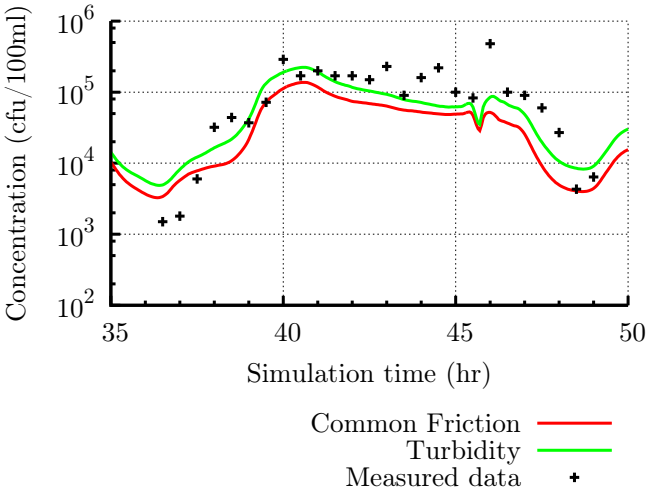

Figure 7.24: Faecal coliform levels due to turbidity

7.3.9 Temperature Effects

In this research study, the water temperature effects on the decay of bacterial fluxes were modelled considering the spatial and temporal variation of temperature. The temperature of the water upstream in the Ribble river was expected to be higher than that of the sea. This was because water from catchments (rain water) is generally warmer due to having travelled through warmer air. Also, the wetted area per mass of water is higher in a river as compared to the sea. In the previous study by Kashefipour (2002), the same water temperature of 14 °C was used in both the

1-D and 2-D parts of the linked model. The event being modelled took place in June 1999. Therefore, it was expected that river temperatures would be higher as compared to the rest of the year.

To evaluate the effects of a higher temperature in the 1-D part of the dynamic linked model, a revised model was set up with a water temperature of 18 °C at the upstream boundary of the 1-D model domain. A water temperature of 14 °C was assumed at the downstream boundary of 2-D model domain. For this case study the equilibrium temperature (T_e) was assumed to be 14 °C, considering that the simulation event occurred in June 1999.

The water temperature was modelled as a solute using a simplified heat balance equation with the source term as given by Edinger and Brady (1974) (see Section 2.7.5 of Chapter 2). The overall heat exchange coefficient K is a complicated function of the water temperature, wind speed, and other meteorological parameters such as the saturated vapour pressure (Thomann and Mueller, 1987). An estimation of the overall heat exchange coefficient was made using formulae given by Edinger and Brady (1974). Kashefipour (2002) used a wind velocity of 10 m/s in some of the scenarios studied. Adopting the same wind velocity here and using equation (2.28) gave a wind function ($f(U_w)$) value of 13.8. Assuming T_m is 14 °C in equation (2.29) gives a coefficient (β_k) of 0.7952. Substituting the wind velocity, wind function value and temperature of 14 °C into equation (2.27) gave an overall heat exchange coefficient, K, of 20.87 $W/m^2/°C$ for windy conditions. Alternatively, assuming that the wind velocity is zero and using equation (2.28) gave a wind function ($f(U_w)$) value of 9.2. Substituting the wind velocity, wind function value and a temperature of 14 °C into equation (2.27) gave an overall heat exchange coefficient, K, of 16.84 $W/m^2/°C$ for no wind conditions. Falconer (1981) assumed a heat exchange co-efficient of 30 $W/m^2/°C$ for studying the background temperature rise in Poole Harbour and Holes Bay due to a power station.

An overall heat exchange coefficient, K, value of 20.0 $W/m^2/°C$ was used for the

Ribble in this research study. The resulting variation of water temperature in the 2-D domain of the model is shown in Figure 7.25. The variation of water temperature

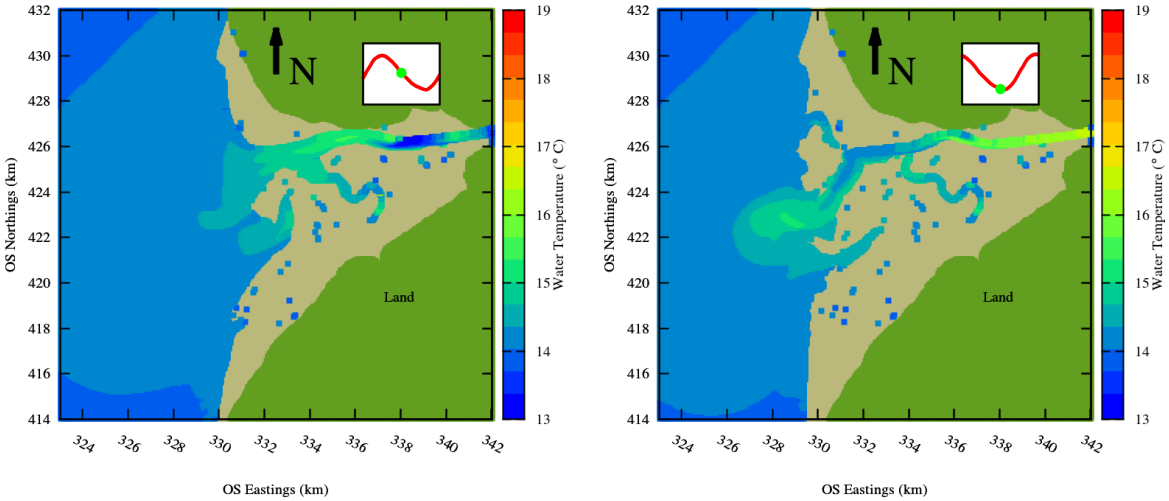

Figure 7.25: Variation of water temperature in 2-D domain of model

within in the model was affected by tides, with the river temperature dominating the values at the mouth of the river. This is more representative of the real physical conditions as compared to using one value of temperature of the two-dimensional domain of the model.

The effect of temperature on the decay rates of the bacterial fluxes was taken into account by using the formulation $k' = k\theta_w^{T-20}$ as given by Chapra (2008). The resulting faecal coliform levels due to the effects of varying water temperature on decay rates are shown in Figure 7.26. The effect of temperature was small but

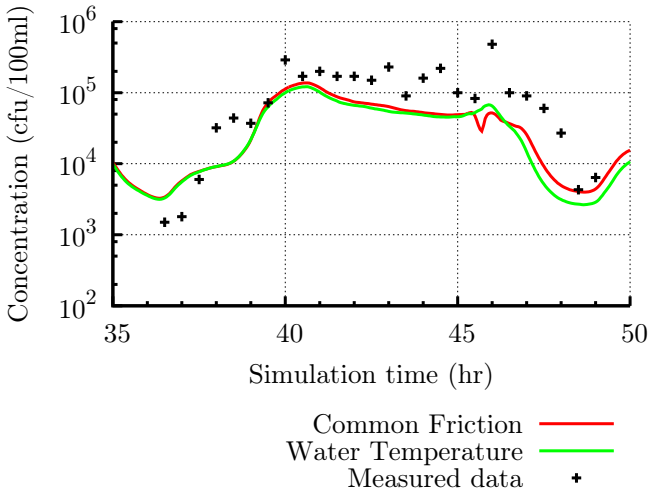

Figure 7.26: Faecal coliform levels at Milepost 7 due to a varying water temperature

important in accurately determining the peak concentrations (Figure 7.26).

7.3.10 Salinity Effects

In this section, the effect of salinity on the decay rates of faecal coliform was modelled. The salinity of freshwater and seawater were assumed to be 0.5 ppt (parts per thousand) and 35 ppt respectively. The 2-D domain of the dynamic linked model was set up with the seawater salinity as a constant solute concentration (no change with time) at the north, south and west boundaries. At the upstream boundaries for the 1-D domain of the model, the solute concentration (salinity) was set as a constant value equal to the freshwater salinity.

Modelling the salinity as a solute with zero decay rate gave the results in Figure 7.28 and 7.27 at different locations. The results show that the seawater

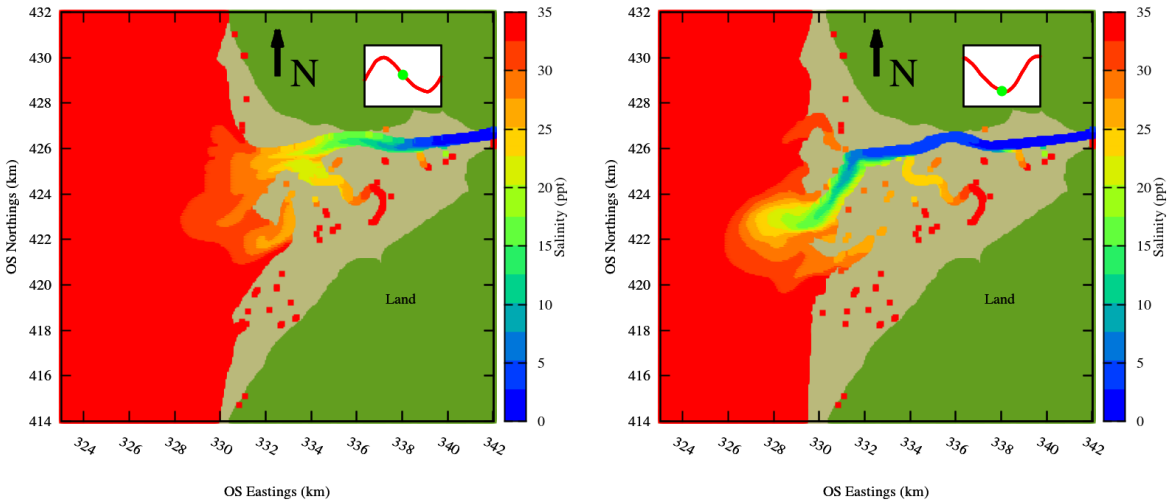

Figure 7.27: Variation of salinity in the 2-D model domain

salinity occurs at the survey points when the water is flowing in the upstream direction (tide coming in). Therefore, salinity was strongly influenced by the tides. Also, further upstream away from 11 Milepost, the effect of the seawater salinity was greatly reduced.

The effect of salinity was then linked to the decay rate of the bacteria. A linear relationship (Mancini, 1978; Thomann and Mueller, 1987; Chapra, 2008) between salinity and decay rate was used [Eq. (2.25)]. The dynamic linked model was set

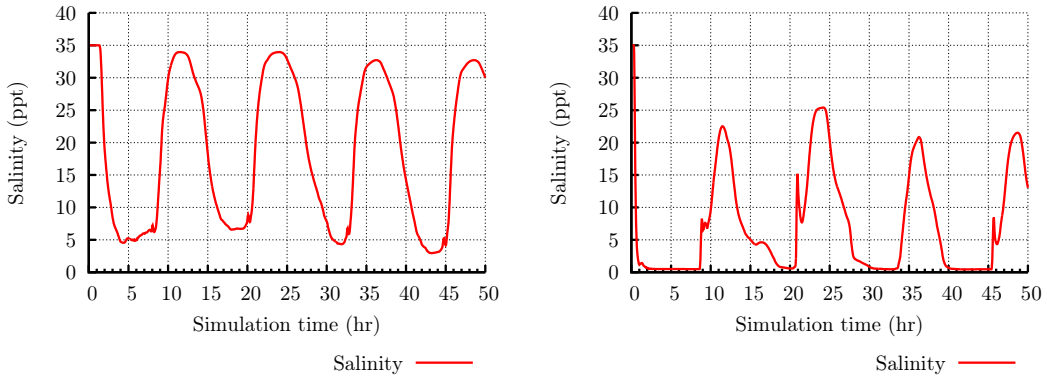

(a) Milepost 11 (b) Milepost 7

Figure 7.28: Salinity variation at two sites along the estuary

up with the salinity proportionality constant, C_{sal}, in Equation 2.25 as 0.02 d^{-1} per ppt. The resulting decay rates were increased in the day time and the night-time due to salinity as shown in Figure 7.29. It was noted that the increased decay rates

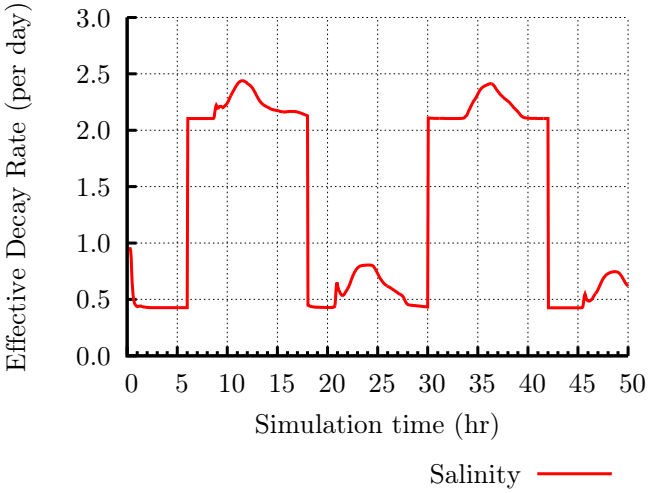

Figure 7.29: Effective decay rates at Milepost 7 due to salinity

occurred with incoming tides and only affected solute (faecal coliforms) that have already made their way downstream and were advected back upstream by the tides. The effects of salinity on the decay were higher further downstream than upstream in the river.

The resulting faecal coliform concentrations at the survey points were not greatly affected by salinity as shown in Figure 7.30. However, it was noted that there was a slight influence on the low concentrations.

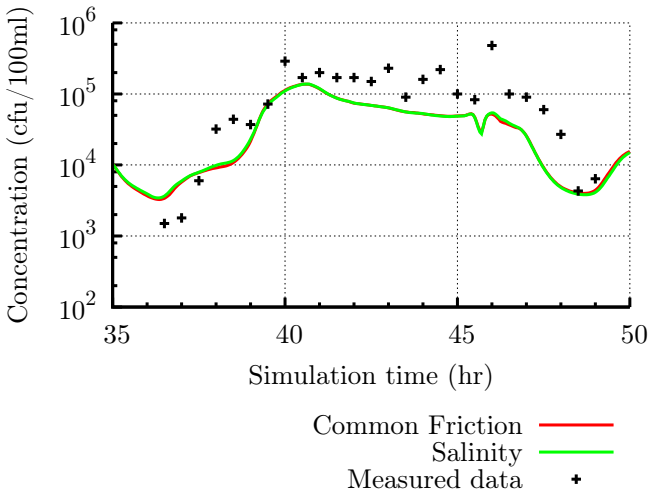

Figure 7.30: Faecal coliform levels at Milepost 7 due to salinity effects

7.3.11 Combined Effects

The model refinements in the previous sections were combined to demonstrate the overall effects of all the variables on the faecal coliform predictions in the Ribble Estuary. This section reviews these combined effects. A summary of the parameters used in the refinements of the original model are given in Table 7.2.

The parameters related to the integrated solutions approach (i.e. common decay, dispersion, friction and boundary) are applied cumulatively (Table 7.2). Then the parameters related to refinement of the bio-kinetic decay process are applied separately before finally combining all of the parameters to study the combined effects. The resulting effective decay rates of the combined model are shown in Figure 7.31.

A comparison of the differing parameter scenarios in Figure 7.32 shows that the combined model had a lower mean absolute error (MAE). The introduction of a common decay rate had a negative impact on the predicted coliform levels. However, this is due to the removal of factors which may affect the river upstream differently to the wider estuary downstream. The effects of solar radiation and turbidity had a greater positive impact on the predicted coliform levels. Therefore the accuracy of the solar radiation and turbidity parameters are important for the Ribble Estuary. Better or more data on solar radiation and turbidity can help improve the ability

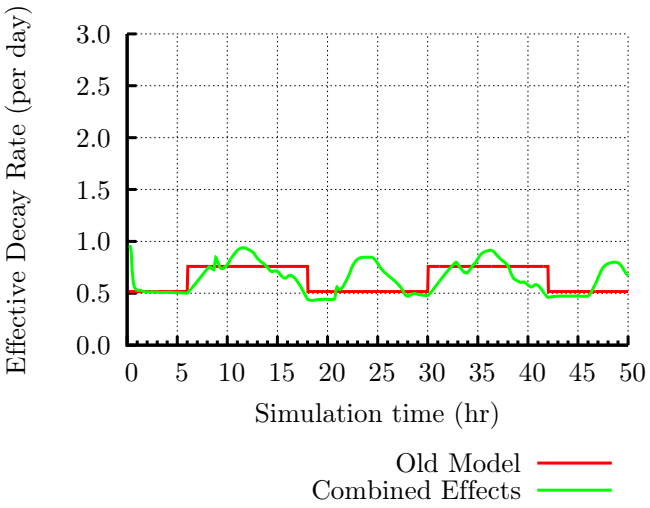

Figure 7.31: Effective Decay Rates (k_b') at Milepost 7 due to combined effects

to predict the quality of the bathing waters. In this research study, a single light extinction coefficient was applied to the estuary. Further refinement of this parameter, considering spatial and temporal variation linked to sediment transport may help further in improving the performance of future models.

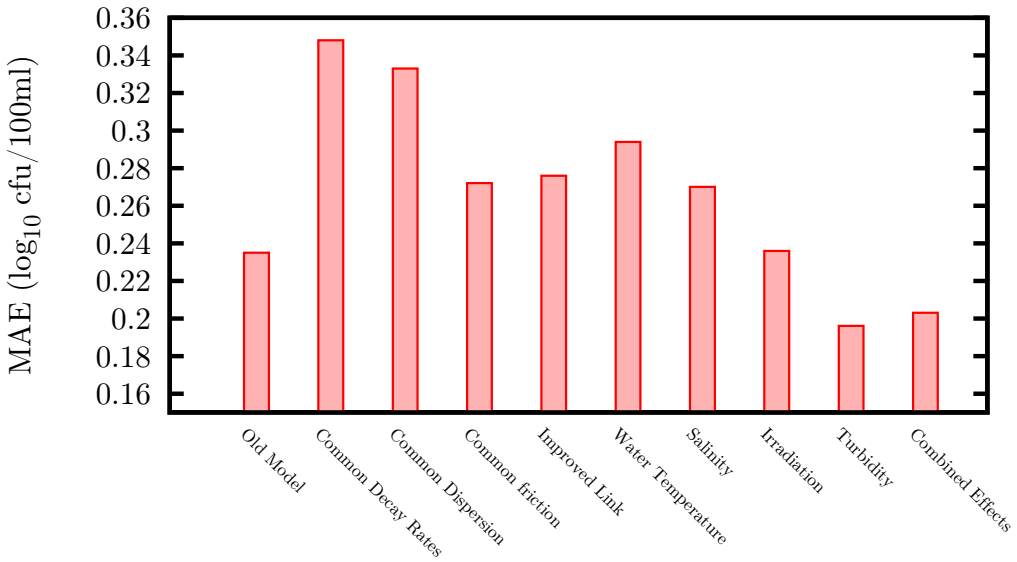

Figure 7.32: Comparison of faecal coliform mean absolute error (MAE)

Several improvements were made to the kinematic representation of the bacterial decay process in the Ribble Estuary numerical model. The main improvements to the kinematic representation of bacterial decay were:

- Decay rate variation with position in the rivers and estuary as opposed to a constant value over whole domain;
- The decay rate due to solar radiation took into account the sinusoidal variation of light intensity during the day;
- Water temperature was modelled as a solute using a heat balance equation. Water temperature also varied with position in the estuary;
- Salinity was modelled as a conservative solute taking into account variations with position between seawater and freshwater;
- Turbidity took account of the extinction coefficient and variations of the depth of water with position in the estuary; and
- Decay rates due to solar radiation were also dependent on water temperature.

The above improvements meant that there were more parameters to calibrate. However, with the implementation of model parallelisation to enable faster execution, more runs of the model could be done in order to achieve better calibration of the input parameters.

7.4 Calibration

In Section 7.3 the revised analysis of the Ribble Estuary was based on approximations of the best estimates of parameters such as the dark decay rate or the light extinction coefficient (k_e). In this Section, the model was calibrated using the method described in Section 6.5 of Chapter 6. The model was refined and improved in terms of bio-kinetic representation and an integrated approach to modelling. However, the accuracy of the predicted coliform levels was still dependent on the input parameters, with more parameters to be calibrated in the new model as compared to the old model. To further improve the accuracy of the predicted coliform levels, the model

was calibrated using a realistic range of values for each parameter. The objective function was minimised for each parameter in succession. For the Manning's number and longitudinal dispersion constant parameters, the model domain was divided into several regions with parameter being varied linearly in each region. The optimised parameter values are shown in Table 7.6. As a result of calibration, the accuracy of

Table 7.6: Optimum values of calibrated parameters

Calibration parameter		Value	Units
Manning's roughness coefficient	Downstream boundary	0.02	$m^{-\frac{1}{3}}s$
	Upstream boundary	0.03	$m^{-\frac{1}{3}}s$
Longitudinal dispersionconstant, k_l	Downstream boundary	25.8	
	Upstream boundary	128.0	
Water temperature, T	Downstream boundary	14.3	°C
	Upstream boundary	16.8	°C
Water Surface Heat Exchange Coefficient, K		29.2	W/m^2/ °C
Salinity	Downstream boundary	38.0	ppt
	Upstream boundary	0.2	ppt
Light extinction coefficient, k_e		1.567	m^{-1}
Faecal Coliform	Base decay rate, k_b	0.5396	day^{-1}
	Equivalent T_{90}	102.4	hr
	Irradiation coefficient, α	2.5e-3	day^{-1} m^2 kW^{-1}

the combined model was slightly improved as shown in Figure 7.33.

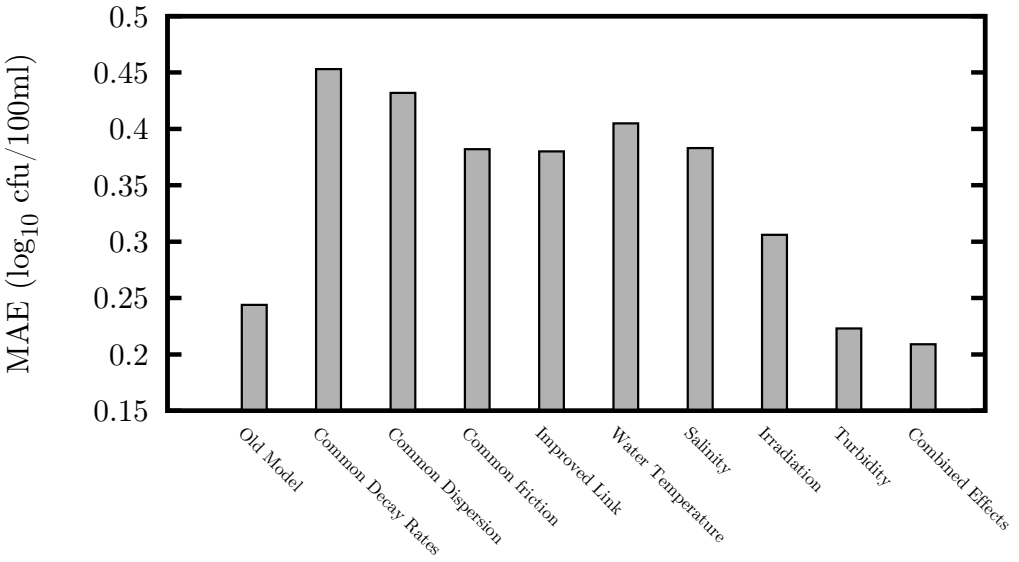

Figure 7.33: Effect of calibration on mean absolute error (MAE)

7.5 GPU Speed Up

7.5.1 Introduction

In this Section, the performance of the Ribble Estuary in terms of speed up due to parallelisation on the GPU using NVIDIA CUDA technology is discussed. The development of the GPU code was described in Section 6.4 of Chapter 6. The performance of the serial code for the Ribble Estuary model is described in Section 7.5.2. The performance of the new parallelised version of the DIVAST code is then described in Section 7.5.3.

7.5.2 Serial Application Performance

The first step of parallelisation of the DIVAST code involved profiling the application to identify potential hot spots which will benefit the most from parallelising the code. The results of the performance profiling for the Ribble Estuary model are shown in Table 7.7. These results are based on the Intel® Fortran compiler and using Computer B (Table 6.6). The results confirmed that HYDMODX and HYDMODY

were the most time intensive (hot spots), taking up about 24 % and 38 % respectively of the total run time. The total number of wet cells in the Ribble Estuary model varied with the tides. At low tide, the number of wet cells was a minimum and therefore there were less cells to be calculated. Whilst at high tide, the number of wet cells was at a maximum. It was therefore important to capture the total run time of the whole simulation time (50 hr) and not just one time step.

Table 7.7: Serial Performance of Ribble Model [a]

No.	Section Name	Time (secs)		Speed Up
		Original	Transpose [b]	
1	HYDTIM	2605	2376	1.10 x
2	HYDPRPS	282	277	1.02 x
3	HYDBND	9	9	1.00 x
4	HYDMODX	613	607	1.01 x
5	HYDMODY	982	724	1.36 x
6	FLDRY	676	642	1.05 x
7	RESETH	43	113	0.38 x

[a] Based on the Intel® Fortran compiler
[b] Arrays are transposed on each time step to avoid inefficient array tranversal due alternating direction scheme

There were 618 cells in the x-direction and 454 cells in the y-direction for the Ribble Estuary model. In the first half time step of the alternating direction scheme, the strip of cells solved with the tri-diagonal algorithm is 618 cells long. Therefore without considering the computer hardware, it will be logical to conclude that the computation time for the first half time step (HYDMODX) will be longer than that of the second half time step (HYDMODY) due to the respective number of cells in each direction. However, the timing results in Table 7.7 show that the second half time step (HYDMODY) takes longer. This is because of the inefficient array traversal for the y-direction as highlighted in the review of the old code in Section 6.4.4.1. This problem can be solved by transposing arrays on every time step for the y-direction calculations (HYDMODY). The additional time for the array transpose was included in sections "HYDMODY" and "RESETH" of the code for timing purposes (Table 7.7). Even though there was a performance penalty for taking the transpose, overall there was a performance gain. The Ribble model is small in terms of domain size and

therefore it is expected that the memory cache can handle the problems associated with traversing arrays better in the inefficient direction. However, for larger model domains the performance degradation is expected to be much larger and the penalty for taking the array transpose is expected to be smaller. Therefore, even though a 10 % time gain is not very significant for the Ribble model, for larger models it is important to traverse arrays in the most efficient direction for serial applications.

In summary, the serial application was tested with one of the best performing compilers (Intel® Fortran compiler) on the market and run on a representative desktop computer for the current times. It was found to run the Ribble Estuary 2D model in 2376 - 2605 sec (approx. 40 - 43 min) which is a run time to simulation time ratio of about 1:70.

7.5.3 Parallel Application Performance

In this section, the performance of the new parallel version of the DIVAST code is assessed for the Ribble Estuary. Sections of the code were timed, synchronising the GPU device with the CPU device at the start and end of each section. The Ribble Estuary model was run for a total simulation time of 50 hr and the sum of the times for each section of code was obtained (Table 7.8). An open source compiler was used for compiling the CPU code. The open source compiler was found to be 10 % slower than the Intel Compiler used in Section 7.5.2 for running the Ribble Estuary model. The code was also parallelised using OpenMP. This gave an estimation of the potential performance of the code on the same desktop computer without the GPU. The parallelised OpenMP version of the code was found to be about 2 x faster than the serial code for the Ribble Estuary model. Two computers were used in the performance tests. Computer B (Table 6.6) based on an Intel i5 processor was found to be about 1.6 x faster than computer A. This was mainly due to better memory access speeds, highlighting the fact that the performance of the code on the desktop computer was mainly memory bound, as opposed to being computationally intensive.

Table 7.8: Timing Results for Ribble Model with NVIDIA Fermi GPU [a]

	Run Time (seconds) Speed Up								
	Computer A				Computer B				
	FORTRAN [b]				FORTRAN [b]			CUDA	
	1 thread		4 threads		1 thread [c]	4 threads			
Total	6879·3	0.6x	4548·0	1.0x	4372·4	2011·5	2.2x	400·2	10.9x
Hydrodynami	4432·8	0.7x	2942·5	1.0x	2917·7	1289·1	2.3x	336·4	8.7x
HYDPRPS	760·8	0.9x	449·8	1.5x	652·4	253·8	2.6x	3·8	172.7x
HYDBND	14·7	0.8x	15·8	0.7x	11·8	13·3	0.9x	1·3	9.1x
HYDMODX	1499·9	0.5x	768·9	1.0x	794·0	339·5	2.3x	217·9	3.6x
HYDMODY	1610·9	0.7x	1109·3	1.0x	1076·6	371·5	2.9x	104·2	10.3x
FLDRY	546·2	0.7x	598·2	0.6x	382·8	310·9	1.2x	8·9	43.0x
Solute	2337·2	0.6x	1486·9	0.9x	1386·2	681·9	2.0x	24·0	57.8x
SOLBND	0·8	0.5x	0·8	0.5x	0·4	0·5	0.8x	1·0	0.4x
DISP	381·5	0.5x	271·7	0.8x	205·8	62·5	3.3x	4·2	49.0x
FACEVALS	1244·6	0.6x	631·7	1.2x	764·9	349·0	2.2x	10·0	76.5x
CONCVALS	446·2	0.6x	303·6	0.9x	289·2	139·3	2.1x	5·8	50.0x
SM_RESET	18·4	0.5x	19·5	0.5x	9·9	9·9	1.0x	1·0	9.9x
DECAY	0·03	0.3x	0·05	0.2x	0·01	0·01	1.0x	1·8	0.005x

[a] Quadro 4000 GPU purchased for PhD research study
[b] compiled with gfortran: An open source Fortran 95/2003 compiler from the GNU Compiler Collection (GCC)
[c] Serial run with Fortran compiled code used as basis of speed up calculation

With the GPU code, the first half time step (HYDMODX=217 sec) was found to take longer than the second half time step (HYDMODY=104 sec). This was because the GPU code was not affected by array traversal problems as in the serial code. Hence, for much larger domains, the performance of the GPU was expected to be significantly better as compared to the serial code.

The performance of the GPU code could be affected by several memory configuration parameters (NVIDIA, 2011a). Different memory block size configurations were tested and a block size of 32 x 6 was found to give the best performance for the Ribble Estuary model. The overall speed up for the hydrodynamics was found to be about 9 x and for the solute transport algorithm a speed up of about 60 x was achieved. The results highlight the fact that differing types of algorithms perform differently on the GPU and the performance is not necessarily a function of the number of computational operations. Sections of code with very little branching, such as HYDPRPS (calculating the Chezy values) and FACEVALS (calculating cell

face concentration values), which were explicit in nature, were found to perform much better than the implicit parts of the code involving the tri-diagonal algorithm. Full parallelisation of the tri-diagonal algorithm can therefore be an important aspect of implementing a parallelised version of the alternating direction implicit scheme. Aackermann and Pedersen (2012) showed that parallelised versions of the tri-diagonal algorithm, such as parallel cyclic reduction (PCR), improved the performance for small, but not for large, domains. The strategy adopted in this research study involved running the typical tri-diagonal algorithm for each thread and running several threads in parallel, as also adopted by Aackermann and Pedersen (2012) for their larger domains.

The GPU architecture used in this research study was released by NVIDIA in 2009. Since then, NVIDIA have released more powerful and energy efficient GPUs, such as the Kepler architecture family. The Ribble Estuary model was also tested on two Kepler architecture devices, made available by Boston HPC Limited (www.boston.co.uk). The Kepler architecture family of GPUs were released by NVIDIA in October 2012 and are therefore a better indicator of current GPU technology performance for scientific computations. The two Kepler devices were a K10 and K20 device. The K10 device had 1536 cuda cores and is designed for better single precision performance (NVIDIA, 2012). The K20 device had 2496 cuda cores and was designed for better double precision performance (NVIDIA, 2012). The high number of cores and memory allowed a block size configuration of 32 x 16 to be used. Timing results of the Ribble Estuary run on the Kepler GPU devices are shown in Table 7.9. The timing results show an improvement in the GPU performance as compared to the Quadro 4000 Fermi GPU. The hydrodynamics was about 1.5 x faster and the solute transport algorithm was about 2.0 x faster as compared to the Fermi architecture GPU. The peak performance was very high, with timing of the section HYDPRPS being about 360 x faster than the serial code. The K20 GPU device performed better than the K10 device, even though the K10 was

Table 7.9: Timing Results for Ribble Model with NVIDIA Kepler GPU [a]

	Run Time (seconds) Speed Up			
	Tesla Kepler K10 GPU		Tesla Kepler K20 GPU	
Total	290·56	15.0 x	257·68	17.0 x
Hydrodynami	229·25	12.7 x	201·99	14.4 x
HYDPRPS	2·11	309.2 x	1·79	364.5 x
HYDBND	1·53	7.7 x	1·60	7.4 x
HYDMODX	134·14	5.9 x	108·52	7.3 x
HYDMODY	85·17	12.6 x	85·25	12.6 x
FLDRY	6·10	62.8 x	4·58	83.6 x
Solute	16·39	84.6 x	11·46	121.0 x
SOLBND	1·15	0.4 x	1·12	0.4 x
DISP	2·21	93.1 x	1·64	125.5 x
FACEVALS	7·18	106.5 x	4·02	190.3 x
CONCVALS	3·55	81.5 x	2·68	107.9 x
SM_RESET	0·77	12.8 x	0·67	14.7 x
DECAY	1·39	0.008 x	1·15	0.01 x

[a] Free test on computer hardware provided by Boston HPC (www.boston.co.uk)

designed for faster single precision and all the calculations were in single precision. This was mainly because of the higher parallelisation available on the K20 device. In the results for the K20 device, the ratio between HYDMODX (108.5 sec) to HYDMODY (85.3 sec) was now approximately the same as the ratio of the number of cells in the x-direction (618) to number of cells in the y-direction (454), showed that the memory access effects were minimal.

In summary, the hydrodynamics part of the code was found to be up to 17 x faster than the serial code and the solute transport algorithm was found to be up to 120 x faster than the serial code for the Ribble Estuary model. The speed up times are very much dependent on the computer that the serial code was run on and therefore can vary between differing authors. However, speed up can also be described in terms of run time to simulation time ratios. For the hydrodynamics the run time to simulation time ratio was 1:890 and for the solute transport the ratio was 1:15700. That is to say, in one second of real time 15 minutes of simulation time of the hydrodynamics can be run and in one second of real time 4.3 hr of simulation time of the solute transport algorithm can be run. There is still a lot of room for

improvement in the speed up as the full potential of the GPU was not utilised, due to time constraints in this research study. Further, code optimisation and reduction of code branching can improve on the performance achieved on the GPU. The DIVAST code involves lots of branching in the computation due to the need to check for wetting or drying cells and other aspects of the algorithm. It is known from the documentation by NVIDIA (2011b,a) that lots of branching can reduce the amount of speed up that parallelisation can achieve on the GPU. This implementation of the DIVAST code has confirmed the potential of parallel computation on the GPU for the hydrodynamic and solute transport sub-models.

7.6 Summary

New improvements of the kinematic representation of bacteria, model domain linking and on integrated approach to modelling have been applied to the Ribble Estuary basin. The modelling results now give a better representation of the physical and biochemical processes. The GPU version of the DIVAST numerical model was applied to the Ribble Estuary model and significant improvements to the execution times were observed. Speed up times of about 17 x were observed for the hydrodynamics and 120 x for the solute transport algorithm. The increased model runtimes allowed for more models runs to be performed in further calibrating the input parameters.

Chapter 8

Application to the Thames Estuary

8.1 Introduction

In this chapter, a new model of the Thames Estuary was built and used to assess the potential benefit of GPU parallel technology to very large models. The Thames Estuary model stretches from the tidal limits at Teddington (Figure 8.1) to Southend-On-Sea, with the various versions of the bed topography being shown in Figure 8.2. The length of the model was about 100 km, with the bed level difference being about 20 m from the upstream boundary to the downstream boundary. The Thames Estuary is particularly vulnerable to flooding and this research study looked at primarily using GPU parallel technology to enhance the ability to predict flood levels to a greater accuracy and carry out long model simulation runs.

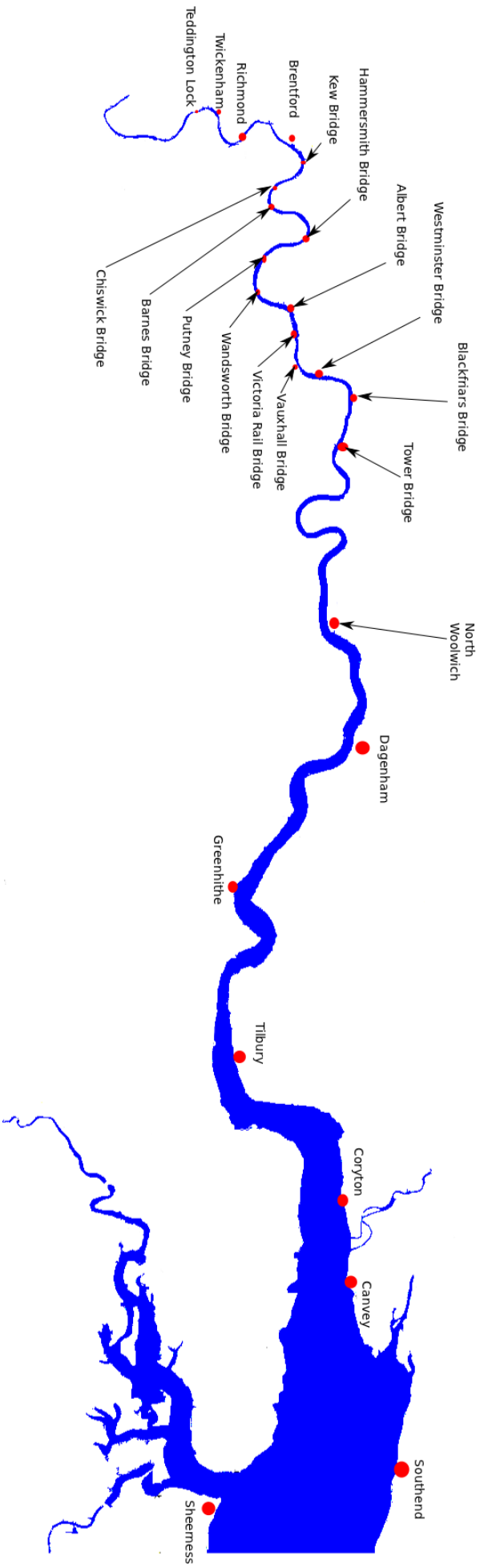

Figure 8.1: Thames Estuary

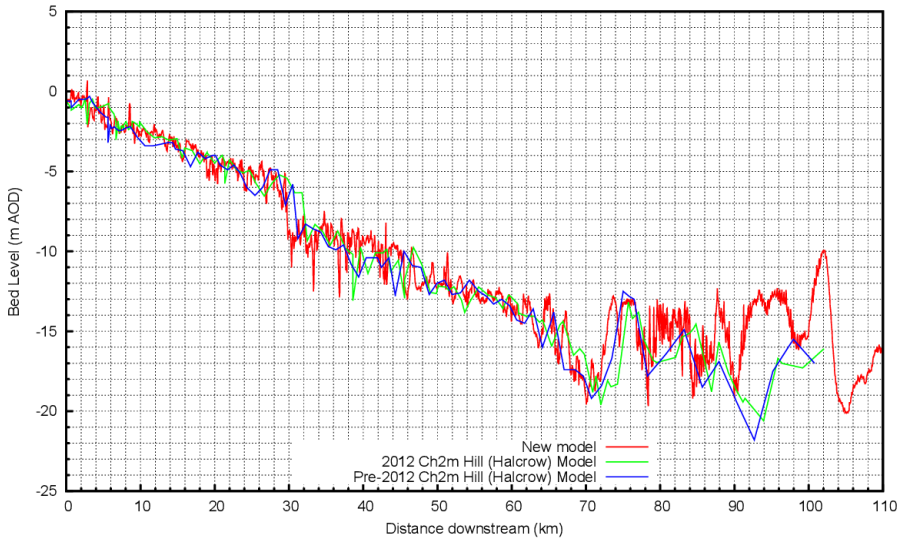

Figure 8.2: Longitudinal section through new Thames Estuary model

8.2 Model Preparation

The bathymetry data for the Thames Estuary was obtained from the Environment Agency. These data included remote sensing data, obtained using Lidar technology, the Port of London Authority (PLA) river bed sounding data, and water level and flow information.

The boundary information for December 2005 was used to build the model. This was acquired during a wet event, with flow at the upstream boundary increasing to about 100 m^3/s (Figure 8.3).

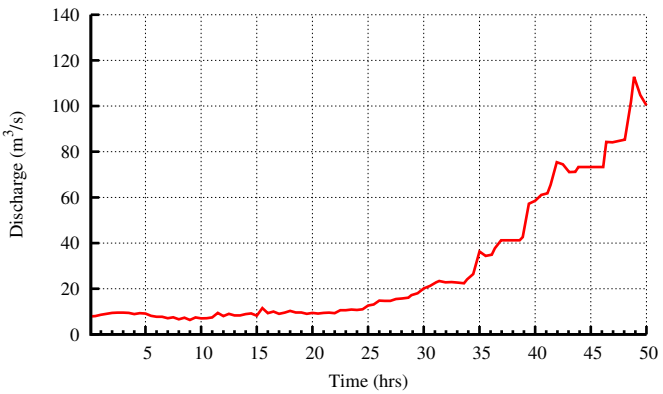

Figure 8.3: Upstream flow boundary

The Lidar data consisted of about 77.4 million points and the PLA data consisted of about 8.6 million points. The Lidar data overlapped the PLA data in the river

region. Some points of Lidar data in the river region needed to be removed and replaced with the PLA data. The river needed to be split into a one-dimensional domain and a two-dimensional domain for the new model. The location of the model grid points did not necessarily coincide with the locations of the Lidar and PLA data. The co-ordinates therefore needed to be interpolated and there was much data to process to generate the new model. An algorithm was therefore written to process the data, which enabled the generation of models of differing grid sizes automatically.

A convex hull algorithm was written and used to find the minimum polygon around the PLA data. This polygon was then used to filter the unwanted Lidar data in the river region, with the data being replaced with the PLA data.

The large number of data points meant that an efficient way of finding the nearest points to a particular location was desirable. A nearest neighbour list (NNL) was therefore used. This type of list is also used in Smoothed Particle Hydrodynamics (SPH) to find the properties of points around a particular location in a scattered data set (Awile *et al.*, 2012; Rogers, 2013).

Interpolation of the bathymetric data were done using Inverse Distance Weighting (IDW). This is one of the most frequently used deterministic models in spatial interpolation. It is used in various commercial software packages, such as ArcGIS. It is relatively fast and easy to compute, and straightforward to interpret. The general idea is based on the assumption that the attribute value of an unsampled point is the weighted average of known values within the neighbourhood, and the weights are inversely related to the distances between the prediction location and the sampled locations (Lu and Wong, 2008). Other deterministic interpolation methods include: Radial Basis Function (RBF) with Gaussian, Inverse Quadratic (IQ) and Inverse Multi-Quadratic (IMQ) formulations. Interpolation predicts values for cells in a raster from a limited number of sample data points. It can be used to predict unknown values for any geographic point data, such as elevation, rainfall, chemical

concentrations, noise levels etc. The weighting function for IDW is given as:

$$w_i = \frac{1}{|x - x_i|^2} \tag{8.1}$$

where $|x - x_i|$ is the distance between the known point (i.e. the scatter point) and the unknown point (i.e. the interpolation point). Any point close to the interpolation point gets a higher weighting, while points further away from the interpolation point get a lower weighting. The bed elevation of the interpolation point is given by:

$$Z = \frac{\sum w_i z_i}{\sum w_i} \tag{8.2}$$

where z_i is the bed elevation at the scatter point. When the interpolation point coincides with the scatter point, the interpolated bed elevation is the same as the elevation at the scatter point, which makes this method a deterministic exact interpolator.

To generate the one-dimensional domain of the model, the centre of the river needed to be predetermined. For such a large data set, manually defining this would have been time consuming. Hence, a river route finding algorithm was developed for this purpose. The algorithm finds the mean direction of the bed slope and follows this direction. This enabled automatic generation of the river route.

The model was made up of a 1D domain upstream and a 2D domain downstream. The dynamically linked boundary was located at Dagenham (see Figure 8.1). Several models of the Thames estuary were generated, one with a similar grid size to the Ribble Estuary and one with a much larger grid size (Table 8.1). All the models had a similar Courant number.

Table 8.1: Properties of Thames Models

	Thames Model 1 (small)	Thames Model 2 (Large)
Time Step Δt (secs)	3.0	0.5
Grid size Δx (m)	50.0	8.3
No. of cells in x-direction	841	4649
No. of cells in y-direction	321	1441
Total No. of cells (million)	0.27	6.7
No. of timesteps	60000	1666
Simulation time (hr)	50.0	0.23

8.3 Model Results

The model was validated by comparing the predicted water elevations with the measured data provided by the Environment Agency (EA), with measured velocities not being available at the time of this study. Comparisons of the predicted surface water elevations and the measured data are shown in Figure 8.4. There was a phase

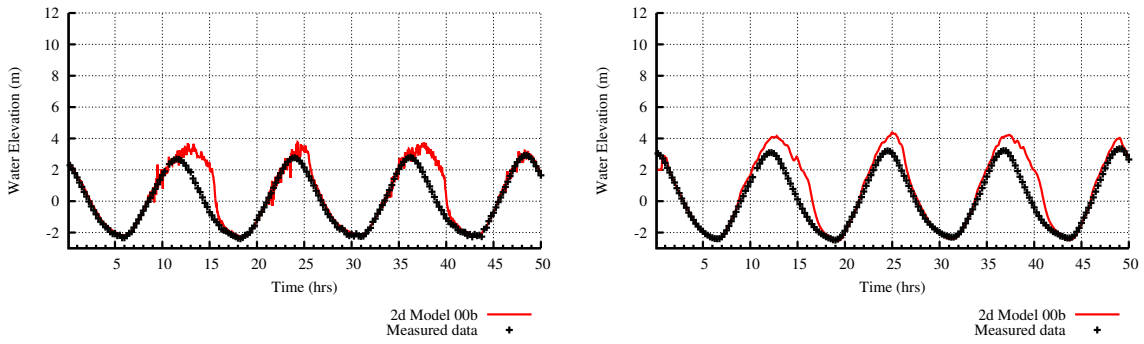

(a) Southend (b) Tilbury

Figure 8.4: Comparison of predicted and measured water elevations at two sites along the Thames Estuary

lag at the peaks of the water surface elevations in Figure 8.4. This can be attributed to the limited amount of data available to calibrate the model. There was no velocity data available at the survey points to calibrate the model. There was only flow data at the upstream boundary and elevation data at the downstream boundary. The Thames Estuary model was very long (over 100 km long) and therefore the effects of having little calibration data was significant. The main aim of using the Thames model was to test the GPU performance and therefore the phase lag in the results did not affect the main line of investigation in this research study.

The Thames Estuary was only used for hydrodynamic modelling. There was no water quality model as data was not available at the time for this. Also, the main problem with the Thames Estuary is flooding and hence it was very important to test the performance of a hydrodynamic model.

8.4 Parallel (GPU) Application Performance

8.4.1 Thames Estuary Model 1

The performance of the small Thames Estuary model was measured and the results of this are given in Table 8.2.

Table 8.2: Timing Results for Thames Model 1 with NVIDIA Fermi GPU [a]

	Run Time (seconds) Speed Up								
	Computer A				Computer B				
	FORTRAN [b]				FORTRAN [b]			CUDA	
	1 thread		4 threads		1 thread [c]	4 threads			
Total	8870	0.7x	6433	0.9x	5917.3	2178	2.7x	934	6.3x
Hydrodynami	8282	0.7x	6055	0.9x	5627.1	2006	2.8x	735	7.7x
HYDPRPS	2802	0.9x	1479	1.6x	2409.0	784	3.1x	12	195.7x
HYDBND	1.1	0.5x	1.6	0.4x	0.6	0.9	0.7x	1.4	0.4x
HYDMODX	2018	0.5x	1321	0.7x	986.1	373	2.6x	502	2.0x
HYDMODY	1900	0.6x	1535	0.8x	1156.6	425	2.7x	193	6.0x
FLDRY	1559	0.7x	1735	0.6x	1074.4	423	2.5x	26	41.9x

[a] Quadro 4000 GPU purchased for PhD research study
[b] compiled with gfortran: An open source Fortran 95/2003 compiler from the GNU Compiler Collection (GCC)
[c] Serial run with Fortran compiled code used as basis of speed up calculation

The Thames Estuary had a smaller time step of 3 secs compared to 9 secs for the Ribble Estuary. The overall time taken to run the Thames model was therefore greater than that of the Ribble model. The speed up of the explicit parts of the code, such as HYDPRPS and FLDRY, was similar to the values for the Ribble model. The HYDMODX and HYDMODY sections of the code took 17.5 % and 20.5 % of the serial run times, which was a lower percentage than that of the equivalent times for the Ribble model. However, the performance of the serial code was much better for the Thames estuary model. The low speed up of the Thames model, as compared

to the Ribble model, can be attributed to the low percentage of wet cells, and the narrow and meandering nature of the river Thames. The narrow meandering nature of the Thames estuary meant that the boundary between wet and dry cells was much longer for the Thames model, as compared to the Ribble Estuary model. At the boundary between wet and dry cells the path of execution was different and the GPU serialises such instructions according to NVIDIA (2011a).

According to NVIDIA (2011a), any flow control instruction (i.e. 'if', 'switch', 'do', 'for', 'while' etc) can significantly affect the instruction throughput by causing threads of the same warp to diverge; that is, to follow different execution paths. If this happens, the different execution paths must be serialized, increasing the total number of instructions executed for this warp. When all the different execution paths have been completed, the threads converge back to the same execution path.

Models with a greater percentage of wet cells can therefore be expected to have a higher speed as compared to using the CPU. This is important because test cases where 100 % of the model domain is wet can result in a much higher speed up for the GPU, but real world applications often do not have 100 % of the domain being wet. It also important to note that the performance is not a function of the percentage of wet cells, but a function of the length and location of the boundary between the wet and dry cells. A model with 100 % of the domain wet does not have this boundary effect.

The Thames estuary model was also tested on two Kepler architecture devices, made available by Boston HPC Limited (www.boston.co.uk). The timing results of this test are shown in Table 8.3.

The results in Table 8.3, show an improved speed up of 11 x for the 2D hydrodynamics models, which is better than the 7.7 x speed up obtained with the Fermi architecture device.

Table 8.3: Timing Results for Thames Model with NVIDIA Kepler GPU [a]

	Run Time (seconds)	Speed Up		
	Tesla Kepler K10 GPU		Tesla Kepler K20 GPU	
Total	752.56	7.8x	751.27	7.9x
Hydrodynami	510.87	11.0x	499.33	11.2x
HYDPRPS	6.15	391.7x	5.24	459.7x
HYDBND	1.96	0.3x	2.11	0.3x
HYDMODX	325.13	3.0x	324.62	3.0x
HYDMODY	159.36	7.3x	154.06	7.5x
FLDRY	17.86	60.2x	12.76	84.2x

[a] Free test on computer hardware provided by Boston HPC (www.boston.co.uk)

8.4.2 Thames Estuary Model 2 (Large)

The large Thames estuary model in Table 8.1 was also run and timed to assess its performance. The performance test results are shown in Table 8.4.

Table 8.4: Timing Results for Thames Model 2 (large) with NVIDIA Fermi GPU [a]

	Run Time (seconds)		Speed Up
	FORTRAN [b] (1 thread [c]) 4 threads	CUDA	
Total	5427·57	581·83	9.3x
Hydrodynami	5426·20	580·55	9.3x
HYDPRPS	915·49	7·39	123.9x
HYDBND	0·15	0·04	3.2x
HYDMODX	1191·51	441·24	2.7x
HYDMODY	2470·26	112·58	21.9x
FLDRY	848·77	19·28	44.0x

[a] Quadro 4000 GPU purchased for PhD research study
[b] compiled with gfortran: An open source Fortran 95/2003 compiler from the GNU Compiler Collection (GCC)
[c] Serial run with Fortran code used as basis of speed up calculation, run on Computer B

The results show that better performance was achieved with the larger model. The overall speed up for the hydrodynamics was about 9.3 x. The x-direction solver had the highest improvement with a speed up of about 20 x. This confirms that some of the speed up of the ADI algorithm is due to the serial code being inefficient in traversing large arrays in the x-direction. It also confirms that for large arrays the inefficiency is significantly greater. The GPU code also performs better with a

larger domain. However, the level of performance is still much lower than that of the explicit code.

The effect of differing domain grid sizes was tested by generating several models of differing grid sizes. The models were then run on the GPU and with the FORTRAN CPU code. The resulting speed up times are presented in Figure 8.5. The results

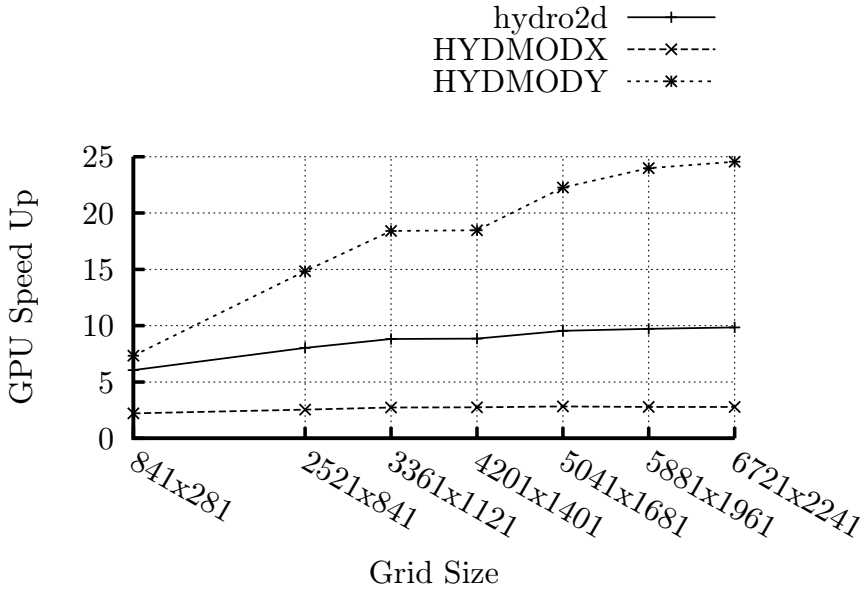

Figure 8.5: Variation of speed up with model grid size for Quadro 4000 GPU

confirmed that the increase in the speed up the in y-direction, with model grid size was much greater than that in the x-direction. It can also be inferred from the results that the performance of square domains will be greater, because a greater proportion of the runtime will be in the y-direction (HYDMODY). Hence the overall speed up of the hydrodynamic model, or the ADI algorithm, can be said to be proportional mainly with the number of cells in the y-direction (8.3), or:

$$\textbf{GPU Speed Up (ADI)} \propto \text{No. of cells Y-direction} \tag{8.3}$$

In November 2013, at the Supercomputing Conference 2013 in Colorado, NVIDIA announced a new High-Performance Computing (HPC) GPU, the Tesla K40. This device has a much greater capacity to run bigger models. The results for performance tests on this GPU show more than a three fold overall speed up was achieved as

compared to the Quadro 4000 device (Figure 8.6) with over 80 fold speed up for HYDMODY. It also confirms the significant potential of current GPU devices to speed up the ADI hydrodynamic model for large model domains.

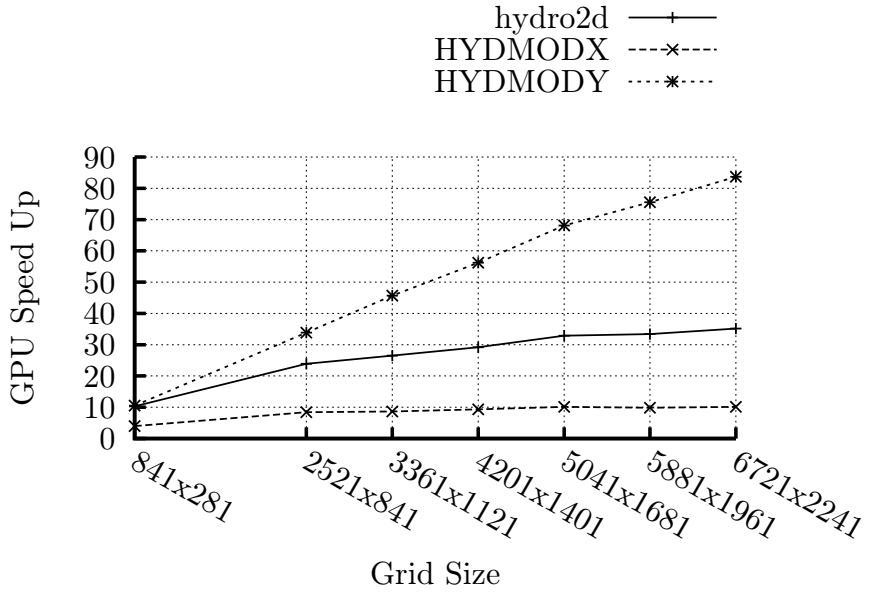

Figure 8.6: Variation of speed up with model grid size for Tesla K40 GPU provided by Boston HPC (www.boston.co.uk)

8.5 Summary

The Thames estuary has been used as a test case for the GPU version of the DIVAST code, and with particular reference to speeding up the code. Models of differing grid sizes were generated using a custom made algorithm from Lidar and the PLA data, provided by the Environment Agency (EA). A similar speed up time was observed for a grid size similar to that of the Ribble Estuary. A higher speed up time of about 10 fold was observed for the largest model tested. The speed up was observed to be mainly dependent on the number of cells in the y-direction. It was inferred that square models with a reduced boundary between wet and dry sections will have a much greater speed up time. In conclusion, GPU technology delivers a significant speed up for the ADI method for free surface flows, with the speed up time being dependent on the domain grid dimensions.

Chapter 9

Conclusions

9.1 General

This research study has been directed mainly at solving and improving the process accuracy of bathing water key pollution constituents and using parallel (GPU) computing to reduce the execution times of large hydro-environmental models.

The European Union is introducing more stringent bathing water quality standards in 2015. These standards are based on monitoring the levels of Faecal Indicator Organisms (FIOs) in bathing waters, with the classification being based on the concentration levels of FIOs. Currently, there are occasional failures to meet the existing standards, even though major civil engineering investment programmes have been carried out to reduce bacterial inputs. For the U.K. the main sources of faecal contamination that are likely to cause non-compliance of bathing waters are now generally from diffuse sources and sediment agitation during storm or high flow events, together with inputs from non-treated Combined Storm-Water Overflows (CSOs). A bathing water may be classified as 'poor' and still remain in compliance with the Directive, provided that adequate management measures, including a bathing prohibition or advice against bathing are implemented. Such measures can only implemented if the water quality can be predicted accurately beforehand or predicted in real time. Having polluted bathing waters which do

not comply with the Bathing Water Directive can have severe social and economic impacts, especially for communities which depend on their beaches for recreation, holiday businesses and/or tourism.

The main objectives of this research were addressed by considering the Ribble River Basin and the receiving waters of the Fylde Coast for the bathing water pollution problem and the Thames Estuary as another case study for evaluating the impacts of parallel (GPU) computing options. The main components of the research undertaken in this study were:

- A C2C (Cloud to Coast) fully integrated approach to modelling flow and solute transport processes in river, estuarine and coastal waters was applied to the Ribble River Basin and Fylde Coast.
- The computational linking of the catchment run-off, river and estuarine coastal models was improved for the Ribble Estuary and Fylde Coast model.
- Based on field and laboratory data, an improved kinetic decay process representation was developed for the Ribble Estuary and Fylde Coast model, through including the impact of salinity, solar radiation, turbidity and water temperature. This also included spatial and temporal variations in the bacterial decay rates.
- A GPU based parallel computing approach was used to enhance the computational speed of the Ribble Estuary and Fylde Coast and the Thames Estuary models.

9.2 Integrated Cloud to Coast (C2C) Modelling Solutions

A previous study of the Ribble Estuary and Fylde Coast was reviewed in the context of a Cloud to Coast (C2C) solutions approach. A number of anomalies were found in

the original study and some key lessons were learnt for the future, particularly in the context of the principle that the raindrop, possibily with attached pollution, does not know whether it is in the catchment, stream, river, estuary or coastal basin. It was observed that differing values and/or formulations of various parameters (decay rate, dispersion coefficient, bed friction) were used in differing domains of the model and, in particular, without good physical or bio-chemical justification. This meant that even though the model gave good calibration with the measured data, the parameters used were not necessarily a good representation of the existing physical and bio-chemical processes.

The previous study was revised with the introduction of a more integrated approach to modelling the hydrodynamic and solute transport processes. This involved introducing: common decay coefficients; common dispersion constants and formulations; and common bed friction formulations in both the one-dimensional and two-dimensional domains of the model.

The resulting faecal coliform levels, after the introduction of common decay coefficients, were found to be lower than those predicted in the original model. The sensitivity of the model to the common decay rates was also tested. The sensitivity was found to depend on the distance from the input source. The greater the distance from the input source, the higher the sensitivity of the concentration levels to the decay rate. This confirmed that the decay rate was a very important parameter for predicting bathing water quality, as bathing waters were often far from the pollution causing input sources. At low decay rates, the predicted coliform concentrations were less sensitive to changes in the decay rate. It was therefore concluded that other factors, such as dispersion and the advection of the coliforms, will have more significant effects on concentration levels at lower decay rates, such as during the night-time.

In the old model, there was great variation in the dispersion coefficient between the values used in the 2-D domain as compared with those used in the 1-D domain.

Better prediction of the lower coliform levels was achieved due to the introduction of a common longitudinal dispersion constant and dispersion formulae in both of the model domains.

In the new refined model, the Manning's number formulation was used to calculate the bed friction in both the 1-D and 2-D domains of the model, as compared to the original model, where a Nikuradse roughness coefficient was used in the 2-D domain and Manning's n in the 1-D domain. The resulting water elevations, current speeds and faecal coliform levels were not significantly different, but were important in ensuring that any predictions are consistent with the more realistic physical parameters.

It was concluded that the integrated approach provided a better representation of the underlying physical and bio-chemical processes involved, in modelling the hydrodynamic and FIO processes through the water system.

9.3 Computational Linking

The length of the link overlap between the 1-D and 2-D domains of the old Ribble Estuary model was about 2.8 km. The overlap typically adopted when linking different models was significantly reduced for the Ribble Estuary model. This eliminated the inconsistent problem of accuracy between the two domains where the overlap area is relatively large such as that in the case of the Ribble Estuary.

9.4 Bio-kinetic Representation

The bio-kinetic representation of bacterial decay was refined by including the temporal and spatial variation of differing factors, such as: solar radiation, turbidity, temperature and salinity.

In the original Ribble Estuary and Fylde Coast model, and alternative models routinely used in industry, the decay rate for the day time is applied instantaneously

at sunrise and stays constant until sunset, when the value instantly reverts back to the night-time decay rate. However, the actual variation of light intensity through the day approximates more to a sinusoidal function as outlined in Section 2.7.3. The revised model was set up with a sinusoidal function representing how the light intensity varies during the day-time, with the light intensity being linked to the decay rate. The resulting peak coliform concentrations were found to be slightly higher. It was concluded that even though the effects were small for this model study, the improved representation contributed to more accurate coliform concentration predictions and a better representation of the bio-kinetic processes in the model.

From observations of the Ribble Estuary, a turbidity maximum exists between the head of the estuary at Penwortham and the Ribble/Douglas confluence. An empirical formula was used to estimate the light extinction coefficient based on turbidity values from a recent survey. The light extinction coefficient was introduced to model the effects of turbidity in the model. The overall coliform concentration levels were found to increase due to the effects of turbidity.

The water temperature effects on the decay of bacterial fluxes were modelled considering the spatial and temporal variation of temperature within the model domains. The water temperature was modelled as a solute using a simplified heat balance equation. The resulting effects of temperature on the decay rates were found to be small but important in improving the accuracy of the model.

Salinity was modelled as a solute with zero decay rate, i.e. it was treated as a conservative tracer. The resulting salinity levels showed that salinity in the model was strongly influenced by the tides. The salinity was then linked to the decay rates. The resulting decay rates were found to increase in the middle of the day time and during night-time. It was concluded that the increased decay rates occurred with the incoming tides and only affected coliforms that have already made their way downstream and were being advected back upstream by the tides. The effects of salinity on the decay rate were higher further downstream than upstream in the

estuary. The resulting coliform concentrations were not greatly affected by salinity. However, there was a slight increase in the lower concentrations.

9.5 Combined effects on predicting bathing water quality

All of the model refinements (i.e. improved bio-kinetic representation, computational linking, integrated approach) were combined and their overall effects on the predicted coliform concentrations were then studied. The combined model was found to have a lower Mean Absolute Error (MAE) of coliform concentration predictions when compared with the original measured data. This confirmed an improved accuracy, when compared to the original model. The introduction of the common decay rate had a negative impact on the predicted coliform levels. The effects of solar radiation and turbidity had a greater positive impact on the predicted coliform levels. Therefore the accuracy of the solar radiation and turbidity parameters are important for the Ribble Estuary and Fylde Coast. The new refined model therefore provided a better understanding of the relative effects of different factors on the water quality indicators.

The improvements to the Ribble Estuary and Fylde can be summarised as follows:

- Decay rate varies with position in the rivers and estuary as opposed to a constant value over whole domain;
- The decay rate due to solar radiation took into account the sinusoidal variation of light intensity during the day;
- Water temperature was modelled as a solute using a heat balance equation. The water temperature also varied with position in the estuary;
- Salinity was modelled as a conservative solute taking into account variations with position between seawater and freshwater;

- Turbidity took account of the extinction coefficient and variations of the depth of water, with position in the estuary; and
- Decay rates due to solar radiation were also dependent on water temperature.

9.6 Parallel Computing

The existing DIVAST code was rewritten to take advantage of parallel computing on the Graphics Processing Unit (GPU). The serial version of the DIVAST code was tested with one of the best performing compilers on the market (i.e. Intel® Fortran compiler) and run on a typical current day standard desktop computer. It was found to run the Ribble Estuary 2D model in 2376 - 2605 sec (approx. 40 - 43 min) which is a run time to simulation time ratio of about 1:70.

The GPU version of the DIVAST numerical model was applied to the Ribble and Thames Estuary models and significant improvements in the execution times were observed. For the Ribble Estuary model, speed up times of up to 17 fold were observed for the hydrodynamics and 120 fold for the solute transport algorithm. A similar speed up time was observed for the Thames Estuary, with the grid size being similar to that of the Ribble Estuary. For larger domains speed up times of up to 90 fold were observed for the Thames Estuary on more recent GPU devices. It was therefore concluded that:

- The GPU speed up was observed to be mainly dependent on the number of cells in the y-direction;
- The order of memory access can slow down computations in traditional computing on the CPU and this was eliminated with GPU computing;
- The increased model runtimes allowed for more models runs to be performed in the sane amount of time, thereby enabling further calibrations for the input parameters;

- More parallelisation can be exploited from explicit numerical schemes in comparison with implicit algorithms;
- The speed up time obtained from the GPU was significant for industrial applications; and
- In the future of computational fluid dynamics, studies will be increasingly undertaken on systems which take advantage of both parallel and serial computing. Future computing architectures will be hybrid systems in which parallel-core GPUs work in tandem with multi-core CPUs

This significantly increased the ability to run more model scenarios, improve calibration, run bigger models and carry out real time water quality forecasting.

In conclusion, GPU technology delivers a significant speed up for the ADI method for free surface flows, with the speed up time being dependent on the domain grid dimensions. This is especially significant for modelling large domains over long time periods.

9.7 Research Impacts

The impacts of this research can also be categorized under Social, Technological, Environmental and Political (STEP) factors. These factors will become more important in the future and can be summarised as follows:

- Social
  - Need for people to lead a more environmentally friendly lifestyle, inclusing more UK holidays ('staycation'). Especially when there is an economic downturn;
  - Vision 2020: Societies will have less impacts on the environment due to changed lifestyle choices

- Technology
  - New Graphics card technology providing a cheaper platform for parallel scientific computations;
  - Companies need to implement the new technology quickly to benefit;
  - It is not easy to implement new technology due to the need to change old habits;
  - Vision 2020: Parallel computing will become the norm. Furthermore, big data management will also become more important and there will be an increased amount of code to be managed by scientific programmers.
- Environmental
  - Seaside resorts like Blackpool (located along the Fylde Coast) face negative economic impacts if beaches are closed;
  - The U.K. could be potentially fined by the E.U. for failing to meet the new Bathing Water Directive;
  - Cheaper graphics cards and supercomputing technology will lead to a lower energy consumption;
  - Vision 2020: Places which need better environmental management will change.
- Political
  - The U.K. needs to comply with the more stringent E.U. Bathing Water Directive
  - The Farmers' Union, utilities companies, local and district councils, manufacturing industries, etc., are all keen to show that they are not responsible for failing Bathing Water Quality; and
  - Vision 2020: Even more stringent environmental lawswill be included in the future.

9.8 Summary

In summary, the Ribble Estuary and Fylde Coast model has been refined to more accurately predict the bathing water quality and use parameters which give a better representation of the existing physical and bio-chemical processes in modelling flow and solute transport in river and coastal basins. This means that the new hydro-environmental model developed through this research project is well suited to forecasting bathing water quality. These research developments reported herein can help the U.K. and other E.U. countries meet the more stringent European legislation in the future. The DIVAST code has also been parallelised to run significantly faster on the GPU, which enables much larger models and with longer time periods to be analysed. This is important for flooding problems and particularly for long term water quality predictions.

Chapter 10

Recommendations for Further Study

10.1 General

The outcomes of this research study have led to further considerations that exceeded the scope of this work. These considerations are outlined in this chapter.

10.2 Computational Linking

The influence line technique was used to combine different reaches implicitly in the 1D model. It would be invaluable to consider combining the one-dimensional and two-dimensional domains implicitly using this technique and then studying the resulting predictions against real data, such as that for the Ribble Estuary and Fylde Coast. The 1D domain currently uses the tri-diagonal technique and so does the 2D domain, hence if different reaches of the 1D domain can be combined using the influence line technique, then it should be feasible to combine the 1D and 2D domains using the same technique. Further investigation is necessary to confirm the possibility of undertaking this approach.

10.3 Bio-kinetic Representation

The Ribble Estuary and Fylde Coast model used in this research study had a grid size of 67m x 67m. For more accurate coliform predictions a more refined grid domain could be adopted with new bathymetric data. The measured data used in this study was limited. In the summer of 2012 further data was collected through the Cloud to Coast (C2C) research project, funded under the Living With Environmental Change (LWEC) Environmental Exposure & Health Initiative (EEHI), jointly funded by the Natural Environment Research Council (NERC), the Medical Research Council (MRC), the Department for Environment, Food & Rural Affairs (Defra) and the Economic & Social Research Council (ESRC). These data were not used due to the limited amount of time available. However, the new data could be used in further research studies. The availability of more measured data can significantly improve the accuracy of the model. For example, the use of the measured solar radiation data, which accounts for cloud cover.

For calibration of larger model domains where refined spatial information is not available, the calibration technique can be made more efficient and faster. It would be quicker to calibrate coarse models and then automatically reduce the grid size for the final runs. This would suit a model that uses the original scattered bathymetry data as input, builds a Nearest Neighbour List (NLL) of the points and then generates the calculation grid at the start of the model run using the grid size specified by the user. The flexibility of the user to change the grid size can also aid in studying the sensitivity of a model to different grid sizes. The model generation algorithm used to prepare the Thames Estuary model in this research study could be adapted for generating the calculation grid at run time.

Including sediment transport will be beneficial to improving the accuracy of the Ribble Estuary and Fylde Coast model. Bacteria attached to sediment continuously advecting in and out of suspension would need to be considered. The sediment transport can also be linked to the turbidity of the water column, creating a more

dynamic model.

This research study uses faecal coliform as the indicator organism. However, the current Bathing Water Directive (European Parliament, 2006) specifies Intestinal enterococci and Escherichia coli (E. coli) in the quality thresholds for coastal water and transitional waters. The decay process for different bacteria can be different. Therefore, in order to be able to relate future studies more accurately with the legislation, E. coli should be used as the indicator organism.

The refined model could also be applied to other sites to further confirm it's benefits.

10.4 Parallel Computing

One of the barriers to fully exploiting the potential of the GPU device was the high level of branching in the DIVAST code, due to having flags for the wet or dry state of each cell. The current code solves the tri-diagonal algorithm by checking for the wet/dry state of each cell and not calculating or skipping the dry cells. In future studies, a revised approach can be adopted so that the matrix solved by the tri-diagonal algorithm has modified recursion coefficients for the dry cells. The coefficients will be replaced with ones or zeros so that the result of the overall equation is suitable for a dry cell. This approach is similar to that adopted when applying the finite element method to structural mechanics, where the stiffness matrix coefficients are modified at the joints to represent restraining or support conditions. This implies that both wet and dry cells will be solved by the tri-diagonal solver without any need for branching. Due to time restraints, this technique was not adopted in this research study but will be highly beneficial for future work using GPU technology.

An explicit hydrodynamic scheme on the GPU will be very fast for small domains based on the results of this research study. It is recommended that for small coarse domains an explicit hydrodynamic scheme is considered. Then the implicit scheme is

only used for large domains, with a small grid size where more accuracy is required.

The code can be revised to use multiple GPUs when the domain size exceeds the memory capacity of one GPU. MPI parallelism will need to be applied to the GPU code developed in this research study. This will only be beneficial for very large domains exceeding the 12 GB memory limit of the Kepler GPU. It is not envisaged that this will be necessary for most models.

The DIVAST code can be rewritten with MPI parallelism and transposing of arrays. This will avoid the problem of transposing arrays in an efficient manner and allow the code to be run on a cluster of CPUs, such as that available with most High Performance Computing (HPC) facilities. GPU technology can then be compared with parallel CPU technology.

The hydrodynamic algorithms of the model can be improved in future studies by adopting a turbulence formulation better suited to more complex flows. The GPU parallised version of the DIVAST code can enable this to be done without adversely impacting on the execution times.

With the improved ability to calibrate the model due to the faster execution times, further studies can be carried on the input parameters, especially those based on empirical relationships such as longitudinal dispersion etc.

Appendices

Appendix A

Ribble Estuary : Input Data

A.1 General

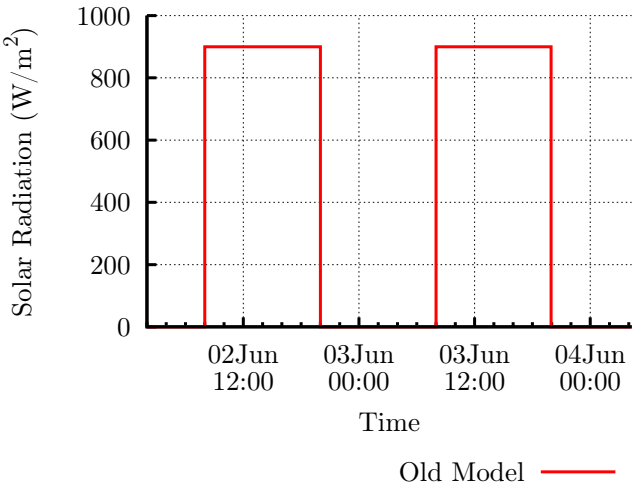

Figure A.1: Variation of Solar Radiation in Old Model

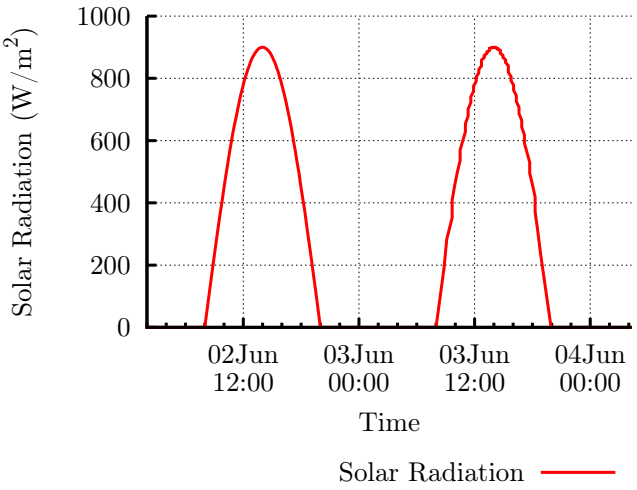

Figure A.2: Variation of Solar Radiation in Revised Model

A.2 One-Dimensional(1D) Model

A.2.1 Bathymetry

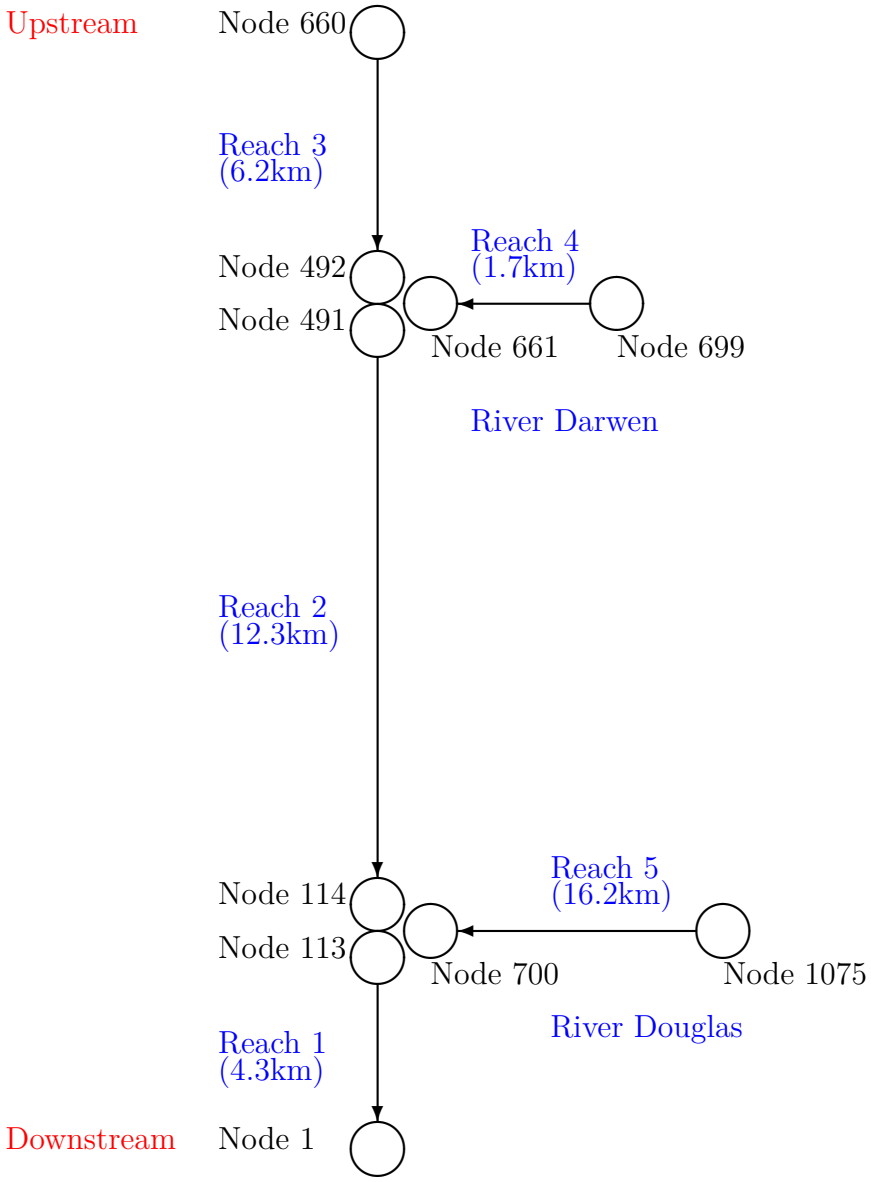

Figure A.3: Schematic of the 1D Ribble model

Table A.1: Manning's Numbers adopted for Ribble Channel Network

Node Number		
Downstream	Upstream	Manning's Number
1	113	0.020
114	491	0.021
492	660	0.026
661	699	0.028
700	760	0.025
761	1075	0.028

A.2.2 Boundary Input Sources

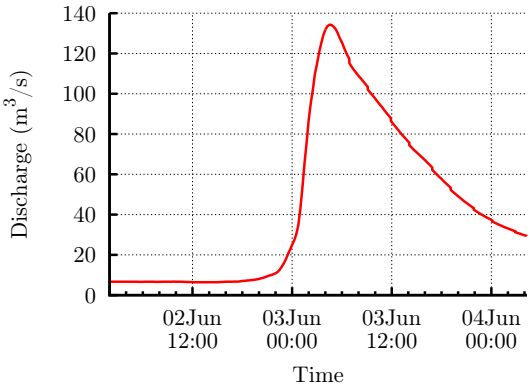

(a) River Ribble

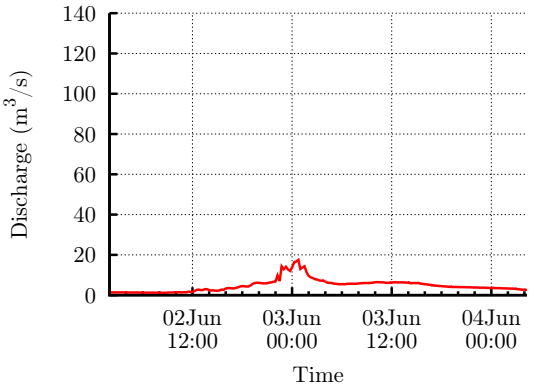

(b) River Darwen

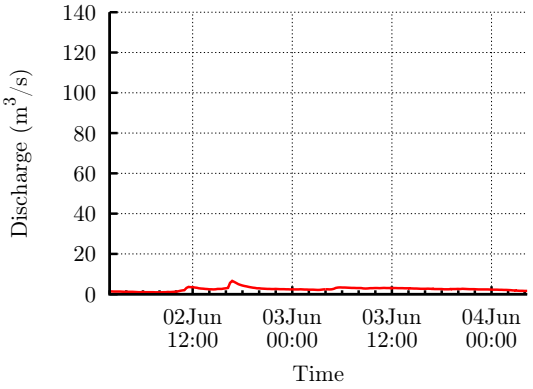

(c) River Douglas

Figure A.4: Upstream Discharges

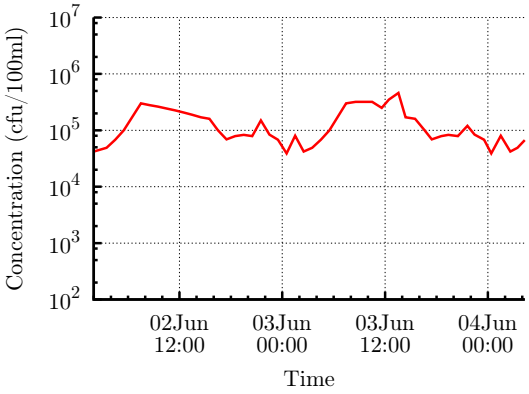

(a) River Ribble

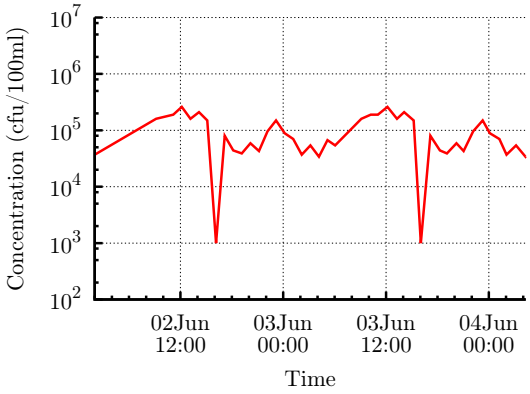

(b) River Darwen

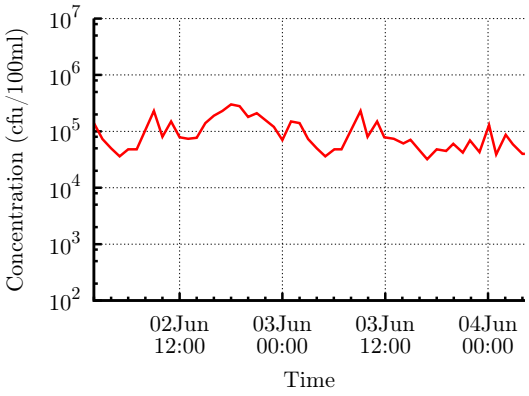

(c) River Douglas

Figure A.5: Upstream Faecal Coliform Concentrations

A.2.3 Lateral Input Sources

Table A.2: Input Sources for 1D Model

No.	Description	Node	Easting (m)	Northing (m)
1	Pool Stream (small river)	59	342312	427010
2	Middle Pool and Dow Brook (small river)	115	343920	429470
3	Freckleton East (CSOs)	116	343920	429470
4	Preston STW (Clifton Marsh)	155	345540	427870
5	Preston, Clifton Marsh (Storm)	158	345710	427930
6	Lea Gate (CSOs)	235	349800	430800
7	Savick Brook and Deep dale Brook (small rivers)	236	347800	430000
8	Surface Water Culvert (CSOs)	310	350135	429288
9	Penwortham (PS)	335	351060	429260
10	PRE0022 (CSOs)	396	352922	428888
11	Penwortham (CSOs)	408	352821	428381
12	PRE0028 (CSO)	421	353061	428201
13	Preston Frenchwood(CSOs)	461	354175	428664
14	Walton-le-Dale (STW)	479	354600	428200
15	Walton-le-Dale (Storm)	479	354600	428200
16	Preston Town East (CSOs)	512	354882	429257
17	Longton (STW)	753	346870	425280
18	Longton (Storm)	753	346870	425280
19	Hesketh Bank (STW)	775	345620	423980
20	Hesketh Bank (Storm)	775	345620	423980
21	Carr Brook (small river)	866	345950	421480
22	Yarrow and Lostock Rivers	938	348100	418800
23	Croston (STW) via Yarrow River	938	348100	418800
24	Croston (Storm) via Yarrow River	938	348100	418800

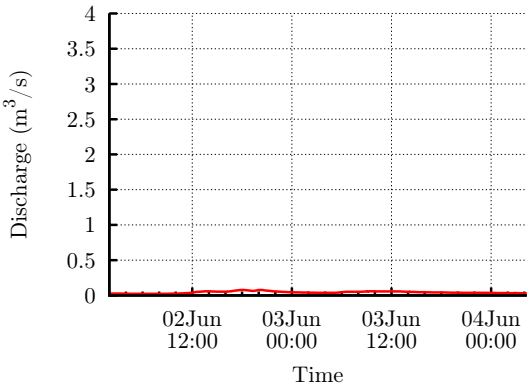

(a) Pool Stream

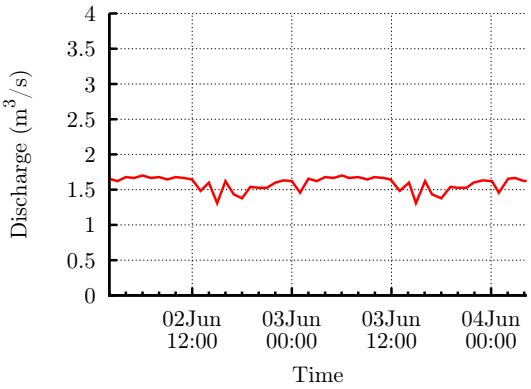

(b) Effluent Discharge at Preston (Clifton Marsh)

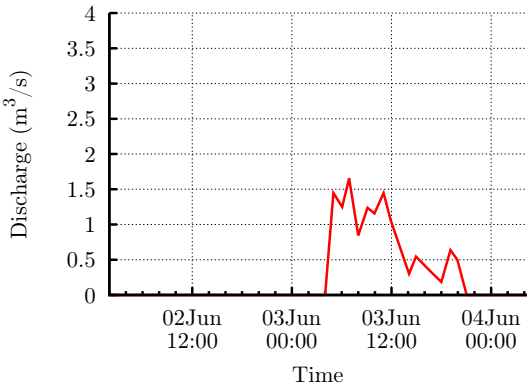

(c) Storm Discharge at Preston (Clifton Marsh)

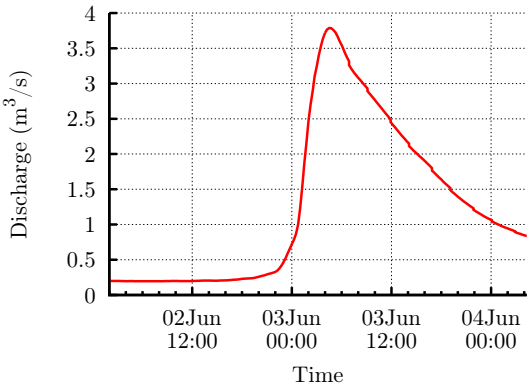

(d) Savick Brook and Deepdale

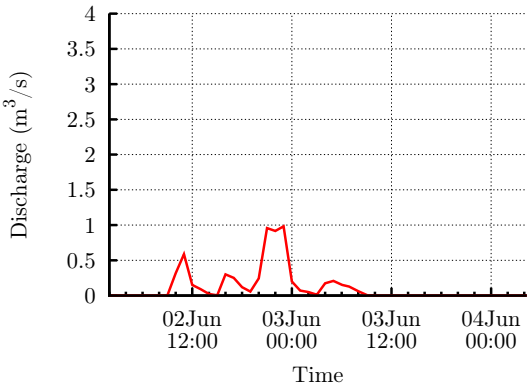

(e) Lea Gate (through Savick Brook)

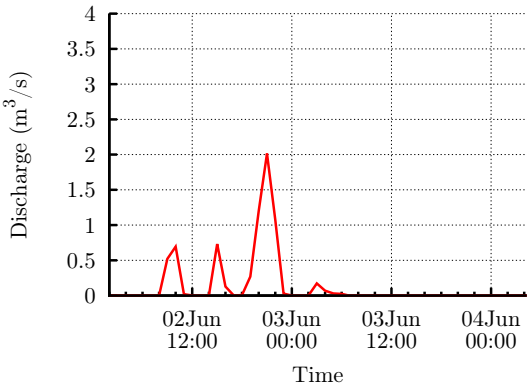

(f) Surface Water Culvert

Figure A.6: Lateral Flow Input Sources (Part 1)

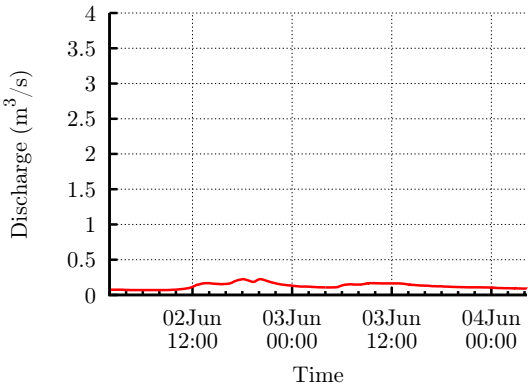

(a) Middle Pool and Dow Brook

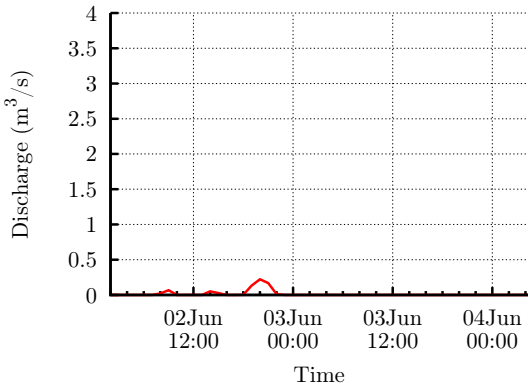

(b) Freckleton (CSOs)

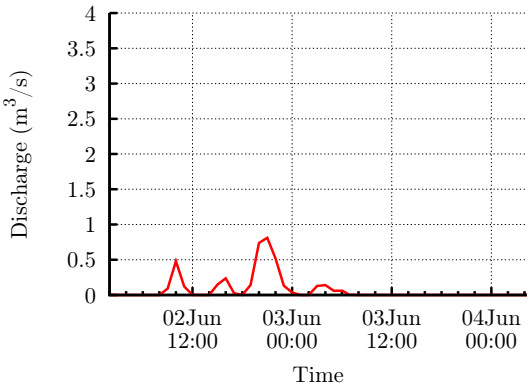

(c) Penwortham (PSS)

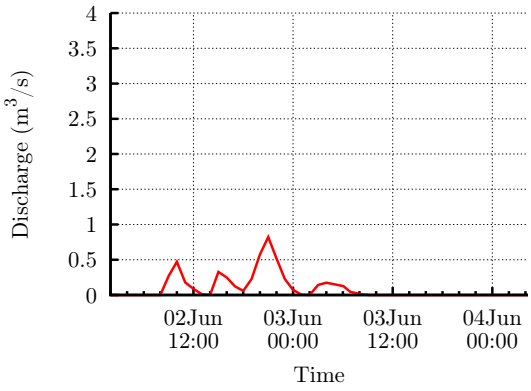

(d) Pre0022 (CSOs)

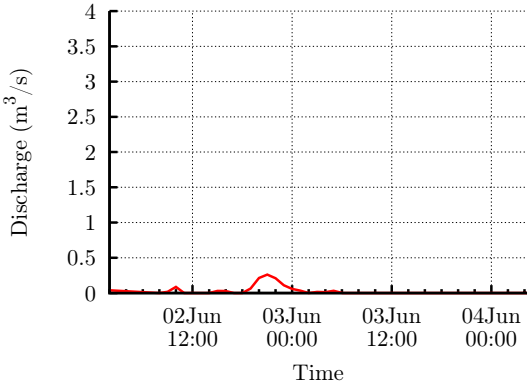

(e) Penwortham (CSOs)

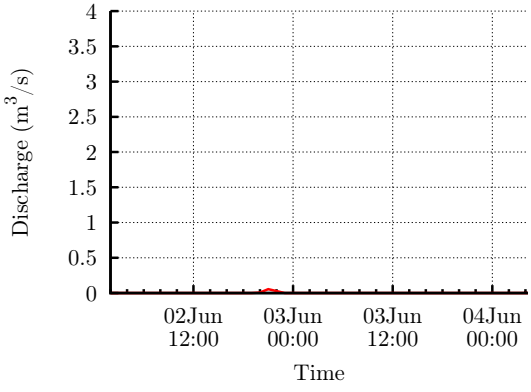

(f) Pre0028 (CSOs)

Figure A.7: Lateral Flow Input Sources (Part 2)

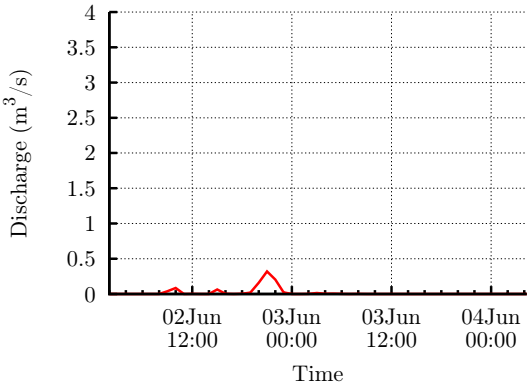

(a) Frenchwood (CSOs)

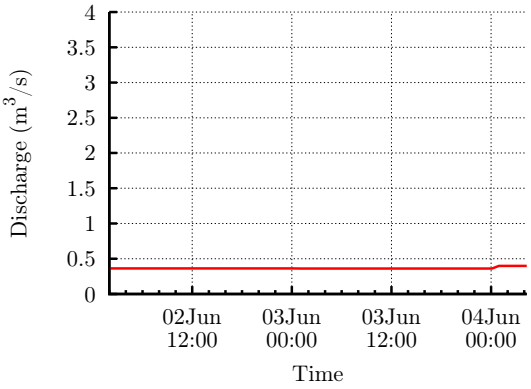

(b) Walton-le-Dale

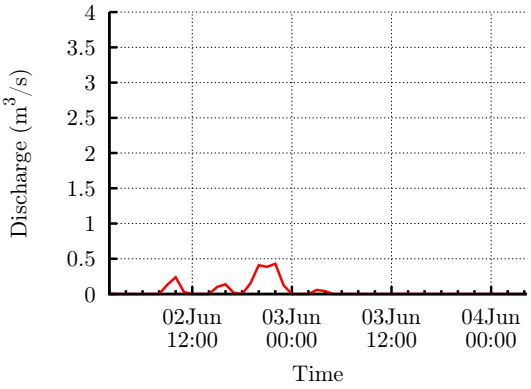

(c) Preston Town East (CSOs)

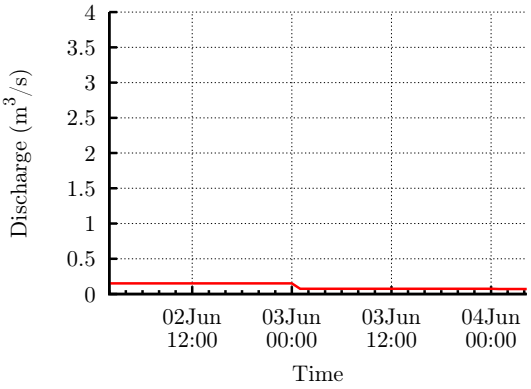

(d) Longton

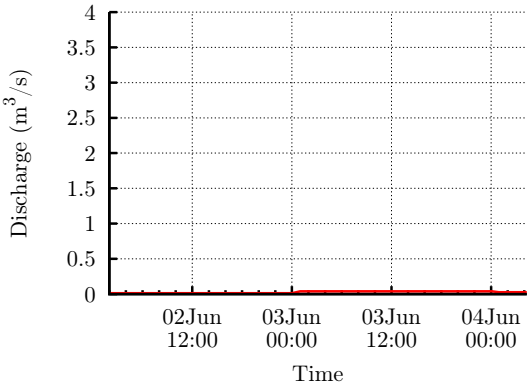

(e) Hesketh Bank

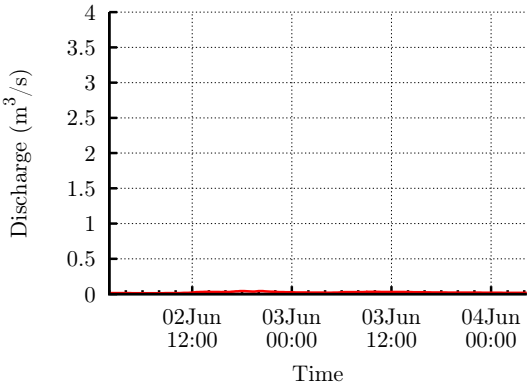

(f) Carr Brook

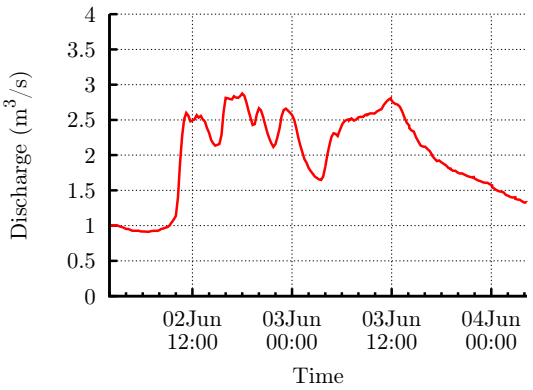

(g) Yarrow and Lostock Rivers

Figure A.8: Lateral Flow Input Sources (Part 3)

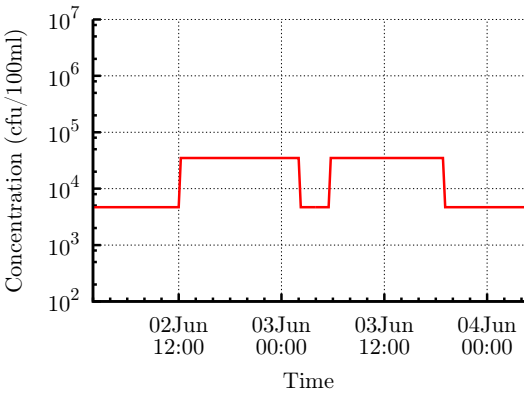

(a) Pool Stream

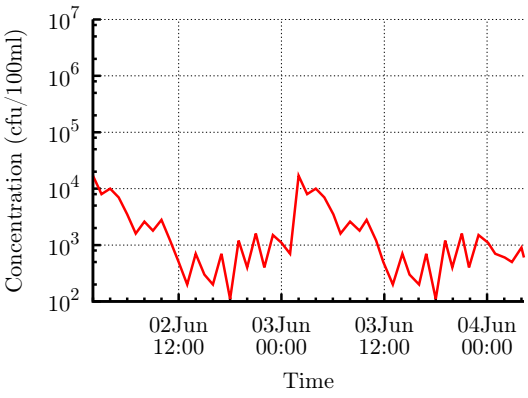

(b) Effluent Discharge at Preston (Clifton Marsh)

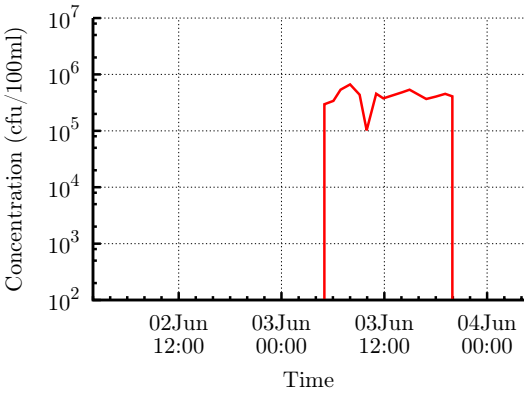

(c) Storm Discharge at Preston (Clifton Marsh)

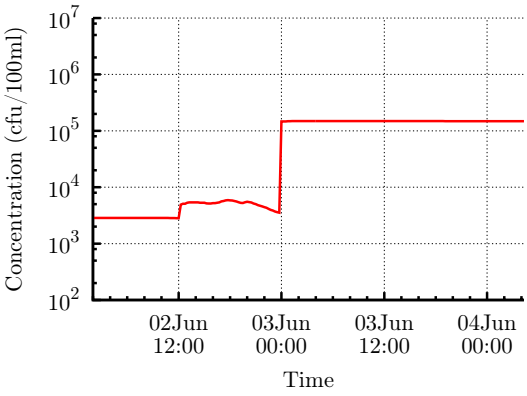

(d) Savick Brook and Deepdale

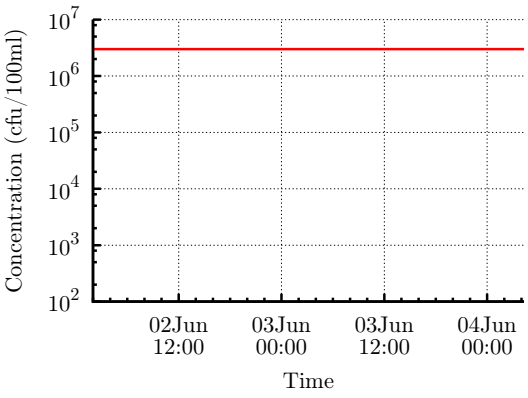

(e) Lea Gate (through Savick Brook)

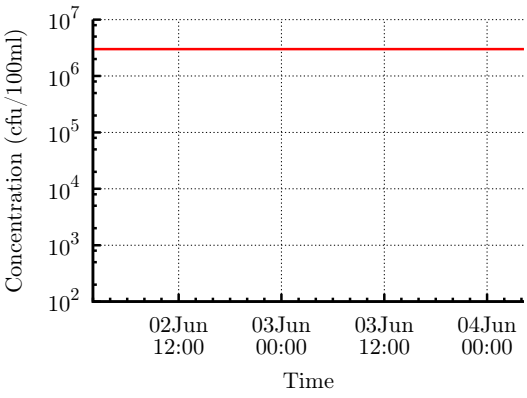

(f) Surface Water Culvert

Figure A.9: Lateral Faecal Coliform Input Sources (Part 1)

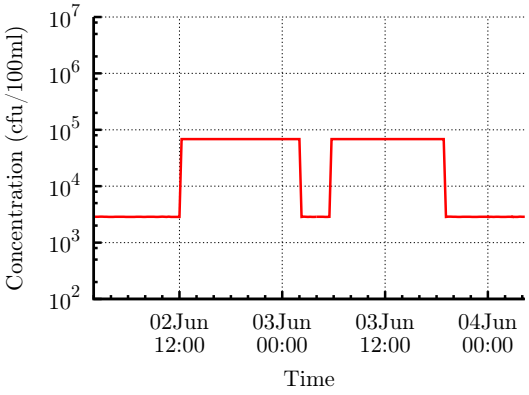

(a) Middle Pool and Dow Brook

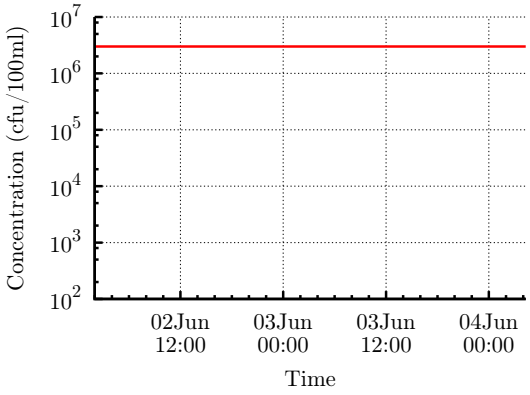

(b) Freckleton (CSOs)

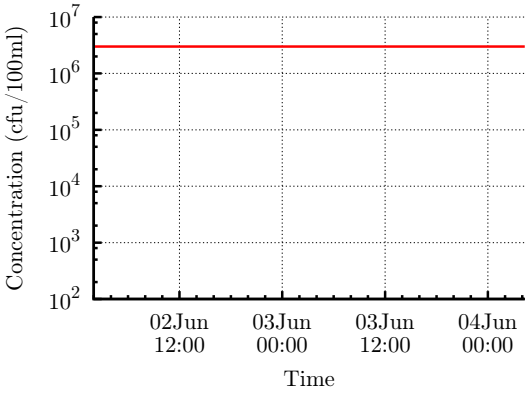

(c) Penwortham (PSS)

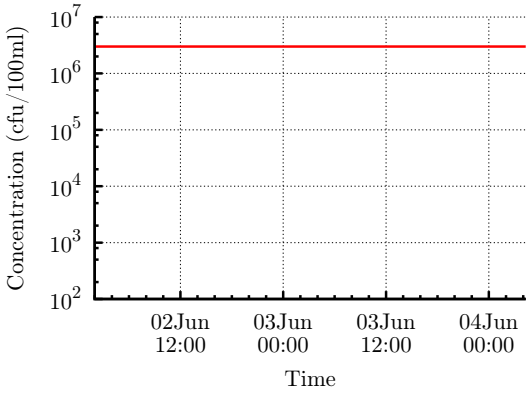

(d) Pre0022 (CSOs)

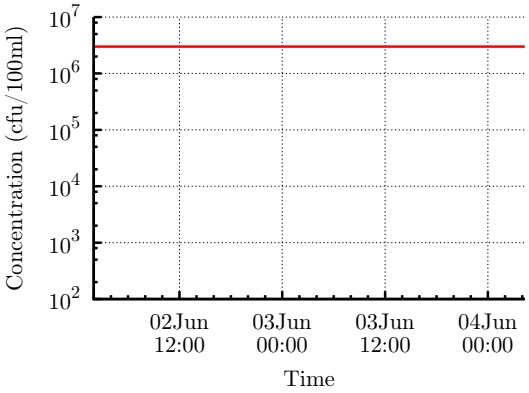

(e) Penwortham (CSOs)

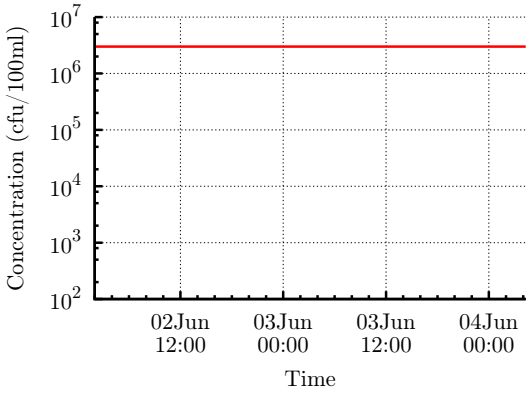

(f) Pre0028 (CSOs)

Figure A.10: Lateral Faecal Coliform Input Sources (Part 2)

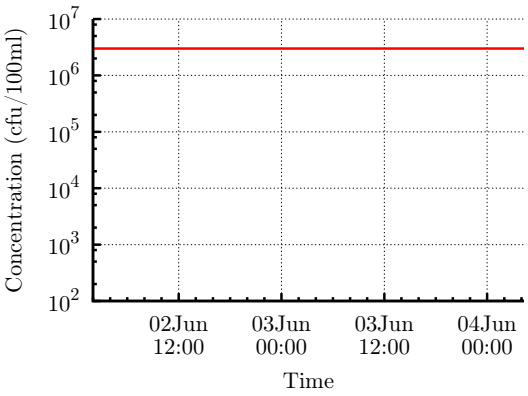

(a) Frenchwood (CSOs)

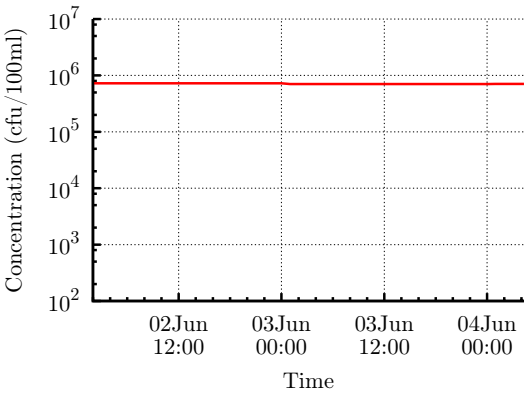

(b) Walton-le-Dale

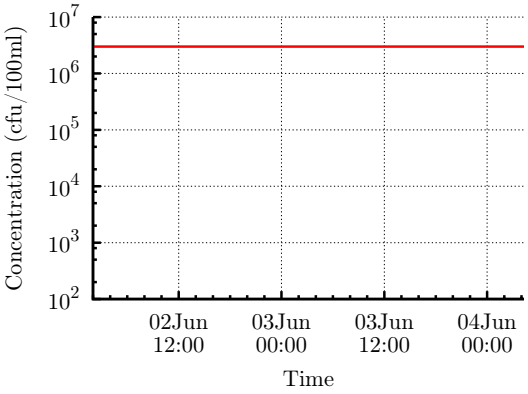

(c) Preston Town East (CSOs)

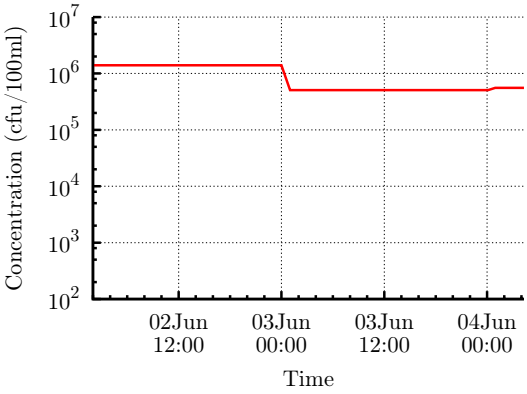

(d) Longton

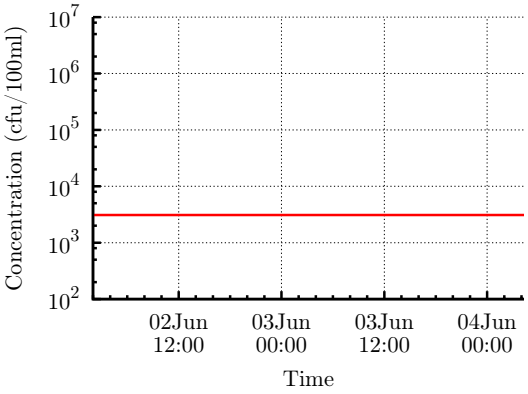

(e) Hesketh Bank

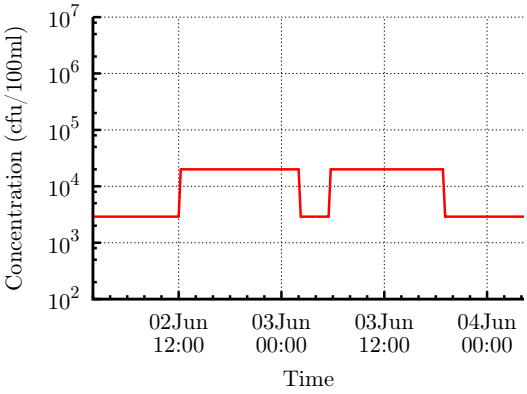

(f) Carr Brook

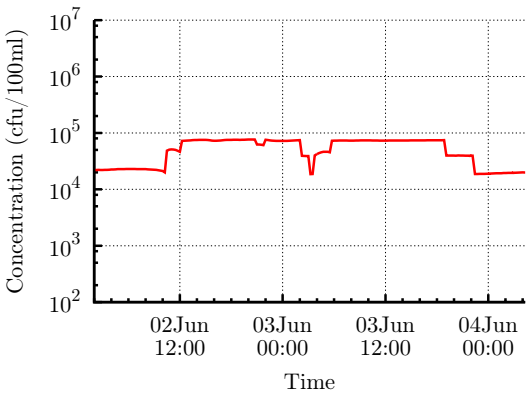

(g) Yarrow and Lostock Rivers

Figure A.11: Lateral Faecal Coliform Input Sources (Part 3)

A.3 Two-Dimensional(2D) Model

A.3.1 Outfall Input Sources

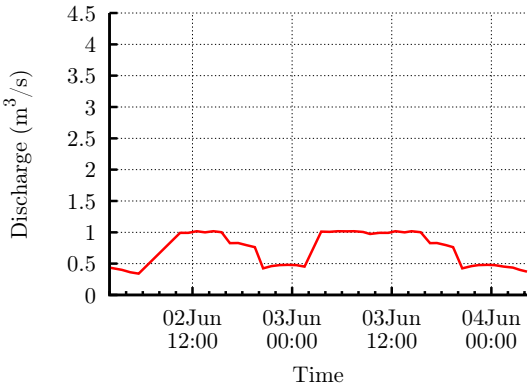

(a) Southport WwTw

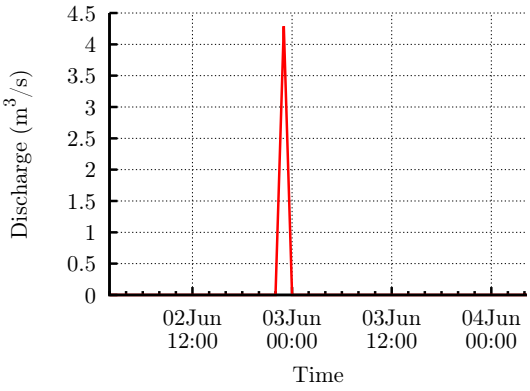

(b) Manchester Square Outfall

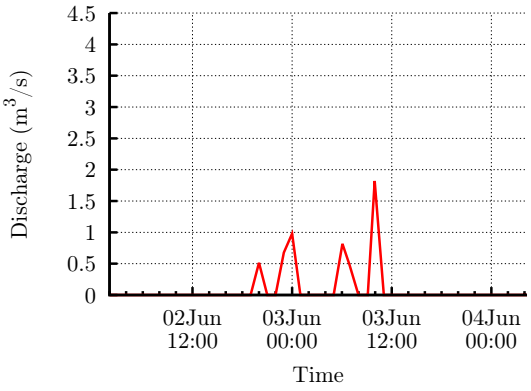

(c) Anchorsholme Outfall

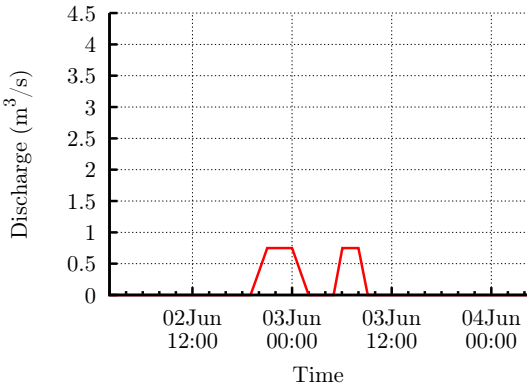

(d) Fairhaven Tanks

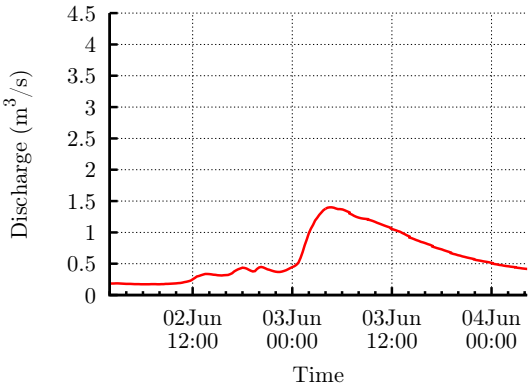

(e) Main Drain

Figure A.12: Outfall Flow Inputs

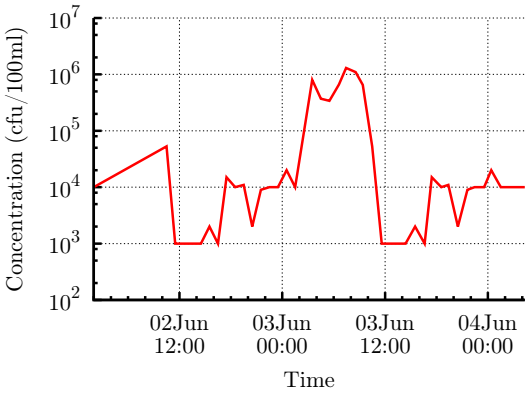

(a) Southport WwTw

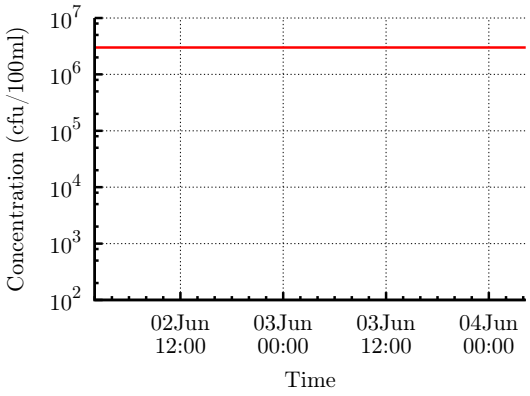

(b) Manchester Square Outfall

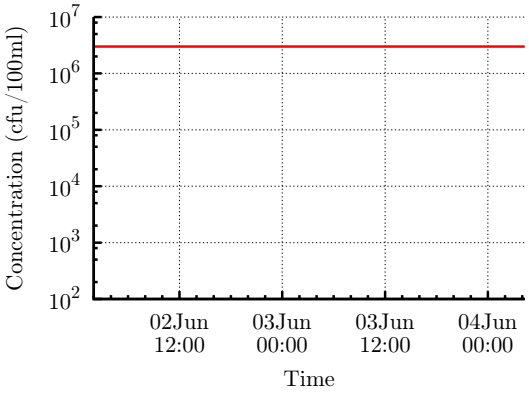

(c) Anchorsholme Outfall

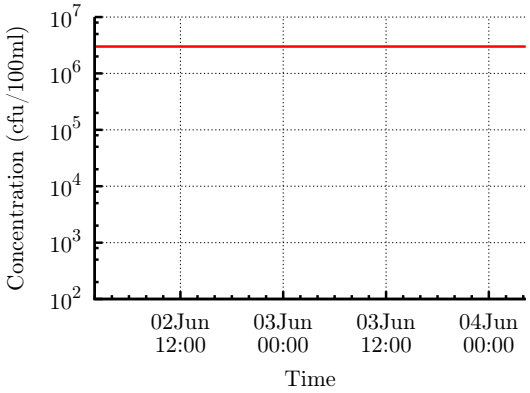

(d) Fairhaven Tanks

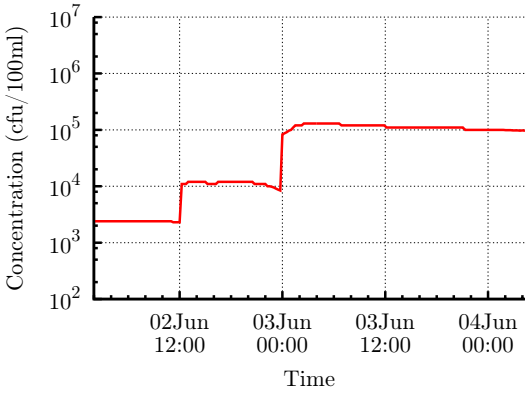

(e) Main Drain

Figure A.13: Outfall Faecal Coliform Inputs

Appendix B

Ribble Estuary : Results

B.1 Previous work (Kashefipour)

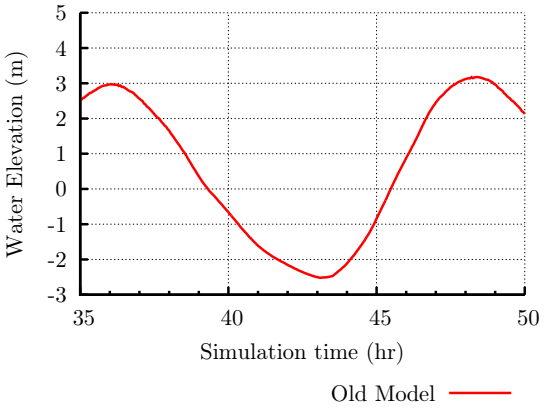

(a) Milepost 11

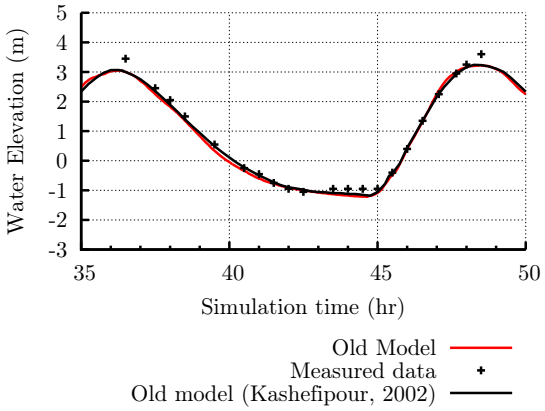

(b) Milepost 7

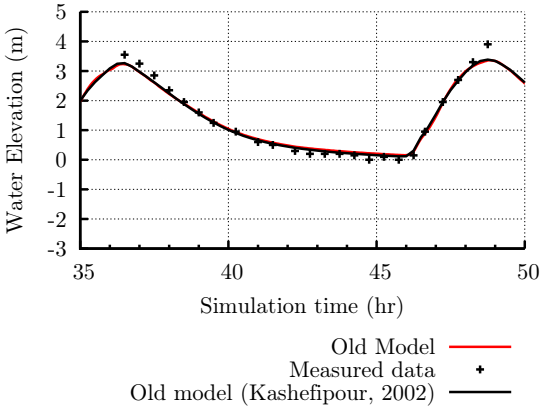

(c) Milepost 3

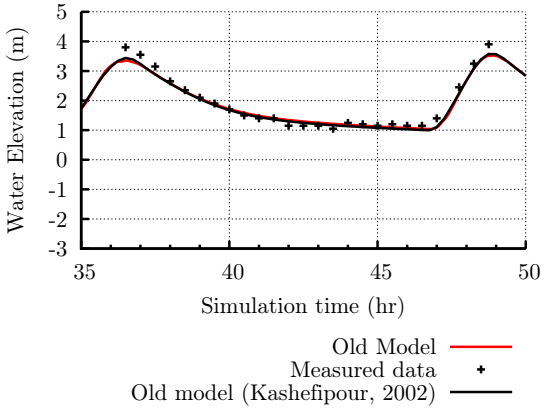

(d) Bullnose

Figure B.1: Water Elevations for old model

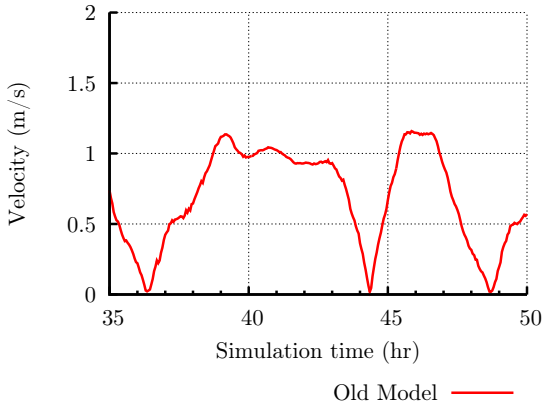

(a) Milepost 11

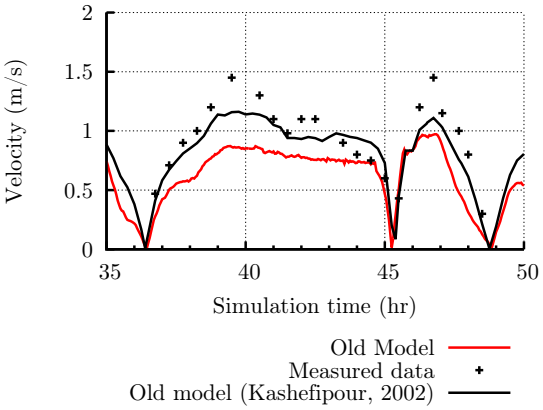

(b) Milepost 7

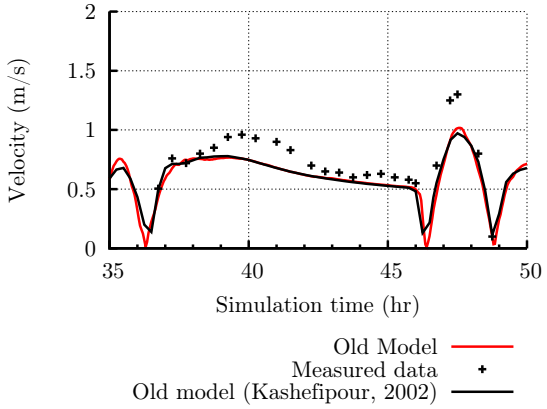

(c) Milepost 3

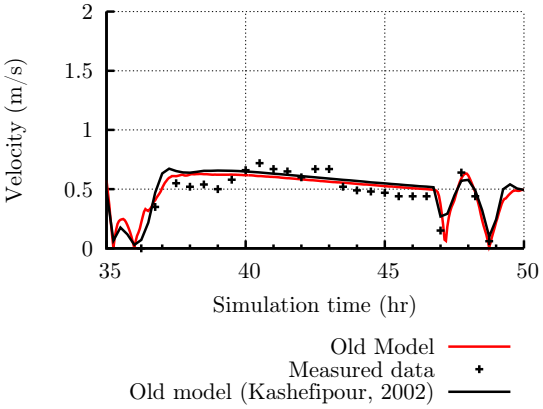

(d) Bullnose

Figure B.2: Velocities for old model

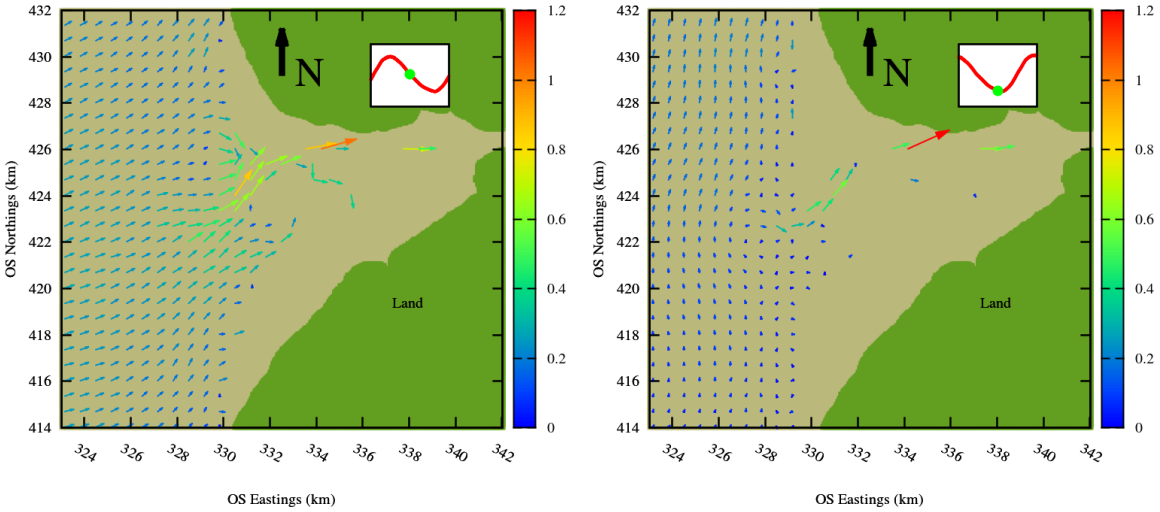

(a) Mid Ebb

(b) Low Tide

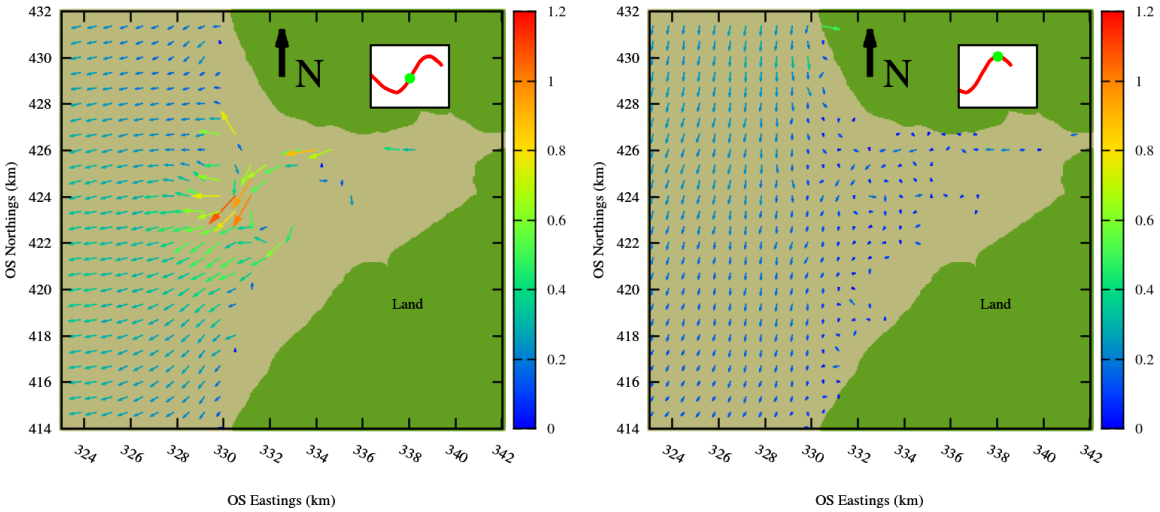

(c) Mid Flood

(d) High Tide

Figure B.3: Flow Directions for old model

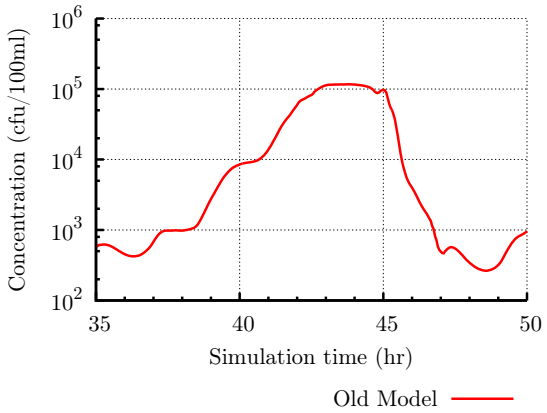

(a) Milepost 11

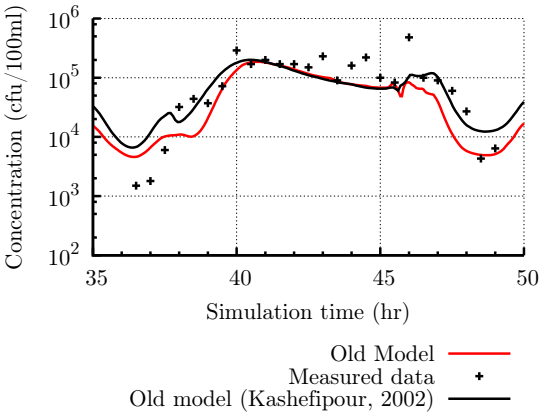

(b) Milepost 7

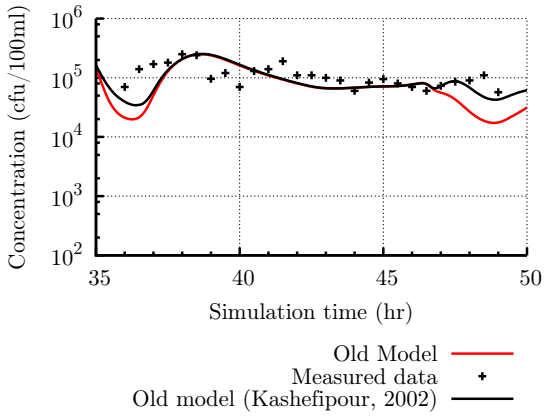

(c) Milepost 3

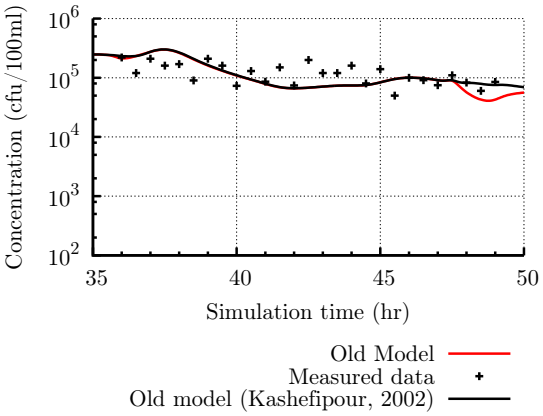

(d) Bullnose

Figure B.4: Faecal Coliform Concentrations for old model

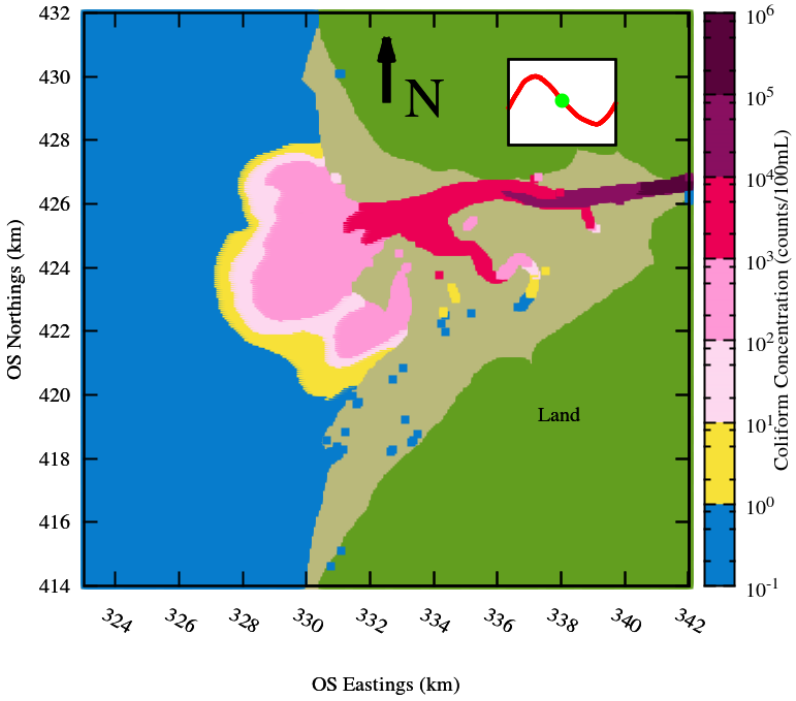

Figure B.5: Faecal Coliform at Mid Ebb

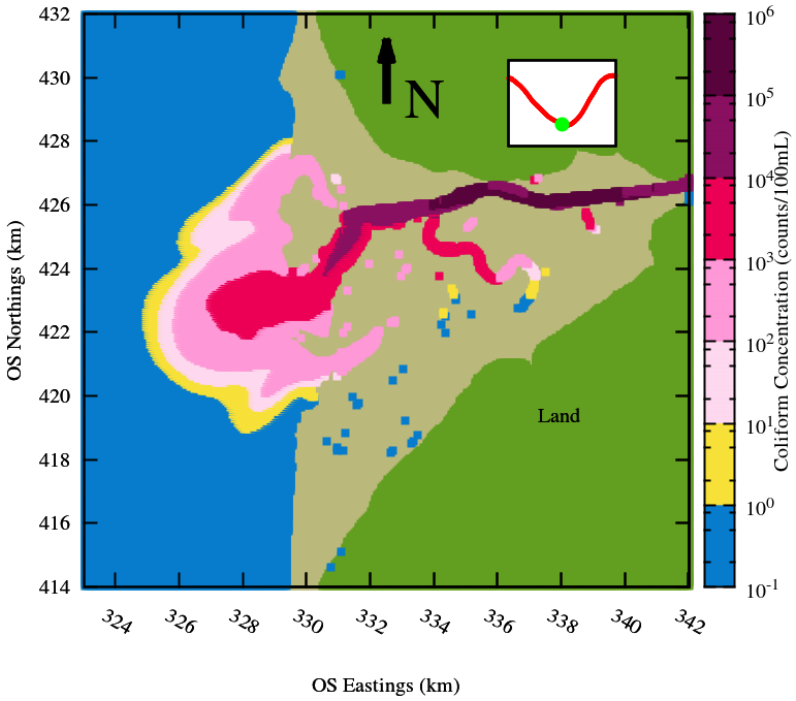

Figure B.6: Faecal Coliform at Low Tide

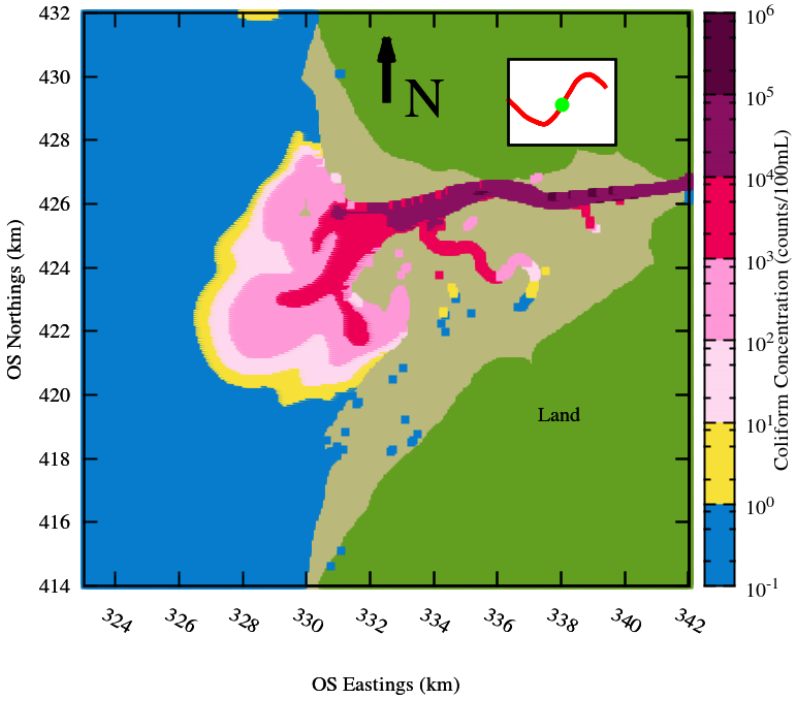

Figure B.7: Faecal Coliform at Mid Flood

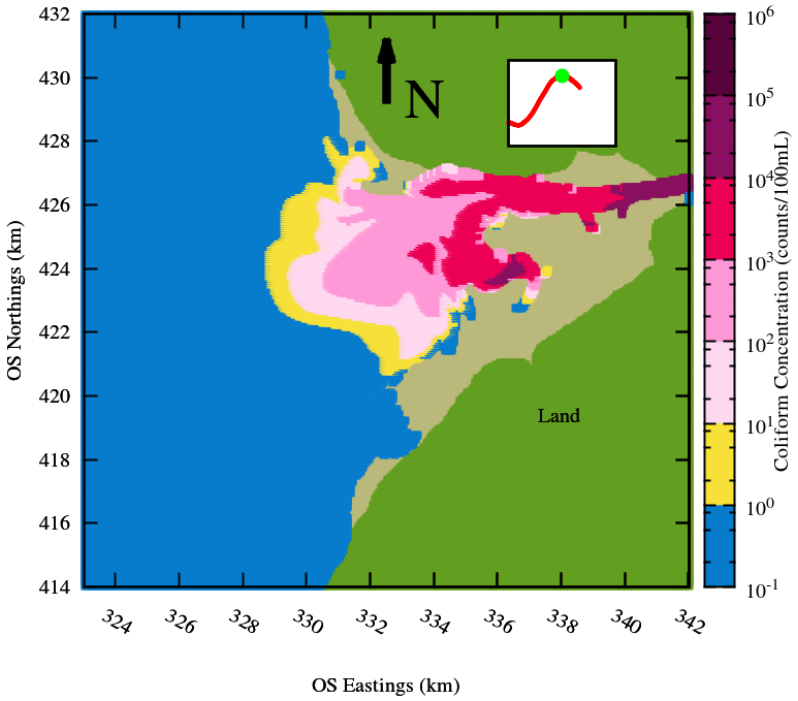

Figure B.8: Faecal Coliform at High Tide

B.2 C2C Scenarios

B.2.1 Common Decay Rates

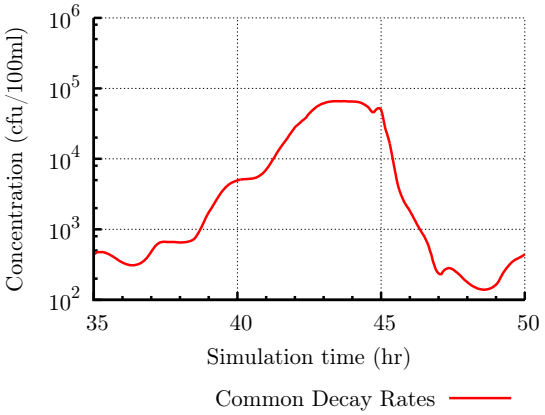

(a) Milepost 11

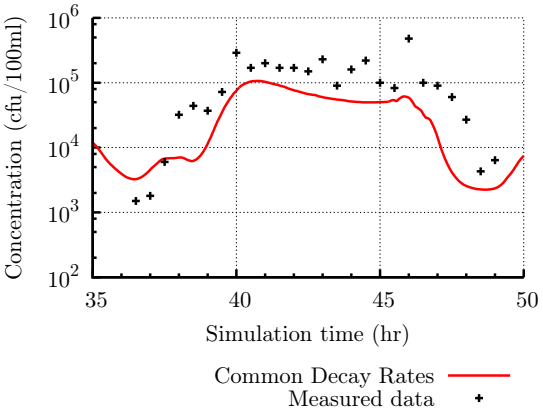

(b) Milepost 7

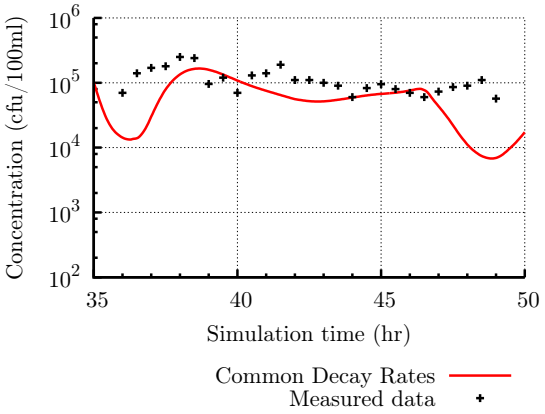

(c) Milepost 3

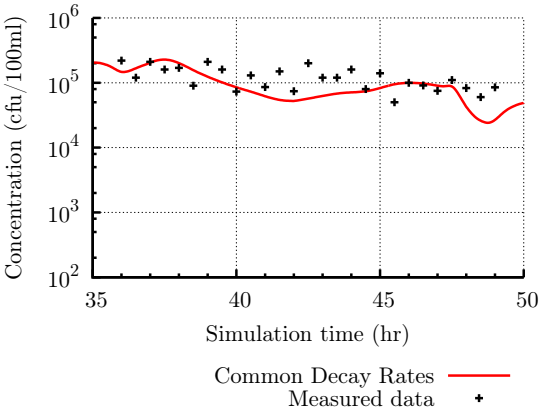

(d) Bullnose

Figure B.9: Faecal Coliform Concentrations due to Common Decay Rates

B.2.2 Common Dispersion

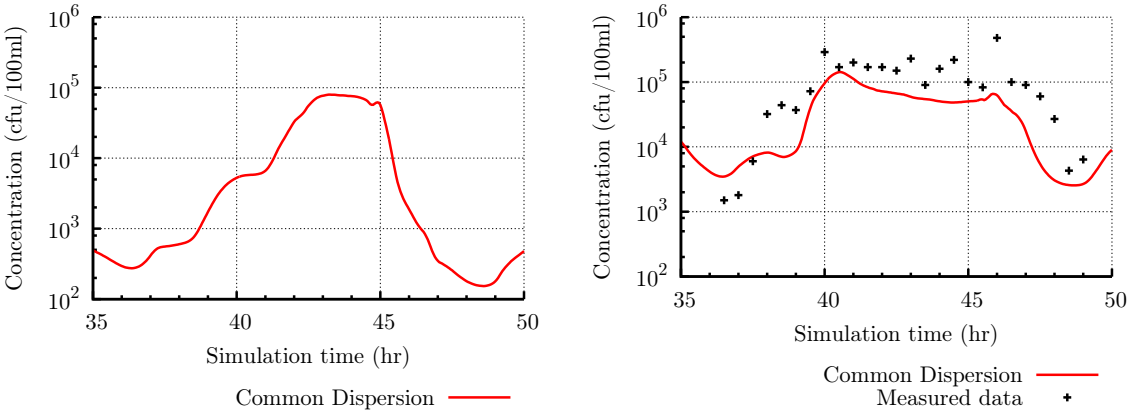

(a) Milepost 11

(b) Milepost 7

(c) Milepost 3

(d) Bullnose

Figure B.10: Faecal Coliform Concentrations due to Common Dispersion

B.2.3 Improved Link

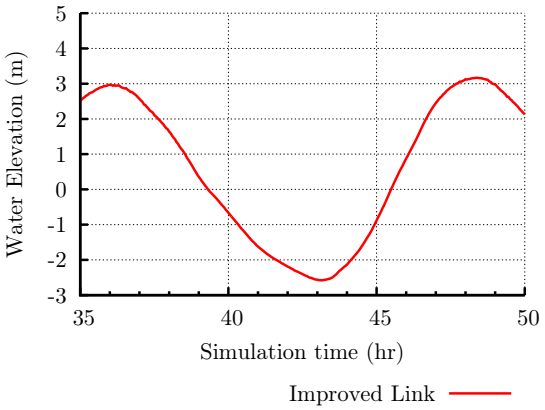

(a) Milepost 11

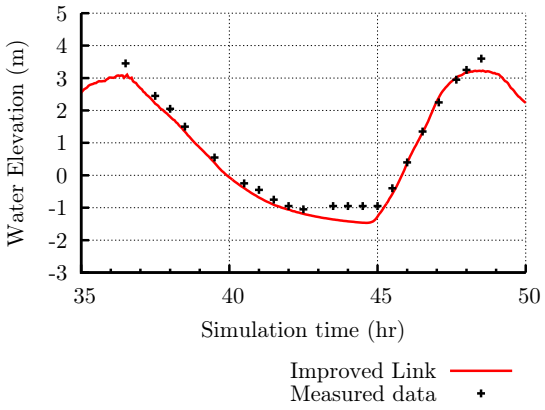

(b) Milepost 7

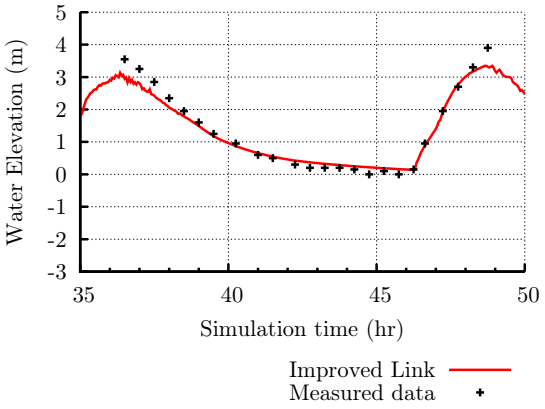

(c) Milepost 3

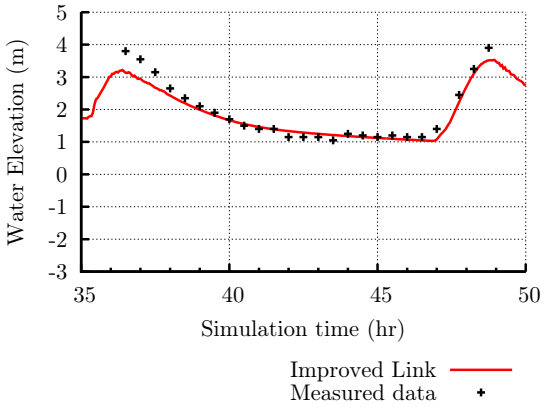

(d) Bullnose

Figure B.11: Water Elevations due to Improved Link

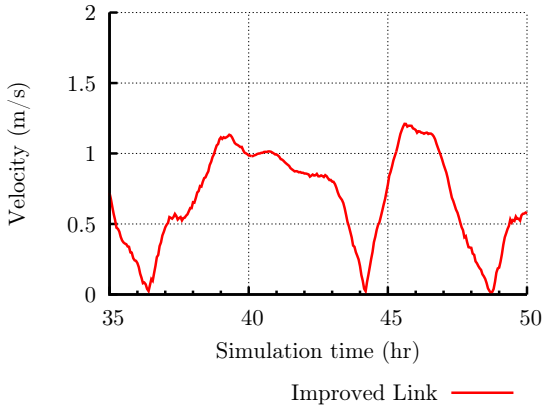

(a) Milepost 11

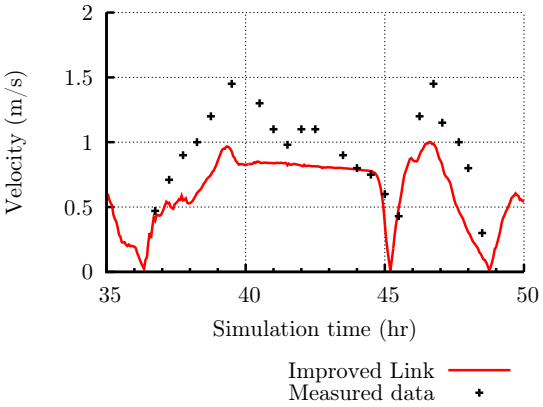

(b) Milepost 7

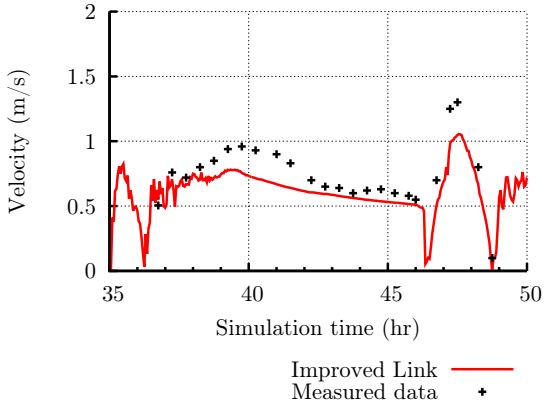

(c) Milepost 3

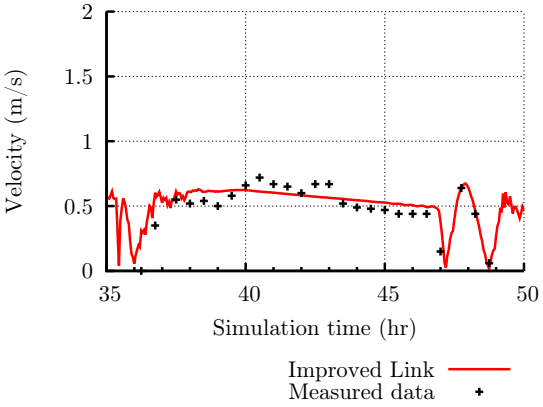

(d) Bullnose

Figure B.12: Velocities due to Improved Link

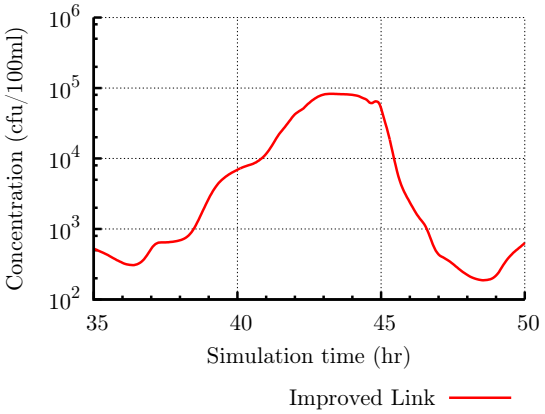

(a) Milepost 11

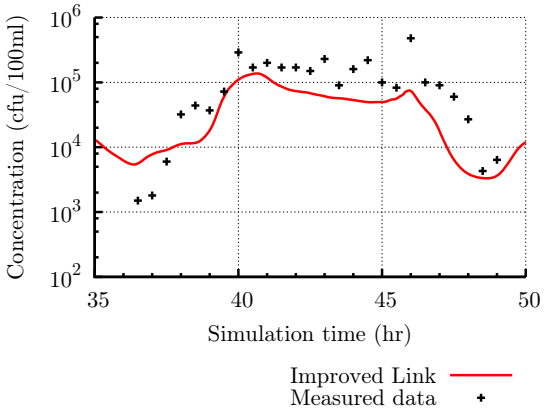

(b) Milepost 7

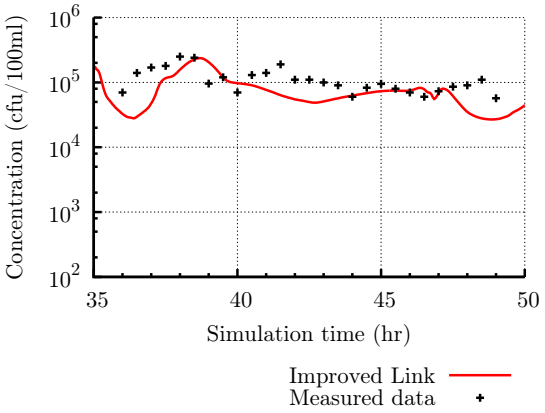

(c) Milepost 3

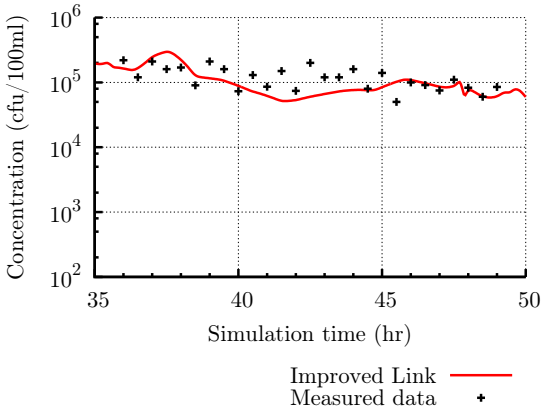

(d) Bullnose

Figure B.13: Faecal Coliform Concentrations due to Improved Link

B.2.4 Common Friction

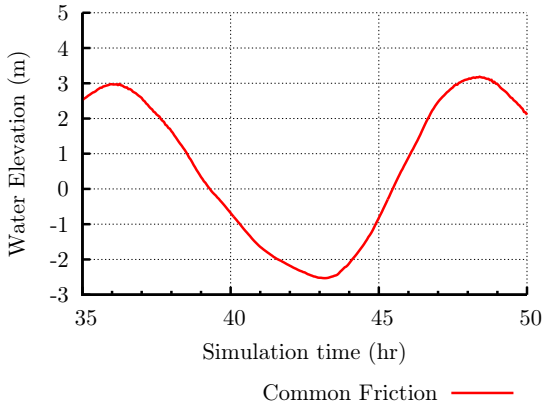

(a) Milepost 11

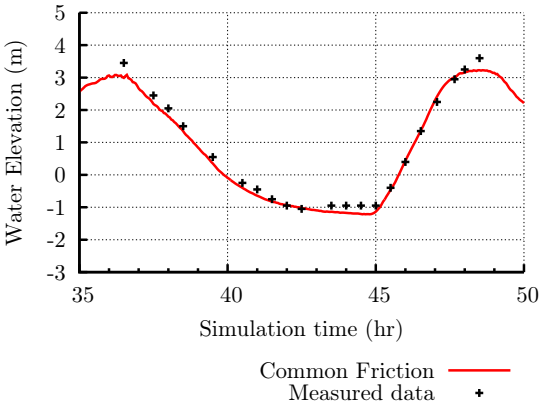

(b) Milepost 7

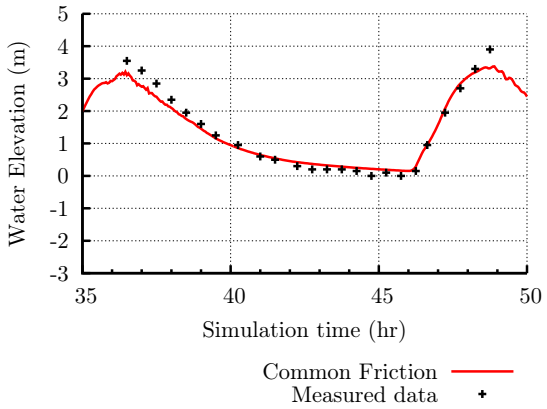

(c) Milepost 3

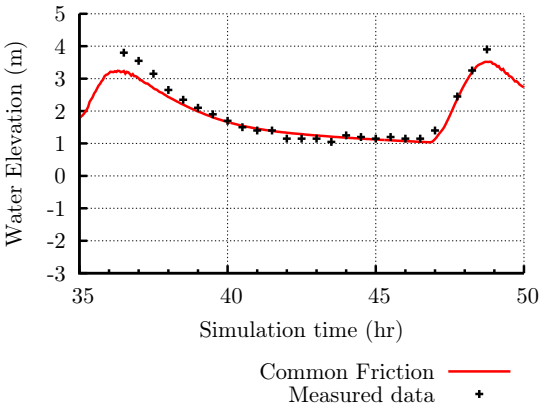

(d) Bullnose

Figure B.14: Water Elevations due to Common Friction

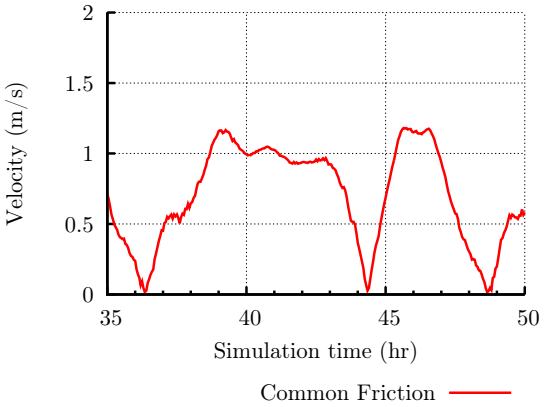

(a) Milepost 11

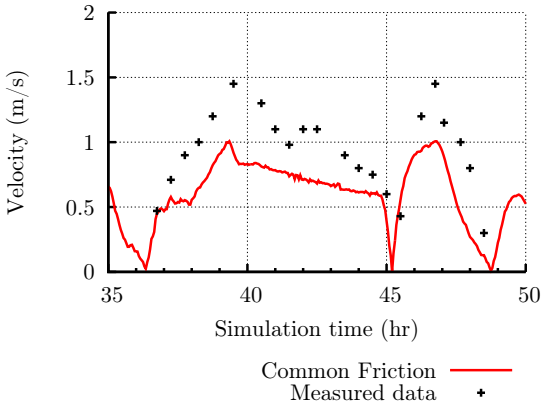

(b) Milepost 7

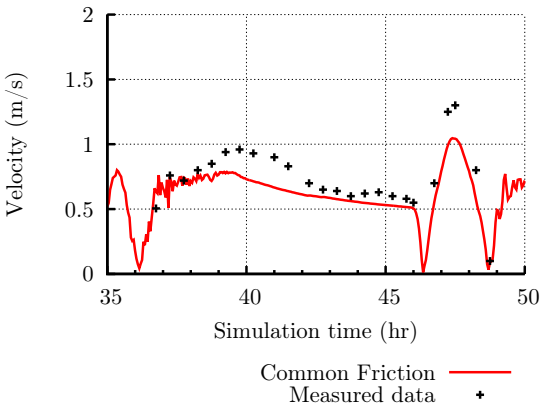

(c) Milepost 3

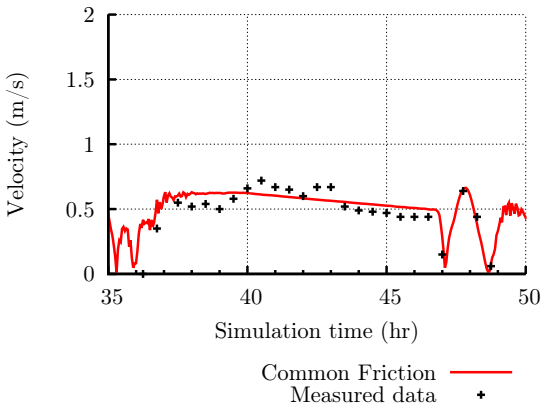

(d) Bullnose

Figure B.15: Velocities due to Common Friction

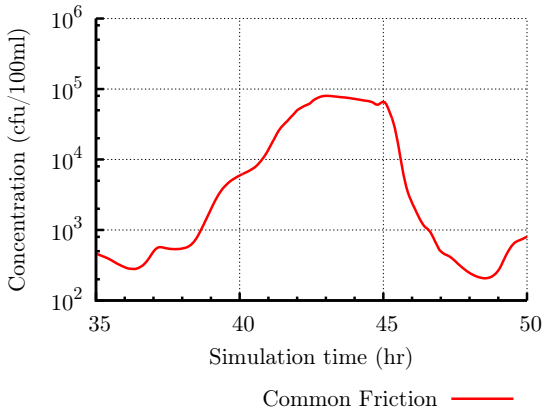

(a) Milepost 11

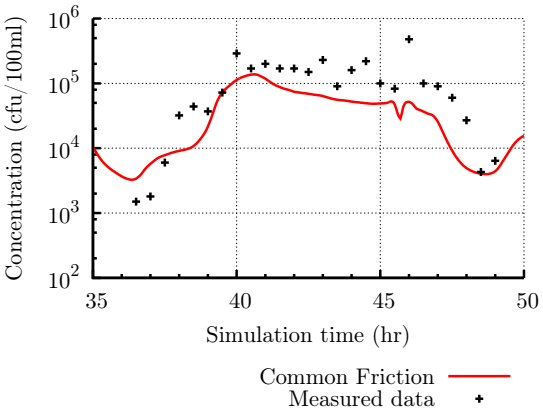

(b) Milepost 7

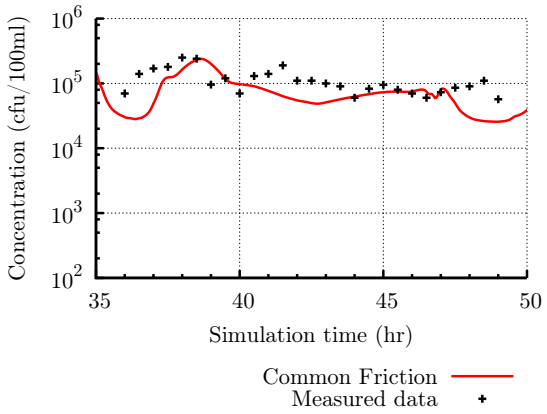

(c) Milepost 3

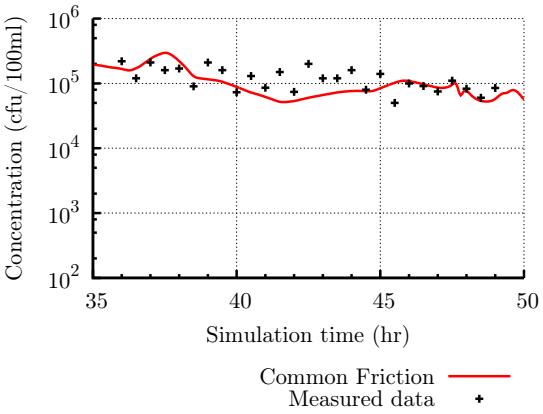

(d) Bullnose

Figure B.16: Faecal Coliform Concentrations due to Common Friction

B.2.5 Water Temperature

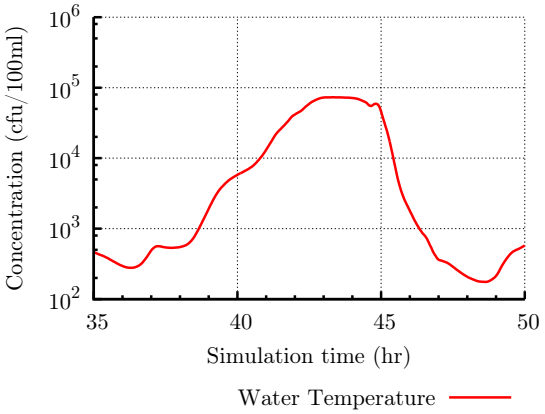

(a) Milepost 11

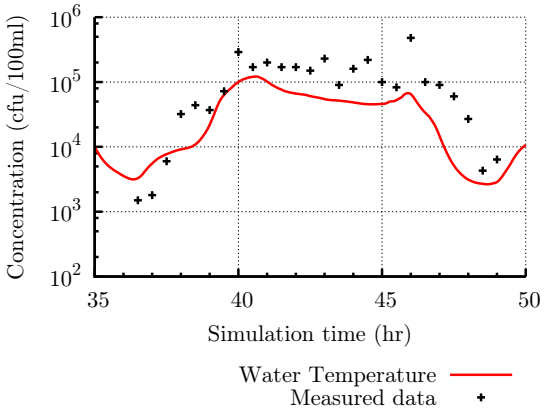

(b) Milepost 7

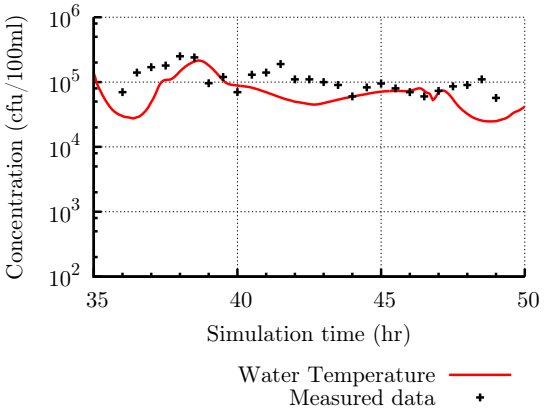

(c) Milepost 3

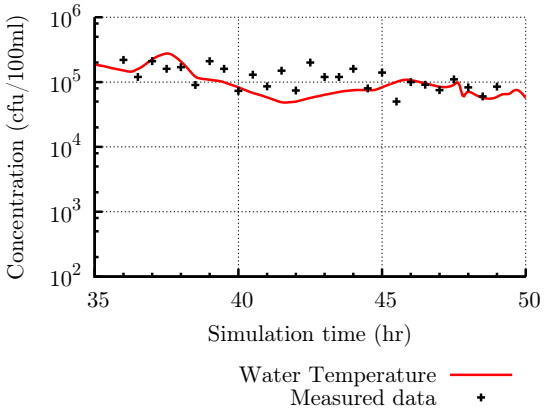

(d) Bullnose

Figure B.17: Faecal Coliform Concentrations due to Water Temperature

B.2.6 Salinity

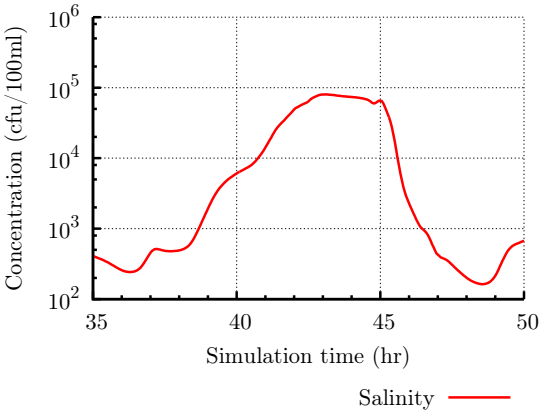

(a) Milepost 11

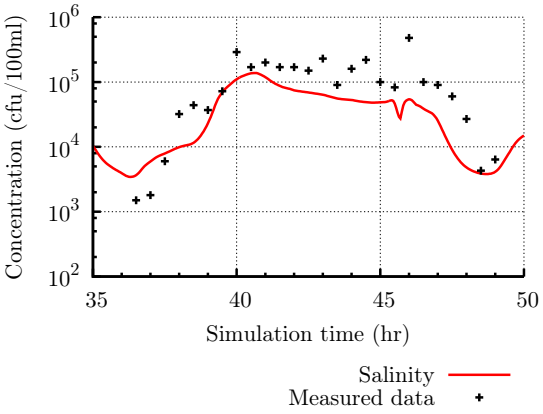

(b) Milepost 7

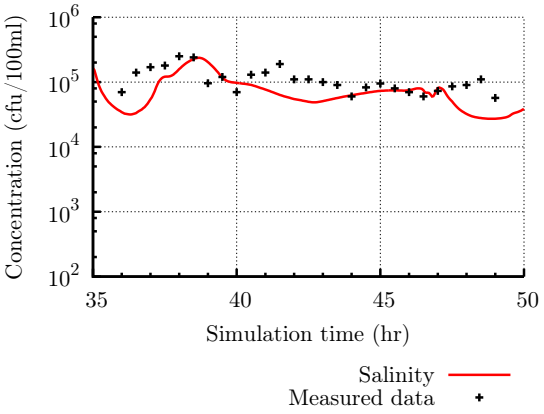

(c) Milepost 3

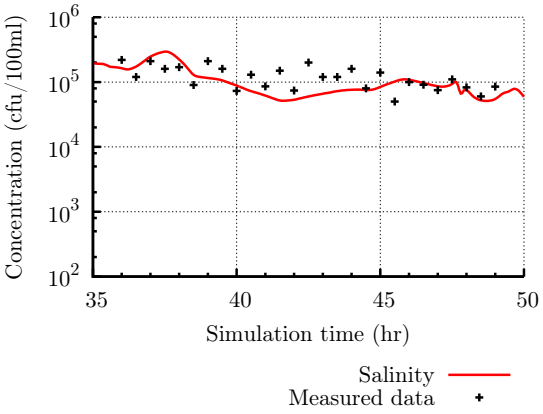

(d) Bullnose

Figure B.18: Faecal Coliform Concentrations due to Salinity

B.2.7 Solar Radiation

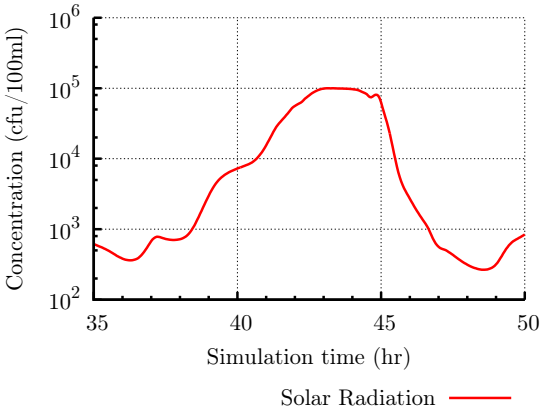

(a) Milepost 11

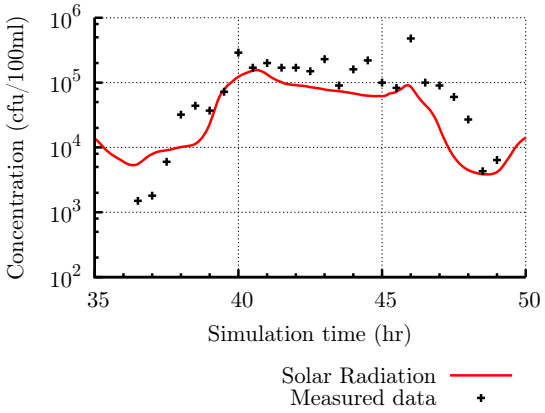

(b) Milepost 7

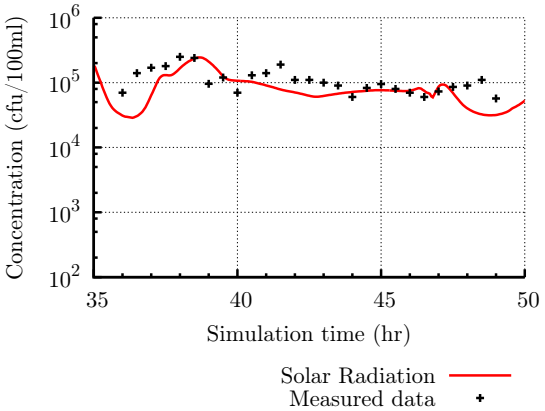

(c) Milepost 3

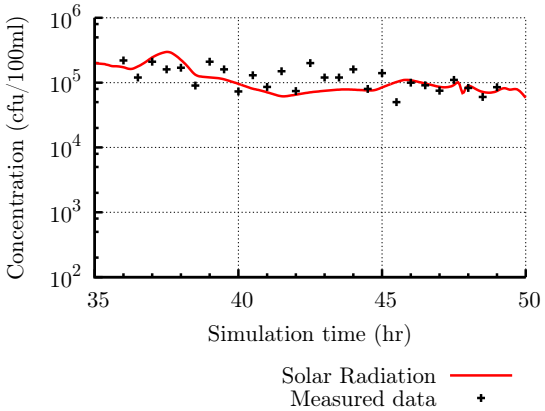

(d) Bullnose

Figure B.19: Faecal Coliform Concentrations due to Solar Radiation

B.2.8 Turbidity

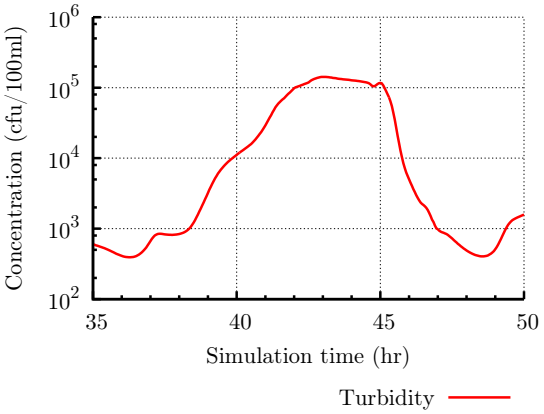

(a) Milepost 11

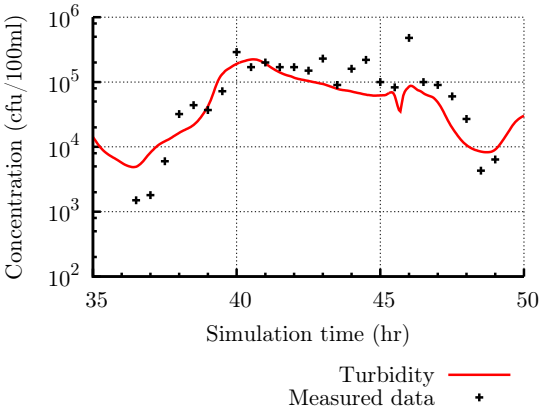

(b) Milepost 7

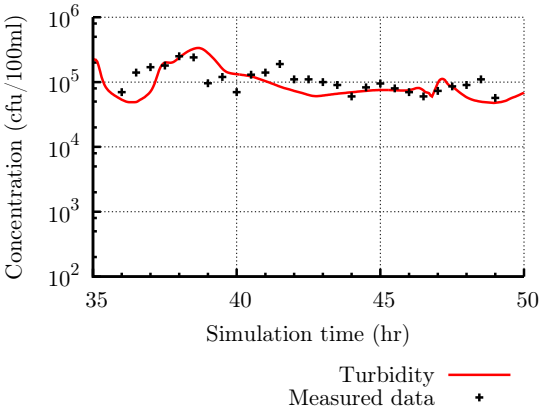

(c) Milepost 3

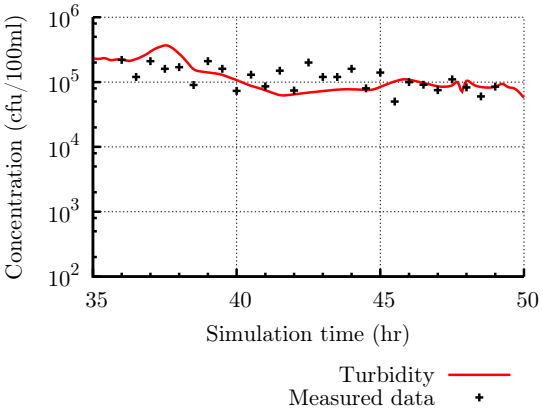

(d) Bullnose

Figure B.20: Faecal Coliform Concentrations due to Turbidity

B.2.9 Combined Effects

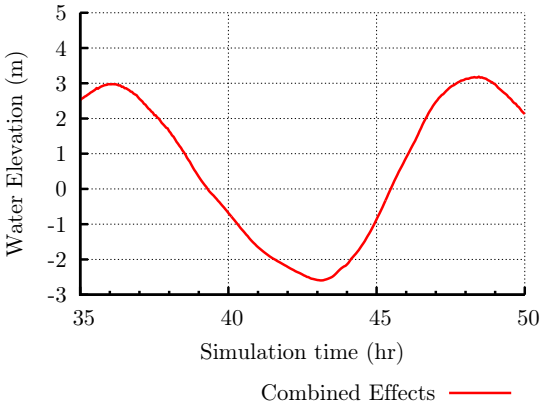

(a) Milepost 11

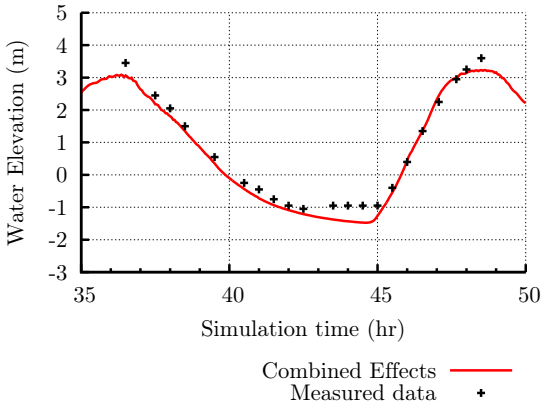

(b) Milepost 7

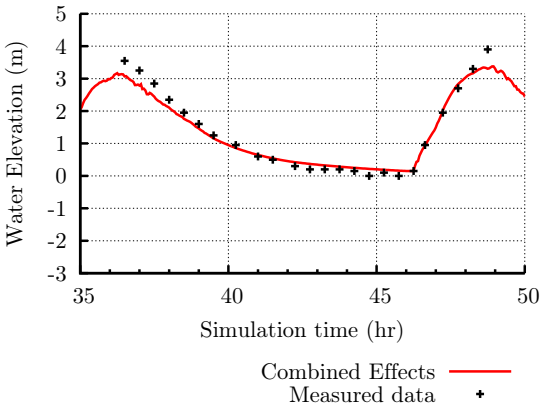

(c) Milepost 3

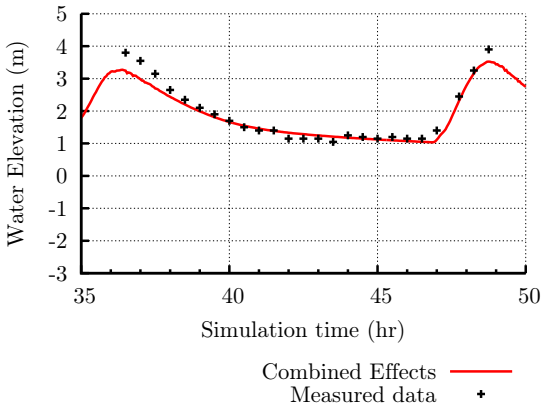

(d) Bullnose

Figure B.21: Water Elevations due to Combined Effects

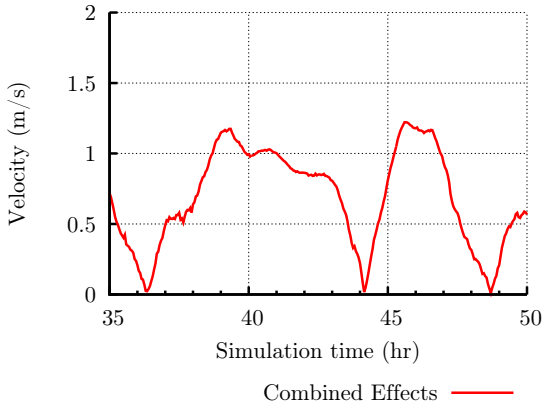

(a) Milepost 11

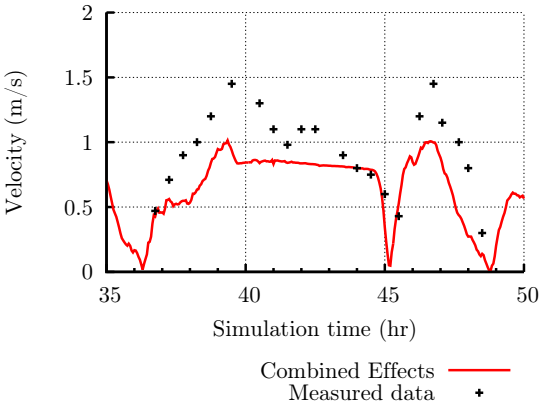

(b) Milepost 7

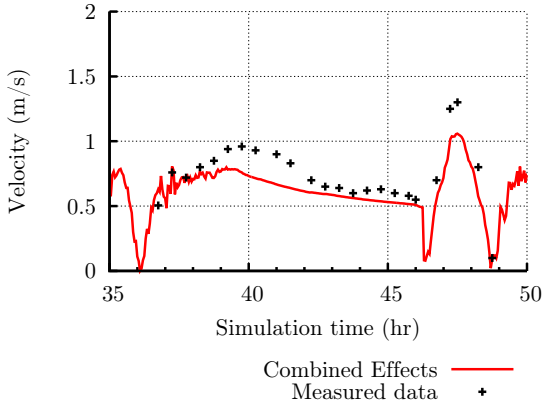

(c) Milepost 3

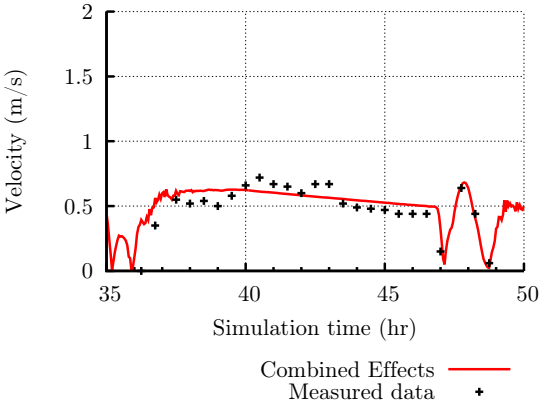

(d) Bullnose

Figure B.22: Velocities due to Combined Effects

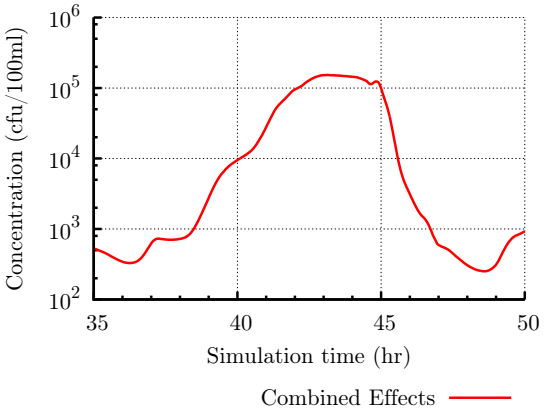

(a) Milepost 11

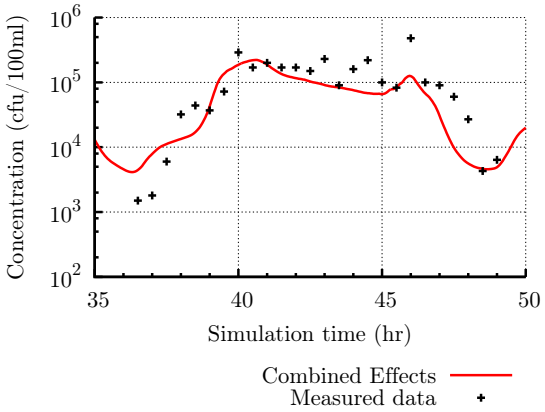

(b) Milepost 7

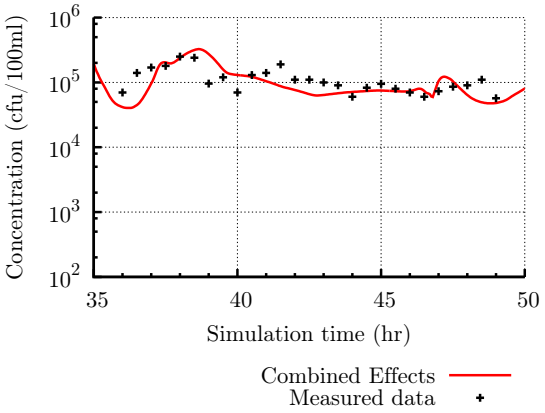

(c) Milepost 3

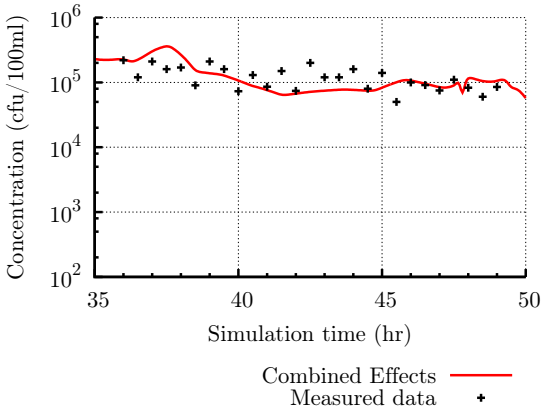

(d) Bullnose

Figure B.23: Faecal Coliform Concentrations due to Combined Effects

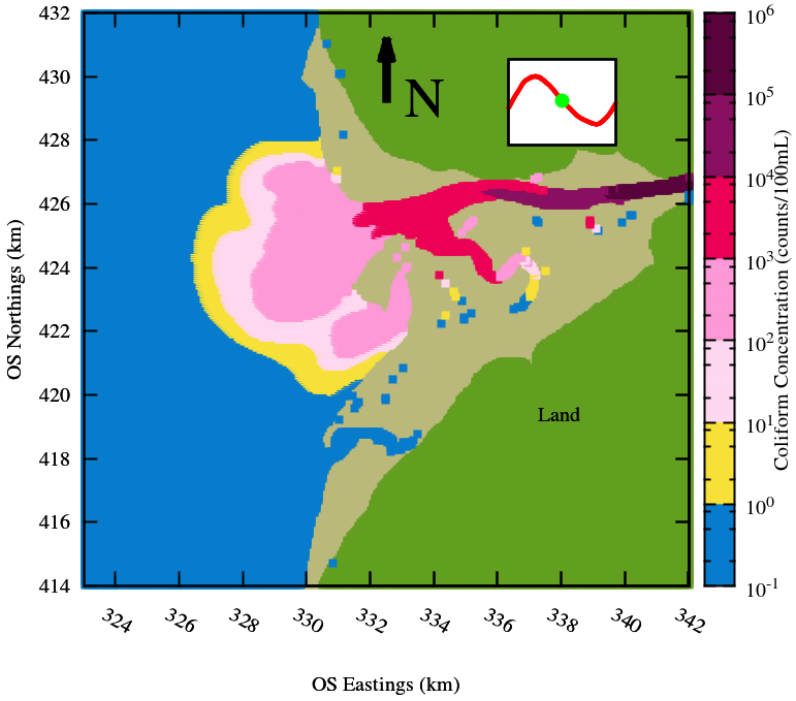

Figure B.24: Faecal Coliform at Mid Ebb due to Combined Effects

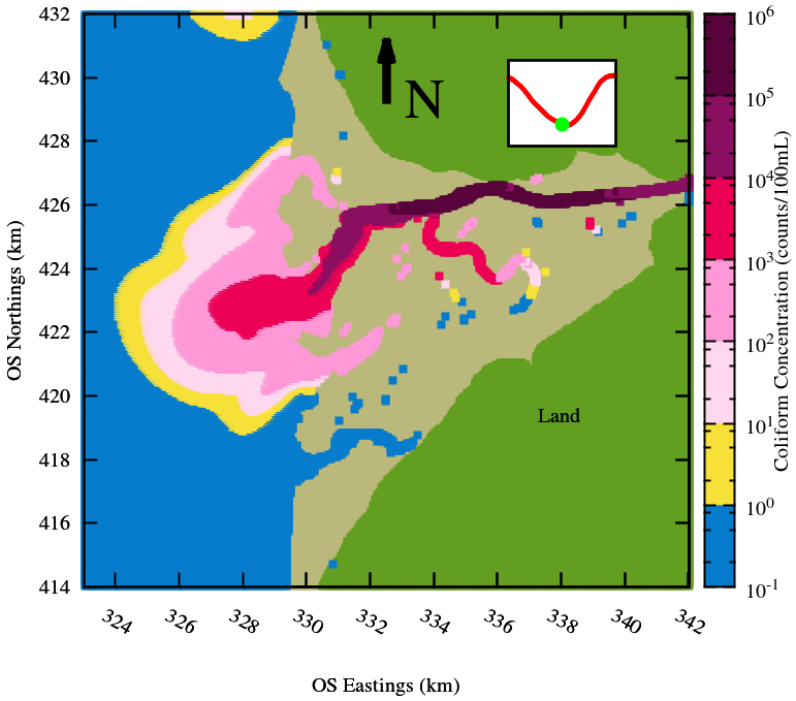

Figure B.25: Faecal Coliform at Low Tide due to Combined Effects

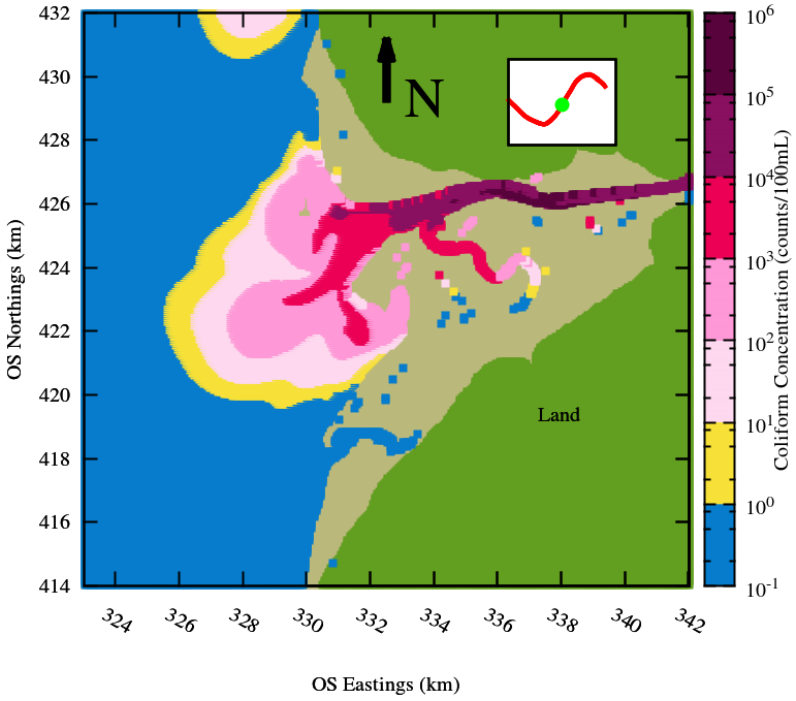

Figure B.26: Faecal Coliform at Mid Flood due to Combined Effects

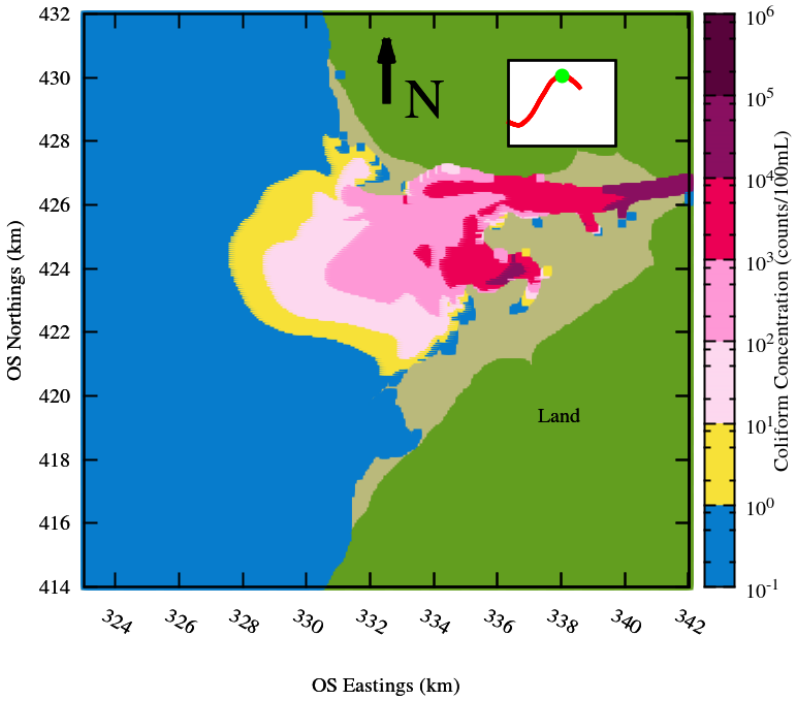

Figure B.27: Faecal Coliform at High Tide due to Combined Effects

B.3 Comparison of C2C Scenarios (Revised Model)

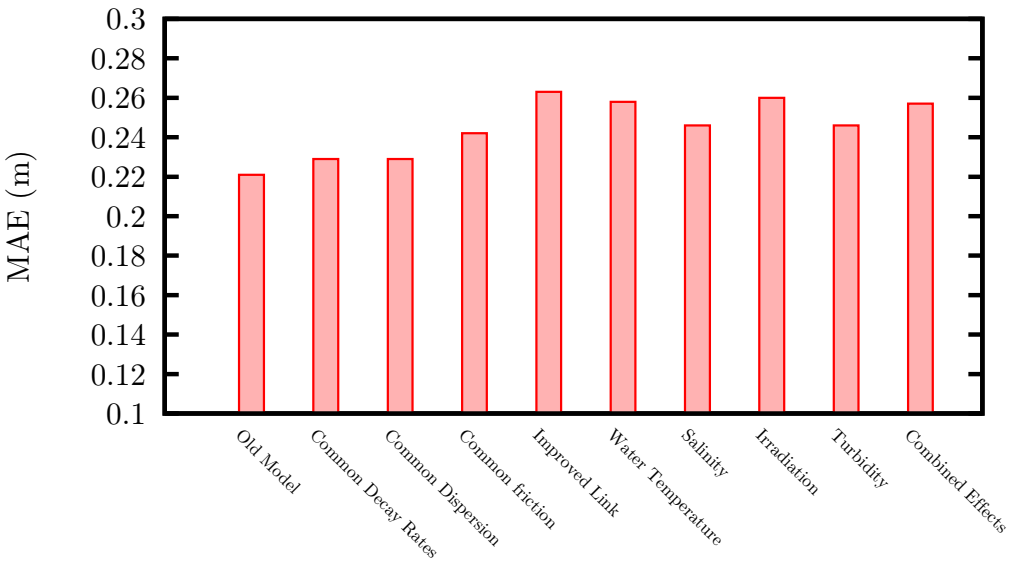

Figure B.28: Comparison of Elevations (Revised Model)

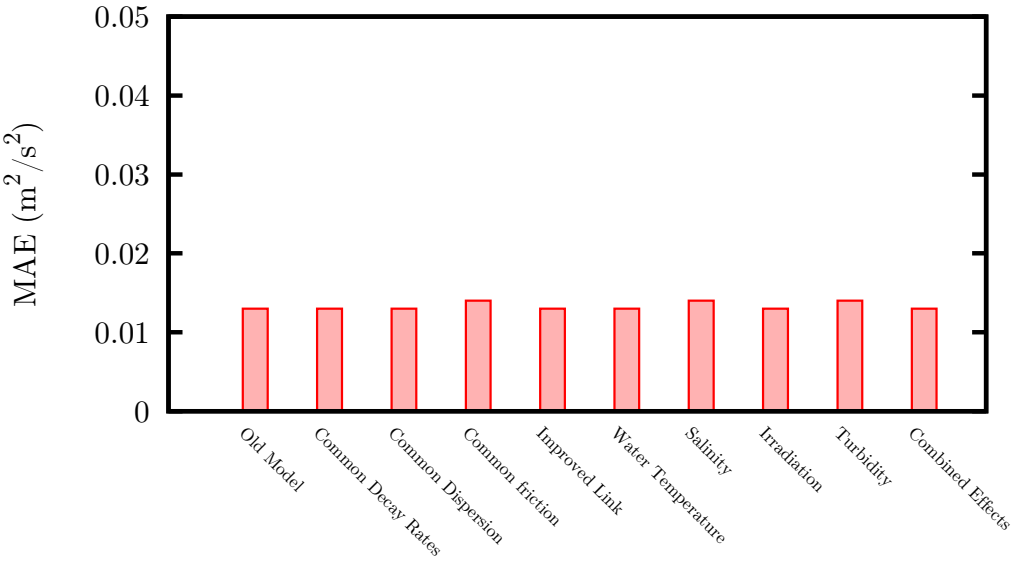

Figure B.29: Comparison of Velocities (Revised Model)

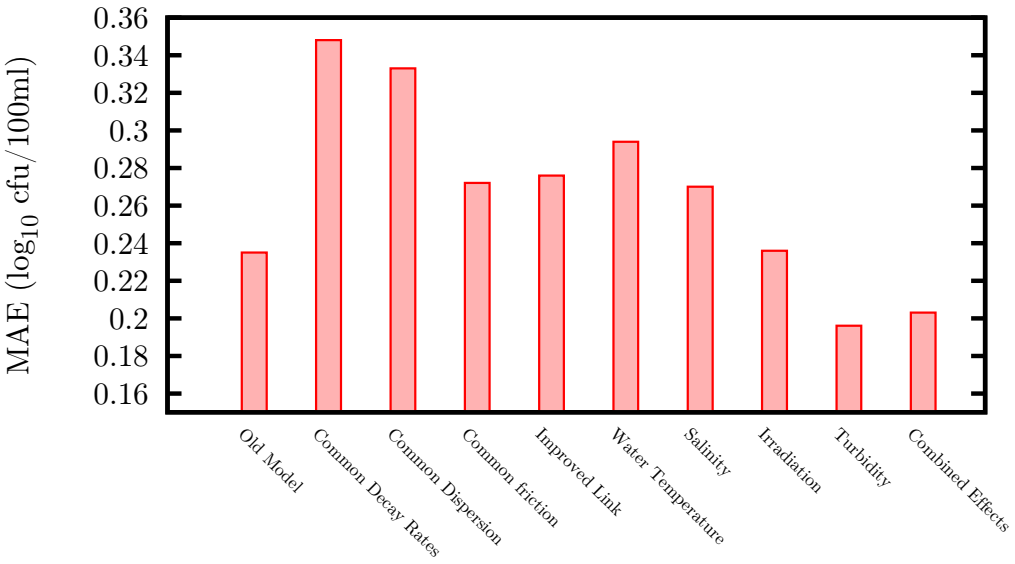

Figure B.30: Comparison of Faecal Coliform Concentrations (Revised Model)

B.4 Calibrated Model

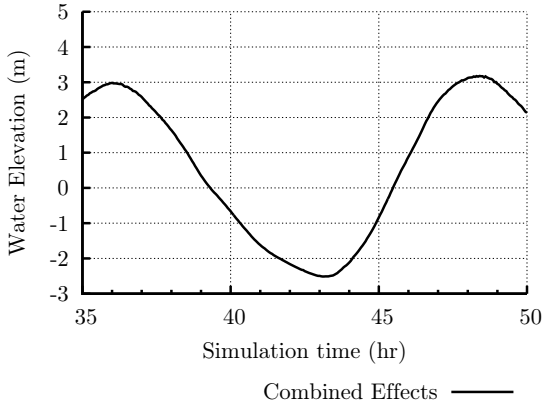

(a) Milepost 11

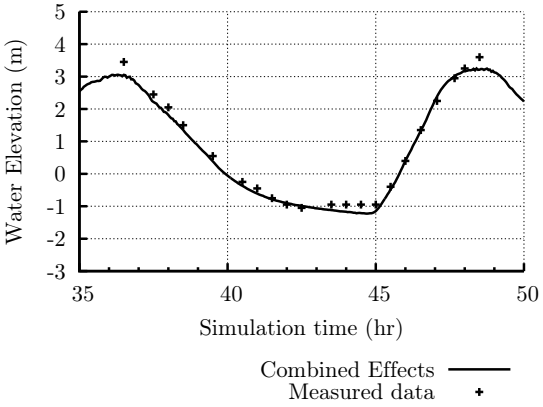

(b) Milepost 7

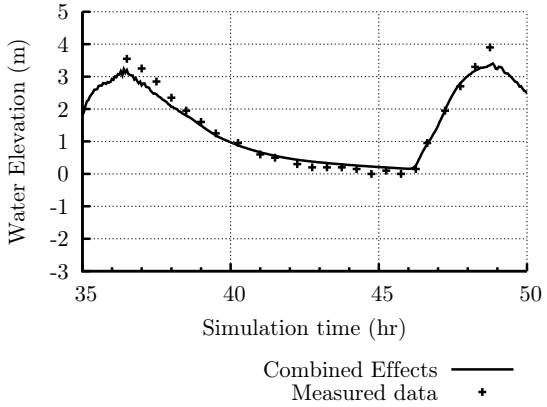

(c) Milepost 3

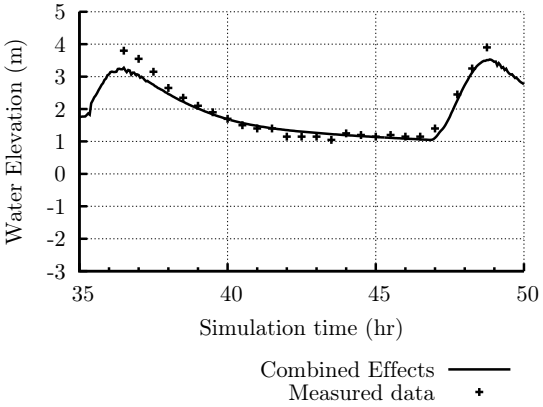

(d) Bullnose

Figure B.31: Water Elevations due to Combined Effects (Calibrated Model)

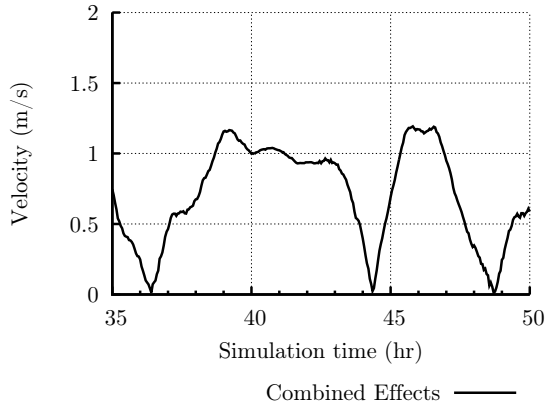

(a) Milepost 11

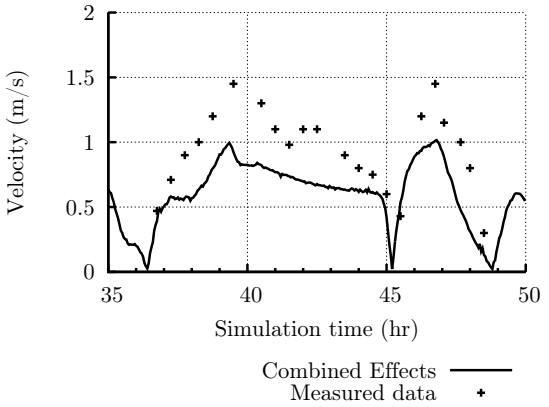

(b) Milepost 7

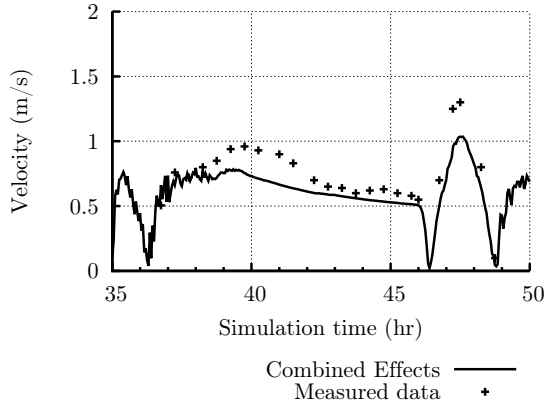

(c) Milepost 3

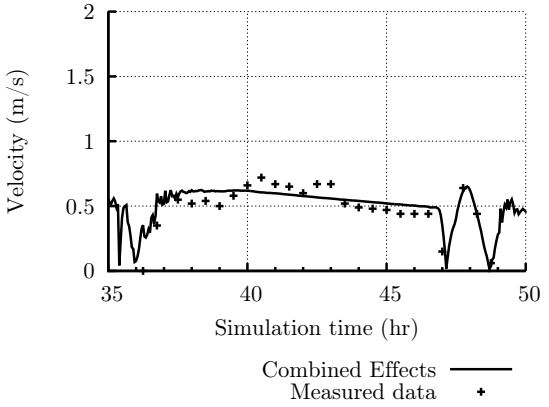

(d) Bullnose

Figure B.32: Velocities due to Combined Effects (Calibrated Model)

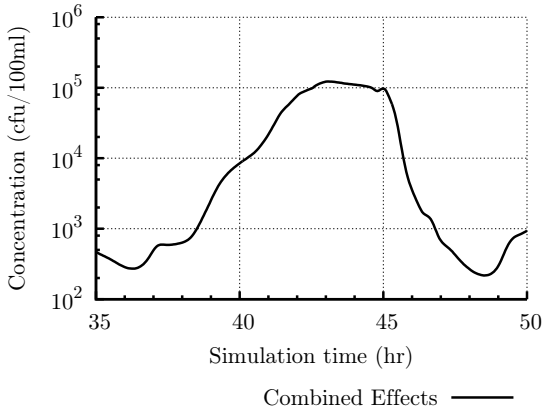

(a) Milepost 11

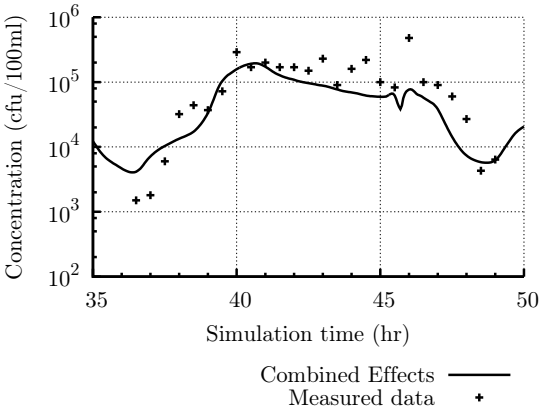

(b) Milepost 7

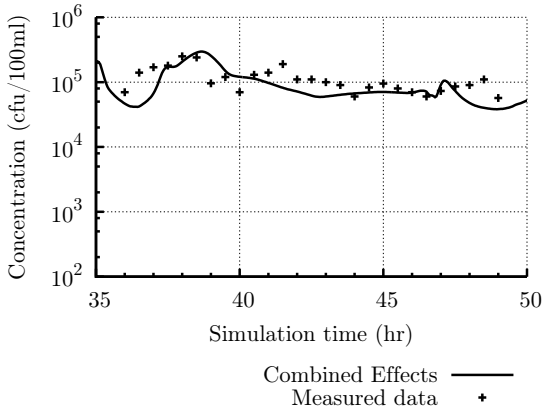

(c) Milepost 3

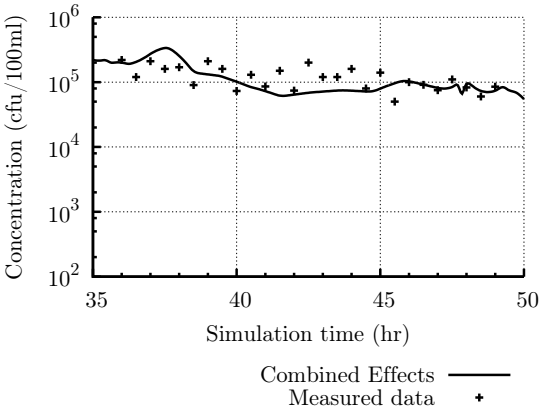

(d) Bullnose

Figure B.33: Faecal Coliform Concentrations due to Combined Effects (Calibrated Model)

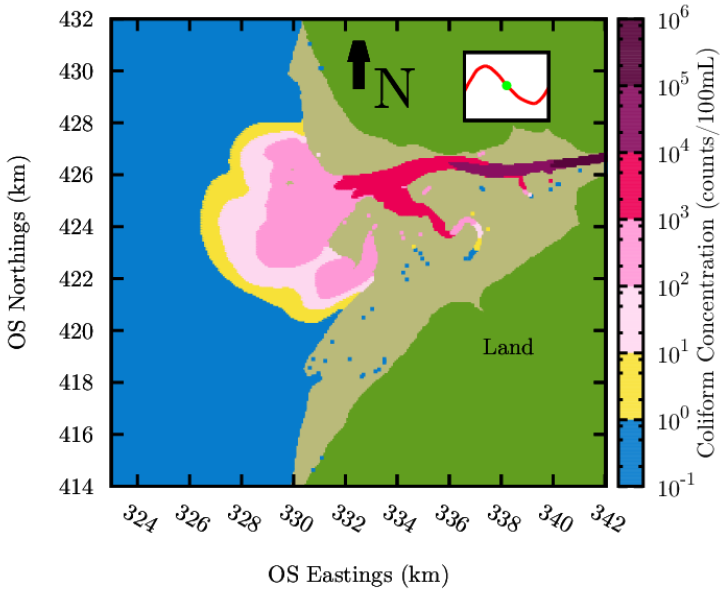

Figure B.34: Faecal Coliform at Mid Ebb due to Combined Effects (Calibrated Model)

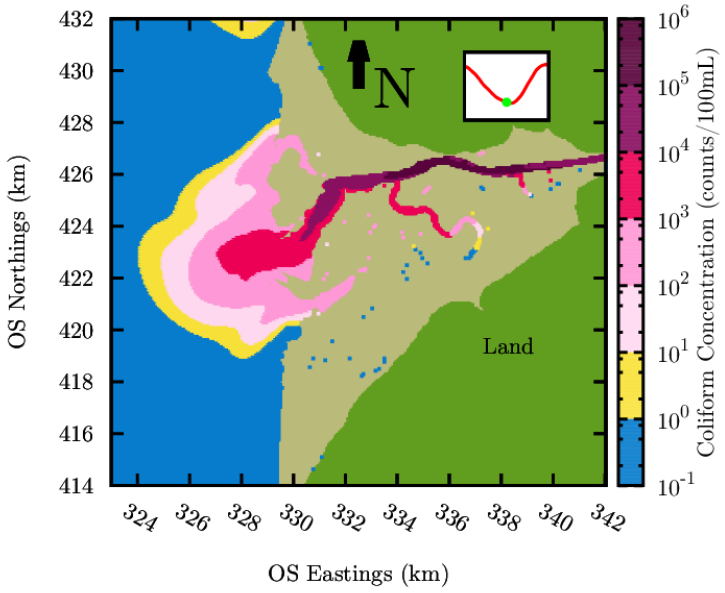

Figure B.35: Faecal Coliform at Low Tide due to Combined Effects (Calibrated Model)

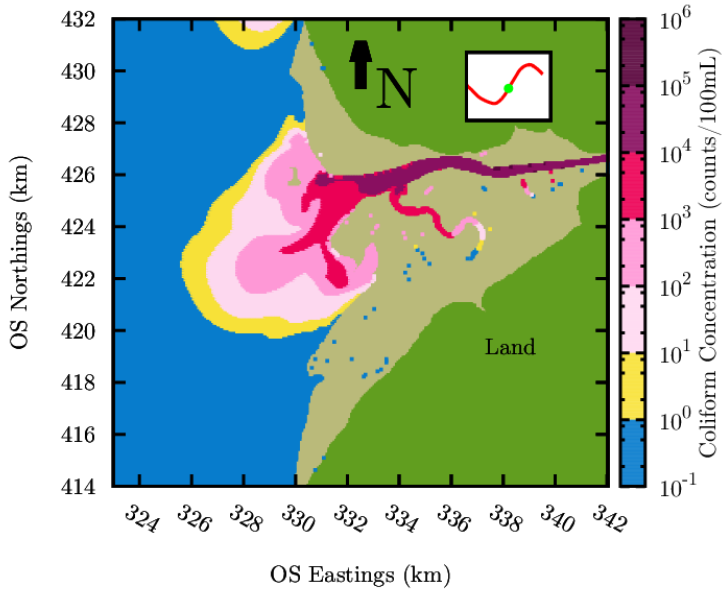

Figure B.36: Faecal Coliform at Mid Flood due to Combined Effects (Calibrated Model)

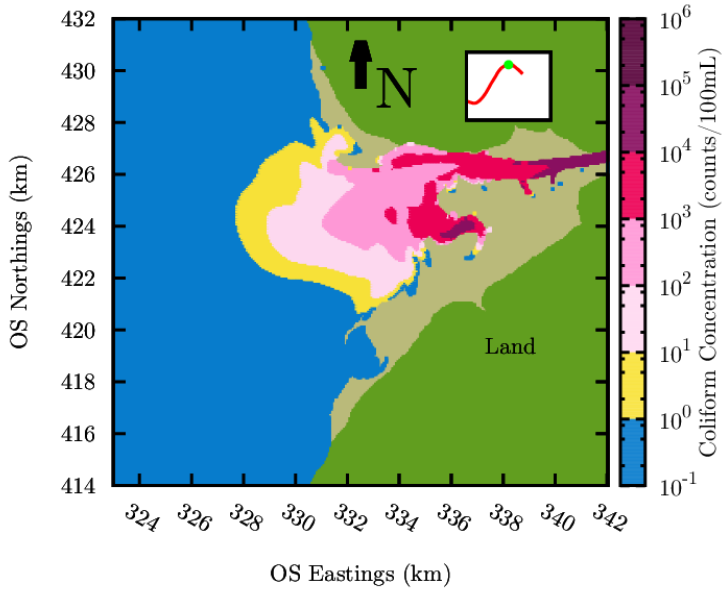

Figure B.37: Faecal Coliform at High Tide due to Combined Effects (Calibrated Model)

B.5 Comparison of C2C Scenarios (Calibrated Model)

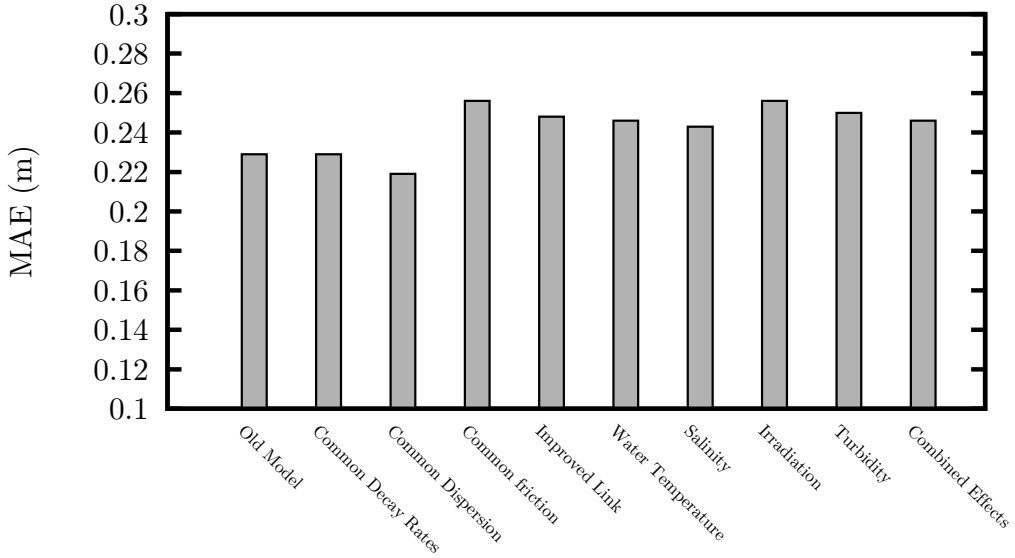

Figure B.38: Comparison of Elevations (Calibrated Model)

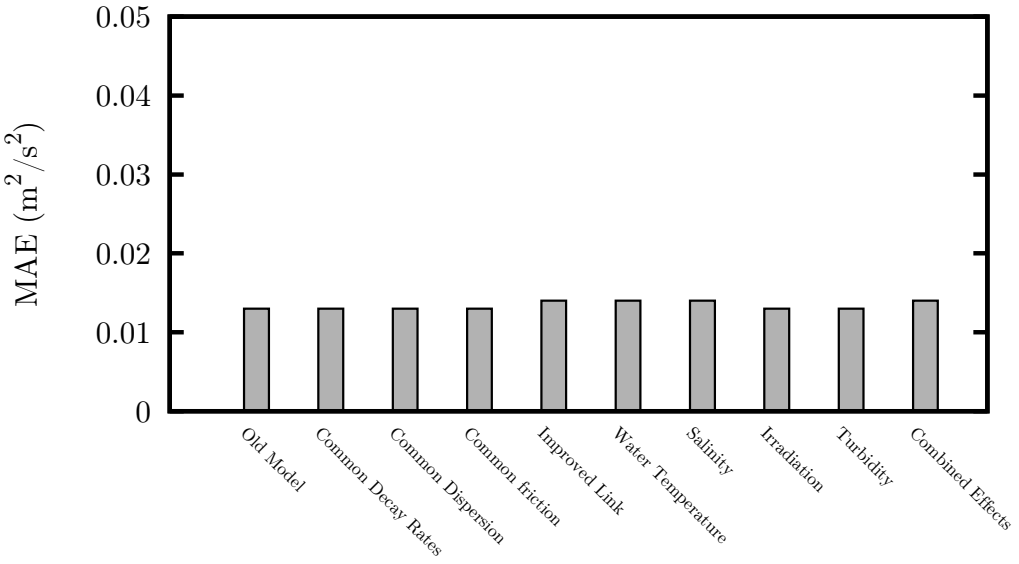

Figure B.39: Comparison of Velocities (Calibrated Model)

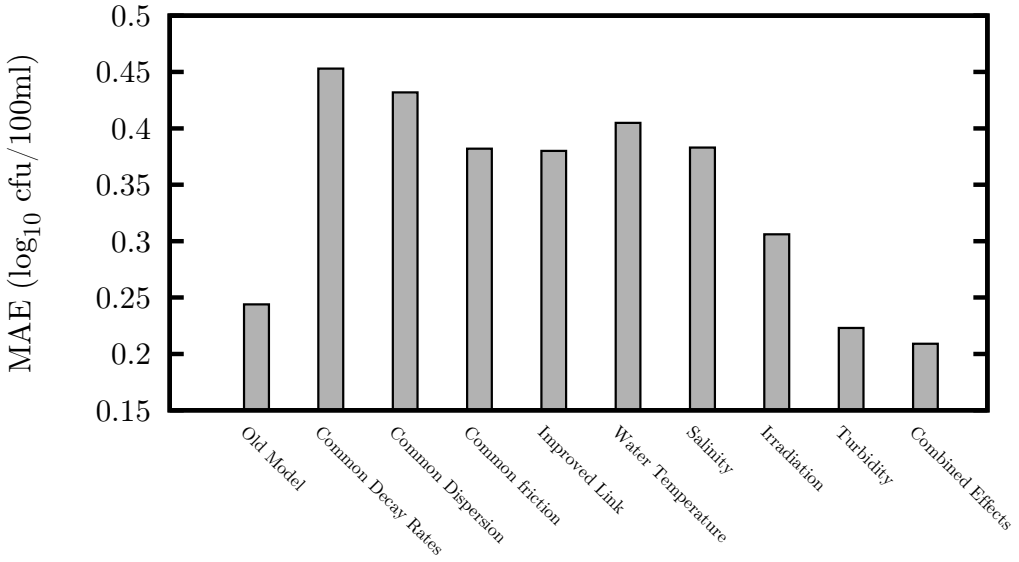

Figure B.40: Comparison of Faecal Coliform Concentrations (Calibrated Model)

Appendix C

Thames Estuary: Input Data

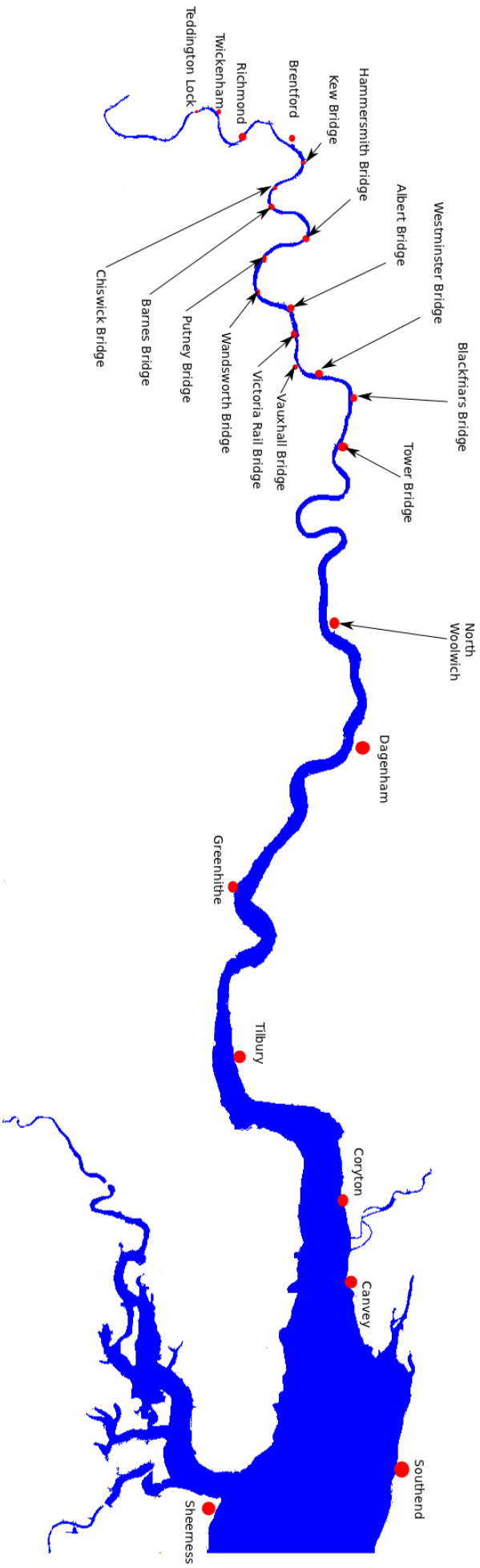

Figure C.1: Thames Estuary

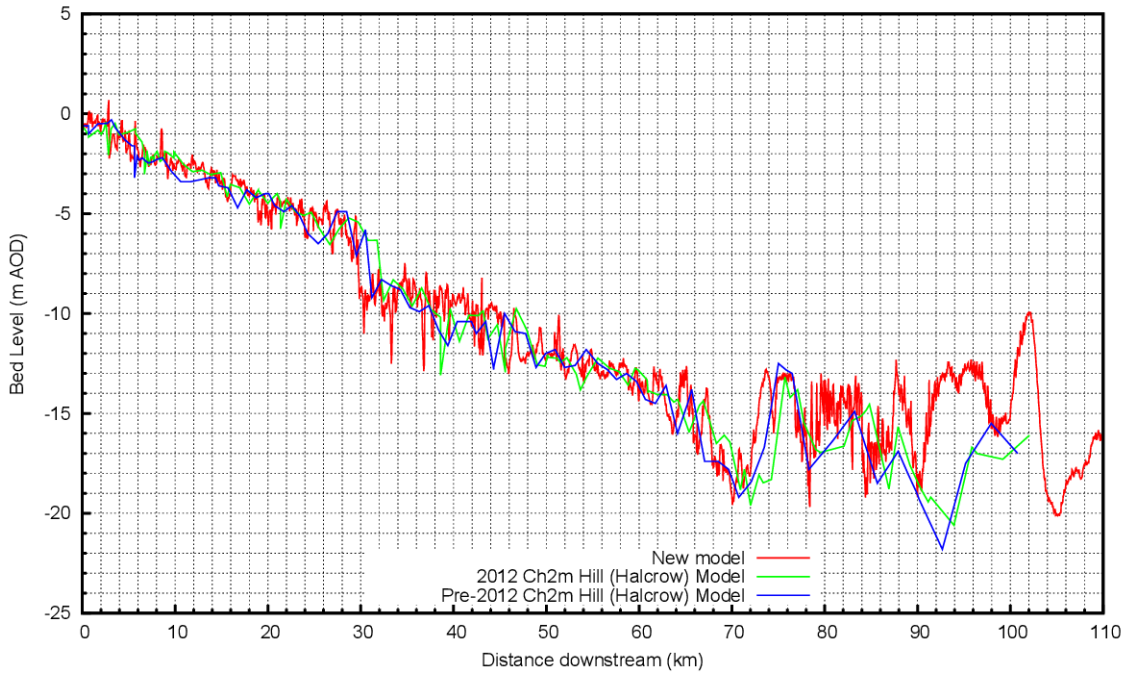

Figure C.2: Longitudinal section through new Thames Estuary model

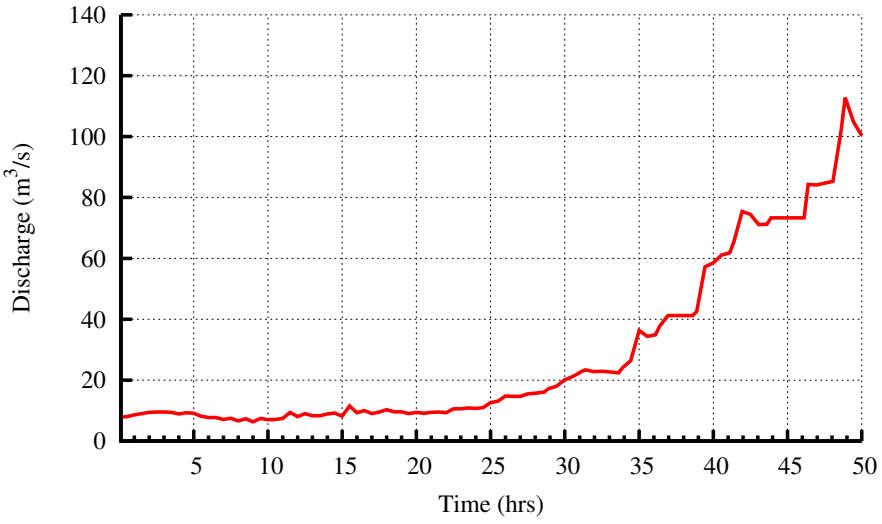

Figure C.3: Upstream flow boundary

Appendix D

Thames Estuary: Results

D.1 Hydrodynamics

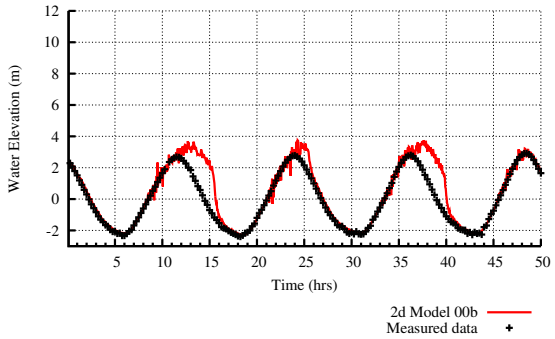

(a) Southend

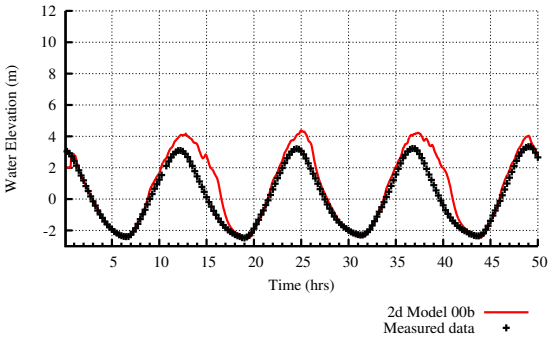

(b) Tilbury

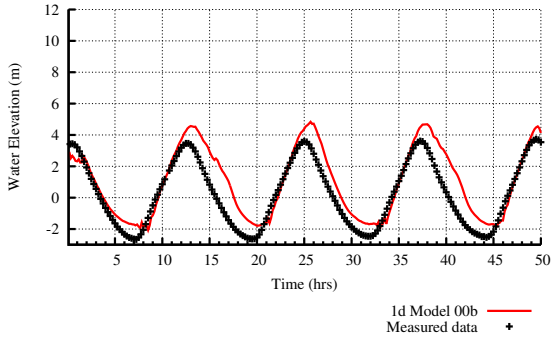

(c) North Woolwich

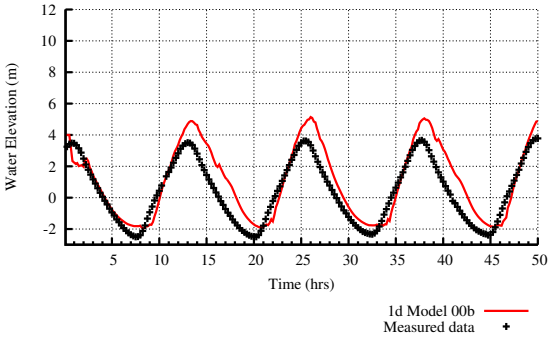

(d) Tower Bridge

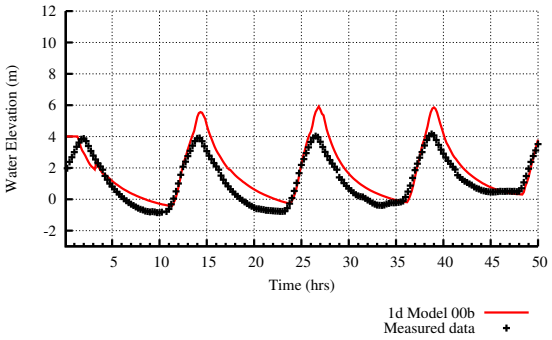

(e) Richmond

Figure D.1: Water Elevations

Appendix E

GPU Code

E.1 Input Files

```
input_"grp_name"/
├── para_cmn.csv ..... Main parameters for both 1D and 2D models
├── props_1d.csv ..... Parameters for 1D model
├── props_2d.csv ..... Parameters for 2D model
├── timprt.csv simulation times when output data for whole 2D grid is required
├── bnd1/
│   ├── hyd_bdnmtm.csv
│   ├── hyd_bnd01.csv
│   ├── hyd_ltnmtm.csv
│   ├── hyd_lat01.csv
│   ├── sol_C02_bdnmtm.csv
│   ├── sol_C02_bnd01.csv
│   ├── sol_C02_ltnmtm.csv
│   └── sol_C02_lat01.csv
├── geo1/
│   ├── 00b_nodeprops_1d.csv
│   ├── 00b_reachprops_1d.csv
│   ├── 00b_bndprops_1d.csv
│   ├── 00b_latprops_1d.csv
│   ├── 00b_trapred_1d.csv
│   ├── 00b_traprops_1d.csv
│   └── rch01/
│       └── 00b_node00001_sect_1d.csv
├── bnd2_"bndname"/
│   ├── bnd2_"bndname"_ref_nmtm.csv
│   ├── bnd2_"bndname"_ref01.csv
│   ├── bnd2_"bndname"_outref.csv
│   ├── bnd2_"bndname"_np_grid.csv
│   ├── bnd2_"bndname"_ibd01_bnddata.csv
│   └── bnd2_"bndname"_jbd01_bnddata.csv
├── geo2/
│   ├── "grp_name"_bedlc.csv
│   ├── "grp_name"_iobd.csv
```

E.2 Source Files

```
cpp/
├── autocalibrate.h
├── autocalibrate.cpp
├── cfdcmn.h
├── cfdcmn.cpp
├── cfd_prog.h
├── cfd_prog.cpp
├── global.h
├── global.cpp
├── m1D_types.h
├── m1D_types.cpp
├── m1D_fns.h
├── m1D_fns.cpp
├── m1D_input.h
├── m1D_input.cpp
├── m1D_output.h
├── m1D_output.cpp
├── m1D_main.h
├── m1D_main.cpp
├── m2D_types.h
├── m2D_types.cpp
├── m2D_fns.h
├── m2D_fns.cpp
├── m2D_input.h
├── m2D_input.cpp
├── m2D_output.h
├── m2D_output.cpp
├── m2D_main.h
├── m2D_main.cpp
├── main.cpp
├── main_lnk.h
├── output_lnk.h
├── output_lnk.cpp
```

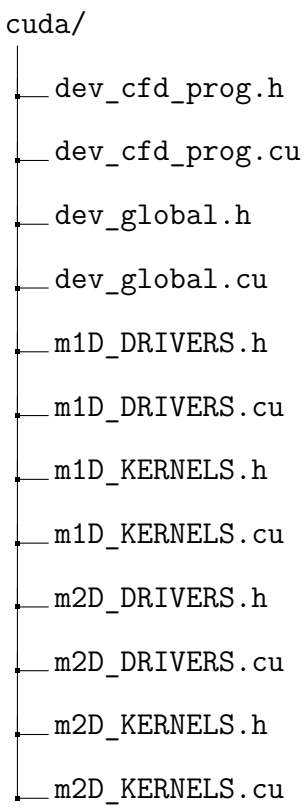

Figure E.3: Cuda Source Files

E.3 Functions

```
main(main.cpp) ..... program starts here
├── run_modcase(cfd_prog.cpp) ..... calibration branch available here
│   └── analyse_modcase(cfd_prog.cpp) . input data variables initialised here
│       ├── get_input_data() ..... read in all input data for model
│       ├── validate_cmn() ..... validate data from para_cmn.csv file
│       ├── ini_sediment() .. calculate derived parameters needed for sediment
│       │   calculation
│       ├── initialise_files() ..... create directories needed for output data
│       ├── preprocessor_1d() ..... 1D derived parameters
│       ├── preprocessor_2d() ..... 2D derived parameters
│       ├── write_mapland() .....
│       ├── write_props_cmn()
│       ├── st_traces_cmn()
│       ├── st_traces_1d()
│       ├── st_traces_2d()
│       ├── cu_cfd_timesteps() OR cpp_cfd_timesteps()
│       ├── end_traces_cmn()
│       ├── end_traces_1d()
│       ├── end_traces_2d()
│       ├── write_results_cmn()
│       ├── dealloc_model_1d()
│       ├── free_prediction_props()
│       ├── free_boundary_2d()
│       └── free_geometry_2d()
└── cpp_prep_thames()
```

Figure E.4: BRIDIVAST_GPU Main function structure

```
cu_cfd_timesteps(dev_cfd_prog.cu) ..... calculations start here
├── gpuDeviceInit() ..... initialise GPU
├── set_constant_cmem_vars() .....
├── set_constant_dmem_vars_1d() .....
├── initl_1d() .....
├── alloc_tracepoint_pred .....
├── set_constant_dmem_vars() ..... 2D device memory
├── cu_alloc_ini_tvars() .....
├── DRIVER_INITL_TVARS() .....
├── ---------- START LOOP ----------
│   ├── DRIVER_GET_LINK_VARS
│   ├── write_hydtrace_lnk
│   ├── write_soltrace_lnk
│   ├── DRIVER_COPY_DtoH
│   ├── DRIVER_DOTRACE_TIMLINK
│   ├── DRIVER_calc_steps_2d
│   ├── calc_step_1d
│   ├── output_step_1d
│   ├── DOTRACE_PRED_1D
│   ├── DRIVER_DOTRACE_IDAT
│   ├── DRIVER_DOTRACE_PRED
│   ├── DRIVER_DOTRACE_MAP_HYD
│   └── DRIVER_DOTRACE_MAP_SOLS
├── ---------- END LOOP ----------
├── get_pred_fitness
├── free_tracepoint_pred
├── free_constant_dmem_vars
├── cu_free_tvars
├── dealloc_model_results_1d
└── free_constant_dmem_vars_1d
```

Figure E.5: BRIDIVAST_GPU cuda function structure

Appendix F

Miscellaneous numerical details

F.1 DIVAST: Hydrodynamic discretisation for second half time step

For the second half time step $\left(n+\frac{1}{2} \rightarrow n+1\right)$, the continuity equation can be written as:

$$\frac{\eta_{i,j}^{n+1}-\eta_{i,j}^{n+\frac{1}{2}}}{0.5\Delta t}+\frac{q_{x_{i+\frac{1}{2},j}}^{n+\frac{1}{2}}-q_{x_{i-\frac{1}{2},j}}^{n+\frac{1}{2}}}{\Delta x}+\frac{q_{y_{i,j+\frac{1}{2}}}^{n+1}-q_{y_{i,j-\frac{1}{2}}}^{n+1}}{\Delta y}=0 \tag{F.1}$$

And the y-direction momentum equation (4.117) can be discretised for the second half time step as:

$$\frac{q_{y_{i,j+\frac{1}{2}}}^{n+1} - q_{y_{i,j+\frac{1}{2}}}^{n}}{\Delta t} + \underbrace{\beta\frac{\left(\hat{V}\hat{q}_y\right)_{i,j+\frac{3}{2}}^{n+\frac{1}{2}} - \left(\hat{V}\hat{q}_y\right)_{i,j-\frac{1}{2}}^{n+\frac{1}{2}}}{2\Delta y} + \beta\frac{(U\hat{q}_y)_{i+\frac{1}{2},j+\frac{1}{2}}^{n+\frac{1}{2}} - (U\hat{q}_y)_{i-\frac{1}{2},j+\frac{1}{2}}^{n+\frac{1}{2}}}{\Delta x}}_{\text{advection}} =$$

$$\underbrace{-2\omega\sin\phi \quad q_{x_{i,j+\frac{1}{2}}}^{n+\frac{1}{2}}}_{\text{coriolis}} + \underbrace{\frac{\rho_a}{\rho}C_w W_y\sqrt{W_x^2+W_y^2}}_{\text{wind stress}} - \underbrace{\frac{g\left(q_{y_{i,j+\frac{1}{2}}}^{n+1} + q_{y_{i,j+\frac{1}{2}}}^{n}\right)\sqrt{\left(\hat{q}_{y_{i,j+\frac{1}{2}}}^{n+\frac{1}{2}}\right)^2 + \left(q_{x_{i,j+\frac{1}{2}}}^{n+\frac{1}{2}}\right)^2}}{2\left(H_{i,j+\frac{1}{2}}^{n+\frac{1}{2}}C_{i,j+\frac{1}{2}}^{n+\frac{1}{2}}\right)^2}}_{\text{bed stress}}$$

$$\underbrace{- gH_{i+\frac{1}{2},j}^{n+\frac{1}{2}}\left[\frac{\frac{1}{2}\left(\eta_{i,j+1}^{n+1} + \eta_{i,j+1}^{n}\right) - \frac{1}{2}\left(\eta_{i,j}^{n+1} + \eta_{i,j}^{n}\right)}{\Delta y}\right]}_{\text{pressure}} + \underbrace{2\varepsilon H_{i,j+\frac{1}{2}}^{n+\frac{1}{2}}\frac{\hat{V}_{i,j+\frac{3}{2}}^{n+\frac{1}{2}} - 2\hat{V}_{i,j+\frac{1}{2}}^{n+\frac{1}{2}} + \hat{V}_{i,j-\frac{1}{2}}^{n+\frac{1}{2}}}{\Delta y^2}}_{\text{turbulent/eddy stress}}$$

$$+ \underbrace{\varepsilon H_{i,j+\frac{1}{2}}^{n+\frac{1}{2}}\frac{\hat{V}_{i+1,j+\frac{1}{2}}^{n+\frac{1}{2}} - 2\hat{V}_{i,j+\frac{1}{2}}^{n+\frac{1}{2}} + \hat{V}_{i-1,j+\frac{1}{2}}^{n+\frac{1}{2}}}{\Delta x^2}}_{\text{turbulent/eddy stress}} + \underbrace{\varepsilon H_{i,j+\frac{1}{2}}^{n+\frac{1}{2}}\frac{U_{i-\frac{1}{2},j}^{n+\frac{1}{2}} - U_{i-\frac{1}{2},j+\frac{1}{2}}^{n+\frac{1}{2}} + U_{i-\frac{1}{2},j+1}^{n+\frac{1}{2}} + U_{i+\frac{1}{2},j+1}^{n+\frac{1}{2}}}{\Delta x\Delta y}}_{\text{turbulent/eddy stress}} \tag{F.2}$$

with $\hat{V}$, $\overline{U}$ and $\overrightarrow{q_y}$ being similar to previous expressions for x-direction at time level $n+\frac{1}{2}$ instead of n.

Note: $\varepsilon H\frac{\partial^2 U}{\partial x\partial y}$ term is ignored in current code

The tri-diagonal forms of the continuity and momentum equations for second half time step can similarly be combined to form a tri-diagonal system of equation for the y-direction:

$$\begin{bmatrix} b_j & c_j & & & & 0 \\ a_{j+\frac{1}{2}} & b_{j+\frac{1}{2}} & c_{j+\frac{1}{2}} & & & \\ & a_{j+1} & b_{j+1} & c_{j+1} & & \\ & & a_{j+\frac{3}{2}} & b_{j+\frac{3}{2}} & \ddots & \\ & & & \ddots & \ddots & c_{\text{jmax}-\frac{1}{2}} \\ 0 & & & & a_{\text{jmax}} & b_{\text{jmax}} \end{bmatrix} \begin{bmatrix} \eta_{i,j}^{n+1} \\ q_{y_{i,j+\frac{1}{2}}}^{n+1} \\ \eta_{i,j+1}^{n+1} \\ q_{y_{i,j+\frac{3}{2}}}^{n+1} \\ \vdots \\ \eta_{\text{jmax}} \end{bmatrix} = \begin{bmatrix} d_j - a_j q_{y_{i,j-\frac{1}{2}}}^{n+1} \\ d_{j+\frac{1}{2}} \\ d_{j+1} \\ d_{j+\frac{3}{2}} \\ \vdots \\ d_{\text{jmax}} - c_{\text{jmax}} q_{y_{i,\text{jmax}+\frac{1}{2}}}^{n+1} \end{bmatrix} \tag{F.3}$$

where the continuity equation recursion coefficients are:

$$\begin{aligned} a_j =& -\frac{\Delta t}{2\Delta y} \\ b_j =& 1.0 \\ c_j =& \frac{\Delta t}{2\Delta y} \\ d_j =& \eta_{i,j}^{n+\frac{1}{2}} - \frac{\Delta t}{2\Delta x}\left(q_{x_{i+\frac{1}{2},j}}^{n+\frac{1}{2}} - q_{x_{i-\frac{1}{2},j}}^{n+\frac{1}{2}}\right) \end{aligned} \tag{F.4}$$

and the momentum equation recursion coefficients are:

$$\begin{aligned} a_{j+\frac{1}{2}} =& -\frac{\Delta t}{2\Delta y} g H_{i,j+\frac{1}{2}}^{n+\frac{1}{2}} \\ b_{j+\frac{1}{2}} =& 1.0 \\ c_{j+\frac{1}{2}} =& \frac{\Delta t}{2\Delta y} g H_{i,j+\frac{1}{2}}^{n+\frac{1}{2}} \\ d_{j+\frac{1}{2}} =& q_{y_{i,j+\frac{1}{2}}}^{n} + \Delta t \times \text{coriolis} - \Delta t \times \text{advection} + \Delta t \times \text{turbulent stresses} \\ & + \Delta t \times \text{wind stress} - \Delta t \times \text{bed stress} - \Delta t \times g H_{i+\frac{1}{2},j}^{n+\frac{1}{2}} \frac{\left(\eta_{i,j+1}^{n} - \eta_{i,j}^{n}\right)}{2\Delta y} \end{aligned} \tag{F.5}$$

F.2 DIVAST flooding and drying scheme

The flooding and drying routine involves several checks which can be summarised as follows:

1. At the beginning of every half time step a drying check is performed on every wet cell

   (a) The water depths of the four cross-sections surrounding each wet cell are calculated. These depths are then compared with a bed roughness height, k_s, which can be related directly to a physical depth. If any of the calculated four side depths becomes less than k_s, then the corresponding depth and the corresponding velocity component (unit width discharge) are both equated to zero. Thus, no flow or solute flux is permitted to

cross the grid cell side until the side is again flooded.

(b) If all four depths for a wet cell are less than k_s, then the grid cell is removed from the computation. As a grid cell is removed, it is assumed that a layer of still water remains over the cell, which is sealed off, and the water elevation and the solute concentration of this dry cell are set to the corresponding values at the previous computation when the cell was still wet. The velocity components at the sides of this cell are then set to zero.

(c) The water depth at the centre of a wet cell is also calculated for each half time step. If the centre depth is less than k_s then the cell is also assumed to be dry.

(d) When the centre depth falls between a predetermined value (typically 2 to $2.5k_s$) and k_s, the cell is considered potentially dry. This cell will be assumed to be dry unless the cell is connected, by way of the depth greater than k_s to an adjacent wet cell whose water elevation is higher than that of the potential dry cell considered and the flow direction from that adjacent wet cell is towards the potentially dry cell. This is more restrictive and most potentially dry cells will be removed during this stage, thereby preventing the average depth over a cell from becoming negative or too close to k_s.

2. At the end of every half time step the flooding check is then performed on every dry cell to check for possible flooding. A currently dry cell will be returned to the computational domain if all of the following conditions are satisfied:

(a) At least one of the four surrounding grid cells is wet and the cross section connecting the dry cell to this wet cell has a depth greater than k_s;

(b) the water elevation of the surrounding wet cells is higher than that of the dry cell under consideration; and

(c) the centre depth of the dry cell is greater than k_s

If a dry grid cell is assumed to flood and thus return to the computational domain at the start of the next half time step, then the depths of the four surrounding cross-sections are first calculated. As can be seen from the above mentioned procedures, this flooding and drying method ensures that a newly flooded cell will not immediately revert to being dry and a newly dried out cell will not flood immediately again on the subsequent performance of the drying and flooding checks. This approach therefore prevents repetitive flooding and drying and the associated occurrence of water surface oscillations (Falconer and Chen, 1991).

References

Aackermann, P. E. and Pedersen, P. J. D., 2012. Development of a GPU-accelerated MIKE21 Solver for Water Wave Dynamics. B.sc. thesis, Department of Informatics and Mathematical Modelling (IMM), Technical University of Denmark.

Abbott, M. B. and Basco, D. R., 1989. Computational fluid dynamics: an introduction for engineers. Longman Scientific & Technical, 425 pp.

Ahmadian, R. and Falconer, R. A., 2012. Assessment of array shape of tidal stream turbines on hydro-environmental impacts and power output. Renewable Energy, 44(0), 318 – 327.

Ahmadian, R., Falconer, R. and Bockelmann-Evans, B., 2012. Far-field modelling of the hydro-environmental impact of tidal stream turbines. Renewable Energy, 38(1), 107 – 116.

Alderisio, K. A. and DeLuca, N., 1999. Seasonal Enumeration of Fecal Coliform Bacteria from the Feces of Ring-Billed Gulls (Larus delawarensis) and Canada Geese (Branta canadensis). Applied and Environmental Microbiology, 65(12), 5628 – 5630.

Armenio, V., 1997. An Improved MAC method (SIMAC) for unsteady high-Reynolds free surface flows. International Journal for Numerical Methods in Fluids, 24(2), 185–214.

Asuncion, M., Mantas, J. A. R. M., Castro, M. J. and Fernandez-Nieto, E., 2012. An MPI-CUDA implementation of an improved Roe method for two-layer shallow

water systems. Journal of Parallel and Distributed Computing, 72(9), 1065 – 1072. [Accelerators for High-Performance Computing].

Atkinson, T. C. and Davis, P. M., 2000. Longitudinal dispersion in natural channels: Experimental results from the River Severn, U.K. Hydrology and Earth System Sciences, 4(3), 345 – 353.

Auer, M. T. and Niehaus, S. L., 1993. Modeling fecal coliform bacteria Field and laboratory determination of loss kinetics. Water Research, 27(4), 693 – 701.

Awile, O., Buyukkececi, F., Reboux, S. and Sbalzarini, I. F., 2012. Fast neighbor lists for adaptive-resolution particle simulations. Computer Physics Communications, 183(5), 1073 – 1081.

Azamathulla, H. M. and Wu, F. C., 2011. Support vector machine approach for longitudinal dispersion coefficients in natural streams. Applied Soft Computing, 11(2), 2902–2905.

Babu, M., Das, V. K. and Vethamony, P., 2006. BOD-DO modeling and water quality analysis of a waste water outfall off Kochi, west coast of India. Environment International, 32(2), 165 – 173. [Marine Pollution and Ecotoxicology].

Bai, S. and Lung, W.-S., 2005. Modeling sediment impact on the transport of fecal bacteria. Water Research, 39(20), 5232 – 5240.

Bai, X., Wang, J., Schwab, D. J., Yang, Y., Luo, L., Leshkevich, G. A. and Liu, S., 2013. Modeling 1993-2008 climatology of seasonal general circulation and thermal structure in the Great Lakes using {FVCOM}. Ocean Modelling, 65(0), 40 – 63.

Bashitialshaaer, R., Bengtsson, L., Larson, M., Persson, K. M., Aljaradin, M. and Hossam, A.-I., 2011. Sinuosity effects on Longitudinal Dispersion Coefficient. International Journal of Sustainable Water and Environmental Systems, 2(2), 77 – 84.

Beeton, A. M., 1958. Relationship Between Secchi Disk Readings and Light Penetration in Lake Huron. American Fisheries Society Trans, 87, 73–79.

Bellair, J., Parr-Smith, G. and Wallis, I., 1977. Significance of diurnal variations in fecal coliform die-off rates in the design of ocean outfalls. Journal of the Water Pollution Control Federation, 49(9), 2022–2030.

Bockelmann, B., Fenrich, E., Lin, B. and Falconer, R., 2004. Development of an ecohydraulics model for stream and river restoration. Ecological Engineering, 22(4-5), 227 – 235.

Boussinesq, J., 1877. Essai sur la théorie des eaux courantes. 1(XXIII), 777.

Boye, B. A., Falconer, R. A. and Akande, K., 2013. Integrated water management solutions from cloud to coast: application to Ribble Basin. In: Proceedings of the 35th IAHR World Congress, volume 4.1. IAHR, Chengdu, China, 1–12.

Brezenski, F. T. and Russomanno, R., 1969. The Detection and Use of Salmonellae in Studying Polluted Tidal Estuaries. Water Pollution Control Federation, 41(5), 725–737.

Briare, C., Abadie, S., Bretel, P. and Lang, P., 2007. Assessment of {TELEMAC} system performances, a hydrodynamic case study of Anglet, France. Coastal Engineering, 54(4), 345 – 356.

Brookes, J. D., Antenucci, J., Hipsey, M., Burch, M. D., Ashbolt, N. J. and Ferguson, C., 2004. Fate and transport of pathogens in lakes and reservoirs. Environment International, 30(5), 741 – 759.

Brown, J. M. and Davies, A. G., 2009. Methods for medium-term prediction of the net sediment transport by waves and currents in complex coastal regions. Continental Shelf Research, 29(11-12), 1502 – 1514.

Buckley, R., Clough, E., Warnken, W. and Wild, C., 1998. Coliform bacteria in streambed sediment in a subtropical rainforest conservation reserve. Water Research, 32(6), 1852–1856.

Burgess, P., 2009. Variation in Light Intensity at different latitudes and seasons, effects of cloud cover and the amounts of direct and diffused light. www.ccfg.org.uk/conferences/downloads/P_Burgess.pdf. Presentation to Continuous Cover Forestry Group (CCFG) Scientific Meeting [Online; accessed July-2012].

Burton, D. J., 1994. Modelling of solute and sediment transport in the Ribble Estuary. University of Birmingham. PhD Thesis.

Burton, D. J., West, J. R., Horsington, R. W. and Randle, K., 1995. Modelling transport processes in the Ribble Estuary. Environment International, 21(2), 131–141.

Carson, E., 2006. Hydrologic modeling of flood conveyance and impacts of historic overbank sedimentation on West Fork Black's Fork, Uinta Mountains, northeastern Utah, USA. Geomorphology, 75(3-4), 368–383.

Casulli, V. and Cattani, E., 1994. Stability, accuracy and efficiency of a semi-implicit method for three-dimensional shallow water flow. Computers & Mathematics with Applications, 27(4), 99 – 112.

Chan, S., Thoe, W. and Lee, J., 2013. Real-time forecasting of Hong Kong beach water quality by 3D deterministic model. Water Research, 47(4), 1631 – 1647.

Chapra, S. C., 2008. Surface Water-Quality Modeling. Waveland Press, Incorporated, 844 pp.

Chen, Y., 1992. Numerical Modeling of Solute Transport Processes Using Higher Order Accurate Finite Difference Schemes. Ph.d. thesis, University of Bradford, England.

Chen, B.-F., 1994. Nonlinear hydrodynamic pressures by earthquakes on dam faces with arbitrary reservoir shapes. Journal of Hydraulic Research, 32(3), 401–413.

Chigbu, P., Gordon, S. and Strange, T. R., 2005. Fecal coliform bacteria disappearance rates in a north-central Gulf of Mexico estuary. Estuarine, Coastal and Shelf Science, 65(1-2), 309–318.

Cho, K. H., Cha, S. M., Kang, J.-H., Lee, S. W., Park, Y., Kim, J.-W. and Kim, J. H., 2010a. Meteorological effects on the levels of fecal indicator bacteria in an urban stream: A modeling approach. Water Research, 44(7), 2189 – 2202.

Cho, K. H., Pachepsky, Y., Kim, J. H., Guber, A., Shelton, D. and Rowland, R., 2010b. Release of Escherichia coli from the bottom sediment in a first-order creek: Experiment and reach-specific modeling. Journal of Hydrology, 391(3-4), 322 – 332.

Cho, K. H., Pachepsky, Y. A., Kim, J. H., Kim, J.-W. and Park, M.-H., 2012. The modified SWAT model for predicting fecal coliforms in the Wachusett Reservoir Watershed, USA. Water Research, 46, 4750 – 4760.

Chubarenko, I. and Tchepikova, I., 2001. Modelling of man-made contribution to salinity increase into the Vistula Lagoon (Baltic Sea). Ecological Modelling, 138(1-3), 87 – 100.

Crabill, C., Donald, R., Snelling, J., Foust, R. and Southam, G., 1999. The impact of sediment fecal coliform reservoirs on seasonal water quality in Oak Creek, {ARIZONA}. Water Research, 33(9), 2163 – 2171.

Crowther, J., Kay, D. and Wyer, M. D., 2002. Faecal-indicator concentrations in waters draining lowland pastoral catchments in the UK: relationships with land use and farming practices. Water Research, 36(7), 1725 – 1734.

Crowther, J., Wyer, M., Bradford, M., Kay, D. and Francis, C., 2003. Modelling faecal

indicator concentrations in large rural catchments using land use and topographic data. Journal of Applied Microbiology, 94(6), 962–973.

Cunha, C. and Rosman, P. C., 2005. A semi-implicit finite element model for natural water bodies. Water Research, 39(10), 2034 – 2047.

Dailey, J. E. and Harleman, D. R. F., 1972. Numerical Model for the Prediction of Transient Water Quality in Estuary Networks. Report NOAA-72120501, Massachusetts Institute of Technology, Cambridge, Massachusetts. 226p.

Deng, Z., Bengtsson, L., Singh, V. and Adrian, D., 2002. Longitudinal Dispersion Coefficient in Single-Channel Streams. Journal of Hydraulic Engineering, 128(10), 901–916.

Deng, Z., Singh, V. and Bengtsson, L., 2001. Longitudinal Dispersion Coefficient in Straight Rivers. Journal of Hydraulic Engineering, 127(11), 919–927.

Douglas, J. F., Gasiorek, J. M., Swaffield, J. A. and Jack, L. B., 2011. Fluid Mechanics. Pearson/Prentice Hall, 6 edition, 1012 pp.

Doxat, J., 1977. The Living Thames: The Restoration of a Great Tidal River. Hutchinson Benham, 96 pp.

Doyle, J. D., Tunnicliff, B., Kramer, R., Kuehl, R. and Brickler, S. K., 1992. Instability of fecal coliform populations in waters and bottom sediments at recreational beaches in Arizona. Water Research, 26(7), 979 – 988.

Drake, J., Bradford, A. and Joy, D., 2010. Application of HEC-RAS 4.0 temperature model to estimate groundwater contributions to Swan Creek, Ontario, Canada. Journal of Hydrology, 389(3-4), 390 – 398.

Dufour, A. P., 1984. Health Effects Criteria for Fresh Recreational Waters. US Environmental Protection Agency.

Edberg, S. C., LeClerc, H. and Robertson, J., 1997. Natural protection of spring and well drinking water against surface microbial contamination. II. Indicators and monitoring parameters for parasites. 23, 179–206.

Edinger, J. E. and Brady, D. K., 1974. Heat Exchange and Transport in the Environment, volume 14. John Hopkins University, Electric Power Research Institute (Palo Alto, California), 125 pp.

Elder, J. W., 1959. The dispersion of marked fluid in turbulent shear flow. Journal of Fluid Mechanics, 5, 544 – 560. Issue 04.

European Environment Agency, 2013. European bathing water quality in 2012. Technical Report No 4/2013, European Union.

European Parliament, C., 2006. Directive 2006/7/EC of the European Parliament and of the Council of 15 February 2006 concerning the management of bathing water quality and repealing Directive 76/160/EEC. In: Journal of the European Union. European Parliament, Council, 15pp.

Falconer, R. A., 1977. Mathematical Modelling of jet-forced circulation in Reservoirs and Harbours. Ph.D. thesis, University of London, London, United Kingdom. 237pp.

Falconer, R. A., 1981. Numerical Model Study of Temperature Distributions in a Harbour. Coastal Engineering Proceedings, 1(18), 454 – 472.

Falconer, R. A., 1986. Water quality simulation study of a natural harbour. Journal of Waterway, Port, Coastal and Ocean Engineering, ASCE, 112(1), 15–34.

Falconer, R. A., 1993. An introduction to nearly horizontal flows. In: Coastal, Estuarial and Harbour Engineer's Reference Book (Edited by Abbott, M. and Price, W.), chapter 2. Taylor & Francis, 27–36.

Falconer, R. A., Akande, K. and Boye, B. A., 2011. Environmental hydraulics: integrated water management solutions from cloud to coast. In: Proceedings of 3rd International Conference on Managing Rivers in the 21st Century, Penang, Malaysia. REDAC and USM Press, 4–14.

Falconer, R. A. and Chen, Y. P., 1991. An improved representation of flooding and drying and wind stress effects in a 2-D numerical model. In: Proceedings of the Institution of Civil Engineers, Part 2, Research and Theory, volume 91. 659–687.

Falconer, R. A. and Hartnett, M., 1993. Mathematical modelling of flow, pesticide and nutrient transport for fish-farm planning and management. Ocean & Coastal Management, 19(1), 37 – 57.

Falconer, R. A. and Lin, B., 1997. Three-dimensional modelling of water quality in the Humber Estuary. Water Research, 31(5), 1092–1102.

Falconer, R. A. and Lin, B., 2001. DIVAST Model Reference Manual. Hydro-environmental Research Centre, Cardiff School of Engineering, Cardiff University, The Parade, Cardiff, CF24 3AA.

Falconer, R. A., Lin, B. L. and Harpin, R., 2005. Environmental modelling in river basin management. International Journal of River Basin Management, 3(3), 169–184.

Falconer, R. A., Lin, B. and Kashefipour, S., 2001. Modelling Water Quality Processes in Riverine Systems. In: Model Validation : Perspectives in Hydrological Science (Edited by M.G.Anderson and Bates, P.), volume 14 of *Model Validation :Perspectives in Hydrological Science*, chapter 14. John Wiley and Sons, Ltd, 357–387.

Fennema, R. and Chaudhry, M., 1990. Explicit Methods for 2D Transient Free Surface Flows. Journal of Hydraulic Engineering, 116(8), 1013–1034.

Ferguson, C., de Roda Husman, A. M., Altavilla, N., Deere, D. and Ashbolt, N., 2003. Fate and Transport of Surface Water Pathogens in Watersheds. Critical Reviews in Environmental Science and Technology, 33(3), 299–361.

Fischer, H. B., 1967a. The mechanics of dispersion in natural streams. Journal of the Hydraulics Division, ASCE, 93(6), 187–216.

Fischer, H., 1967b. The Mechanics of Dispersion in Natural Streams. KH-P. W.M. Keck Laboratory of Hydraulics and Water Resources, California Institute of Technology, 14 pp.

Fischer, H. B., 1969. The effect of Bends on Dispersion in Streams. Water Resources Research, 5(2), 496 – 506.

Fischer, H. B., List, E. J., Koh, R. C. Y., Imberger, J. and Brooks, N. H., 1979. Mixing in Inland and Coastal Waters. Academic Press Inc, San Diego, 483 pp.

Fletcher, C. A. J., 1991. Computational Techniques for Fluid Dynamics: Specific Techniques for Different Flow Categories, volume 2 of *Springer Series in Computational Physics*. Springer-Verlag, Berlin, 2nd edition, 493 pp.

Fujioka, R. S., Hashimoto, H. H., Siwak, E. B. and Young, R. H., 1981. Effect of sunlight on survival of indicator bacteria in seawater. Applied and Environmental Microbiology, 41(3), 690–696.

Galland, J.-C., Goutal, N. and Hervouet, J.-M., 1991. TELEMAC: A new numerical model for solving shallow water equations. Advances in Water Resources, 14(3), 138 – 148.

Gameson, A. L. H. and Gould, D. J., 1975. Effects of solar radiation on the mortality of some terrestrial bacteria in sea water. In: Discharge of Sewage from Sea Outfalls: Proceedings of an International Symposium Held at Church House, London, 27 August to 2 September 1974 (Edited by Gameson, A. L. H.), 22. Pergamon Press, London, 209–219.

Gameson, A. and Saxon, J., 1967. Field studies on effect of daylight on mortality of coliform bacteria. Water Research, 1(4), 279 – 295.

Gao, G., Falconer, R. A. and Lin, B., 2011. Numerical modelling of sediment-bacteria interaction processes in surface waters. Water Research, 45, 1951–1960.

Garcia-Armisen, T. and Servais, P., 2007. Respective contributions of point and non-point sources of E. coli and enterococci in a large urbanized watershed (the Seine river, France). Journal of Environmental Management, 82(4), 512 – 518.

Geldreich, E. E., 1970. Applying Bacteriological Parameters to Recreational Water Quality. American Water Works Association, 62(2), 113–120.

Geldreich, E., 1978. Bacterial populations and indicator concepts in feces, sewage, stormwater and solid wastes. In: Indicators of viruses in water and food (Edited by Berg, G.). Ann Arbor Science, 51–97.

Geldreich, E. E., 1996. Pathogenic agents in freshwater resources. Hydrological Processes, 10(2), 315 – 333.

Gerba, C. P., 2000. Assessment of Enteric Pathogen Shedding by Bathers during Recreational Activity and its Impact on Water Quality. Quantitative Microbiology, 2(1), 55–68.

Godfrey, R. and Frederick, B., 1970. Stream Dispersion at Selected Sites. Geological Survey professional paper. U.S. Government Printing Office, 38 pp.

Goyal, S. M., Gerba, C. P. and Melnick, J. L., 1977. Occurrence and distribution of bacterial indicators and pathogens in canal communities along the Texas coast. Applied and Environmental Microbiology, 34(2), 139–149.

Guber, A. K., Shelton, D. R., Pachepsky, Y. A., Sadeghi, A. M. and Sikora, L. J., 2006. Rainfall-Induced Release of Fecal Coliforms and Other Manure

Constituents: Comparison and Modeling. Applied Environmental Microbiology, 72(12), 7531–7539.

Guoqing, L., Yanran, Z., Yuguo, S., Xilai, Z. and Chengcheng, W., 2012. Optimal Design of Wetland Ecological Water in the Shuangtaizi Estuary, Panjin. Procedia Environmental Sciences, 12, Part B(0), 1404 – 1410. [2011 International Conference of Environmental Science and Engineering].

Hansen, I. S., 1996. Aquatic numerical modelling - A management tool regarding dispersion and decay of pollutants. Resources, Conservation and Recycling, 16, 167 – 177.

Henderson, F. M., 1966. Open channel flow. Macmillan Publishing Co., 522 pp.

Hipsey, M. R., Antenucci, J. P. and Brookes, J. D., 2008. A generic, process-based model of microbial pollution in aquatic systems. Water Resources Research, 44(7), 1–26.

Howell, J. M., Coyne, M. S. and Cornelius, P. L., 1995. Fecal Bacteria in Agricultural Waters of the Bluegrass Region of Kentucky. Journal of Environmental Quality, 24(3), 411 – 419. Plant and Soil Sciences Faculty Publications.

Huang, W. and Foo, S., 2002. Neural network modeling of salinity variation in Apalachicola River. Water Research, 36(1), 356 – 362.

Hunter, N. M., Bates, P. D., Neelz, S., Pender, G., Villanueva, I., Wright, N. G., Liang, D., Falconer, R. A., Lin, B., Waller, S., Crossley, A. J. and Mason, D. C., 2008. Benchmarking 2D hydraulic models for urban flooding. In: Proceedings of the Institution of Civil Engineers: Water Management, volume 161. 13 – 30.

Jones, J. E. and Davies, A. M., 2006. Application of a finite element model (TELEMAC) to computing the wind induced response of the Irish Sea. Continental Shelf Research, 26(12-13), 1519 – 1541. [Recent Developments in

Physical Oceanographic Modelling: Part III] [Recent Developments in Physical Oceanographic Modelling: Part III].

Kalyanapu, A. J., Shankar, S., Pardyjak, E. R., Judi, D. R. and Burian, S. J., 2011. Assessment of {GPU} computational enhancement to a 2D flood model. Environmental Modelling & Software, 26(8), 1009 – 1016.

Kashefipour, S., 2002. Modelling Flow, Water Quality and Sediment Transport Processes in Riverine Basins. Ph.D. thesis, Cardiff University, UK.

Kashefipour, S. M. and Falconer, R. A., 2002. Longitudinal dispersion coefficients in natural channels. Water Research, 36(6), 1596–1608.

Kashefipour, S. M., Lin, B. and Falconer, R. A., 2006. Modelling the fate of faecal indicators in a coastal basin. Water Research, 40(7), 1413–1425.

Kashefipour, S., Lin, B., Harris, E. and Falconer, R. A., 2002. Hydro-environmental modelling for bathing water compliance of an estuarine basin. Water Research, 36(7), 1854–1868.

Kay, D., Jones, F., Wyer, M., Fleisher, J., Salmon, R., Godfree, A., Zelenauch-Jacquotte, A. and Shore, R., 1994. Predicting likelihood of gastroenteritis from sea bathing: results from randomised exposure. The Lancet, 344(8927), 905 – 909.

Kay, D., Stapleton, C., Wyer, M., McDonald, A., Crowther, J., Paul, N., Jones, K., Francis, C., Watkins, J., Wilkinson, J., Humphrey, N., Lin, B., Yang, L., Falconer, R. and Gardner, S., 2005a. Decay of intestinal enterococci concentrations in high-energy estuarine and coastal waters: towards real-time T90 values for modelling faecal indicators in recreational waters. Water Research, 39(4), 655–667.

Kay, D., Wyer, M., Crowther, J., Stapleton, C., Bradford, M., McDonald, A., Greaves, J., Francis, C. and Watkins, J., 2005b. Predicting faecal indicator fluxes using digital land use data in the UK's sentinel Water Framework Directive catchment: The Ribble study. Water Research, 39(16), 3967–3981.

Kay, D., Wyer, M. D., Crowther, J., Wilkinson, J., Stapleton, C. and Glass, P., 2005c. Sustainable reduction in the flux of microbial compliance parameters from urban and arable land use to coastal bathing waters by a wetland ecosystem produced by a marine flood defence structure. Water Research, 39(14), 3320–3332.

Kim, G., Yur, J. and Kim, J., 2007. Diffuse pollution loading from urban stormwater runoff in Daejeon city, Korea. Journal of Environmental Management, 85(1), 9 – 16.

Kinsman, B., 2002. Wind Waves: Their Generation and Propagation on the Ocean Surface. Dover Phoenix Editions. Dover Publications, 676 pp.

Koussis, A. and Rodriguez-Mirasol, J., 1998. Hydraulic Estimation of Dispersion Coefficient for Streams. Journal of Hydraulic Engineering, 124(3), 317–320.

Kueh, C., Tam, T.-Y., Lee, T., Wong, S., Lloyd, O., Yu, I., Wong, T., Tam, J. and Bassett, D., 1995. Epidemiological study of swimming-associated illnesses relating to bathing-beach water quality. Water Science and Technology, 31, 1 – 4. [Health-Related Water Microbiology 1994] [Selected Proceedings of the International Symposium organised by the {IAWQ} Specialist Group on Health-related Water Microbiology as part of Water Quality International '94, 17th Biennial Conference of the International Association on Water Quality].

Kuo, J.-T., Wang, Y.-Y. and Lung, W.-S., 2006. A hybrid neural-genetic algorithm for reservoir water quality management. Water Research, 40(7), 1367 – 1376.

Lai, C., 1977. Computer Simulation of Two-dimensional Unsteady Flows in Estuaries and Embayments by the Method of Characteristics: Basic Theory and the Formulation of the Numerical Method. Water-resources investigations. U.S. Geological Survey, 72 pp.

Lamb, H., 1932. Hydrodynamics. Cambridge University Press, 6th edition, 768 pp.

Leonard, B. P., 1979. A stable and accurate convective modelling procedure based on quadratic upstream Interpolation. Computer Methods in Applied Mechanics and Engineering, 19, 59 – 98.

Leonard, B. P., 1988. ULTIMATE - Universal Limiter for Transport Interpolation Modelling of the Advective Transport Equation. Technical Memorandum TM-100916 ICOMP-88-11, NASA, Institute for Computational Mechanics in Propulsion Lewis Research Center Cleveland, Ohio 44135.

Leonard, B., 1991. The ULTIMATE conservative difference scheme applied to unsteady one-dimensional advection. Computer Methods in Applied Mechanics and Engineering, 88(1), 17 – 74.

Levasseur, A., Shi, L., Wells, N. C., Purdie, D. A. and Kelly-Gerreyn, B. A., 2007. A three-dimensional hydrodynamic model of estuarine circulation with an application to Southampton Water, {UK}. Estuarine, Coastal and Shelf Science, 73(3-4), 753 – 767.

LeVeque, R., 2002. Finite Volume Methods for Hyperbolic Problems. Cambridge Texts in Applied Mathematics. Cambridge University Press, 558 pp.

Liang, D., Falconer, R. A. and Lin, B. L., 2007. Linking one- and two-dimensional models for free surface flows. Proceedings of the ICE - Water Management, 160(3), 145 – 151.

Lin, B. and Falconer, R. A., 1995. Modelling Sediment Fluxes in Estuarine Waters Using a Curvilinear Coordinate Grid System. Estuarine, Coastal and Shelf Science, 41, 413–428.

Lin, B., Syed, M. and Falconer, R. A., 2008. Predicting faecal indicator levels in estuarine receiving waters-An integrated hydrodynamic and ANN modelling approach. Environmental Modelling & Software, 23(6), 729–740.

Liu, H., 1977. Predicting dispersion coefficient of stream. Journal of the Hydraulics Division, ASCE, 103(1), 59 – 69.

Liu, G. R., 2010. Meshfree Methods: Moving Beyond the Finite Element Method. CRC Press Taylor & Francis Group, 2 edition, 770 pp.

Lu, G. Y. and Wong, D. W., 2008. An adaptive inverse-distance weighting spatial interpolation technique. Computers & Geosciences, 34(9), 1044 – 1055.

Lyons, M., 1997. The dynamics of suspended sediment transport in the ribble estuary. Water, Air, and Soil Pollution, 99(1-4), 141–148.

Magazine, M., Pathak, S. and Pande, P., 1988. Effect of Bed and Side Roughness on Dispersion in Open Channels. Journal of Hydraulic Engineering, 114(7), 766–782.

Maier, H. R., Jain, A., Dandy, G. C. and Sudheer, K., 2010. Methods used for the development of neural networks for the prediction of water resource variables in river systems: Current status and future directions. Environmental Modelling & Software, 25(8), 891 – 909.

Mancini, J. L., 1978. Numerical estimates of coliform mortality rates under various conditions. Water Pollution Control Federation, 50(11), 2477–2484.

Mansilha, C. R., Coelho, C. A., Heitor, A. M., Amado, J., Martins, J. P. and Gameiro, P., 2009. Bathing waters: New directive, new standards, new quality approach. Marine Pollution Bulletin, 58(10), 1562 – 1565.

Massey, B. S. and Ward-Smith, J. A., 2006. Mechanics of Fluids. Number 1 in Mechanics of Series. Taylor & Francis, illustrated edition, 722 pp.

McCambridge, J. and McMeekin, T., 1979. Protozoan predation of Escherichia coli in estuarine waters. Water Research, 13(7), 659 – 663.

McCambridge, J. and McMeekin, T. A., 1981. Effect of solar radiation and predacious microorganisms on survival of fecal and other bacteria. Applied and Environmental Microbiology, 41(5), 1083–1087.

McDonald, A. and Kay, D., 1981. Enteric bacterial concentrations in reservoir feeder streams: baseflow characteristics and response to hydrograph events. Water Research, 15(8), 961 – 968.

McQuivey, R. and Keefer, T., 1974. A Simple Method for Predicting Dispersion in Streams. Journal Environmental Div, ASCE, 100, 997 – 1011.

Motamarri, S. and Boccelli, D. L., 2012. Development of a neural-based forecasting tool to classify recreational water quality using fecal indicator organisms. Water Research, 46(14), 4508 – 4520.

Moulinec, C., Denis, C., Pham, C.-T., RougÃ©, D., Hervouet, J.-M., Razafindrakoto, E., Barber, R., Emerson, D. and Gu, X.-J., 2011. TELEMAC: An efficient hydrodynamics suite for massively parallel architectures. Computers & Fluids, 51(1), 30 – 34.

Neelz, S. and Pender, G., 2009. Desktop review of 2D hydraulic modelling packages. Technical Report SC080035, Environment Agency.

Neelz, S. and Pender, G., 2010. delivering benefits through evidence: Benchmarking of 2D Hydraulic modelling packages. Technical Report SC080035/SR2, Environment Agency.

Nicholis, G., 2006. Infection risks from water in natural and man-made environments. Eurosurveillance, 11, 76–78.

NVIDIA, 2011a. CUDA C Best Practices Guide. Design Guide DG-05603-001_v4.0, NVIDIA.

NVIDIA, 2011b. NVIDIA CUDA C Programming Guide. Manual Version 4.1, NVIDIA.

NVIDIA, 2012. Tesla Kepler GPU accelerators. Datasheet, NVIDIA.

Oke, T., 1987. Boundary Layer Climates. University Paperbacks. Methuen, 2nd edition.

Oliver, R. L., Hart, B. T., Olley, J., Grace, M., Rees, C. and Caitcheon, G., 1999. The Darling River : Algal growth and the cycling and sources of nutrients. http://www2.mdbc.gov.au/___data/page/307/darling_algal_growth-whole.pdf, Murray-Darling Basin Commission Project M386.

Orlob, G. T., Jorgensen, S. E., Beck, M. B., Loucks, D. P., Gromiec, M. J., Mauersberger, P., Harleman, D. R. F., Vasiliev, O. F., Jacquet, J. and Watanabe, M., 1983. Mathematical modeling of water quality: streams, lakes, and reservoirs. International Series on Applied Systems Analysis. Wiley, illustrated edition, 518 pp.

Ostfeld, A. and Salomons, S., 2005. A hybrid genetic - instance based learning algorithm for CE-QUAL-W2 calibration. Journal of Hydrology, 310(1-4), 122 – 142.

Pachepsky, Y. A. and Shelton, D. R., 2011. Escherichia Coli and Fecal Coliforms in Freshwater and Estuarine Sediments. Critical Reviews in Environmental Science and Technology, 41(12), 1067–1110.

Paglieri, L., Ambrosi, D., Formaggia, L., Quarteroni, A. and Scheinine, A., 1997. Parallel computation for shallow water flow: A domain decomposition approach. Parallel Computing, 23(9), 1261 – 1277. <ce:title>Parallel computing methods in applied fluid mechanics</ce:title>.

Pappenberger, F., Beven, K., Horritt, M. and Blazkova, S., 2005. Uncertainty in the

calibration of effective roughness parameters in HEC-RAS using inundation and downstream level observations. Journal of Hydrology, 302(1-4), 46 – 69.

Parker, F., 1961. Eddy diffusion in reservoirs and pipelines. Journal of the Hydraulics Division, ASCE, 87(3), 151 – 171.

Pond, K., 2005. Water Recreation and Disease: Plausibility of Associated Infections : Acute Effects, Sequelae, and Mortality. Emerging Issues in Water and Infectious Disease Series. World Health Organization, illustrated edition, 239 pp.

Post, D., Kinsey-Henderson, A., Stewart, L., Roth, C. and Reghenzani, J., 2003. Optimising drainage from sugar cane fields using a one-dimensional flow routing model: a case study from Ripple Creek, North Queensland. Environmental Modelling & Software, 18(8-9), 713 – 720. [The Modelling of Hydrologic Systems].

Prandtl, L., 1926. Über die ausgebildete Turbulenz. Verhandlungen des II. Internationalen Kongresses für Technische Mechanik, 62–75. Reprinted in Ludwig Prandtl Gesammelte Abhandlungen,2,736-751.

Prüss, A., 1998. Review of epidemiological studies on health effects from exposure to recreational water. International Journal of Epidemiology, 27(1), 1–9.

Rehmann, C. R. and Soupir, M. L., 2009. Importance of interactions between the water column and the sediment for microbial concentrations in streams. Water Research, 43(18), 4579 – 4589.

Richtmyer, R. D., 1963. A survey of difference methods for nonsteady fluid dynamics. 63. National Center for Atmospheric Research.

Ritter, J. A., 2010. Water Quality. Principles and practices of water supply operations. American Water Works Association.

Roache, P. J., 1972. Computational Fluid Dynamics. hermosa publishers, 434 pp.

Rodriguez, L. B., Cello, P. A., Vionnet, C. A. and Goodrich, D., 2008. Fully conservative coupling of HEC-RAS with {MODFLOW} to simulate stream-aquifer interactions in a drainage basin. Journal of Hydrology, 353(1-2), 129 – 142.

Rogers, B. D., 2013. Smoothed Particle Hydrodynamics (SPH) : A two-day short course. Course notes, University of Manchester. [Course held on 24-25th January 2013].

Rossmann, J. S. and Dym, C. L., 2009. Introduction to Engineering Mechanics : A Continuum Approach. CRC Press Taylor & Francis Group, 472 pp.

Rowinski, P. M., Piotrowski, A. and Napiorkowski, J. J., 2005. Are artificial neural network techniques relevant for the estimation of longitudinal dispersion coefficient in rivers? / Les techniques de reseaux de neurones artificiels sont-elles pertinentes pour estimer le coefficient de dispersion longitudinale en rivieres? Hydrological Sciences Journal, 50(1), null–187.

Schets, F. M., Schijven, J. F. and de Roda Husman, A. M., 2011. Exposure assessment for swimmers in bathing waters and swimming pools. Water Research, 45(7), 2392 – 2400.

Schlichting, H., 1979. Boundary-Layer Theory. McGraw-Hill, 817 pp.

Schoen, M. E., Small, M. J. and VanBriesen, J. M., 2010. Bayesian model for flow-class dependent distributions of fecal-indicator bacterial concentration in surface waters. Water Research, 44(3), 1006 – 1016.

Seo, I. and Baek, K., 2004. Estimation of the Longitudinal Dispersion Coefficient Using the Velocity Profile in Natural Streams. Journal of Hydraulic Engineering, 130(3), 227–236.

Seo, I. and Cheong, T., 1998. Predicting Longitudinal Dispersion Coefficient in Natural Streams. Journal of Hydraulic Engineering, 124(1), 25–32.

Servais, P., Garcia-Armisen, T., George, I. and Billen, G., 2007. Fecal bacteria in the rivers of the Seine drainage network (France): Sources, fate and modelling. Science of The Total Environment, 375(1-3), 152 – 167. [Human activity and material fluxes in a regional river basin: the Seine River watershed][Seine Special Issue].

Shaughnessy, E. J., Katz, I. M. and Schaffer, J. P., 2005. Introduction to fluid mechanics. Oxford University Press, 1056 pp.

Shore, J. A., 2009. Modelling the circulation and exchange of Kingston Basin and Lake Ontario with {FVCOM}. Ocean Modelling, 30(2-3), 106 – 114.

Singh, K. P., Basant, A., Malik, A. and Jain, G., 2009. Artificial neural network modeling of the river water quality: A case study. Ecological Modelling, 220(6), 888 – 895.

Sinton, L. W., Finlay, R. K. and Lynch, P. A., 1999. Sunlight Inactivation of Fecal Bacteriophages and Bacteria in Sewage-Polluted Seawater. Applied and Environmental Microbiology, 65(8), 3605–3613.

Sinton, L., Hall, C. and Braithwaite, R., 2007. Sunlight inactivation of Campylobacter jejuni and Salmonella enterica, compared with Escherichia coli,in seawater and river water. Journal of Water and Health, 5(3), 357–365.

Smith, R., 1977. Long-term dispersion of contaminants in small estuaries. Journal of Fluid Mechanics, 82(1), 129 – 146.

Smith, J., Edwards, J., Hilger, H. and Steck, T., 2008. Sediment can be a reservoir for coliform bacteria released into streams. Journal of General and Applied Microbiology, 54(3), 173–179.

Smith, R. J., Twedt, R. M. and Flanigan, L. K., 1971. Relationships of Indicator and Pathogenic Bacteria in Stream Waters. Water Pollution Control Federation, 45(8), 1736–1745.

Solic, M. and Krstulovic, N., 1992. Separate and combined effects of solar radiation, temperature, salinity, and pH on the survival of faecal coliforms in seawater. Marine Pollution Bulletin, 24(8), 411–416.

Solic, M., Krstulovic, N., Jozic, S. and Curac, D., 1999. The rate of concentration of faecal coliforms in shellfish under different environmental conditions. Environment international, 25(8), 991–1000.

Stelling, G. S., Wiersma, A. K. and Willemse, J. B. T. M., 1986. Practical Aspects of Accurate Tidal Computations. Journal of Hydraulic Engineering-asce, 112, 802 – 817.

Sutter, H., 2005. The Free Lunch Is Over : A Fundamental Turn Toward Concurrency in Software. http://www.gotw.ca/publications/concurrency-ddj.htm. [Online; accessed March-2012].

Sverdrup, H., Johnson, M. and Fleming, R., 1942. The oceans, their physics, chemistry, and general biology. Prentice-Hall, inc.

Tang, H., Kraatz, S., Wu, X., Cheng, W., Qu, K. and Polly, J., 2013. Coupling of shallow water and circulation models for prediction of multiphysics coastal flows: Method, implementation, and experiment. Ocean Engineering, 62(0), 56 – 67.

Tayfur, G. and Singh, V., 2005. Predicting Longitudinal Dispersion Coefficient in Natural Streams by Artificial Neural Network. Journal of Hydraulic Engineering, 131(11), 991–1000.

Taylor, G. I., 1954. The dispersion of matter in turbulent flow through a pipe. In: Proceedings of the Royal Society of London, volume 223. 446 – 468.

Thomann, R. and Mueller, J., 1987. Principles of surface water quality modeling and control. Harper Collins Publishers Inc, 644 pp.

Timoshenko, S. P. and Goodier, J. N., 1970. Theory of Elasticity. McGraw-Hill, 567 pp.

Toprak, Z. F., SavcI, M. E. and AvcI, C., 2004. Predicting longitudinal dispersion coefficient in natural streams using fuzzy logic. In: Hydrology: Science & Practice for the 21st Century (Edited by Webb, B., Arnell, N., Onof, C., MacIntyre, N., Gurney, R. and Kirby, C.), volume 1. 379–388.

Toro, D. M. D., 1978. Optics of turbid estuarine waters: Approximations and applications. Water Research, 12(12), 1059 – 1068.

Townsend, S., 1992. The relationships between salmonellas and faecal indicator concentrations in two pools in the Australian wet/dry tropics. Journal of Applied Microbiology, 73(2), 182–188.

United Utilities, 2013. Enhancing Preston's sewer system. http://www.unitedutilities.com/Preston.aspx. [Online; accessed June-2013].

US Environmental Protection Agency, 1986. Ambient Water Quality Criteria for Bacteria.

Valliappan, S., 1981. Continuum mechanics fundamentals. Balkema academic and technical publications. A.A. Balkema, 228 pp.

Villaret, C., Hervouet, J.-M., Kopmann, R., Merkel, U. and Davies, A. G., 2013. Morphodynamic modeling using the Telemac finite-element system. Computers & Geosciences, 53(0), 105 – 113. [Modeling for Environmental Change].

Weare, T. J., 1976. Instability in Tidal Flow Computational Schemes. Journal of the Hydraulics Division, ASCE, 102, 569 – 580.

West, J. R. and Mangat, J. S., 1986. The determination and prediction of longitudinal dispersion coefficients in a narrow shallow estuary. Estuarine, Coastal and Shelf Science, 22, 161 – 181.

Whitelaw, K. and Andrews, M. J., 1988. The Effects of Sewage Sludge Disposal on the Outer Thames Estuary. Water Science and Technology, 20(6-7), 183–191.

Wilkinson, J., Kay, D., Wyer, M. and Jenkins, A., 2006. Processes driving the episodic flux of faecal indicator organisms in streams impacting on recreational and shellfish harvesting waters. Water Research, 40(1), 153 – 161.

World Health Organization, 2003. Guidelines for safe recreational water environments. 1.

Wu, W., 2008. Computational River Dynamics. Taylor & Francis, 494 pp.

Wu, Y. and Falconer, R. A., 2000. A mass conservative 3-D numerical model for predicting solute fluxes in estuarine waters. Advances in Water Resources, 23(5), 531 – 543.

Wu, X. and Tang, H., 2010. Coupling of {CFD} model and {FVCOM} to predict small-scale coastal flows. Journal of Hydrodynamics, Ser. B, 22(5, Supplement 1), 284 – 289.

Wu, G. and Xu, Z., 2011. Prediction of algal blooming using {EFDC} model: Case study in the Daoxiang Lake. Ecological Modelling, 222(6), 1245 – 1252.

Wyer, M. D., Crowther, J. and Kay, D., 1998a. Faecal indicator organism sources and budgets for the Ogwr catchment, south Wales. Report to dwr cymru and the environment agency, CREH, University of Wales. 38pp (plus Figures and Tables).

Wyer, M. D., Jackson, G., Kay, D., Yeo, J. and Dawson, H., 1994. An Assessment of the Impact of Inland Surface Water Input to the Bacteriological Quality of Coastal Waters. Water and Environment Journal, 8(5), 459–467.

Wyer, M. D., Kay, D., Crowther, J., Whittle, J., Spence, A., Huen, V., Wilson, C., Carbo, P. and Newsome, J., 1998b. Faecal-Indicator Budgets for Recreational

Coastal Waters: A Catchment Approach. Water and Environment Journal, 12(6), 414–424.

Wyer, M. D., Kay, D., Dawson, H. M., Jackson, G. F., Jones, F., Yeo, J. and Whittle, J., 1996. Delivery of microbial indicator organisms to coastal waters from catchment sources. Water Science and Technology, 33(2), 37 – 50. [Uncertainty, Risk and Transient Pollution Events] [Selected Proceedings of the {IAWQ} Interdisciplinary International Symposium on Uncertainty, Risk and Transient Pollution Events].

Wyer, M., O'Neill, G., Kay, D., Crowther, J., Jackson, G. and Fewtrell, L., 1997. Non-outfall sources of faecal indicator organisms affecting the compliance of coastal waters with directive 76/160/EEC. Water Science and Technology, 35(11–12), 151 – 156. [Health-Related Water Microbiology 1996][Selected Proceedings of the IAWQ 8th International Symposium on Health-related Water Microbiology 1996].

Xia, J., Falconer, R. A., Lin, B. and Tan, G., 2010a. Modelling flood routing on initially dry beds with the refined treatment of wetting and drying. International Journal of River Basin Management, 8(3-4), 225–243.

Xia, J., Lin, B., Falconer, R. A. and Wang, G., 2010b. Modelling dam-break flows over mobile beds using a 2D coupled approach. Advances in Water Resources, 33(2), 171 – 183.

Xu, M., Yu, L., Zhao, Y. and Li, M., 2012. The Simulation of Shallow Reservoir Eutrophication Based on MIKE21: A Case Study of Douhe Reservoir in North China. Procedia Environmental Sciences, 13(0), 1975 – 1988. [18th Biennial {ISEM} Conference on Ecological Modelling for Global Change and Coupled Human and Natural System].

Yang, C. and bo Jiang, C., 2011. A new model for predicting bed evolution in estuarine area and its application in yellow river delta. Journal of Hydrodynamics, Ser. B, 23(4), 457 – 465.

Yang, C., Jiang, C. and Kong, Q., 2010. A graded sediment transport and bed evolution model in estuarine basins and its application to the Yellow River Delta. Procedia Environmental Sciences, 2(0), 372 – 385. [International Conference on Ecological Informatics and Ecosystem Conservation (ISEIS 2010)].

Yang, L., Lin, B., Kashefipour, S. M. and Falconer, R. A., 2002. Integration of a 1-D river model with object-oriented methodology. Environmental Modelling & Software, 17(8), 693–701.

Yuan, D., Lin, B., Falconer, R. and Tao, J., 2007. Development of an integrated model for assessing the impact of diffuse and point source pollution on coastal waters. Environmental Modelling & Software, 22(6), 871 – 879.

Yuen, M., 2008. Analytical Solutions to the Navier-Stokes Equations. Journal Mathematical Physics, 49(113102), 13.

Zeng, Y. and Huai, W., 2013. Estimation of longitudinal dispersion coefficient in rivers. Journal of Hydro-environment Research, (0), –. [In Press].

Zhang, Q. and Stanley, S. J., 1997. Forecasting raw-water quality parameters for the North Saskatchewan River by neural network modeling. Water Research, 31(9), 2340 – 2350.

Zhou, J., Falconer, R. A. and Lin, B., 2014. Refinements to the {EFDC} model for predicting the hydro-environmental impacts of a barrage across the Severn Estuary. Renewable Energy, 62(0), 490 – 505.

Zienkiewicz, O. C. and Taylor, R. L., 1989. The Finite Element Method: Basic formulation and linear, volume 1. McGraw-Hill Book Company (UK) Limited, 648 pp.